Transient Optical Picocavities Within Coupled Plasmonic Nanostructures

Jack Peter Griffiths

Nanophotonics Group

Department of Physics

University of Cambridge

This dissertation is submitted for the degree of

Doctor of Philosophy

Homerton College **September 2021**

Declaration

This thesis is the result of my own work and includes nothing which is the outcome of work done in collaboration except as declared in the Preface and specified in the text. I further state that no substantial part of my thesis has already been submitted, or, is being concurrently submitted for any such degree, diploma or other qualification at the University of Cambridge or any other University or similar institution except as declared in the Preface and specified in the text. It does not exceed the prescribed word limit for the relevant Degree Committee.

Abstract

Transient Optical Picocavities Within Coupled Plasmonic Nanostructures - Jack Peter Griffiths

Plasmonic nanocavities, such as a nanometre scale gap between a gold nanoparticle and gold mirror (NPoM), confine light beyond the free space diffraction limit. While these enhanced field intensities allow resolvable measurements of vibrational scattering from only a few hundred molecules, ensemble averaging destroys all information on individual molecular local environments.

In this thesis, I first investigate the single molecule vibrational scattering from a molecule placed into NPoM using a DNA structure. The DNA complicates the response, which is time variant with transient features suggestive of possible picocavity formation. Picocavities are transient atomic scale features on the metal surfaces which further confine fields (effective volume <1 nm^3) with strong field gradients that locally alter the rules for vibrational scattering efficiency. These can alter the spectral response of a single nearby molecule (isolating it spectrally) and were previously noted in NPoM at cryogenic temperatures.

I change the gap material to a molecular monolayer to simplify the system and explore room temperature picocavities. I use automated analysis of large experimental datasets to detect and isolate transient vibrational scattering. Picocavity generation is found to depend on the local chemical environment near the gold surface. Picocavities are observed to chemically interact with the molecule being optically probed. This perturbs bond strengths across the molecule with the strength and direction of this perturbation being highly sensitive to the relative picocavity location on a < 0.1Å scale. This single molecule – metal atom system is explored by comparing experimental data to a theoretical Density Function Theory model.

Next, I extract the spatial distribution of picocavity formation in the gap by comparing transient scattering at two simultaneous wavelengths of light. Picocavities are found to more likely form at regions of higher optical intensity within the NPoM gap. This suggests that light plays a direct role in the yet undetermined picocavity generation mechanism.

Acknowledgements

There are so many people to acknowledge and thank for the submission of this thesis that it is inevitable that I will miss people. I apologise in advance for that.

I'll start with my supervisor Jeremy Baumberg, who noticed my PhD application on the online system and contacted me despite me having (against recommendation) not spoken to him before applying. A great motivator, I am grateful for the opportunities he has provided to experience, learn and grow. It's hard to overstate the importance Bart de Nijs has had on the daily progress of my PhD. With a consistently level and pragmatic head, I firmly believe that everyone needs at least one person like Bart as both a colleague and friend. I'm grateful for the Nanophotonics group members who made me feel so welcome when I arrived including Will, Cloudy, Marie-Elena, Rohit, Marlous, Sean and Alex C de P. I couldn't have asked for better friends and collaborators to go through the PhD alongside as the likes of Demelza, Junyang, Charlie and David. I could fill this page with names of Nanophotonics members past and present, so know that if you are not named here you too helped form the friendly and collaborative work environment that I would be lucky to find again. I was fortunate to have had such fantastic collaborators outside of the research group, including Tamás Földes who has been a pleasure to work so closely alongside over the last three years.

Outside of the lab, it was The State (Andy, Sarah, Padideh, Will and Eoin) who played a big role in making Cambridge feel like home. After the first year turnover of college members, I am thankful for PhD friendships with Ezra, Joe and Guy.

I would like to thank my family, but in particular my Mum who never once doubted my goals or tried to temper my expectations.

Finally, I am grateful for Lily who is, by far, the best thing to have come out of my time in Cambridge.

List of Publications Related to This Research

1. J Griffiths, B de Nijs, R Chikkaraddy, J Baumberg. *Locating Single-Atom Optical Picocavities using Wavelength-Multiplexed Raman Scattering*. ACS Photonics (Accepted Sept 2021)

2. J Griffiths, T Földes, B de Nijs, R Chikkaraddy, D Wright, W Deacon, D Berta, C Readman, D-B Grys, E Rosta, J Baumberg. *Resolving Sub-Angstrom Ambient Motion through Reconstructions from Vibrational Spectra.* Nat. Commun. (in review Sept 2021)

3. Q Lin, S Hu, T Földes, J Huang, D Wright, J Griffiths, B de Nijs, E Rosta, J Baumberg. *Optical Suppression of Energy Barriers in Molecule-Metal binding*. Nat. Mater. (in review Sept 2021)

4. J Huang, D-B Grys, J Griffiths, B de Nijs, M Kamp, Q Lin, J Baumberg. *Tracking interfacial single-molecule pH and binding dynamics via vibrational spectroscopy.* Science Advances, 7 ,23, 2021

5. D Wright, Q Lin, D Berta, T Földes, A Wagner, J Griffiths, C Readman, E Rosta, E Reisner, J Baumberg. *Mechanistic study of immobilised molecular electrocatalyst by in-situ gap plasmon assisted spectro-electrochemistry*. Nature Catalysis, 4, 157–163, 2021

6. R Chikkaraddy, V Turek, Q Lin, J Griffiths, B de Nijs, U Keyser, J Baumberg. *Dynamics of deterministically positioned single-bond surface-enhanced Raman scattering from DNA origami assembled in plasmonic nanogaps.* J. Raman Spectrosc. 52, 2, 348-354, 2020

7. M Kamp, B de Nijs, N Kongsuwan, M Saba, R Chikkaraddy, C Readman, W Deacon, J Griffiths, S Barrow, O Ojambati, D Wright, J Huang, O Hess, O Scherman, J Baumberg. *Cascaded nanooptics to probe microsecond atomic-scale phenomena*. P.N.A.S. 177, 26, 14819-14826, 2020

8. M Cheetham, J Griffiths, B de Nijs, G Heath, S Evans, J Baumberg, R Chikkaraddy. *Out-of-Plane Nanoscale Reorganization of Lipid Molecules and Nanoparticles Revealed by Plasmonic Spectroscopy*. J. Phys. Chem. Lett. 11, 8, 2875-2882, 2020

9. C Carnegie, M Urbieta, R Chikkaraddy, B de Nijs, J Griffiths, W Deacon, M Kamp, N Zabala, J Aizpurua, J Baumberg. *Flickering nanometre-scale disorder in a crystal lattice tracked by plasmonic flare light emission*. Nat. Commun. 11, 682, 2020

10. C Carnegie, J Griffiths, B de Nijs, C Readman, R Chikkaraddy, W Deacon, Y Zhang, I Szabó, E Rosta, J Aizpurua, J Baumberg. *Room-Temperature Optical Picocavities below 1 nm3 Accessing Single-Atom Geometries*. J. Phys. Chem. Lett. 9, 24, 7146–7151, 2018

Table of Contents

Chapter 1: Introduction

1.1 The Confinement of Light

In a 2016 lecture, I learnt that optical fields could be confined beyond the diffraction limit that is imposed on the photons describing normal light. By using different solutions to Maxwell's equations (plasmons), this allows you to optically probe a smaller region of space than I was previously taught. The importance placed on the diffraction limit up to that point felt, in the moment, like some sleight-of-hand. This confinement requires you to couple light with structures of certain metals – namely gold, silver, aluminium or copper. This can be as simple as a roughened metal surface[1] but the Nanoparticle-on-Mirror (NPoM) structure used in this thesis is formed from a gold nanoparticle spaced nanometres from a gold surface (Fig. 1.1a). When illuminated at the correct resonant wavelength, this generates an enhanced field in the gap between them with an effective volume ~x10^5 smaller than what can be accomplished in free space[2].

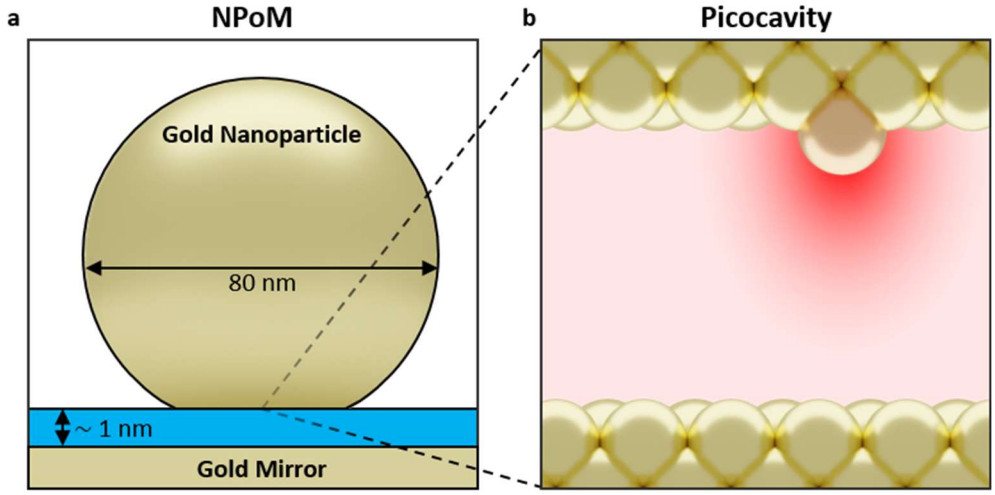

Figure 1.1 | NPoM and Picocavity Geometry. a, Schematic of the Nanoparticle-on-Mirror, formed from a nanoparticle spaced nanometres from a mirror surface. In this thesis, both nanoparticle and mirror are gold. This resonantly enhances the optical field in the gap defined by a spacer material. The possible nanoparticle crystal shapes are averaged over here to a truncated sphere. **b,** A picocavity describes a transient atomic scale structure within a plasmonic gap. This further enhances fields to a <1 nm^3 effective volume. The atomic structure around this feature is undetermined. Neither subfigure is drawn to scale.

A few months later, when I was going to meet my future PhD supervisor Prof. Jeremy Baumberg, I was reading a manuscript published by his group about the *picocavity*[3]. This describes an optical field with an effective volume of <1 nm^3 (~x10^7 smaller than the diffraction limit). It was modelled as the enhanced field around a transient atomic scale feature on the surface of the NPoM gap (Fig. 1.1b). After breaking the diffraction limit, this represents an extreme in this new regime of optical field confinement. While picocavities offer further enhancement to the confined field strength beyond that already provided in the NPoM gap, it is the field gradient generated by the localisation of this enhancement that is key to experimental observations. Extending over the scale of only a single molecule, this gradient changes how that molecule responds to Raman scattering.

Raman scattering describes the inelastic scattering of light from the vibrational modes of a material (or specifically a molecule in this thesis). This process has a low cross section that is enhanced by a factor up to 10^{12} in plasmonic cavities such as the NPoM gap. This is known as Surface Enhanced Raman Scattering (SERS). Scattering from a field that is spatially homogenous (on a molecular length scale) follows certain selection rules that govern which vibrational modes scatter efficiently. In the strong field gradient of a picocavity, these rules no longer hold. This provides a scattering signal from nominally 'dark' vibrational modes originating from a single molecule even when the NPoM contains many molecules in the gap. Without averaging over the SERS of multiple molecules, the energy of these transient modes can be observed to change over time as this molecule interacts with the environment.

Picocavities and their model as an atomic scale surface feature are intriguing for a number of reasons. By optically accessing a single molecule in ambient conditions they offer a potential route for observing catalytic, redox or other chemical reactions through the change in SERS spectrum without averaging the measurement over many molecules at different points in the chemical cycle. As the effective cavity volume is so small, the coupling between the cavity and the vibrational modes is large enough that the system is well described by the theory of optomechanics[3]. Although this theory was developed to be applied to dielectric cavities that move in response to optical radiation pressure, this offers a way to explore it at the smallest length scales. Many catalytic processes rely on the interaction of molecules with low coordination metal surfaces[4]. This is also key to many molecular electronics constructs[5]. If picocavities are found to interact with molecules within their enhanced field, and if this

interaction can be successfully characterised using SERS, then this offers a possible route towards optically interrogating these interactions.

After SERS was first reported in 1977 by Albrecht and Creighton[1], this sparked decades of debate around whether the observed enhancement is electromagnetic or chemical in nature. As presented in this work, it is now generally considered an electromagnetic effect. While transient SERS peaks with the signatures of being single molecule in origin have been reported for a few decades[6], the picocavity model is only a few years old. This means that there are many questions waiting to be answered and the possibility remains for significant modifications to the proposed theories. In my view, the key unanswered questions involve the mechanism by which picocavities are created and destroyed and the local structure of the metal surface around a picocavity. While the fields of a picocavity can be approximately modelled by using a protrusion from a homogenous metallic medium, the local atomistic structure accommodating this protrusion must influence the final fields given the structure's scale.

In this thesis, picocavities are investigated within the NPoM construct. A molecule is found that interacts strongly with the low coordination gold feature, providing a highly dynamic SERS response that can be compared to computational models of the system. Measurements of picocavities using two simultaneous SERS scattering wavelengths extracts the spatial distribution of picocavity formation and shows a greater generation rate where optical field strengths are largest. This will be useful in the future development of picocavity generation mechanisms.

1.2 Thesis Outline

Chapter 2 describes the theory behind the light-matter interactions explored and exploited in this thesis. The Drude model is derived to describe the optical properties of metals and used to explore plasmons, which are confined fields generated by coupling light to electrons near a metal surface. The NPoM construct is described in detail along with analytical approximations for the resonant frequencies at which it confines light. Raman scattering is described and some intuition is derived for how the symmetries of a vibrational mode dictate

whether or not it is able to scatter light efficiently. This also describes how these symmetries are broken under the application of a strong field gradient. Picocavities are discussed, providing context and describing their previous characterisation in NPoM at cryogenic temperatures.

Chapter 3 describes common experimental and analysis techniques that are used throughout the thesis. This includes synthesis protocols for NPoM constructs and the experimental procedures for dark field and Raman scattering measurements. The numerical techniques Finite Difference Time Domain and Density Functional Theory are described as methods for predicting optical fields and Raman scattering spectra respectively.

Chapter 4 is the first experimental chapter of this thesis which preliminarily tests NPoM constructs with a DNA Origami (DNAo) spacer as a platform for single molecule SERS. This DNAo allows individual molecules to be placed at specific locations within the NPoM gap as the structure is synthesised. While the experiments are not designed to investigate picocavities, the resulting observations lead to the picocavity research in the following chapters. In SERS measurements of the DNAo alone, transient and spectrally dynamics SERS lines reminiscent of picocavities are observed. The single molecule added to the NPoM has a high energy C≡C bond with vibrational energies spectrally separated from the DNAo response. Transient lines are also observed in this spectral region and drift in vibrational energy on the timescale of seconds suggesting undetermined interactions on this slow (compared to picosecond molecular vibrations) timescale. This system is not explored beyond preliminary observations due to the complexity of the DNAo macromolecule.

Chapter 5 simplifies the system by using the same molecular monolayer NPoM spacer from previous NPoM picocavity measurements at cryogenic temperatures[3]. By increasing the temporal resolution, transient SERS modes are observed at room temperature that pass the picocavity characterisation tests set out in that previous work. Due to the results of Chapter 4, a modified gap spacer molecule is also used with an additional nitrile group (high energy -C≡N bond) near the nanoparticle surface. Using a method for automatically detecting picocavity events over many NPoMs, it is found that this change to the molecule increases picocavity lifetimes by ∼x3. A spectral signature is identified indicating a strong interaction between the picocavity and nitrile group. This is used to show a 1:9 asymmetry in picocavity

formation from the surface of the nanoparticle compared to the gold mirror. This indicates the importance of the local chemical environment in picocavity formation and stability.

Chapter 6 explores the picocavity-nitrile interaction identified in Chapter 5. This uses experimental measurements alongside a Density Functional Theory model where the molecular vibrational energies are calculated as a gold atom (representing the picocavity) is systematically moved around the nitrile group. The interaction is shown to be energetically favourable. As the model simplifies the experimental system, the predicted vibrational energies do not agree precisely with experiment and transient SERS mode energies cannot be used to invert the position of the picocavity relative to the molecule. Instead, a method is presented to invert this position over time using the dynamics of these transient mode energies. This is achieved for a 14 s transient event which returns an trajectory for the picocavity confined near to a plane and seemingly representing thermal wandering of a picocavity adatom between interstitial sites on the nanoparticle facet.

Chapter 7 compares picocavity SERS measured simultaneously at two scattering wavelengths. As the spatial profile of the optical field strength in the NPoM gap is wavelength dependant, this is shown to provide information on the picocavity location. Methods are developed and described to isolate the transient picocavity SERS from a series of consecutive spectra. By combining numerical simulations of NPoM field distributions with an analytical model, experimental observations support greater picocavity formation where optical intensities are largest. This suggests that optical fields play a direct role in the mechanism of picocavity formation.

Chapter 8 summaries the work contained within Chapters 4-7 and discusses a future outlook.

Chapter 2: Background and Theory

2.1 Introduction

In this chapter, we will cover the relevant theory required for this thesis. This will build upon the basics of how light is described by travelling wave solutions to Maxwell's equations for electromagnetic fields. We will discuss how coupling light to free electrons at metal surfaces leads to alterative solutions (plasmons) that confine fields to sub-wavelength regions of space. We will focus in particular on the Nanoparticle-on-Mirror (NPoM) construct that supports these confined fields. Used throughout this thesis, this is formed from a gold nanoparticle narrowly separated from a gold surface and tightly confines optical fields in the gap defined between them.

While confining and enhancing an optical field modifies all light-matter interactions, we will focus on the inelastic scattering of light from the vibrational modes of matter (Raman scattering). We will discuss the rules which determine whether a vibration scatters light efficiently, which normally apply in NPoM, and how these selection rules are broken in presence of a strong field gradient.

These discussions will be combined to consider picocavities, which are a main element of study in this thesis. These transient atomic scale features on the surfaces of structures like NPoM enhance fields further in their direct vicinity. The localisation of the resulting enhanced field (effective volume <1 nm^3) generates strong field gradients which break the Raman scattering selection rules over a sub-molecule sized region of space. These therefore offer a stochastic method to optically interrogate the vibrational modes of a single molecule within an ensemble.

2.2 Light in Free Space

2.2.1 Travelling Solutions to Maxwell's Equations

Classical electromagnetic fields are described at each point of space ($\boldsymbol{x}$) and time (t) by the Macroscopic Maxwell's equations. In an environment with no external sources of charge or current, these combine to give the *wave equation* linking the evolution of electric field $\boldsymbol{E}(\boldsymbol{x}, t)$ in space to the displacement field $\boldsymbol{D}(\boldsymbol{x}, t)$ in time

$$\nabla \times \nabla \times \boldsymbol{E}(\boldsymbol{x}, t) = -\mu_0 \frac{\partial^2 \boldsymbol{D}(\boldsymbol{x}, t)}{\partial t^2} \tag{2.1}$$

through the constant vacuum permeability μ_0. When an electric field is incident upon a medium, this induces local net charge densities that influence the total surrounding field. The displacement field captures the combination of the incident electric field and medium response. The simplest description of the relation between the electric and displacement fields assumes a linear relationship between them (i.e. if the electric field doubles, the displacement field also doubles). In this regime of linear optics (and non-magnetic materials), the two fields are linked by the constant vacuum permittivity ε_0 and medium permittivity $\varepsilon(\boldsymbol{x}, t)$

$$\boldsymbol{D}(\boldsymbol{x}, t) = \varepsilon_0 \int \varepsilon(\boldsymbol{x} - \boldsymbol{x}', t - t')\, \boldsymbol{E}(\boldsymbol{x}', t')\, d\boldsymbol{x}' dt' \,. \tag{2.2}$$

As this makes the wave equation linear, its solution can be written as any superposition of harmonic plane wave solutions $\propto e^{i(\boldsymbol{k}\cdot\boldsymbol{x} - \omega t)}$ where $\boldsymbol{k}$ and ω are the wavevector and angular frequency of the plane wave respectively. Working in terms of $\boldsymbol{k}$ and ω simplifies equation 2.2 with a Fourier transform providing

$$\boldsymbol{D}(\boldsymbol{k}, \omega) = \varepsilon_0 \varepsilon(\boldsymbol{k}, \omega) \boldsymbol{E}(\boldsymbol{k}, \omega). \tag{2.3}$$

The same Fourier transform converts the wave equation to

$$\boldsymbol{k} \cdot (\boldsymbol{k} \cdot \boldsymbol{E}) - k^2 \boldsymbol{E} = -\frac{\omega^2}{c^2} \varepsilon \boldsymbol{E} \tag{2.4}$$

where the vacuum speed of light $c = (\varepsilon_0 \mu_0)^{-\frac{1}{2}}$. For transverse ($\boldsymbol{k} \perp \boldsymbol{E}$) solutions, this reduces to the dispersion relation

$$k^2 = {k_0}^2 \varepsilon(\boldsymbol{k}, \omega), \qquad k_0 \equiv \frac{\omega}{c} \tag{2.5}$$

that must be satisfied by any valid solution to the wave equation. Note that for longitudinal waves ($\boldsymbol{k} \parallel \boldsymbol{E}$) there is a different constraint $\varepsilon(\boldsymbol{k}, \omega) = 0$.

We consider a simplified (but common) medium in which ε can be approximated as constant spatially ($\varepsilon(\boldsymbol{k}, \omega) = \varepsilon(\omega)$), for which the wave equation reduces further to the *Helmholtz equation*

$$\nabla^2 \boldsymbol{E} = -k_0^2 \, \varepsilon(\omega) \, \boldsymbol{E}. \tag{2.6}$$

Generally, the dielectric function $\varepsilon(\omega)$ is a complex function. When $\mathrm{Re}[\varepsilon(\omega)] > 0$ each plane wave solution component is a travelling wave describing propagating light. In quantum mechanics, these travelling wave solutions are quantised into the bosonic light particles *photons.* A medium where this is true for all ω is a *dielectric*. $\mathrm{Im}[\varepsilon(\omega)] > 0$ attenuates the strength of the field with propagation and therefore encodes the loss characteristics of the medium. When $\mathrm{Re}[\varepsilon(\omega)] < 0$, the travelling waves become evanescent solutions that decay in field strength without propagation. We briefly note the relationship of $\boldsymbol{k}$ to the wavelength of the light $\lambda = \frac{2\pi}{\mathrm{Re}[k]}$ which is a more common descriptor.

When manipulating propagating light (for example, with lenses and mirrors), it is well known that diffraction limits how tightly the field can be focussed perpendicular to the propagation direction. Fittingly, this is known as the *diffraction limit*[7]. This confinement of light of wavelength λ is limited to $\sim \lambda/2$. A similar limit is met when confining light within a dielectric optical cavity. In the simplest case where light reflects between two parallel mirrors separated by distance L, the boundary conditions at the points of reflection mean that this cavity only supports waves for which $L = \frac{n\lambda}{2}$ where n is a positive integer.

2.2.2 Quantifying Field Confinement

When light is trapped between two mirrors, it is simple to define the region of space in which the field is confined by looking at where the field strength drops to zero. If a field is instead decaying in one or more dimension (for example, if it is evanescent), this decay can be considered a form of confinement despite the field strength only approaching zero in the infinite limit. This becomes more important when talking about alternative solutions to Maxwell's equations in section 2.4.

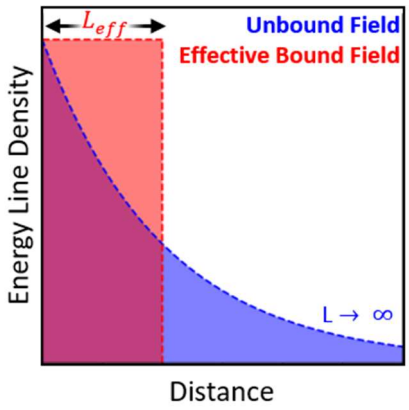

Figure 2.1 | Effective Cavity Length. A field decays in energy density exponentially with distance (blue). The maximum energy density defines a hypothetical field of uniform energy density up to length L_{ef} (red). These fields contain the same total energy. This defines the effective cavity length of the decaying field.

A common definition of the effective volume (V_{eff}) of a field relates the maximum and total energy density (u) of the field. More specifically, it is defined by the hypothetical volume that contains the same total energy as the field when filled uniformly with the field's maximum energy density[8] (Fig. 2.1). More succinctly,

$$V_{eff} = \frac{\int u \, dV}{\max[u]}. \tag{2.8}$$

This definition is consistent with relations between an optical cavity volume and, for example, Purcell spontaneous emission enhancement[9] or light-matter coupling[10].

2.3 Optical Properties of Ideal Metals

A metal is characterised by a fixed lattice of positive ions with a sea of delocalised electrons. The action of optical fields on this electron sea provides metals with a characteristic optical response. Here, we will consider the simple *Drude model* of metals. In this model, an electron is free to move within the lattice to counter any net electric fields that arise. With no external field applied, this gives the metal a net zero charge density at equilibrium with no net fields within the material. Upon the application of a harmonic field $\boldsymbol{E} = \boldsymbol{E_0}(\boldsymbol{k})\, e^{-i\omega t}$, any given electron (of charge $-e$ where e is the elementary charge) responds to the resulting force. As the electron moves away from the equilibrium position, the charge screening of surrounding electrons prevents the formation of a restoring force. Instead, this screening provides resistance to the electron motion captured within an effective electron mass m^*. The displacement of the electron ($\boldsymbol{x}$) evolves as described by Newton's 2nd law of motion

$$\frac{d^2\boldsymbol{x}}{dt^2} = -\frac{e}{m^*}\boldsymbol{E} - \gamma\frac{d\boldsymbol{x}}{dt} \tag{2.9}$$

where the parameter γ controls the strength of linear damping in the system. Searching for steady state harmonic solutions, we find that

$$\boldsymbol{x} = \frac{e}{m(\omega^2 + i\gamma\omega)}\boldsymbol{E}. \tag{2.10}$$

In section 2.2.1, the displacement field $\boldsymbol{D}$ was introduced as the sum of the incident electric field and any induced fields within the material. As the electron is displaced, an instantaneous dipole $-e\boldsymbol{x}$ is generated. A number density n of electrons responding in the metal generates a polarisation field (electron dipole moment per unit volume) of

$$\boldsymbol{P} = -ne\boldsymbol{x}. \tag{2.11}$$

The optical response of the system can therefore be written as

$$\boldsymbol{D} = \varepsilon_0\boldsymbol{E} + \boldsymbol{P} = \varepsilon_0\varepsilon\boldsymbol{E} \tag{2.12}$$

$$\varepsilon(\omega) = 1 - \frac{\omega_p^2}{\omega^2 + i\gamma\omega}, \qquad \omega_p \equiv \frac{ne^2}{\varepsilon_0 m^*} \tag{2.13}$$

where ω_p is the intrinsic plasma frequency of the metal. For noble metals (e.g. gold), this simple model must be extended to well describe the regime $\omega \gg \omega_p$ by the addition of a constant polarisation field to more realistically reflect the electronic band structure of the material[11]. This introduces the material specific dielectric constant ε_∞ such that

$$\varepsilon(\omega) = \varepsilon_\infty - \frac{\omega_p^2}{\omega^2 + i\gamma\omega}. \tag{2.14}$$

While $\varepsilon(\omega)$ is a complex function, each input parameter to the function is a real number. This can therefore be decomposed into real and imaginary components controlling the dispersion and decay of travelling wave solutions respectively. These are written as

$$\mathrm{Re}[\varepsilon(\omega)] = \varepsilon_\infty - \frac{\omega_p^2}{\omega^2 + \gamma^2} \tag{2.15}$$

$$\mathrm{Im}[\varepsilon(\omega)] = \frac{\gamma\,\omega_p^2}{\omega\,(\omega^2 + \gamma^2)}. \tag{2.16}$$

Note that as ω increases, $\mathrm{Re}[\varepsilon(\omega)]$ can switch from negative to positive in sign. This means that metals only support travelling wave solutions above a frequency threshold where the electric field direction switches too quickly to be screened effectively by electrons with finite inertia.

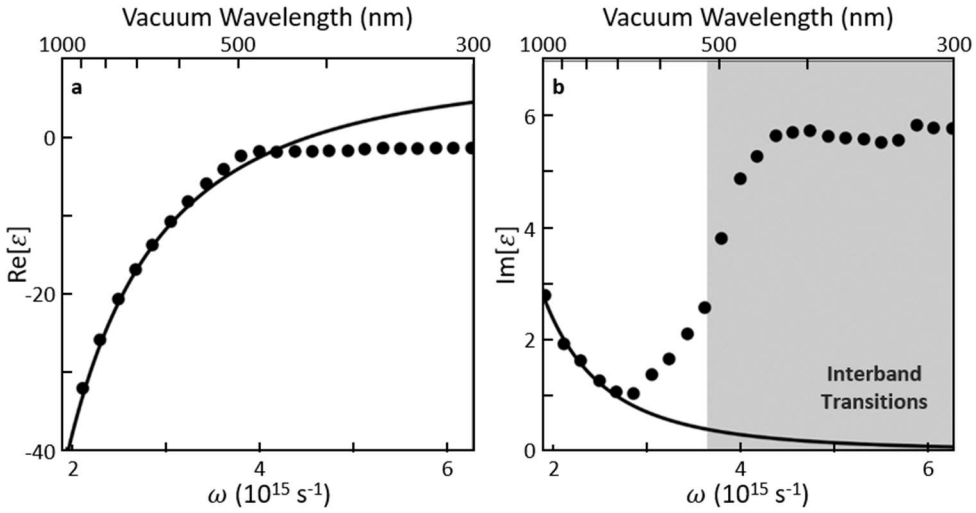

Figure 2.2 | Drude Model for Gold. The **a,** real and **b,** imaginary dielectric function of gold measured by Johnson-Christy[12] (points) compared to a Drude model approximation (line) where ε_∞ = 9.4, ω_p = 13.8 × 10^{15} s^{-1} and γ = 10^{14} s^{-1}. There is a good agreement at lower frequencies below the onset of interband transitions that are not described by the model.

This model is shown in figure 2.2 for gold along with experimental values from Johnson and Christy[12]. This model is in good agreement with the data at frequencies below the onset of electronic interband transitions. While this can be improved within the *Drude-Lorentz* model[11] by adding Lorentz-oscillator terms to the free electron response to describe these transitions, the Drude model is a good estimate for the dielectric function of gold in the wavelengths considered in this thesis (>500 nm) where the real part dominates the response.

2.4 Plasmons

Plasmon polaritons (or simply plasmons) represent alternative optical field solutions to photons that exist at the interface of metallic and dielectric materials. These include transverse (Surface Plasmon Polaritons) and longitudinal (Localised Surface Plasmon Polaritions) solutions. In both cases, these solutions contain a decaying field component in one or more dimension providing greater field confinement than is possible in free space (section 2.2). In all cases here, the optical response of any metallic mediums will be treated using the Drude model (section 2.3).

2.4.1 Surface Plasmon Polaritons

Surface Plasmon Polaritons (SPPs) are travelling wave solutions that propagate along a metal-dielectric interface. The simplest geometry that supports these solutions consists of two half-spaces separated by the flat x-y plane in Cartesian geometry such that

$$\varepsilon(\omega) = \begin{cases} \varepsilon_1(\omega) \text{ for } z < 0 \\ \varepsilon_2 \text{ for } z > 0 \end{cases}. \tag{2.17}$$

Note that ε_2 is a constant to pre-define this half-space as dielectric. We define Re[ε_2] > 0. As we search for harmonic solutions, the Helmholtz equation (equation 2.6) applies. Due to the symmetry of the system, we search for solutions propagating parallel to the interface and arbitrarily set this propagation along the x-axis. This gives

$$\boldsymbol{E}(\boldsymbol{x}) = \boldsymbol{E}_0(z)e^{i(kx-\omega t)} \tag{2.18}$$

$$\frac{\partial^2 \boldsymbol{E}_0(z)}{\partial z^2} = -(k_0^2 \varepsilon - k^2)\boldsymbol{E}_0(z) \tag{2.19}$$

with a similar equation dictating the evolution of the magnetic fields (which have not been discussed). This system of equations supports two independent sets of solutions, but only one is non-trivial describing non-zero electric field components along x and z and a non-zero magnetic component along y. These solutions decay exponentially away from the interface

$$E_{0\,x,z} \propto \begin{cases} e^{-L_1 z} \text{ for } z > 0 \\ e^{L_2 z} \text{ for } z < 0 \end{cases}. \tag{2.20}$$

Keeping the total field energy finite requires $L_1, L_2 > 0$ ensuring that the field strength does not increase without bound. At $z = 0$, field continuity constraints dictate that

$$\frac{L_1}{L_2} = -\frac{\varepsilon_1}{\varepsilon_2} \tag{2.21}$$

requiring that the real part of the dielectric function switches sign at the interface. This is satisfied, below a frequency threshold, by ε_1 representing a metallic medium. These decay lengths are given by

$$L_{1,2}^2 = k^2 - k_0^2 \varepsilon_{1,2}. \tag{2.22}$$

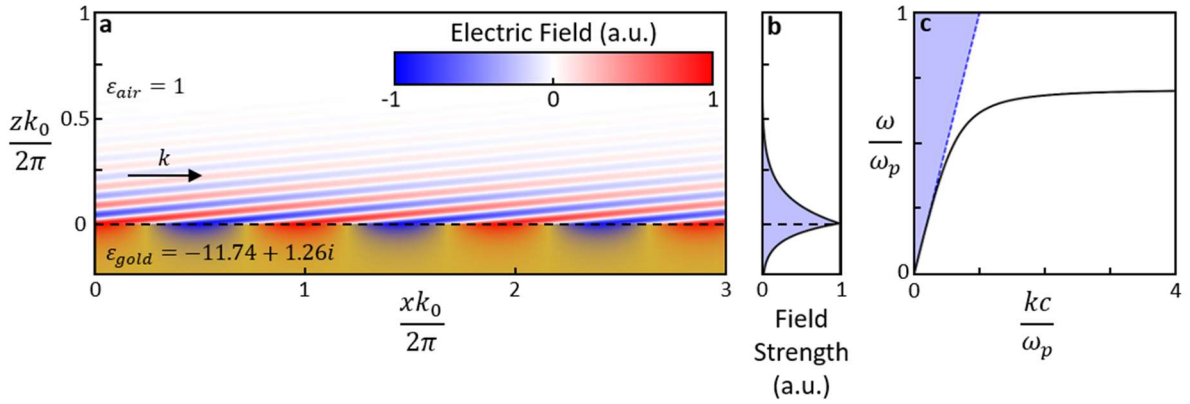

Figure 2.3 | SPP Field Profile. a, The electric field profile of a Surface Plasmon Polariton at a flat air-gold interface at a vacuum wavelength of 633 nm. **b,** Average field strength with distance from the interface, displaying sub-wavelength confinement. **c,** The SPP dispersion relation for a lossless Drude metal with $\varepsilon_\infty = 1$. The light cone of possible frequency-wavevector pairs for light in the dielectric space (shaded) is never crossed by the SPP line.

An SPP field profile at a gold-air interface is shown in figure 2.3a at a free space wavelength $\lambda_0 = \frac{2\pi}{k_0}$ = 633 nm. The field strength decays over a length scale $< \lambda_0$, confining the field to a sub-wavelength region perpendicular to the interface (Fig. 2.3b). The dispersion relation of a single interface SPP is given by

$$\frac{\omega}{k} = c\sqrt{\frac{\varepsilon_1(\omega) + \varepsilon_2}{\varepsilon_1(\omega)\,\varepsilon_2}} \tag{2.23}$$

which is shown in figure 2.3c for a lossless Drude metal with $\varepsilon_\infty = 1$. At low wavenumbers (large wavelengths), the system asymptotically approaches the linear dispersion of photons in the dielectric half-space propagating parallel to the interface. In the opposing large wavenumber limit, the frequency of the supported mode approaches an asymptotic limit known as the *surface plasmon frequency.* With a group velocity approaching zero in this limit, the solution gains an electrostatic character. For a lossless dielectric, this frequency is given by

$${\omega_{sp}}^2 = \frac{{\omega_p}^2}{\varepsilon_\infty + \varepsilon_2} - \gamma^2. \tag{2.24}$$

In the dielectric half-space, photons of frequency ω can have a wavevector component parallel to the interface up to $\sqrt{\varepsilon_2}\ \omega/c$ (equation 2.5). As this light cone (Fig. 2.3c, shaded) is never crossed by the SPP dispersion curve, photons and SPPs cannot couple without somehow bridging the momentum mismatch. In practice, the near fields generated by surface imperfections at the interface are sufficient to allow SPPs to optically de/excite with low efficiency although the surface can be patterned with an ordered grating to improve this[13]. This converts light into evanescence fields near the interface which can be decomposed into a sum of plane waves of constant frequency but varying wavevector. One of these may then overlap with the SPP dispersion curve. Another common way to achieve this is *prism coupling* using the evanescent component of light reflecting at an internal prism surface[14,15]. The optical excitation of SPPs is widely used in sensing due to the high sensitivity of the momentum matching condition to the dielectric properties of the sub-wavelength region near the interface[16–19].

Note that as the propagation of SPPs includes the coupled response of free electrons within a metal, these fields are heavily damped with a characteristic decay length along the propagation direction of typically 10 to 100 µm in the optical regime[11].

Although the theory of a single interface system has been explored here, SPPs are also supported by multi-interface systems. The simplest extension, and the most conceptually relevant to later discussions, involves a dielectric medium sandwiched between metals. If the two interfaces are close enough, the SPP fields supported by each interface couple. This is known as the metal-insulator-metal (MIM) system which supports two independent sets of travelling solutions[11] (Fig. 2.4).

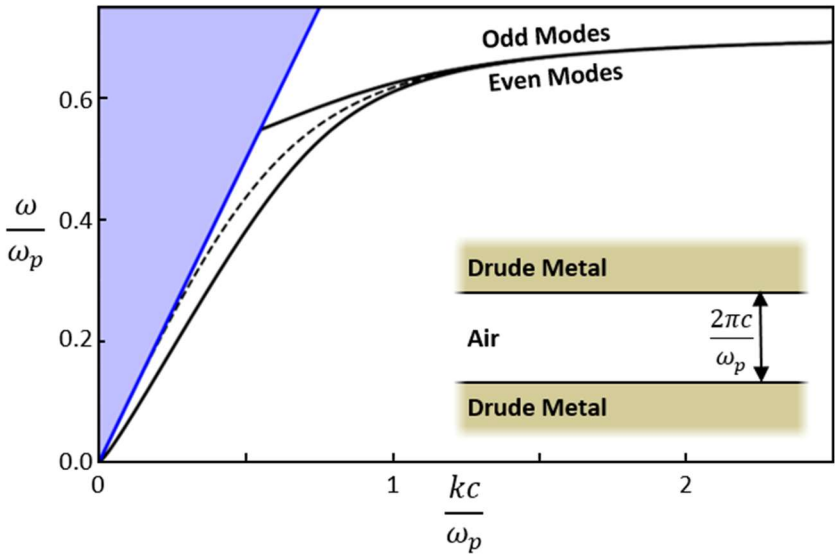

Figure 2.4 | MIM Dispersion. The dispersion curves for SPP modes supported by two lossless Drude metal surfaces (ε_∞ = 1) separated in air (ε = 1) by the plasma wavelength of the metal (solid lines). The identical modes on each individual surface (dashed line) couple and hybridise into two sets of modes depending on whether the local charge distribution is symmetric or anti-symmetric (even or odd) between the two surfaces. Shaded region indicates the light cone of possible frequency-wavevector pairs for photons in air.

2.4.2 Localised Surface Plasmon Polaritons

Localised Surface Plasmon Polaritons (LSPs) are supported by metallic volumes embedded within a dielectric medium (or vice versa). Here, we consider a sphere of radius a and homogenous dielectric function $\varepsilon_s(\omega)$ embedded at the origin in a medium with homogenous dielectric function $\varepsilon_m(\omega)$. An optical plane wave is incident with wavelength $\lambda \gg a$. This electrostatic limit allows the field to be treated at any point in time as the spatially homogenous $\boldsymbol{E_0}(t)$. In this limit, the problem reduces to the Laplace equation for the electrostatic potential (ψ) of the system

$$\nabla^2\psi = 0, \qquad \boldsymbol{E} = -\nabla\psi. \tag{2.25}$$

This can be solved under the applicable boundary conditions at the origin, sphere surface and infinite distance requiring that the field remain finite, follow continuity constraints and tend back to the incident plane wave respectively. We find that the electric field inside and outside of the sphere is given by

$$\boldsymbol{E}_{in} = \frac{3\varepsilon_m}{\varepsilon_s + 2\varepsilon_m}\boldsymbol{E_0} \tag{2.26}$$

$$\boldsymbol{E}_{out} = \boldsymbol{E_0} + \frac{3\boldsymbol{n}(\boldsymbol{n}\cdot\boldsymbol{p}) - \boldsymbol{p}}{4\pi\varepsilon_0\varepsilon_m}\frac{1}{r^3} \tag{2.27}$$

where r is the distance from the origin, $\boldsymbol{n}$ is a unit vector pointing from the origin and $\boldsymbol{p}$ is an emergent effective dipole moment

$$\boldsymbol{p} = 4\pi\varepsilon_0\varepsilon_m a^3\frac{\varepsilon_s - \varepsilon_m}{\varepsilon_s + 2\varepsilon_m}\boldsymbol{E_0}. \tag{2.28}$$

This effective dipole modifies the electric field in the vicinity of the sphere, enhancing the field strength in a sub-wavelength region near the metal surface (Fig. 2.5a). Note that this additional field does not require the momentum matching techniques of SPPs (section 2.4.1) and can be excited by incident light of any frequency and polarisation. However, the strength of this dipole is frequency dependant as it depends on the relative values of $\varepsilon_s(\omega)$ and $\varepsilon_m(\omega)$. This response is maximised in the condition $\mathrm{Re}[\varepsilon_s] = -2\mathrm{Re}[\varepsilon_m]$, justifying the assertion that this is a metallic sphere in a dielectric space (or vice versa).

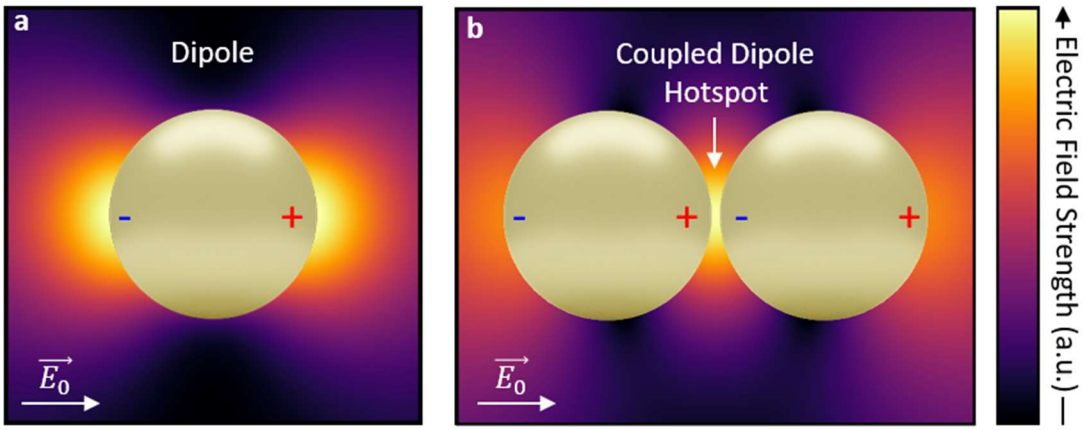

Figure 2.5 | LSP Field Profile. a, The dipolar field of a Local Surface Plasmon supported by an arbitrarily small sphere. **b,** The bright hybridisation of dipolar modes supported by two small spheres with field enhancement maximised between them.

From the equations for the fields of a dipole emitter, the scattering and absorption cross sections of this geometry are

$$C_{sca} = \frac{8\pi}{3}\left|\frac{\varepsilon_s - \varepsilon_s}{\varepsilon_s + 2\varepsilon_m}\right|^2 k^4 a^6 \tag{2.29}$$

$$C_{abs} = 4\pi\,\mathrm{Im}\left[\frac{\varepsilon_s - \varepsilon_s}{\varepsilon_s + 2\varepsilon_m}\right] k a^3 \tag{2.30}$$

respectively where k is the wavevector of the incident radiation[11]. Note that $C_{sca}/C_{abs} \propto a^3$ such that the sphere size dictates whether the system predominantly absorbs the radiation (due to non-radiative damping within the metal) or scatters it (re-coupling to light in the dielectric space). In this thesis, the 80 nm diameter gold nanoparticles used are in the scattering dominant regime.

Outside the limit $a \to 0$ where the sphere size become comparable to the wavelength of the incident light, the electrostatic approximation used here breaks down as different parts of the sphere experience different field strengths at the same time. The resulting LSP field can be described as a linear superposition of infinite resonant modes of which the dipolar solution is

the lowest order[11]. Away from idealised geometries like a sphere, the fields must be solved numerically (section 3.7).

If multiple particles are close enough that the LSP field of one can meaningfully act on the free electrons of the other, the LSP modes of the particles will couple. This is in exact analogy to the coupling of SPPs supported by two nearby interfaces (section 2.4.1). Considering just the dipolar modes of two spherical metal particles for simplicity, this results in two hybridised plasmon resonances delocalised across both particles. For one resonance, the dipoles of both particles oscillate in anti-phase and the net dipole moment is zero. This mode is described as *optically dark* as it is not excited by an incident plane wave. The other resonance has dipoles oscillating in-phase and is *optically bright* (Fig. 2.5b). In contrast to the resonances of a single nanoparticle, coupled modes can only be excited along a single polarisation axis. Perpendicularly polarised light rotates the dipolar field from each particle and leads to uncoupled (or more accurately less coupled) *transverse* modes.

Generally, coupled resonances localise and confine the optical field in the gap between the particles further than is possible with an uncoupled LSP. This high field intensity region is known as a *plasmonic hotspot*[20] (Fig. 2.5b).

2.5 Nanoparticle-on-Mirror

2.5.1 What is Nanoparticle-on-Mirror?

Coupled plasmonic structures can be broadly segmented into two families based on their method of synthesis. *Top-down* synthesis refers to subtractive manufacturing on the nanoscale in which material is removed from a bulk volume to leave behind the desired structure. Top-down techniques include photolithography and the higher resolution electron-beam lithography (EBL)[21,22]. The resolution of photolithography can be improved beyond the diffraction limit using plasmons[23]. An example bowtie antenna structure formed using EBL is shown in figure 2.6a. These methods maximise fine control over the final structure but must usually be created in a clean-room using labour intensive methods. The available technology

can limit the final resolution of features that can be created and the reliability of synthesis, as with EBL where the electron beam used to define the structure has a finite size.

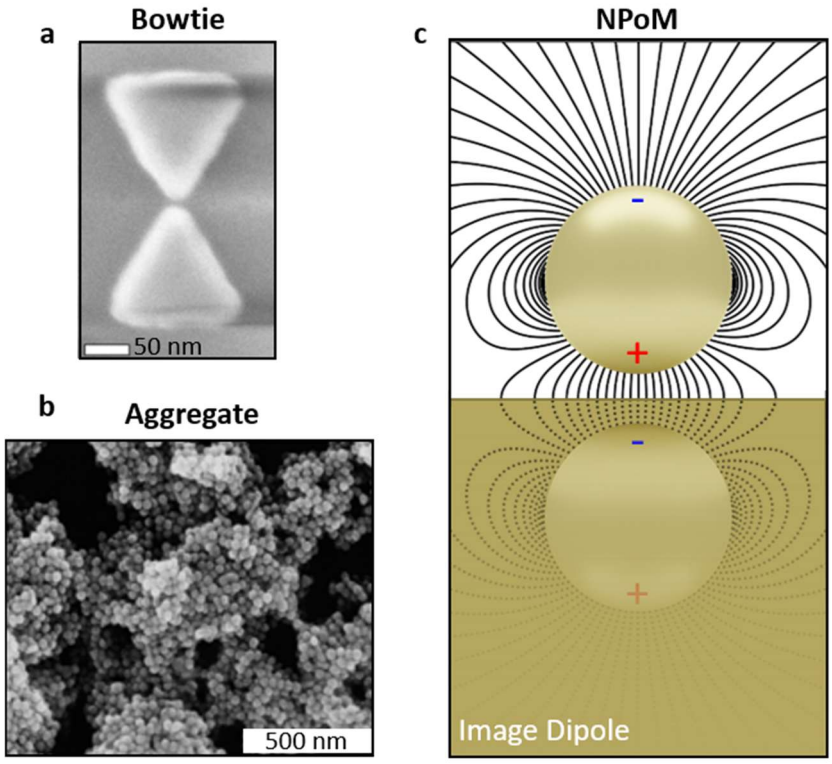

Figure 2.6 | Coupled Plasmonic Structures. Scanning Electron Microscope images of **a**, a bowtie antenna[24] and **b,** nanoparticle aggregates[25] (reproduced). **c**, Schematic of a Nanoparticle-on-Mirror with a spherical gold particle placed close to gold surface. As the field lines (solid) must reach the metal perpendicular to the surface, it is equivalent to the additional presence of an image particle in the gold surface (dashed).

In *bottom-up* synthesis, building-block materials are combined in a controlled but stochastic manner. In the simplest case, salt may be added to a suspension of gold nanoparticles. In suspension, gold nanoparticles are coated in capping ligand molecules to provide stabilising charges that keep them separated through electrostatic repulsion. With the salt screening these charges, the particles aggregate with the capping ligands defining small gaps between them (Fig. 2.6b). Each of these gaps contains a plasmonic hotspot[25]. By controlling parameters such as the aggregation time, the nanoparticle size or replacing the salt with a cross linker

molecule to drive the aggregation instead, the process can be directed statistically without any control over the formation of any given aggregate[25,26]. Bottom-up synthesis can also describe considerably more complicated protocols. For example, DNA origami describes a technique where specific strands of functionalised DNA self-assemble into 3D constructs that can incorporate metal structures[27].

The simplest form of aggregated nanoconstruct is arguably the nanoparticle dimer formed of only two nanoparticles with one resulting hotspot. In practice, controlling an aggregation process to efficiently generate dimers without an excess of larger aggregates is challenging. Instead, this thesis uses an effective dimer construct known as the Nanoparticle-on-Mirror (NPoM) as the default plasmonic cavity[2,28]. This is formed from a gold nanoparticle spaced from a locally flat gold surface (mirror) by a thin spacer layer (Fig. 2.6c), which can be achieved by first defining the spacer layer (section 2.5.4) before depositing nanoparticles from suspension (section 3.2.3). An NPoM structure is formed at every resulting nanoparticle location on the sample with the nanoparticle stabilising charge (discussed above) preventing them from aggregating on the surface. As discussed in section 2.3, any field entering a metal and oscillating below a critical frequency is quickly screened. In the electrostatic limit this occurs instantaneously at the metal boundary and, to adhere to boundary conditions, all field lines must approach this boundary at a perpendicular angle. Placing a charge near the interface, the resulting field up to the metal is equivalent to as if a second charge of opposite sign had been placed reflected in the interface. This effective *image charge* consolidates the collective effects of the free electrons in the metal. Therefore, the charge oscillations in the plasmonically resonant nanoparticle are mirrored by an effective image nanoparticle in the nearby gold surface and a dimer-like plasmonic hotspot is generated in the nanoparticle-mirror gap (Fig 2.6c). In contrast to dimer synthesis, this aligns all of the coupled mode excitation axes between constructs in a known direction.

2.5.2 Electrical Circuit Model of a Spherical NPoM

As discussed in section 2.4.2, a gold nanoparticle of finite size (and the NPoM construct it defines) supports an infinite number of plasmonic resonances. While the supported modes

of NPoM are a subject of numerical study[29–31], an understanding of all NPoM modes is not required for this thesis. Instead, we will here focus on how the lowest order coupled resonance is dependent on parameters such as particle size and particle-mirror spacing.

The resonances of a plasmonic system can be characterised using dark-field Rayleigh scattering which directly probes the scattering cross section (section 3.3). In such measurements, the 80 nm diameter NPoM structures used in this thesis usually display two characteristic features in the optical regime (Fig. 2.7a). The first, found in the 500-600 nm region, corresponds to the uncoupled *transverse* resonances of the system. The coupled resonances are seen at lower energy (700 – 800 nm). In this thesis, such spectra are used to check for NPoM formation. The large width (~100 nm full-width-at-half-maximum) of these modes relates directly to the highly damped nature of plasmonic resonances. Differences in precise size and shape between nanoparticles influences the resulting plasmonic modes and, experimentally, sometimes more than two features are seen. However, this will be neglected here for simplicity and the coupled feature will be modelled as the lowest order dipolar coupled mode of the system which usually dominates[29].

An initial intuition for the behaviour of the NPoM coupled resonance wavelength with system parameters (e.g. nanoparticle size, gap size etc.) can be gained by considering the particle as perfectly spherical. Modelling the gold as a Drude metal (section 2.3), the system can be described using an equivalent electrical circuit formed of two identical inductor-capacitor circuits (for the particle and its image) coupled through a capacitor representing the nanoparticle-mirror separation (Fig. 2.7b). This model is directly taken from Benz et. al.[32]. For a nanoparticle of radius R, a nanoparticle-mirror spacing d and a gap dielectric permittivity ε_g, the resonance wavelength λ_d of this circuit is found to be

$$\frac{\lambda_d}{\lambda_p} = \sqrt{\varepsilon_\infty(R) + 2\varepsilon_g(1 + 2\eta)} \tag{2.31}$$

where λ_p is the plasma wavelength ($2\pi c/\omega_p$) and η is the ratio of capacitances between the gap and nanoparticle. This ratio can be expressed as

$$\eta = {\varepsilon_g}^{\chi} \ln\left(1 + \theta^2 \frac{R}{2d}\right) \tag{2.32}$$

where $\chi \approx 2.28$ is a constant and $\theta \approx \frac{\pi}{5}$ is set by the lateral extent of the field confined in the gap and represents the angular area of the sphere contributing to the effective capacitance. It should be noted that the resonance wavelength of a single uncoupled nanoparticle increases weakly with particle size due to electrodynamic effects. This is accounted for here by allowing ε_∞ to be a slowly increasing function $\varepsilon_\infty(R)$. This phenomenological modification can be extracted from experimental measurements, varying ε_∞ from 12.1 to 13.3 for particle diameters from 10 nm to 80 nm.

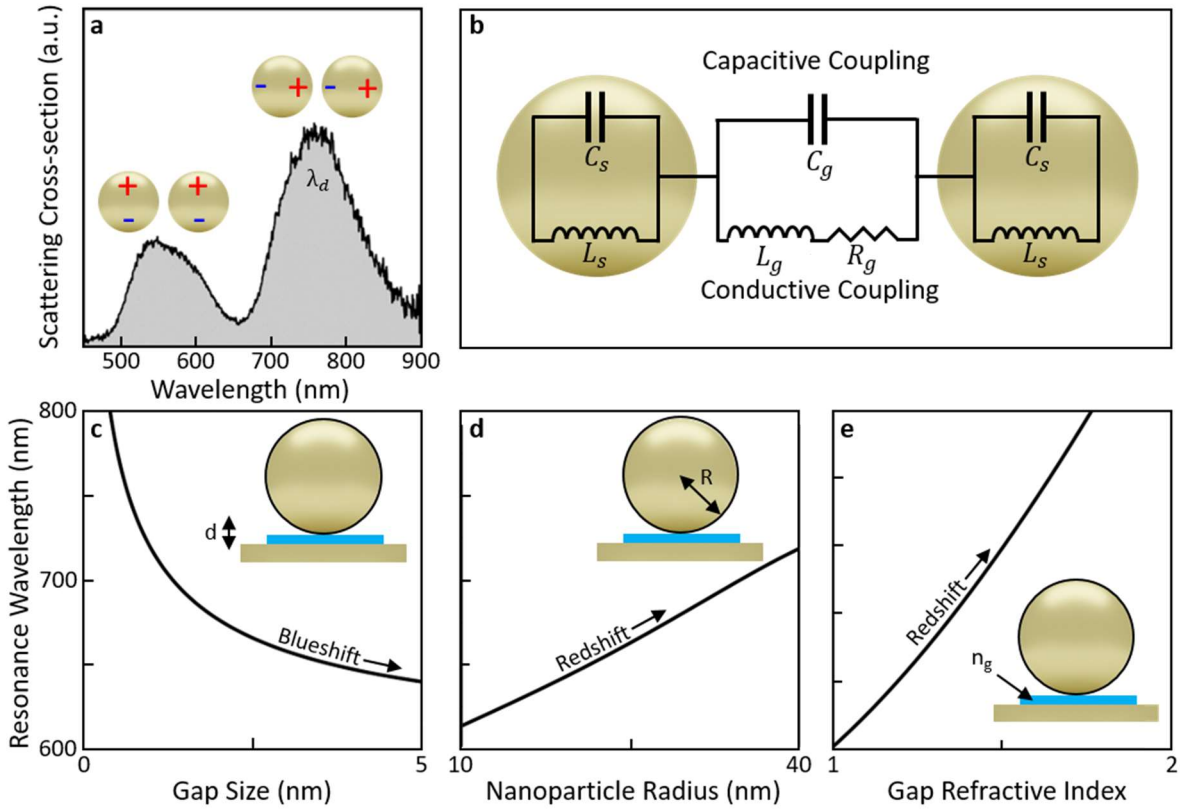

Figure 2.7 | NPoM Circuit Model. a, Characteristic dark field elastic scattering spectrum of an NPoM construct formed from an 80 nm nanoparticle separated from a gold mirror by a monolayer of non-conductive molecule biphenyl-4-thiol. The transverse and coupled optical resonances of the system are well separated. **b,** Equivalent circuit model for the lowest order coupled NPoM resonance with capacitive and conductive coupling. In the case of no conduction, the relationship between the mode resonance and **c,** gap size, **d**, nanoparticle size and **e,** refractive index. Fixed parameters are R=40 nm, d=1 nm and n_g=1.5.

This model describes well the experimentally observed trends of the NPoM system and agrees well with numerical simulations of spherical particles[32]. All system parameters that increase the capacitive coupling between particles, such as an increase in particle size, a decrease in particle-mirror spacing or an increase in gap refractive index, lead to a red shift in the resonant wavelength (Fig. 2.7c-e). As the gap size approaches zero, the resonant wavelength increases without bound in this model. This is countered in reality by the onset of charge tunnelling between the metal surfaces, introducing a conductive path to the effective circuit that shorts the system capacitance (Fig. 2.7b). This conductivity induced blue shift is also important when considering NPoM spacer materials that are not electrically insulating[33]. Note that this NPoM mode description closely resembles how two separated macroscopic metal spheres act as an antenna for electromagnetic radiation. For this reason, this plasmonic mode is sometimes referred to as an *antenna mode.*

It should be noted that this model, along with extensions accounting for non-local and quantum effects, has been found to experimentally break down in the extreme limit of gap sizes <0.5 nm where the coupled resonance is more sensitive to the particle-mirror separation than theory would predict[34]. However, this regime is not considered in this thesis.

Within the NPoM gap, fields at resonance are confined to an effective volume

$$V \approx \frac{\pi}{2\ln(2)}\frac{d^2}{n_g^2}R \tag{2.33}$$

where n_g is the gap refractive index[2]. The maximum field enhancement can be estimated as

$$\frac{\mathrm{E_{max}}}{\mathrm{E_0}} = 4\sqrt{\ln(2)\,\mathrm{Q}\,\mathrm{n_g}}\frac{\mathrm{R}}{\mathrm{d}} \tag{2.34}$$

where $\mathrm{Q} \approx 15$ is the quality factor of the plasmonic cavity[2]. This enhancement approaches 600 for nanometre scale gaps. It is important to note that for gaps <5 nm, the field in the gap is highly polarised perpendicular to the mirror surface.

2.5.3 Flat Nanoparticle Crystal Facets

In reality, gold nanoparticles (or at least, the commercial particles used commonly and in this thesis) are not spherical but form a variety of crystal shapes[35] including cuboctahedron, rhombicuboctahedron and pentagonal bipyramid (Fig 2.8a-c). These all have flat faces known as facets. Unless physically hindered[36], an NPoM will form with a facet down as this maximises the Van der Waals attraction between the particle and mirror. While the resonance trends discussed in section 2.5.2 still hold, the change to the system geometry perturbs the resonant wavelengths of the supported NPoM modes. Note that this introduces another difference between the NPoM and dimer geometries as the nanoparticle and its image by definition always have the same crystal shape and are oriented as mirror images of one another.

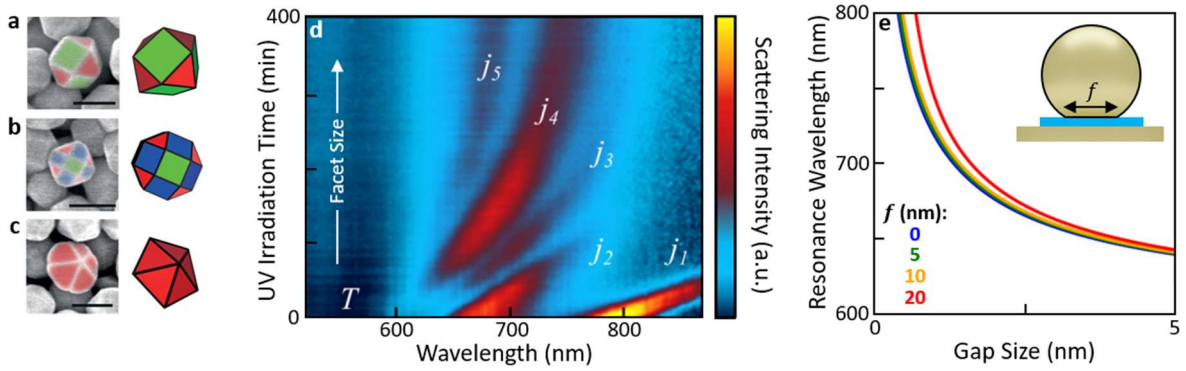

Figure 2.8 | Nanoparticle Facets. SEM images of gold nanoparticles[35] showing **a**, cuboctahedron, **b,** rhombicuboctahedron and **c,** pentagonal bipyramid. False colour indicates varying lattice planes. (Reproduced). **d,** Sequential dark field scattering spectra of an NPoM nanostructure formed from an 80 nm diameter gold nanoparticle and a 0.6 nm molybdenum disulphide spacer[37]. The observed plasmonic resonances (labelled j_i) tune under UV irradiation. (Reproduced). **e**, The NPoM circuit model modified to account for hybridisation with gap modes. This models a 80 nm diameter particle truncated to generate a varying facet diameter (f) and spaced 1 nm from the mirror with a gap refractive index of 1.5.

In section 2.5.2, the limit of a perfectly spherical nanoparticle was taken. Here, we take a different limit and zoom in tightly on the particle-mirror gap. On a small scale, the flat facet means that the NPoM gap resembles an MIM system where a dielectric is sandwiched

between two parallel metal spaces. These systems support SPPs (section 2.4.1) with continuous dispersion relations. However, the finite extent of the facet in relation to the SPP propagation length discretises this continuous dispersion into a set of supported modes. This is identical to how light is discretised into a set of discrete modes when confined between two mirrors. These *gap modes* cannot efficiently couple to light and are optically dark (due to the SPP momentum matching problem, section 2.4.1). However, by zooming out again to consider the whole NPoM structure these can hybridise to the bright NPoM antenna modes already discussed. The influence of this hybridisation on the final observed modes can be investigated numerically by modelling the nanoparticle as a sphere truncated to generate a single facet of varying size (averaging over the possible nanoparticle crystal shapes)[30]. Experimentally, the perturbation of NPoM modes by the lower facet can be observed by using UV irradiation to increase the facet size over time[37] (Fig. 2.8d).

To efficiently calculate the expected NPoM coupled mode resonance from the system parameters, the analytical circuit model (equation 2.31) can be hybridised with the numerically observed gap modes using an ad hoc coupling strength set by comparison to full numerical results[30] (Fig. 2.8e)[*]. Note that the use of a truncated sphere to model the average nanoparticle shape leads to the facet size input parameter taking on an effective character compensating for these approximations. In experimental measurements, a spread of coupled mode wavelengths is observed due to the variation in nanoparticle size (~10% for the commercial nanoparticles used in this thesis, see section 3.2.3) and shape between NPoMs. When comparing these measurements to this model, the average observed wavelength is used.

It is important to note that modelling the NPoM resonances as the hybridisation of separate *antenna* and *gap* modes is done here to provide intuition to the NPoM system. The most accurate way to extract the resonances of any particular plasmonic construct is by solving the system numerically (section 3.7).

[*]For application in this work, this model was supplied by Prof. Jeremy Baumberg.

2.5.4 Experimental Gap Materials

Depending on the application, a range of materials can be used to define the NPoM gap. When optical emitters are placed in the gap, the spontaneous emission rate is enhanced by the increased local density of states within the plasmonic cavity (the Purcell effect)[38]. For this reason, quantum dots[39–41] or dye molecules[42–44] (sometimes within molecular hosts) are sometimes used to define the gap. Mono- or multi-layer inorganic materials[45,46], such as transition metal dichalcogenides, can provide a robust cavity with a high enough exciton density to approach strong light-matter coupling at room temperature[47].

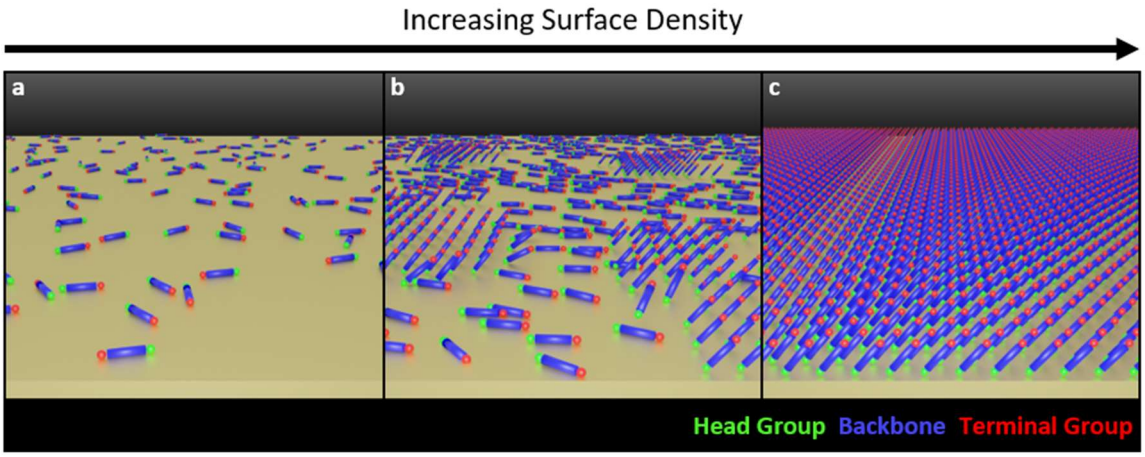

Figure 2.9 | SAM Formation. Schematic representation of SAM formation with increasing molecule surface density. **a,** At low density, the head group binds the molecules to the substrate. **b,** As density increases, interactions between molecular backbones leads to spontaneous ordering. **c,** At high density, energy is minimised by all molecules being bound into the substrate via the head group and interacting with one another via the molecular backbones in a regular lattice.

In this thesis, two types of gap materials are used. One type (Chapters 5-7) is a Self-Assembled Monolayer (SAM) of thiolated bi-phenyl molecules. As the name suggests, a SAM is a close packed monolayer of molecules that self-assembles on a surface. This forms a consistent NPoM cavity with fixed dimensions while providing access to molecules in the gap to interact with the field[32,33,35]. In general, a SAM molecule can be described as a combination of three parts: the *head group*, *backbone* and *terminal group*[48]. The head group binds the molecule to

a surface. At low deposition densities, this will lead to molecules sparsely coating the surface (Fig. 2.9a). As the molecular surface density increases, intermolecular interactions facilitated by the backbone leads to some spontaneous ordering (Fig. 2.9b). At maximum surface density, the system energy is minimised by the molecules forming a close packed lattice with the head group still bound to the surface (Fig. 2.9c). The terminal group is not involved in SAM formation and functionalises the SAM for some other purpose.

An example SAM molecule used in this thesis is biphenyl-4-thiol (BPT, Fig. 2.10a). This is formed of two phenyl rings attached to a thiol functional group. This thiol is the head group which binds strongly to gold. The phenyl rings form the backbone, leading to intermolecular interactions through π-π stacking of the ring electron orbitals. This molecule does not contain a terminal group. Another molecule used in this thesis is 4'-cyanobiphenyl-4-thiol (NC-BPT), an otherwise identical molecule apart from the addition of a nitrile terminal group (Fig. 2.10b). Studies of biphenyl SAMs, which are normally carried out in vacuum using methods such as Scanning Tunnelling Microscopy (STM), show that the exact lattice formation of a SAM can vary spatially and form grains in analogy to crystal packing[49] (Fig. 2.10c,d)

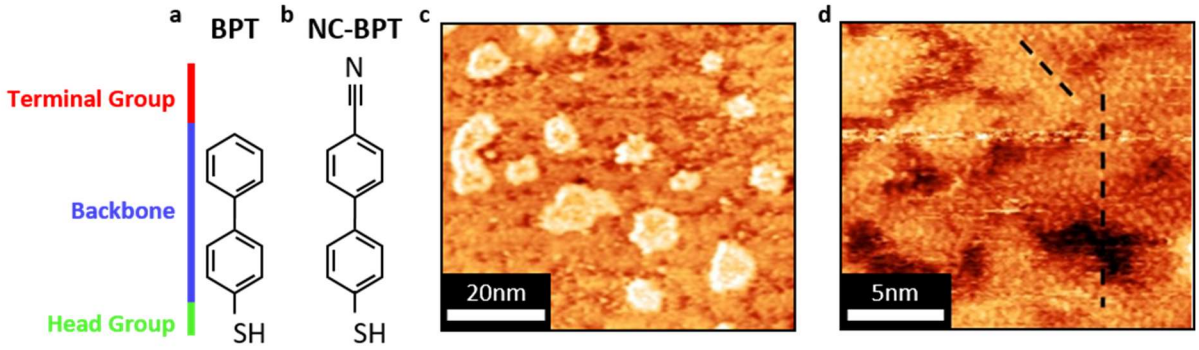

Figure 2.10 | Biphenyl Thiol SAMs. Molecules **a,** biphenyl-4-thiol (BPT) and **b,** 4'-cyanobiphenyl-4-thiol (NC-BPT) used to form SAMs. **c,d,** Scanning Tunnelling Microscopy images of a BPT SAM at different magnifications[49] (reproduced).

There is some debate and ambiguity as to the mechanism by which thiolated SAMs bind to gold[50–53]. For our purposes, this centres on the possible restructuring of the gold surface and role of surface adatoms in head group binding. A study of small gold nanoclusters suggests

that each pair of adjacent thiol groups is bridged by an oxidised Au(1) atom bound to both[54]. It is unclear how this would translate to a template stripped bulk gold surface as used in this thesis (section 3.2.1). As the gold surface cannot be imaged once a close packed SAM has formed upon it, this has been the subject of numerical study[55,56]. This is relevant to this thesis investigating atomic scale metal features in the NPoM cavity. The characteristic optical signatures of these features, which will be discussed in section 2.8, are only seen transiently and do not support the constant presence of gold adatoms in the NPoM gap. Speculatively, it is possible that the Van der Walls attraction between the gold particle and mirror could lead to further surface restructuring upon NPoM formation. Alternatively, a closely spaced regular array of adatoms could behave more like a single atom layer of a low electron density metal than a set of individual adatoms within the plasmonic cavity. This thesis offers no clear solution to this debate, and the gold surfaces within an NPoM cavity are here assumed to normally contain no surface adatoms.

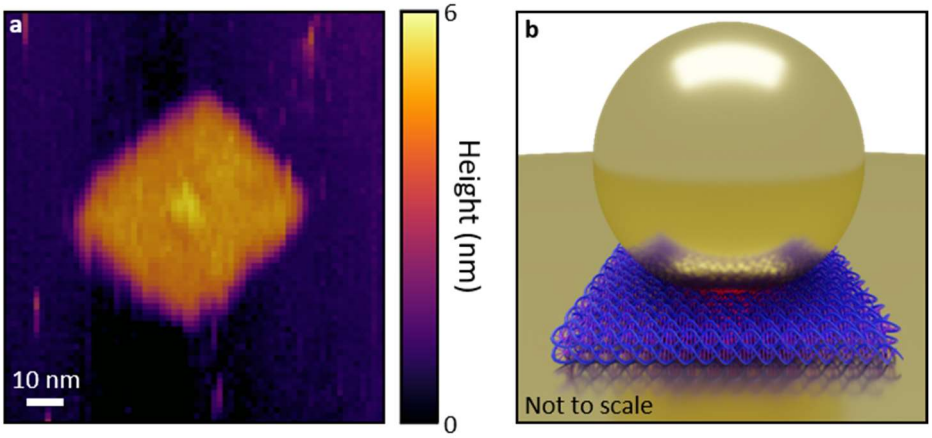

Figure 2.11 | DNAo NPoMs. a, Atomic Force Microscopy image of a DNAo plate formed of two layers of DNA[57]. This is 4.5 nm tall with increased height as the centre observed from extra DNA strands designed to anchor an Au nanoparticle (reproduced) **b,** Render of an NPoM construct using a DNAo plate as the gap spacer.

The other type of spacer material used in this thesis (Chapter 4) is DNA origami (DNAo). This describes a versatile nanotechnology in which a segment of single stranded viral DNA is folded into a desired 3D shape by selectively joining points together using a large number of shorter

(staple) strands[58]. With the correct DNA strands mixed together, the desired structure self-assembles under thermal annealing in order to minimise system energy. This DNA can be functionalised with thiol groups to bind to gold. This has been used to self-assemble a range of plasmonic nanostructures[27] from bowtie antennas[59] to nanoparticle dimers[60] (or even nanoparticles arranged in the shape of a bowtie antenna![61]). In 2017, Chikkaraddy et. al. used a rectangular plate of DNAo as an NPoM gap spacer[57] (Fig. 2.11). Thiol functionalisation ensured that the structure bound to the gold mirror surface. Overhangs of DNA protruding from the plate were complimentary to DNA attached to gold nanoparticles, positioning a nanoparticle directly above the DNAo. A molecule of interest functionalised with a short strand of DNA can be incorporated into such an NPoM gap with a lateral precision of $\pm$1.5 nm. This structure, and variations upon it, is investigated in Chapter 4.

2.6 Raman Scattering

Raman scattering describes the inelastic scattering of optical fields from the vibrational modes of a system. Due to the small cross section of this process, this benefits greatly from the increased optical intensity of a plasmonically enhanced field. To maximise relevance to this thesis, this process will be discussed here in terms of molecular vibrations. However, the bulk of this discussion is generalizable to non-molecular systems.

2.6.1 Normal Modes of Molecular Vibrations

To define a vibrational mode, we will consider a toy example. Two identical masses m are each attached to their own fixed wall using a perfect spring of spring constant k. A third spring attaches the two masses together. The system is shown in figure 2.12. Ignoring any damping within the system, any arbitrary displacement of either mass will cause both masses to move back and forth in a way that initially appears complex and dynamic.

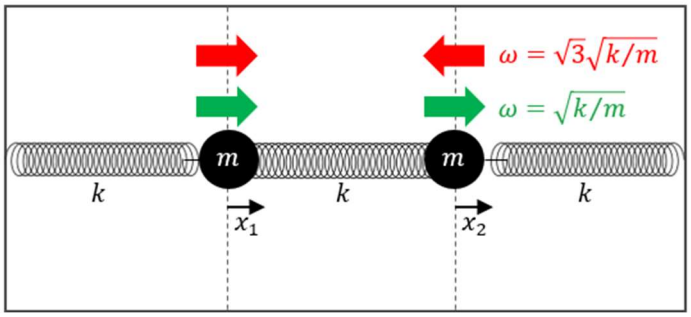

Figure 2.12 | Vibrational Normal Modes. Diagram of two spring-coupled masses. This system contains two independent harmonic solutions at differing frequencies ω, with the masses moving in-phase (green) or in anti-phase (red).

The displacement of each mass from the equilibrium configuration is given by x_1, x_2 (Fig. 2.12). We can combine these displacements into one system vector $\boldsymbol{v} \equiv (x_1, x_2)$. The evolution of the system over time is given by Newton's 2nd law of motion

$$\frac{d^2\boldsymbol{v}}{dt^2} = -\omega_0^2 \underline{\underline{M}}\boldsymbol{v}, \quad \omega_0^2 \equiv \frac{k}{m}, \quad \underline{\underline{M}} \equiv \begin{pmatrix} 2 & -1 \\ -1 & 2 \end{pmatrix}. \tag{2.35}$$

Searching for harmonic solutions, we define $\boldsymbol{v} \equiv \boldsymbol{A}e^{-i(\omega t+\phi)}$ where $\boldsymbol{A}$, ω and ϕ are unknown. This reveals the system to be an eigenvector problem

$$\underline{\underline{M}}\boldsymbol{A} = \frac{\omega^2}{\omega_0^2}\boldsymbol{A} \tag{2.36}$$

with two independent solutions vibrating with different frequencies ω. These are $\omega = \omega_0$ with $x_1 = x_2$ (in-phase motion) and $\omega = \sqrt{3}\omega_0$ with $x_1 = -x_2$ (anti-phase motion). These represent the fundamental vibrational modes of the system. As equation 2.35 is linear, the general system solution is given by the sum

$$\boldsymbol{v} = C_1 \begin{pmatrix} 1 \\ 1 \end{pmatrix} e^{-i(\omega_0 t+\phi_1)} + C_2 \begin{pmatrix} 1 \\ -1 \end{pmatrix} e^{-i(\sqrt{3}\omega_0 t+\phi_2)} \tag{2.37}$$

where $C_{1,2}$ and $\phi_{1,2}$ are constants set by the initial positions and velocities of the two masses. This represents all possible system behaviour.

Reductively, the vibrations of a molecule can also be modelled as those of a connected network of masses and springs representing the molecular structure. In a harmonic

approximation of the molecular bond energies, the spring constants in this analogy must be calculated by solving the system's energy landscape quantum mechanically (section 3.8). The vibrations of a molecule are, in a harmonic approximation, therefore also a linear superposition of system specific vibrational normal modes of varying frequency/energy. For a molecule, these energies are dependent on (and can dynamically change due to) any interactions with the local environment.

2.6.2 Surface Enhanced Raman Scattering

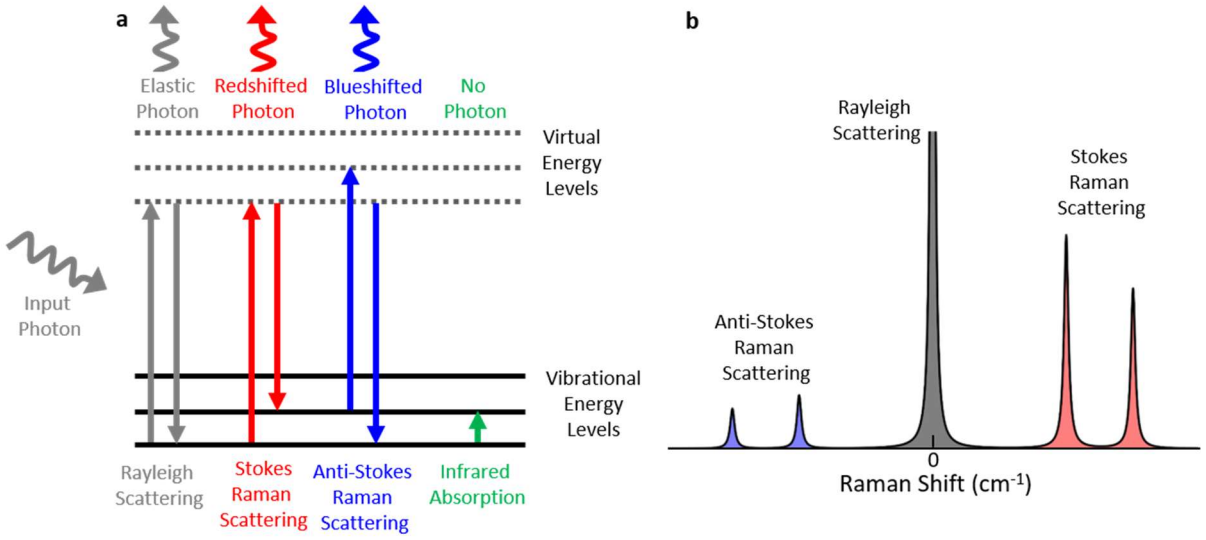

Figure 2.13 | Raman Scattering. a, Schematic transition diagrams for the interaction of a vibrational mode and photon. Rayleigh, Stokes and anti-Stokes scattering are mediated by virtual energy levels. Infrared absorption involves direct photon absorption. **b,** Schematic Raman scattering spectrum measured by the change in scattered photon energy (Raman shift). Rayleigh scattering provides a large response at zero. Vibrational modes generate symmetric scattering peaks around zero corresponding to their vibrational energy.

Each molecular vibrational mode of frequency ν represents a quantum harmonic oscillator with energy levels evenly spaced by $h\nu$. Raman scattering describes the exchange of a quantum of energy $h\nu$ between a vibrational mode and an incident photon of frequency $\nu_p > \nu$. Unable to absorb this photon to excite the vibrational mode directly, as in infrared

absorption, the system instead excites to a *virtual* energy level. This is followed by the emission of a photon of frequency $\nu_p \pm \nu$, resulting in a net single level de/excitation of the vibrational mode and a corresponding blue/red shift of the scattered photon (Fig. 2.13a). The virtual vibrational level is a useful construct here representing the underlying superposition of *vibronic* states – molecular states involving both electrons and the movement of the nuclei – that mediate this process.

Raman scattering is further separated depending on whether the scattered photon is red shifted (Stokes scattering) or blue shifted (anti-Stokes scattering). These changes in photon energy are conventionally measured in Raman shift [cm^{-1}] with positive values assigned to Stokes scattering. If the system is illuminated with a monochromatic light source such as a laser, the distribution of measured Raman shift generates a spectrum where each vibrational mode generates 2 peaks mirrored around zero at its vibrational frequency (Fig. 2.13b). As anti-Stokes scattering requires the vibrational mode to be excited above the ground state before the scattering event, it is a lower probability process than Stokes scattering at thermal equilibrium. The anti-Stokes : Stokes ratio for a given vibrational mode therefore provides information on the phonon population of the mode either due to thermal energy or some external pumping mechanism. This ratio is given by

$$\frac{I_{\text{anti-Stokes}}}{I_{\text{Stokes}}} = \left(\frac{\nu_p + \nu}{\nu_p - \nu}\right)^4 e^{-\frac{h\nu}{k_B T}} \tag{2.38}$$

where T is the effective temperature of the system and k_B is Boltzmann's constant. The exponential component of this equation captures the relative thermal populations of the ground and first excited vibrational energy states while the other component captures the dependence of a Raman scattering event on the energy of the incident photon[62]. The spectral positions and relative intensities of Raman scattering peaks are intrinsic properties of a scattering material and are regularly used for both sensing and for identifying unknown substances[63–66]. The physical origin of the varying scattering cross sections between vibrational modes (and the resulting relative Raman peak intensities) is discussed in section 2.6.3. The width of each Raman scattering peak collected from a single molecule is a direct measurement of the damping and corresponding phonon lifetime associated with that vibrational mode. A set of molecules measured simultaneously will provide slight variations in vibrational mode energies reflecting each molecule's interaction with its local environment.

This distribution of mode energies convolves with the fundamental width of each vibrational mode to broaden the resulting observed Raman peak. A change in Raman peak width over time is indicative of some change in this underlying distribution of vibrational mode energies.

If the excitation to the virtual energy level is followed by a symmetric de-excitation to the same starting energy, this is known as Rayleigh scattering. As an elastic process, the cross section of Rayleigh scattering normally exceeds that of Raman scattering by a few orders of magnitude. This generates a large peak centred at 0 cm^{-1} in any Raman spectrum.

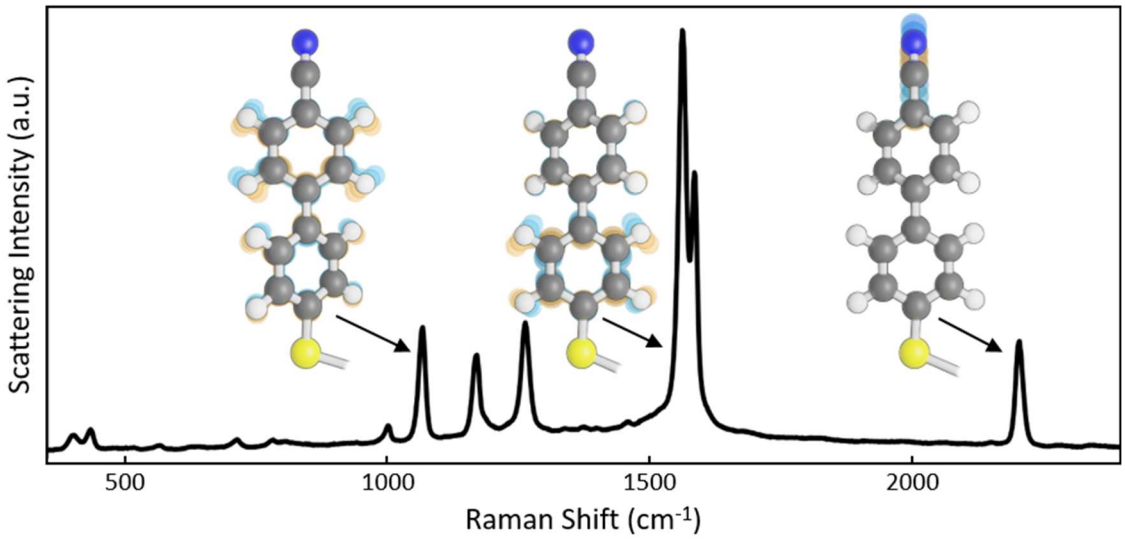

Figure 2.14 | SERS Spectrum. Example SERS spectrum of molecule 4'-cyanobiphenyl-4-thiol measured in NPoM using a 80 nm nanoparticle and a 633 nm laser. The corresponding vibrational modes of three vibrations are shown. Colours blue and orange represent opposite extrema of each vibration.

In comparison to other light-matter interactions, Raman scattering is a low efficiency process with a cross section ~x10^{14} smaller than that for absorption[67]. This requires the experimental use of long measurement times and/or bulk material samples. In Surface Enhanced Raman Scattering (SERS), the measurement material is placed within a plasmonically enhanced field that compensates for the low scattering cross section. Within a plasmonic cavity, such as the gap of an NPoM (section 2.5), the resulting scattering is highly sensitive to the local enhanced field strength (E) with an $\propto E^4$ dependence[11]. Although the underlying theory is beyond the necessary scope for this work, this can intuitively be thought of as due to the plasmonic

enhancement of both the incident ($\propto E^2$) and scattered ($\propto E^2$) fields. As a cost for this large improvement in signal, scattering peaks in SERS spectra are broadened due to the damped nature of the mediating plasmonic resonance. In NPoM, this tends to dominate other contributions to observed SERS peak widths and gives p a characteristic width on the order of 10 cm^{-1}.

An example NPoM SERS spectrum is shown in figure 2.14 with a selection of peaks labelled with their corresponding vibrational mode.

2.6.3 Raman Selection Rules

For a given molecule, not all vibrational modes undergo Raman scattering with equal efficiency with some being effectively dark with cross sections approaching zero. Here, we aim to develop some intuition as to why some modes scatter better than others without requiring a full understanding behind the theory of Raman scattering. This will be achieved by considering the interaction between the molecule and light to be that of a classical electric field $\boldsymbol{E}$ and an effective point electric dipole moment $\boldsymbol{\mu}$. The energy of this interaction is given by $-\boldsymbol{\mu} \cdot \boldsymbol{E}$. Upon interaction with the field, the dipole moment can be linearly expanded as

$$\mu_i = \mu_i^p + \sum_j \alpha_{ij} E_j + \cdots \quad i,j = \{x,y,z\} \tag{2.39}$$

where μ_i^p is the permanent dipole moment intrinsic to the structure of the molecule and the polarisation tensor α_{ij} describes the linear response between a field applied along direction j and the induced dipole along direction i. As the molecule undergoes a vibration, the molecular structure deforms and the resulting effective point dipole moment changes. This vibrational motion is described using a normal coordinate Q that encodes how far the structure is from equilibrium. This would oscillate harmonically in time during a vibration. Our expression for $\boldsymbol{\mu}$ can be expanded to first order with respect to Q to give

$$\mu_i = \left(\mu_i^p\big|_{Q=0} + \sum_j \left(\alpha_{ij} E_j\right)\big|_{Q=0} \right) + \left(\frac{d\mu_i^p}{dQ}\bigg|_{Q=0} Q \right) + \left(\sum_j \frac{d\alpha_{ij} E_j}{dQ}\bigg|_{Q=0} Q \right) + \cdots$$

$$\equiv \mu_i{}^0 + \mu_i{}^{\text{IR}} + \mu_i{}^{\text{Raman}} + \cdots . \tag{2.40}$$

While the term $\mu_i{}^0$ contains no Q dependence, the remaining terms give rise to the light-matter interactions normally labelled as Infrared absorption ($\mu_i{}^{\text{IR}}$) and Raman scattering ($\mu_i{}^{\text{Raman}}$). Note that the decision to separate these processes is somewhat arbitrary here and that they describe different components of the same light-matter interaction. The Raman term can be rewritten as

$$\mu_i{}^{\text{Raman}} = \left[\sum_j \frac{d\alpha_{ij}E_j}{dQ}\bigg|_{Q=0}\right]Q = \left[\sum_j \frac{d\alpha_{ij}}{dQ}\bigg|_{Q=0} E_j + \sum_j \frac{dE_j}{dQ}\bigg|_{Q=0} \alpha_{ij}\right]Q \tag{2.41}$$

which splits the process into two contributions. The first term states that the dipole moment associated with Raman scattering depends on how much the polarisability of the molecule changes during a vibration. If the vibration contains a degree of symmetry such that movement of two or more atoms lead to polarisability changes that cancel out, then that vibrational mode will not scatter efficiently. The reflection of molecular and vibrational symmetries in whether a mode can efficiently scatter or not is known as the Raman selection rules.

The second term depends on how the electric field experienced by the effective point dipole changes as the molecule vibrates. In essence, this depends on the spatial gradient of the incident field. For visible light incident on a molecule in vacuum, this is a small enough effect to be dominated by the first term by a factor of $\sim 10^3$ [68]. For this reason, Raman scattering regularly refers only to the first term of equation 2.41. When cross sections are calculated numerically (section 3.8), only this term is normally included. When the field gradient is significant over the extent of the molecule, the arguments of vibrational mode symmetry break down and scattering cross sections become dependent on the precise field over the molecule. In this regime, it can be said that the Raman selection rules are broken. Alternatively, and in analogy to how Infrared absorption and Raman scattering are separated, this can be considered an independent process known as *Gradient-field Raman*[68] or, in this thesis, *Gradient Raman*.

Ignoring Gradient Raman, the Raman scattering intensity I from a vibrational mode is written as

$$I = \left(\underline{\underline{\alpha}}^{\text{Raman}}\, \boldsymbol{E}\right) \cdot \boldsymbol{E} \propto \left(\left.\frac{d\underline{\underline{\alpha}}}{dQ}\right|_{Q=0} \boldsymbol{E}\right) \cdot \boldsymbol{E} \tag{2.42}$$

where $\underline{\underline{\alpha}}^{\text{Raman}}$ is known as the Raman tensor. Note that Raman cross sections are dependent on the orientation of the field polarisation relative to the molecule. When cross sections are calculated numerically (section 3.8), this regularly averages over all polarisations. Unless otherwise stated, this is true throughout this thesis. Not shown here, the scattering intensity is also dependant on the frequency of the incident light (a factor hidden in the proportionality constant in equation 2.42). This factor can also be included in the numerical calculations (section 3.8). Note that the description of Raman in this thesis refers specifically to cases where the laser frequency is non-resonant with the electronic transitions of the molecule (known as Resonant Raman or SERRS). This applies to all systems measured experimentally in this thesis.

2.7 Spectrally Broad NPoM SERS Backgrounds

A portion of any plasmonically enhanced field must penetrate into a metal in order to couple with the free electrons. In strong analogy to Raman scattering, this light can inelastically scatter off of the electronic energy levels of the metal in a process known as Inelastic Light Scattering or Electronic Raman Scattering (ERS)[69]. As these levels form a continuous band, this scattered light contributes to a continuous SERS background from NPoM constructs (Fig. 2.15). For anti-Stokes ERS, this background decays exponentially as it requires electrons to be thermally excited above the Fermi level of the metal. For Stokes ERS, the background is intuitively expected to be approximately flat. However, a spectral shape is introduced by the varying efficiency by which light is out-coupled from the NPoM cavity to be detected. Under continuous SERS measurements at high enough incident optical powers, the surface atoms of the nanoparticle can restructure and cause an increase in facet size[37,47]. This can lead to a slow change in the ERS background over time as the plasmonic resonance shifts.

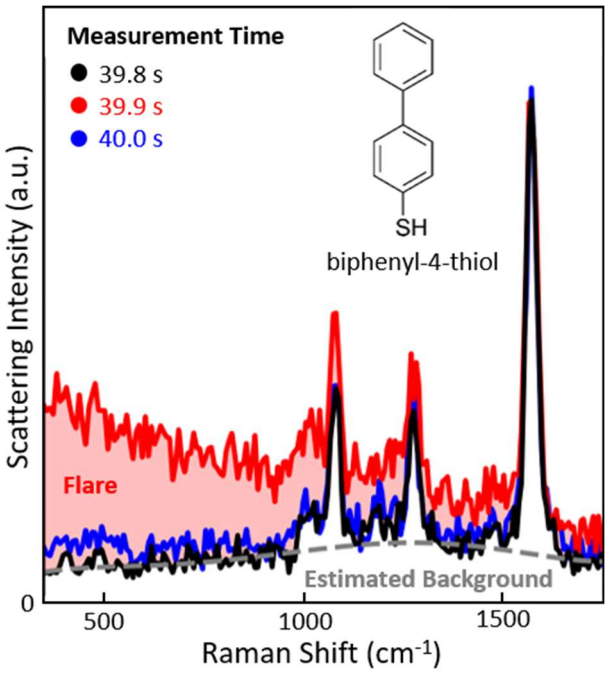

Figure 2.15 | SERS Background. Sequential SERS spectra of a biphenyl-4-thiol self-assembled monolayer within an NPoM cavity formed using an 80 nm Au nanoparticle. Spectra captured using a 633 nm laser and a ~0.1 s spectrum integration time. Each spectrum has a broadband background (grey) as well as narrow SERS peaks. Transient broadband flare events (red) are observed.

When measuring sequential NPoM SERS spectra over time, large transient increases in background emission are occasionally observed (Fig. 2.15). These *flare* events are characterised by a broadband emission with a Gaussian spectral profile whose occurrence frequency is dependant both on the incident optical power and gap spacer material[70]. While the mechanism of these events is not fully understood, it seems to relate to a transient decrease in the plasma frequency of the gold over a small (<3 nm) region. This leads to increased field penetration into the gold. In 2021, Chen et. al. suggested that this was due to the light induced formation of new domain boundaries in the metal[71]. These transient events are found to last for hundredths of a second, and multiple weaker events occurring over the span of a spectrum integration time is likely a source of short timescale variation in the observed SERS background.

Note that ERS is not the only likely contributor to the SERS background intensity resulting from fields inside the metal. For example, other processes include plasmonically enhanced

photoluminescence from hot carriers within the metal[72] and the heavily damped scattering from image molecules (or image versions of whatever is inside the NPoM gap)[73]. The NPoM SERS background is not a key point of study for this thesis. When required, it is removed from spectra using a polynomial estimate.

2.8 Picocavities

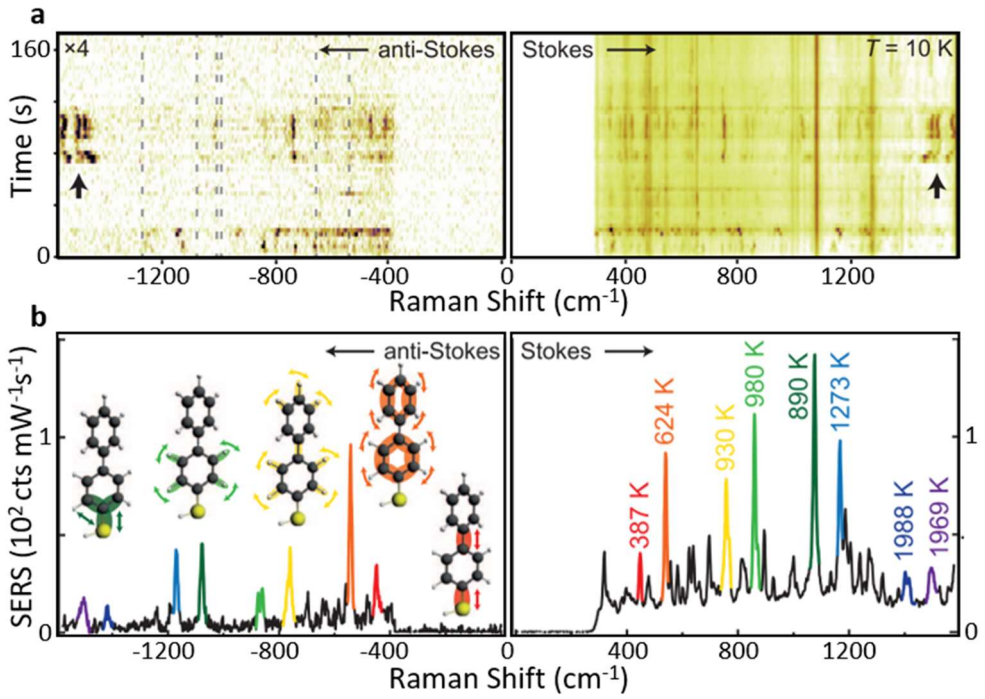

Figure 2.16 | Transient SERS in NPoM. a, SERS spectra of a biphenyl-4-thiol NPoM structure taken at 10 K with a 633 nm laser, showing the appearance of transient vibrational modes. **b,** An example spectrum with transient modes matched to their corresponding molecular vibrations given by Density Functional Theory. SERS intensity ratios for Stokes and anti-Stokes photons provide an effective temperature for each transient mode. Reproduced from Benz et. al.[3].

When measuring SERS from a plasmonic cavity over time, vibrational modes can transiently and stochastically appear and disappear across the spectrum. This is sometimes known as spectral blinking and can result in scattered light intensity increases suggesting 10^{14}-10^{15} field enhancement factors and effective scattering cross sections comparable to those of absorption for organic fluorescent dyes[6,74]. In 2005, it was known that the rate of these events

is dependent on the sample temperature and incident optical power[6]. When measuring SERS from more than one molecule, any perturbations to the vibrational modes due to changes in the molecular local environment quickly average out to a stable spectrum over time. This is known as ensemble averaging. For these transient modes, spectral wandering suggested a possible single molecule origin.

In 2016, Benz et. al. explored SERS blinking in NPoM at cryogenic temperatures using a biphenyl-4-thiol (BPT, section 2.5.4) SAM[3]. During each event, different sets of transient lines were seen corresponding to dark vibrational modes of the BPT. Spectral wandering of 0.1 to 1 $cm^{-1}s^{-1}$ was observed, re-enforcing previous observations. During these events, the rest of the spectrum was unaffected (Fig. 2.16). These transient lines were found to persist if the laser irradiation was removed. The sudden appearance of dark vibrational modes is suggestive of Gradient Raman (section 2.6.3). However, a sufficient field gradient present over the scale of any single molecule requires a physical, optically driven and reversible change to the NPoM structure generating field confinements on a <1 nm^3 scale.

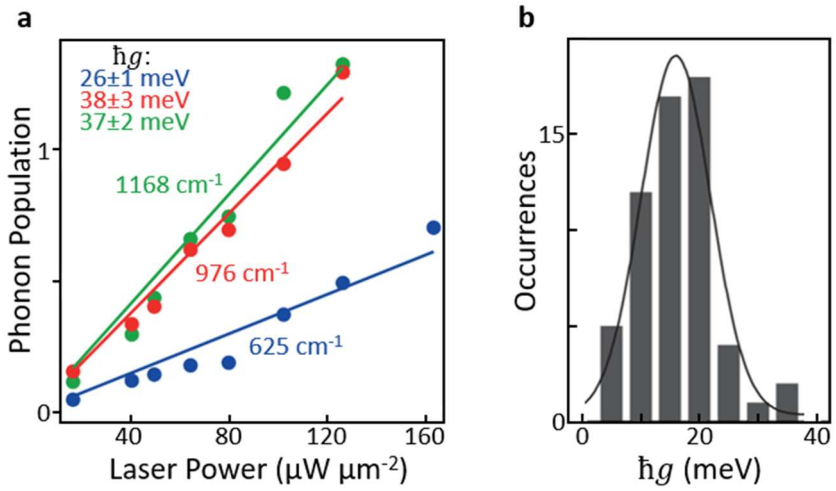

Figure 2.17 | Transient Optomechanical Pumping. a, Example Stokes : anti-Stokes intensity ratios (converted to phonon populations) for a number of transient SERS modes with varying incident laser power. **b,** Distribution of measured vibration - optical cavity coupling strength taken from the gradients of these power dependence measurements over 50 transient events. Reproduced from Benz et. al.[3].

Comparing the Stokes : anti-Stokes scattering intensity ratios, the transient modes were found to be pumped above thermal equilibrium to effective temperatures up to 2000 K. Significant coupling between a mechanical system and an optical cavity is described by the theory of optomechanics and characterised by coupling parameter g. This normally describes dielectric cavities in which some component flexes in response to the optical radiation pressure. Here, this was instead applied to the coupling of single molecule vibrational modes and a plasmonic cavity. From laser power dependant SERS measurements from over 50 transient events, $\hbar g$ was extracted over a range of 5 – 40 meV with an average of $\sim$15 meV (Fig. 2.17). This can be compared to $\hbar g < 1$ μeV for conventional optomechanical systems. These values further suggested the presence of an optical cavity of effective volume <1 nm^3.

As a possible source of this *optical picocavity*, Benz et. al. classically modelled an atomic scale protrusion at the centre of the nanoparticle facet using Finite Difference Time Domain (FDTD, section 3.7) simulations. This indeed provided an effective cavity volume of <1 nm^3 with the sharp feature acting as a lightning rod for the optical field (Fig. 2.18). This model was supported by the frequency of observed events with varying laser power, indicating a critical energy barrier of 0.7 eV comparable to the activation energy of adatom diffusion on gold. Urbieta et. al. later explored the validity of this classical calculation by comparing classical simulations of atomically sharp Na nanoparticle corners to atomistic Time Dependent Density Functional Theory (TDDFT)[75]. In this quantum framework, the high field enhancement over small confined regions (and the resulting strong field gradients) was conserved (Fig. 2.19). Over the last few years, publications have been produced further exploring the extreme field confinement offered by atomically sharp plasmonic metal features both analytically and numerically[76–79], as well as how to incorporate the resulting fields into predictions of modified SERS scattering intensities[80].

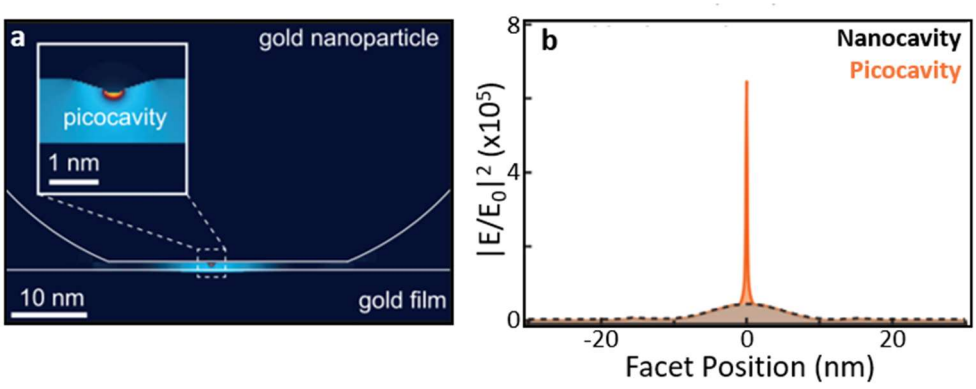

Figure 2.18 | Enhanced Field Around an Atomic Feature. a, Field strength around an atomic scale protrusion from an NPoM cavity calculated using FDTD. **b**, Field intensity enhancement across the NPoM gap with and without the protrusion. Reproduced from Benz et. al.[3].

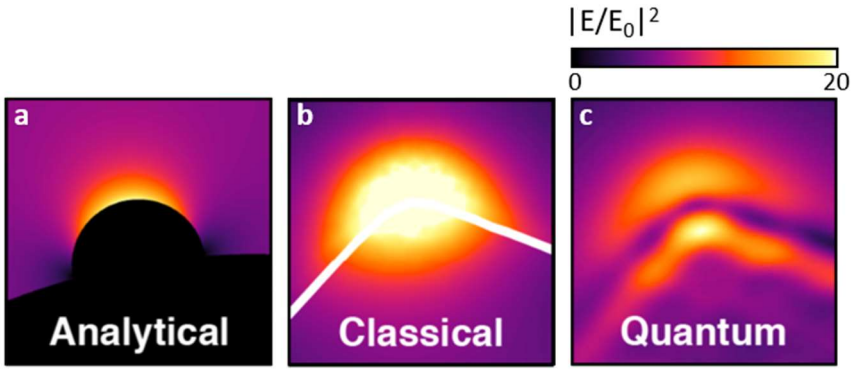

Figure 2.19 | Classic and Quantum Modelling. The plasmonic field enhancement at an atomically sharp corner of a Na nanoparticle in **a,** an analytical approximation **b,** a classical simulation and **c,** an atomistic Time Dependent Density Functional Theory calculation. Reproduced from Urbieta et. al.[75].

It is important to emphasise that these picocavities are not just observed in NPoM constructs, having been reported in other geometries such plasmonic molecular break junctions[81] and Tip Enhanced Raman Spectroscopy (TERS)[82]. In TERS, a gold tip replaces the nanoparticle in NPoM, allowing the cavity to be moved over the sample. Experimentally, the plasmonic field has been used, in vacuum and cryogenic conditions, to scan and map the structure of a molecule by the Raman (or other optical) response[83–86]. This requires a greater field confinement than can nominally be generated by the geometry which may the result of atomic tip features.

2.9 Conclusion

In this chapter, I have described how metal nanostructures exploit plasmons to generate regions of enhanced optical field intensity that are smaller than the free space wavelength of the incident light. I have focused primarily on the Nanoparticle-on-Mirror (NPoM) construct that is exclusively used throughout the experimental section of this thesis (Chapters 4-7). This enhancement is predominantly utilised here for Surface Enhanced Raman Scattering (SERS) where the scattering of light from the vibrational modes of a system is enhanced. In NPoM, this allows you to experimentally measure hundreds of molecules rather than the hundreds of thousands or millions of molecules measured in normal Raman scattering. I have explained how the scattering cross section of a vibrational mode may be calculated under the assumption of a spatially homogenous field. These cross sections change in the presence of a strong field gradient over the molecule with methods to efficiently estimate these changes currently under active development[80]. Finally, I have described the observation of transient vibrational modes in SERS spectra from plasmonic nanostructures and their characterisation in NPoM at cryogenic temperatures[3]. This effect is modelled by a transient atomic scale feature (a picocavity) on the NPoM metal surface with the resulting locally inhomogeneous field altering the SERS cross sections for a single molecule. Once transient SERS modes are observed in Chapter 4, this phenomenon becomes the key source of study for this thesis.

There are many open questions surrounding the picocavity model. For example, it is a requirement of the model that the gold surfaces defining the NPoM cavity be atomically flat when a picocavity event is not occurring. This may require the surfaces to undergo some restructuring during NPoM formation but this has not yet been investigated. The mechanism by which picocavities are generated, and whether it is thermally or optically driven, is unknown. Similarly, it is unknown how the gold surface locally structures around a picocavity protrusion. When numerically calculating the field around a picocavity, the bulk gold has previously been treated as a homogenous medium while ignoring the atomic structure. While this model is also applied within this thesis, it seems reasonable that the local atomic structure would have a meaningful impact on the final enhanced field. Finally, it has not yet been investigated how the presence of the low coordination number gold in proximity to the molecule within the picocavity field influences this molecule through chemical interaction.

Chapter 3: Common Processes and Methods

3.1 Introduction

This chapter contains an overview of processes and techniques used commonly throughout this thesis. This includes the synthesis protocols for NPoM constructs and the experimental systems for dark field scattering and SERS measurements. The numerical methods Finite Difference Time Domain and Density Function Theory, which numerically solve electromagnetic fields and the Raman spectra of molecules respectively, are also briefly discussed.

3.2 Sample Synthesis

3.2.1 Gold Mirror Synthesis

The gold substrates in this thesis are produced using template stripping. This describes a technique for transferring the natural flatness of a silicon wafer onto a layer of deposited metal[87]. A silicon wafer is cleaned from surface impurities using Decon-90, water, ethanol and isopropanol. A Lesker E-beam evaporator is used to deposit a 100 nm layer of gold. Additional small (approximately 5 x 5 mm) silicon pieces are adhered to this gold layer using Epo-Tek 377 epoxy cured for 2 hours at 150 ^{o}C on a hot plate. This is gradually cooled to room temperature at a rate of $\sim$1 °C/min to prevent cracking from thermal constriction. A piece of silicon peeled away from the wafer removes the gold layer. The flat gold layer directly deposited onto the silicon surface is now the top surface of the sample. Measured over micrometres, this process has been shown to reduce the surface roughness by an order of magnitude to approximately $\pm$0.2 nm compared to evaporation alone[87]. This roughness is reduced again over distance scales of 100s of nm. For our purposes, we aim to minimise surface roughness over the tens of nm scale of an NPoM gap.

3.2.2 Gap Material Synthesis

3.2.2.1 DNAo

The DNA Origami (DNAo) constructs used in Chapter 4 are assembled as outlined in Chikkaraddy et. al.[57]. This is summarised here.

A 7560-base single stranded viral DNA scaffold is isolated from M13mp18 derivative (Tilibit nanosystems). This is mixed at a 10 nM concentration with a 100 nM concentration of staple DNA strands in a 14 mM MgCl2, 1 × TE buffer. TE buffer is a common buffer solution used in procedures involving DNA that is designed to increase its solubility. The DNA hybridises and folds over an annealing cycle where the mixture is heated to 65 ^{o}C before being cooled to 36 ^{o}C over a period of 23 hours. After this, the sample is held at 4 ^{o}C. The solution is filtered through a 100 kDa Amicon filter using a 2 mM MgCl2, 0.5 x TE buffer. The buffer is washed and re-filtered three times. This separates the DNAo from unfolded or excess DNA. A template stripped gold substrate is placed with the DNAo in a 11 mM MgCl2, 0.5 x TBE buffer overnight to allow the DNAo to attach to the gold surface[*].

3.2.2.2 Biphenyl SAMs

Self-assembled monolayers (SAMs) of biphenyl-4-thiol and 4'-cyanobiphenyl-4-thiol, used in Chapters 5-7, are formed on the template stripped gold surface by submerging it in a 200proof ethanol solution of 1 mM (Chapters 5-6) or 0.1 mM (Chapter 7) of the SAM molecule overnight[†]. The sample is then rinsed with ethanol.

[*] DNAo samples in this thesis are designed and synthesised by Vladimir Turek of University of Cambridge

[†] Due to a respiratory sensitivity, SAM formation is carried out by collaborators including Cloudy Carnegie, Bart de Nijs and Demelza Wright of University of Cambridge. The difference in molecule solution concentration is a preference of these collaborators giving SAM formation in both cases.

3.2.3 NPoM Synthesis

Nanoparticles are deposited by placing a 20 µL droplet of commercial 80 nm Au nanoparticle colloidal suspension (BBI Solutions, OD1) onto the sample with SAM or DNAo NPoM gap spacer already present. These commercial nanoparticles are charge stabilised using citrate capping ligands. After 20 s, the droplet is removed using deionised water and the sample is dried with nitrogen.

For DNAo samples (Chapter 4), this process is modified as the nanoparticles are first functionalised with 5' thiol modified 20× poly T DNA strands to hybridise with the DNAo constructs. These particles are left to form NPoM structures for 30 min before the sample is washed with Milli-Q water and dried with nitrogen.

NPoM formation across the sample is checked using dark field scattering (section 3.3). The nanoparticles have a size range of 10% as stated on the manufacturer datasheet. Ignoring effects such as varying nanoparticle crystal shape, this polydispersity generates an expected spread for measured NPoM coupled resonance wavelengths of 10s of nm (Fig. 3.1).

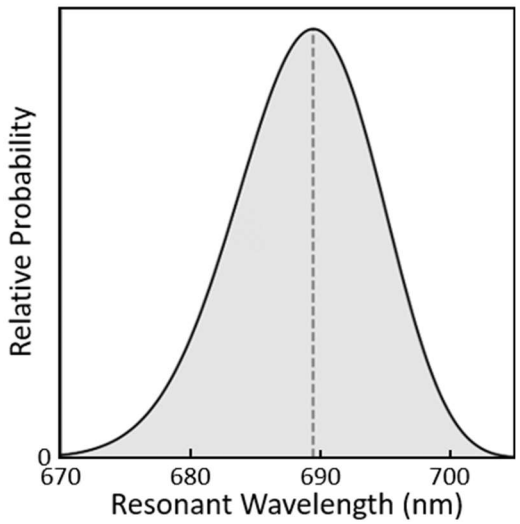

Figure 3.1 | NPoM Resonance Distribution. From the NPoM coupled resonance circuit model (section 2.5.2), the expected plasmon resonance distribution from spherical (un-faceted) nanoparticles of diameter (80±4) nm. A gap size of 1.3 nm and gap refractive index of 1.45 are used, characteristic of a biphenyl-4-thiol monolayer[33].

3.3 Dark Field Scattering Measurements

During an elastic scattering process, light is incident on a sample and a proportion s at a given wavelength is scattered away from its original path. Two distinct forms of measuring this scattering are available depending on whether the scattered or un-scattered (reflected/transmitted) light is collected. These are known as *dark field* and *bright field* measurements respectively to reflect whether the measurement looks dark or bright in the absence of scattering.

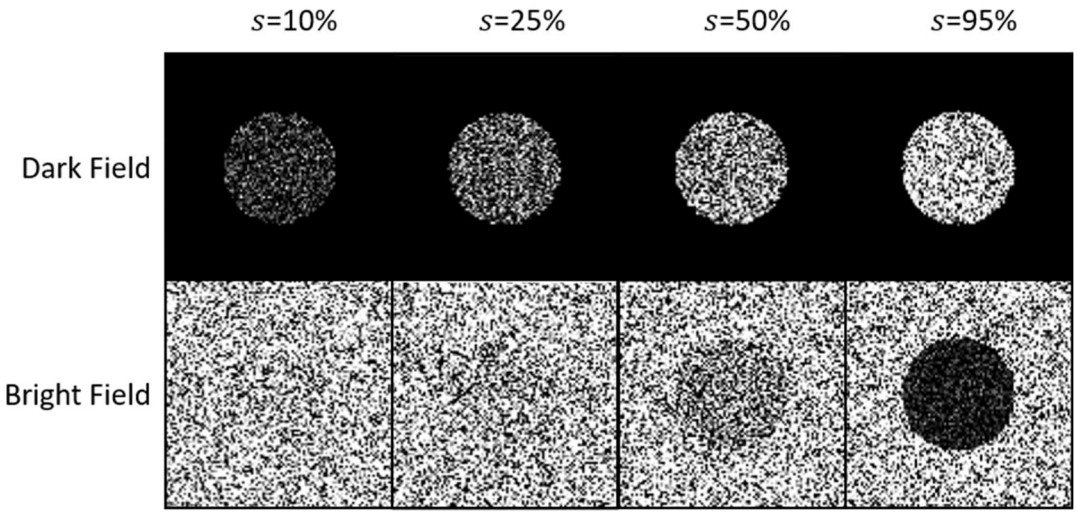

Figure 3.2 | Comparing Dark and Bright Field Scattering. Simulated dark field and bright field scattering images from a circular object scattering a fraction s of the incident light intensity. The noise on each pixel is drawn from a normal distribution with a standard deviation equal to the square root of the pixel intensity, approximating photon shot noise. The colour scale is thresholded at the values of zero and the incident intensity.

Although the absolute difference in signal between the measured object and background is the same for both measurement techniques (s times the incident light intensity), they each provide a very different measurement contrast compared to the background noise. Although there are multiple sources of noise in an optical measurement, we will focus here on photon shot noise as an example. This results from the number of photons incident on a detector in

a fixed length of time being sampled from a Poisson distribution, giving a noise level $\propto \sqrt{I}$ on any intensity measurement I. For bright field measurements, this means that weak scattering can become difficult to resolve from the higher background noise level. This is demonstrated conceptually in figure 3.2 which ignores all other sources of background noise.

The NPoM constructs in this thesis display a scattering efficiency on the order 1%. Therefore, the dark field scattering measurement technique is used. The separation of scattered and un-scattered light is deceptively simple and is shown in figure 3.3a. Broadband light is incident from a halogen bulb. The central portion of this is blocked leaving an annulus of light to interact with the sample. The returning light is passed through a complementary beam block, removing light that simply reflected from the sample (and some fraction of that which scattered). The remaining scattered light is measured using a commercial Ocean Optics spectrometer.

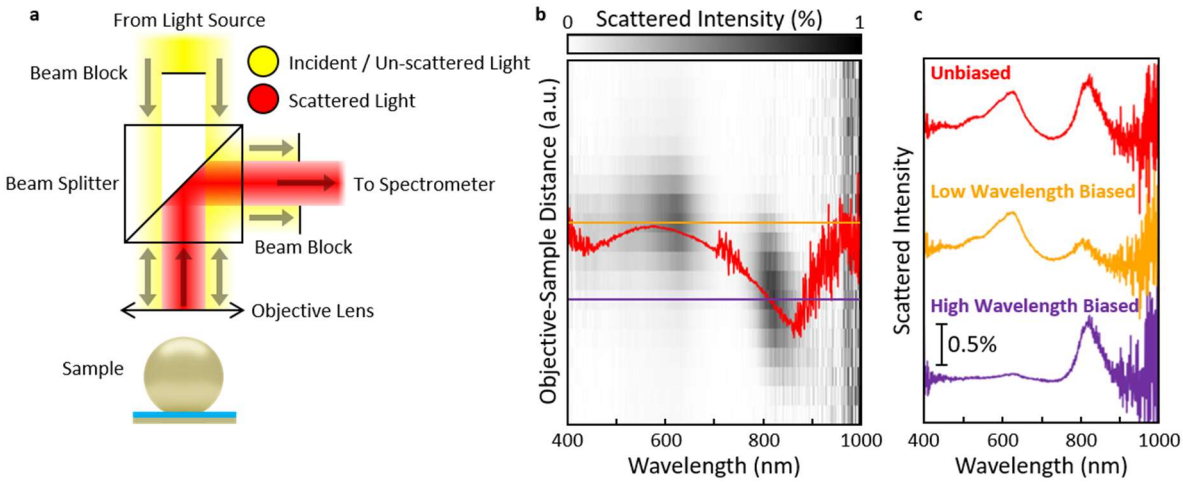

Figure 3.3 | Dark Field Scattering. a, Diagram of the experimental set up for measuring dark field scattering. **b,** An example NPoM dark field spectrum varies with the distance between the object lens and sample due to chromatic aberration. Orange and purple lines indicate fixed measuring distances that bias the measurement towards lower or high wavelengths respectively. Red line indicates the centroid (peak intensity maximising) distance for each wavelength. This curve is noisy at regions of low signal to noise ratio. **c,** Extracted scattering spectra following each distance-wavelength curve indicated by colour in **b**.

As neither the halogen light emission nor the system collection efficiency is spectrally flat, this will modify any scattering spectra measured from NPoM constructs. To account for this, all measurements are taken relative to a LabSphere Reflectance Standard white light scatterer which is assumed to scatter with effectively 100% efficiency.

Due to chromatic aberration, the measured scattering spectrum can depend strongly on the distance between the objective lens and sample. This is accounted for by measuring the spectrum while varying this distance. For each wavelength, the measured intensity is assumed to peak with distance following a Gaussian curve. The centroid distance is found and linear interpolation is used to extract the intensity at that optimum (intensity maximising) distance. An example of this process is shown in figure 3.3b,c. Note that regions where this optimum distance curve (shown in red) is smooth represents wavelengths where the scattering signal is resolvable from the noise. As the incident intensity of the halogen bulb drops at ~900 nm and noise begins to dominate the spectrum, the switch in gradient sign for this curve is unphysical. In this thesis, all dark field spectra are taken using a 0.1 s integration time.

3.4 SERS Measurements

To collect a SERS spectrum, incoming laser light is focussed down to a diffraction limited spot using an objective lens. For the two wavelengths of light used in this thesis, this is a spot diameter of ~350-400 nm for 633 nm light or ~440-490 nm for 785 nm light depending on the numerical aperture (NA) of the objective lens used. Scattered light is collected through this same lens and directed onto a different optical path using a beam splitter. The higher intensity elastic Rayleigh scattering is removed by passing the light through one or more notch filters (THORLABS NF633-25 for 633 nm and THORLABS NF785-33 for 785 nm) which block light near the laser wavelength. The light is spatially separated by wavelength using a spectrometer before being imaged using an Andor Newton EMCCD cooled to -90 ^{o}C to minimise electronic noise. This is shown schematically in figure 3.4. The lasers and spectrometers used in these measurements vary throughout this thesis as discussed in section 3.5. The assignment of each pixel of the CCD to a measurement wavelength is performed using known emission lines from an Ocean Optics HPX-2000 lamp. In this thesis,

this calibration is double checked and referenced against a commercial Renishaw Raman measurement system.

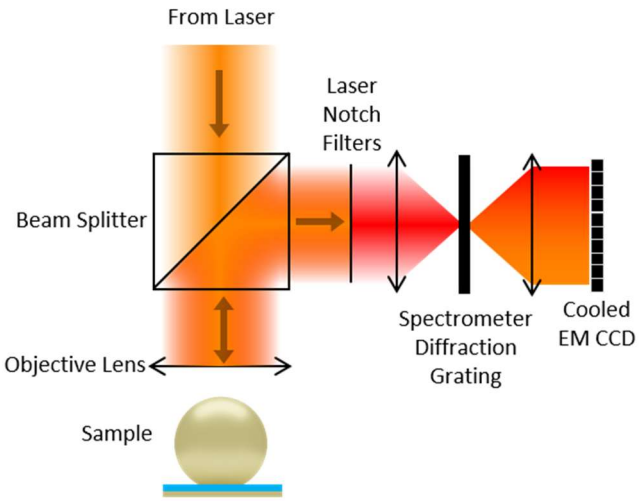

Figure 3.4 | SERS Measurements. Diagram of an experimental set up for measuring SERS.

3.5 Experimental System

In this thesis, two experimental systems are used based on the same core design. These systems, although modified by me over time, were already constructed at the beginning of this work. These systems combine dark field scattering (section 3.3) and SERS (section 3.4) measurement capabilities and are constructed around commercial Olympus BX-51 microscopes. The design of these systems is shown in a simplified diagram in figure 3.5. The differing versions of these systems over time are labelled according to the included components as shown in table 3.1. Here, each of these components is described in detail.

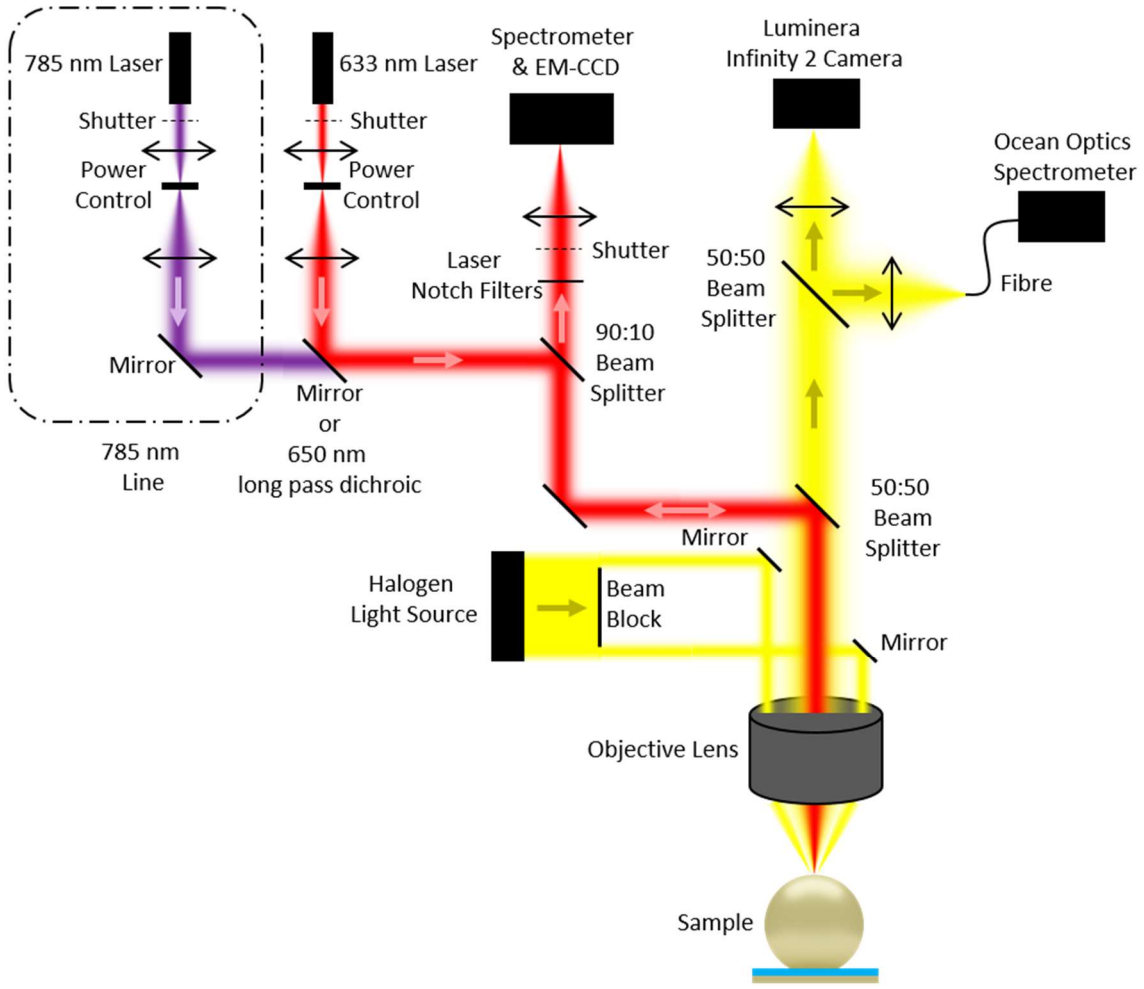

Figure 3.5 | Experimental System. Simplified diagram of experimental set up for simultaneous measurement of dark field scattering and SERS. Optional 785 nm laser path also shown.

3.5.1 Lasers

The laser wavelength used most commonly in this thesis is 633 nm. This is either generated from a HeNe laser or a diode Matchbox laser from Integrated Optics. The latter replaced the former over the course of this work due to a smaller footprint (6 cm v ~1 m length) allowing for a more compact experimental set up.

In Chapter 7, SERS is taken with both 633 nm and 785 nm simultaneously. This is achieved using an additional 785 nm Integrated Optics Matchbox laser. This joins the same laser excitation path using a dichroic filter that is transparent to one wavelength and reflective to the other (Fig. 3.5).

3.5.2 Power Control

It is generally recommended by manufacturers that lasers be run at the maximum operating voltage. Therefore, some external means are required to lower and control the power. In this thesis, this is initially a motorised THORLABS wheel with slots for neutral density (ND) filters of varying strengths. This is replaced with a THORLABS ELL18K continuous rotation stage upon which is mounted a continuously variable ND filter wheel. This provides finer power control. This is eventually also replaced with an acoustic optical modulator (AOM) that can vary the beam power at MHz rates.

The optical power on the sample is measured using a THORLABS PM16-121 power meter.

3.5.3 Spectrometer

Two spectrometers are used for SERS measurements in this thesis depending on the experimental set up. The first is an Andor Shamrock 303i-B spectrometer using a 600l/mm diffraction grating with 650 nm blaze. The second is a HORIBA Triax 320 spectrometer using either a 600 l/mm diffraction grating with 750 nm blaze or 150 l/mm grating with an 800 nm blaze. A diffraction grating with a smaller number of lines per mm (l/mm) projects a larger spectral range onto the CCD at the expense of spectral resolution.

3.5.4 Objective Lens

Initially, an Olympus LMPlanFLN 100× 0.8NA BD objective lens is used to focus the light onto the sample and collect scattered light. As the transmission of this lens drops >700 nm, a Zeiss EC Epiplan-Neofluar 100× 0.9NA DIC objective lens is also used (Fig. 3.6). This is important for both SERS collected with a 785 nm laser or 633 nm SERS from vibrational modes >2000 cm^{-1} (>725 nm). For the same reason, an Olympus MPLFLN 100x 0.9NA BD objective lens is used in Chapter 7.

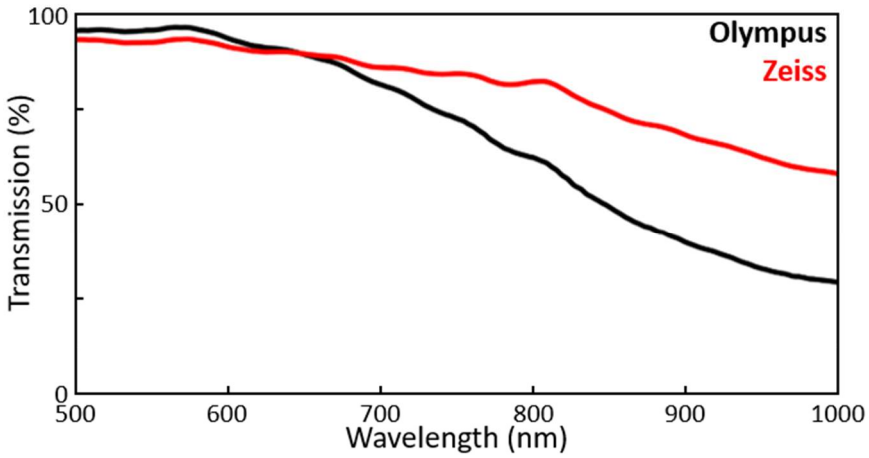

Figure 3.6 | Objective Lens Transmission. Transmission curves for the Olympus LMPlanFLN 100× 0.8NA BD and Zeiss EC Epiplan-Neofluar 100× 0.9NA DIC objective lenses. The Zeiss data is provided by the manufacturer. The Olympus manufacturer data is absent for >700 nm, and is experimentally measured here in comparison to the Zeiss (Savitzky-Golay smoothed to supress noise).

Set Up Version	Laser(s)	Power Control	Spectrometer	Objective Lens
A	633 nm HeNe	Discrete Wheel	Andor	Olympus LMPlanFLN
B	633 nm Diode	Continuous Wheel	HORIBA (600 l/mm)	Zeiss
C	633nm Diode	AOM	HORIBA (600 l/mm)	Zeiss
D	633 +785 nm Diode	AOM	HORIBA (150 l/mm)	Olympus MPLFLN

Table 3.1 | Experimental Components. Varying versions of the experimental set-up defined by the different combination of constituent components.

3.6 Automated Data Collection

Many pieces of lab equipment, including the stage holding the sample, cameras, spectrometers and various shutters, are electronic and addressable from a PC. This means that data collection can be automated when measurements of many NPoM constructs are required. This system identifies possible NPoMs by the dark field scattering image (Fig. 3.7) which shows a characteristic green spot (transverse plasmon mode) with a red ring (coupled plasmon mode). Each NPoM is moved directly below the centre of the objective lens in turn.

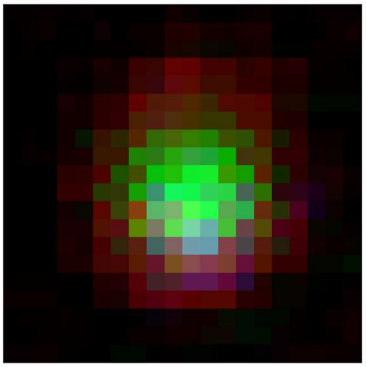

Figure 3.7 | NPoM Scattering Image. Dark field scattering image of an NPoM formed from an 80 nm gold nanoparticle spaced from a gold mirror using a monolayer of biphenyl-4-thiol. This scattering is characterised by a green spot surrounded by a red ring.

I was able to build upon this core system[†] as required for experimental automation. As an example, this system could be used to automatically change the intensity of incident laser light upon real time detection of changes to the SERS spectrum.

[†] The automated system for detecting and moving NPoMs was developed by William Deacon and Richard Bowman of University of Cambridge.

3.7 Finite Difference Time Domain Simulations

Finite Difference Time Domain (FDTD) simulations here describe a method to numerically solve Maxwell's equations. This discretises the continuous system into a 3D mesh of points at which local optical properties (e.g. the dielectric function) are defined. This allows the user to model arbitrary optical systems.

All FDTD calculations presented in this thesis are carried out using the commercial software *Lumerical FDTD*[88].

3.8 Density Functional Theory

Density Functional Theory (DFT) is a technique for calculating the electronic structure of a material[89,90]. In this thesis, it is used exclusively on organic molecules. Solving the Hamiltonian for the ground state energy of a molecule allows the vibrational normal modes to be extracted along with the polarisability tensor and its derivatives. This allows the Raman spectrum of a molecule to be predicted. DFT uses approximations to the full Hamiltonian to generate a numerical solution.

A DFT calculation depends on a number of user input hyper-parameters that control the calculation complexity. Some of these are:

1. *The DFT Basis Set*: This is a finite set of functions that are linearly summed to approximate an electronic wavefunction. This wavefunction decomposition allows the underlying partial differential equations that must be solved to be converted into algebraic equations suitable for a computer.

2. *The Hybrid Functional:* This describes the approximation used for the exchange-correlation energy of the system. In this thesis, the common 'B3LYP' is used[91].

3. *The Dispersion Corrections:* This describes approximations for the energy contributions of weak long range correlation effects (such as London forces)[92].

All of the DFT calculations† in this thesis are carried out using the commercial Gaussian09 program[93]. As briefly stated in section 2.6.3, the Raman scattering cross section of a vibrational mode is dependent on the energy of the incident light relative to the vibrational energy. DFT calculations can return two values for this cross section. *Raman Activity* ignores this dependence and returns a value directly proportional to the change in molecular polarisability during a vibration. This is an intrinsic property of the molecule. In contrast, *Raman Intensity* includes this modifying factor. For the work presented within this thesis, the precise comparison of relative peak heights between experimental and calculated SERS spectra is not important. As it is an intrinsic property, Raman Activity is therefore used generally in this thesis unless otherwise stated. This program can apply an internal scaling factor to calculated vibrational mode energies to mitigate intrinsic approximation errors. In this thesis, this is not applied and all post-calculation scaling of vibrational energies in mentioned in the text.

3.9 Bayesian Information Criterion

Regularly throughout this thesis, experimental data must be fit to a model where the optimum model complexity (i.e. number of parameters) is not known. For example, an experimental SERS spectrum could be modelled as a polynomial background (of unknown order) plus a set of Gaussian or Lorentzian peaks (of unknown number). This spectrum will also contain noise. Within Bayesian statistics, models can be quantitatively compared based on how well they describe the data without overfitting the noise. However, these processes are computationally complex. Instead, this thesis makes use of an approximation for this comparison metric known as the Bayesian Information Criterion (BIC)[94]. This is defined as

$$\mathrm{BIC} = k\ln(N) - 2\ln(L) \tag{3.1}$$

where k is the number of model parameters, N is the number of measured samples and L is the maximised likelihood of the model. This is a minimising function (the optimum model

† For this thesis, DFT support is provided by collaborator Tamas Földes of University College London who carries out DFT calculations as mentioned in the text.

returns the lowest value) and is decreased by both lowering the model complexity and increasing the model likelihood.

As an example, consider a spectrum formed from N discrete elements $\{x_i, y_i\}$. A model is provided for the underlying noiseless spectrum $M(x_i; \theta)$ where θ represents a set of n model parameters. We assume that the experimental noise is normally distributed with standard deviation σ. The log-likelihood is given by

$$\ln(L) = -\frac{1}{2}\sum_{i=0}^{N}\left[\ln(2\pi\sigma^2) + \left(\frac{y_i - M(x_i;\theta)}{\sigma}\right)^2\right] \tag{3.2}$$

giving a BIC of

$$\mathrm{BIC} = (n+1)\ln(N) + \sum_{i=0}^{N}\left[\ln(2\pi\sigma^2) + \left(\frac{y_i - M(x_i;\theta)}{\sigma}\right)^2\right]. \tag{3.3}$$

3.10 Computation

All analysis contained within this thesis is carried out using the Python 2 programming language[95]. Any novel analysis techniques or algorithms are explained in detail in the relevant chapters.

All 3D schematics and models are generated using the open source program Blender[96].

3.11 Conclusion

In this chapter, I have briefly covered methods and techniques that are used repeatedly throughout this thesis, including sample synthesis, dark field and SERS measurements and the experimental design used carry out these measurements. This will be referred to as required throughout the experimental chapters (Chapters 4-7) where this experimental design is used to measure NPoM constructs.

Chapter 4: Dynamic Single Molecule SERS in DNA Constructed Plasmonic Nanostructures

4.1 Introduction

As discussed in section 2.5.4, DNA Origami (DNAo) describes the process of mixing a long segment of single stranded viral DNA with a set of short DNA strands of specific sequences to bind and fold into some 3D structure. By functionalising parts of this structure (for example, by including a thiol group for gold binding) this can be used to self-assemble coupled plasmonic nanostructures[27]. In 2016, Chikkaraddy et. al.[57] followed previous work forming DNAo nanoparticle dimers[60,97] to use DNAo as an NPoM spacer material (Fig. 4.1a,b). This DNAo structure was a rectangular plate of size 45 x 55 nm. From atomic force microscopy (AFM), the two layers of DNA gave the structure a height of 4.5 nm when measured outside of the NPoM gap. The DNAo was functionalised to both attach to the gold mirror and capture an 80 nm diameter gold nanoparticle (AuNP) to form an NPoM structure (section 2.5.4). Dye molecules were pre-functionalised with a particular staple DNA strand designed to incorporate into a particular location within the DNAo. This created NPoM constructs with a maximum of one dye molecule within each gap and with the lateral position of this dye known to a resolution ±1.5 nm. This work investigated the plasmonically enhanced photoluminescence from this dye.

Both before and after the time frame of the work presented in this chapter (2017-2018), multiple manuscripts have been published exploring different DNAo constructs designed to incorporate single molecules for SERS measurements[59,98–101] . Such measurements would not suffer from any *ensemble averaging* where scattering from a set of molecules averages over any variation in the individual responses of each molecule. Depending on the molecule measured, a single molecule measurement has the potential to uncover time dependent interactions with the local environment or transient binding/isomerisation behaviour.

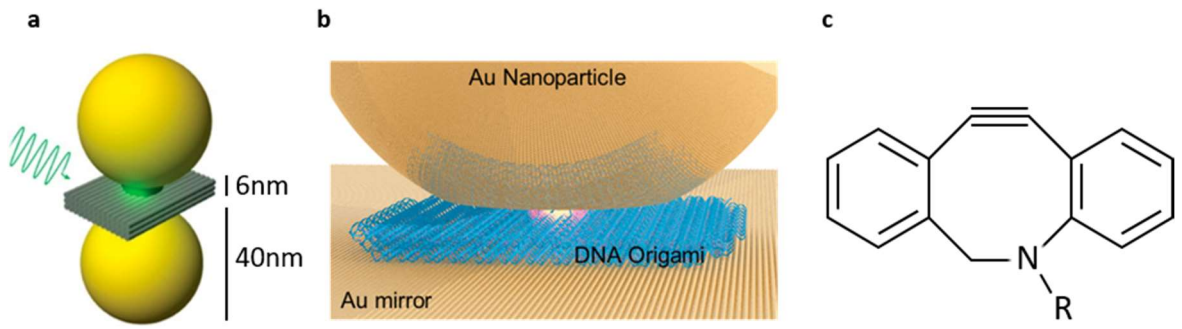

Figure 4.1 | DNAo Coupled Plasmonic Structures. a, Coupled AuNP dimer structure formed using a 3 layer DNAo structure used in the work of Kühler et. al.[60] (reproduced) **b,** 2-Layer DNAo NPoM structure used in the work of Chikkaraddy et. al.[57] (reproduced) and in this chapter. **c,** The structure of DBCO. Here, the group R is a strand of DNA.

In this chapter, the DNAo NPoM structure used by Chikkaraddy et. al.[57] is briefly investigated for suitability as a robust platform for single molecule SERS. (Fig. 4.1b)[*]. The DNAo NPoM construct alone is found to generate a highly dynamic and variable SERS response with transient vibrational modes displaying significant spectral wandering over time. This is in contrast to literature descriptions of DNAo plasmonic constructs where individual spectra are generally shown and such a dynamic time response is not mentioned[98,99,101]. Due to this dynamic response, the structure is not considered an ideal platform from which to isolate additional single molecule SERS. However, this SERS response is interesting in isolation and could represent some dynamic interaction between the DNA and gold surfaces. The sudden and transient appearance of bright and dynamic SERS lines is highly reminiscent of picocavities previously characterised in NPoM at cryogenic temperatures[3] (section 2.8). Due to the complexity of possible interactions that could be occurring between such a large macromolecule as DNA and the gold surface, this system is not studied further here beyond these observations.

Single molecules of dibenzoclyclooctane (DBCO) are incorporated into the centre of the NPoM cavities (Fig. 4.1c). As this molecule contains a C≡C bond, this provides a high energy stretching vibrational mode that is spectrally separated from the complex SERS response of

[*] DNAo constructs designed and synthesised by Vladimir Turek of University of Cambridge. All measurements and analysis by me.

the DNAo alone. Experimentally, this spectral region is found to contain a number of closely spaced vibrational modes compared to the single mode predicted by DFT (section 3.8). This suggests that this mode is being split by some interaction with the Au surfaces and/or the DNAo itself. As with measurements of the DNAo alone, some of these single molcule SERS modes are transient and show both discrete jumps and continual directional drifts in vibrational energy over a 10 s timescale. In preliminary measurements, these transient modes are found to persist when the laser irradiation is removed, suggesting that the laser light plays a role in their generation and destruction. This also aligns with observations of picocavities in NPoM.

The observation of single molecule SERS from DBCO in DNAo NPoM was published in the Journal of Raman Spectroscopy[102].

4.2 Characterisation of DNAo NPoMs

4.2.1 DNAo NPoMs in Dark Field and SERS

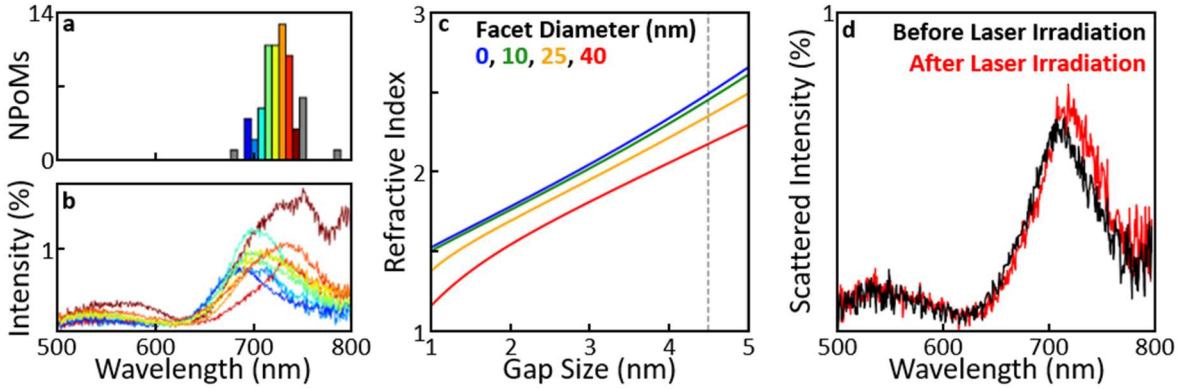

Figure 4.2 | DNAo NPoM Dark Field. a, Extracted coupled plasmonic mode wavelengths from dark field scattering of 2-layer DNAo NPoMs. **b,** The average dark field scattering spectrum from each coloured set of coupled mode positions. **c,** Combinations of gap refractive index, NPoM gap size and facet size to provide the observed 725 nm average coupled mode position, based on a 80 nm diameter nanoparticle. Grey line indicates the nominal gap size of 4.5 nm. **d,** Example NPoM dark field spectrum before and after irradiation with 709 μW of 633 nm laser power for >70 s.

The DNAo NPoMs (see section 3.2.2.1 for synthesis protocol) are first characterised using dark field scattering. These measurements show the expected transverse (<600 nm) and coupled (>700 nm) NPoM plasmonic modes (Fig. 4.2a,b). As discussed in section 2.5, the lower energy coupled modes represent plasmonic resonances delocalised over the nanoparticle and its charge image (creating large field enhancements in the NPoM gap) while the transverse modes represent resonances more strongly localised on the nanoparticle. We consider only the lower order coupled resonance to dominate the coupled region, although this is a simplification and some spectra do show multiple resonances in the coupled mode region. These are ignored when extracting the average coupled mode resonance (Fig. 4.2a). This gives an average coupled mode resonance wavelength ~725 nm in agreement with the previous observations of Chikkaraddy et. al.[57]. As an observation, it is noted that the transverse to coupled mode intensity ratio is small here for unknown reasons when compared to NPoM measurements using molecular monolayers later in this thesis (Chapter 5).

Using the analytical NPoM coupled resonance model (section 2.5), combinations of NPoM gap sizes, gap refractive indices and AuNP facet diameters are shown in figure 4.2c that result in a 725 nm coupled mode wavelength. Even considering the possible compression of the DNAo plate from 4.5 nm in height when within the NPoM gap, this model requires a gap refractive index of ~2. While this high value agrees with previous measurements of both this system[57] and AuNP dimers constructed with DNAo[60,97], this is in disagreement with measurements of 1.3 - 1.6 for DNA measured in non-plasmonic systems[103,104].

The effective refractive index of macromolecules such as DNA is known to be complicated to assign with complex screening interactions between different sections of the negatively charged DNA backbone and ions in the surrounding solvent. For non-origami double stranded DNA, this has led to development of models that vary the effective refractive index with DNA strand length[105]. In plasmonic scattering measurements of single nanoparticles coated in doubled stranded DNA by Liu et. al.[106], this model well describes an effective DNA refractive index increase from 1.6 to >2 as the DNA shell is increased in thickness to almost 20 nm. For a shell thickness of ~5 nm (the height of our DNAo construct), the refractive index is increased only to ~1.65. While the NPoM gap is nominally dry (as the sample is not stored or measured in liquid), the solvent environment within the nanoscale gap is unknown. The ordered and packed structure of DNAo may factor in increasing the effective refractive index further.

Within the NPoM gap, image charges of the DNA and ions within the nearby metal surfaces may also modify the system. Therefore, this high effective refractive index may actually represent a reasonable value.

Note that if the DNAo construct has significant conductance, this would blue shift the resonance and further increase the refractive index required to explain the observed result (section 2.5). In literature, conductance measurements of DNA have varied widely from insulating to well-conducting depending on the sequence and conformation being measured. The dominant charge transport mechanisms are still being determined[107,108] . It is possible that a conductivity measurement could be made of this DNAo structure in situ using the recent experimental protocol of Kos et. al.[109] to electrically contact individual NPoM constructs.

The SERS response of the DNAo NPoM is characterised using 633 nm laser irradiation and experimental set up A (section 3.5). In figure 4.3, scans of 100 consecutive spectra are taken for each of 71 NPoMs using a 1 s integration time per spectrum and ~700 μW of incident laser power. A measurement taken away from any NPoM construct is subtracted to remove any non-NPoM background response. The dark field coupled resonance mode does red shift slightly during these measurements (Fig. 4.2d) indicating that the incident laser power is allowing the nanoparticle facet to begin to grow[37]. In the coupled mode analytical model, the change displayed in figure 4.2d corresponds to a 10 nm diameter facet growing to 23 nm or a 40 nm facet growing to 45 nm depending on the refractive index set for the gap and assuming a 4.5 nm gap size. To be a practical platform for single molecule SERS, the DNAo response should be stable in time so that it can be isolated from any additional single molecule signal. Instead, three main features are observed that vary between NPoMs with similar reasonable dark field scattering spectra (Fig. 4.3). First, each measurement contains a bright broadband response that can transiently increase in intensity. Second, stable SERS lines are sometimes seen. Third, transient and spectrally dynamic SERS lines are sometime observed. These features will be discussed in turn.

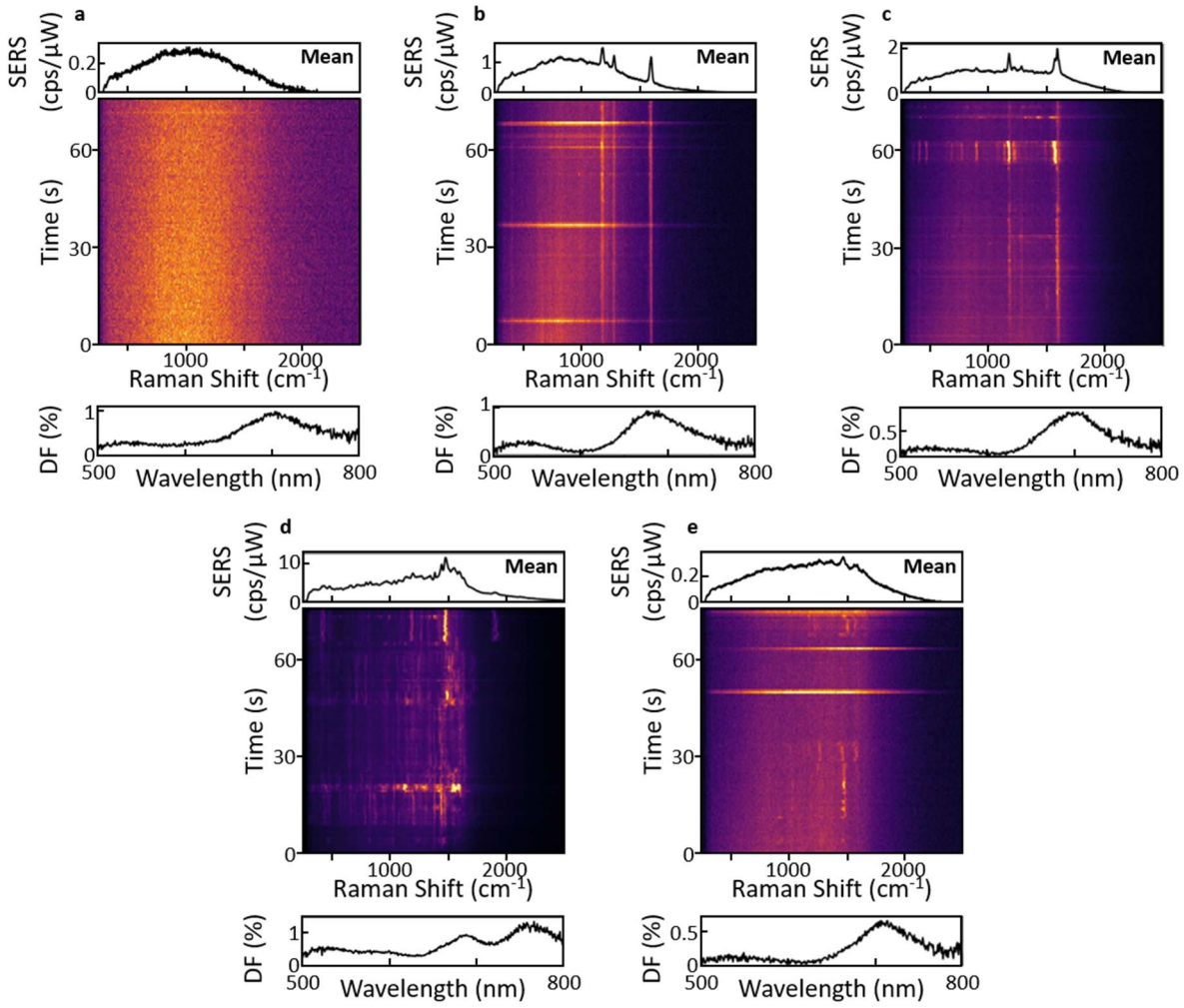

Figure 4.3 | DNAo NPoM SERS. Examples series of consecutive SERS spectra from 2-layer DNAo NPoMs using ~700 μW of 633 nm laser excitation and a 1 s spectrum integration time. Each time scan of spectra is shown alongside the mean SERS spectrum and the dark field scattering spectrum from that NPoM. Observed responses include **a,** only a broadband response **b,** persistent SERS lines with transient broadband events **c,** persistent lines with transient but non-dynamic lines and **d,e**, transient and dynamic SERS lines.

For some NPoMs, the broad background response is the only resolvable feature in the SERS spectra. In figure 4.3a, the peak of this signal (~ 1000 cm^{-1} = 675 nm) does not correspond to the wavelength of the dark field scattering coupled mode (~ 1500 cm^{-1} = 700 nm) so it is unlikely that this is due to light penetrating the Au metal (section 2.7). Although DNA does exhibit fluorescence, this peaks in the UV and has a low quantum yield of ~10^{-4} at room temperature[110]. This can be enhanced a few orders of magnitude by the Purcell effect in a

plasmonic field[111]. If bright fluorescence were somehow produced, the observed peak could be the overlap of the fluorescence emission tail at visible wavelengths and the plasmonic response controlling how efficiently that light is coupled out of the NPoM gap. This would not explain how this UV fluorescence would be being excited. Figures 4.3b,e display examples of additional transient broadband emission lasting multiple seconds with varying peak emission energy for each transient event. If some broadband DNA response is being observed, these could represent some change in conformation or charge. It is possible that these events instead represent flares (section 2.7), which describe greater penetration of light into the gold due a transient change in gold structure over a small region. If this is the case, these observations display an order of magnitude increase in event lifetime compared to those reported using molecular monolayer NPoM spacers[70]. This could suggest a significant interaction between the DNA and gold surface.

For 15 (21%) NPoMs, a triplet of persistent SERS lines are observed (Fig. 4.3b,c). These vibrational energies (1184 cm^{-1}, 1284 cm^{-1}, 1603 cm^{-1}) do not overlap well with nucleotide modes previously observed in DNAo nanoparticle dimers[60,97]. This alone does not rule out that they originate from the DNA. It is possible that these lines are the result of some residual citrate on the AuNPs not fully displaced by the thiolated single strand DNA coating. Citrate is a capping ligand that coats the commercial AuNPs and has characteristic vibrational lines at 1604 cm^{-1} and $\sim$1300 cm^{-1} (as well as many that do not match the lines observed here)[112].

Finally, 28 (39%) NPoMs display transient and spectrally dynamic SERS lines (Fig. 4.3c-e). Without some additional SERS enhancement, any change to the intensities of Raman lines requires some physical change to the structure of the DNA. Examples include charging or conformation changes. Such changes would also modify vibrational mode energies. Given the size and complexity of the DNAo macromolecule, the dynamic SERS could indicate changing interactions between differing sections of the DNA or between the DNA and gold surface. As an alternative interpretation, the sudden appearance of transient bright SERS lines is very similar to the effects of picocavities characterised in NPoMs at cryogenic temperatures[3]. As discussed in section 2.8, these transient atomic scale features on the gold surfaces generate regions of strong optical field gradient that locally alter the selection rules for efficient Raman scattering while enhancing scattering cross sections. These hypotheses for the observed SERS dynamics may be related with DNA-gold surface interactions aiding to generate and stabilise

picocavities at room temperature (producing the transient SERS lines) while also dynamically perturbing the DNAo vibrational energies (producing the SERS line dynamics).

As cryogenic picocavity measurements showed a strong laser power dependence to the rate of transient SERS line generation[3], large SERS datasets using a range of reduced laser powers could provide more evidence towards the origin of the observed dynamic SERS response. Unfortunately, these measurements were not carried out at the time that these DNAo samples were available.

4.2.2 Reducing DNAo in the Optical Cavity

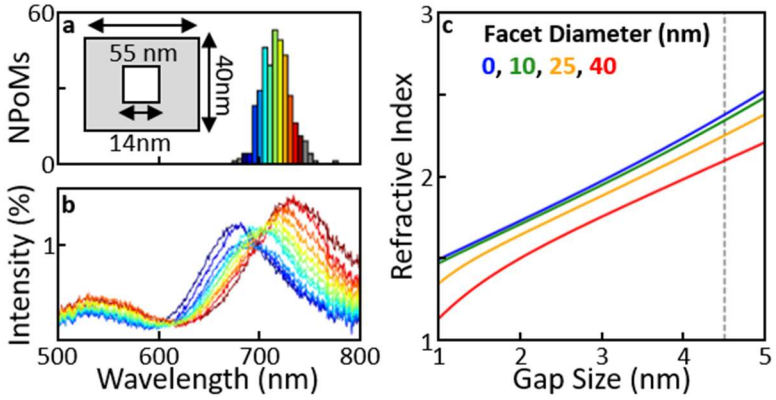

Figure 4.4 | DNAo Pore NPoM Dark Field. a, Extracted coupled plasmonic mode wavelengths from dark field scattering of 2-layer Pore DNAo NPoMs. Inset: Top-down Pore DNAo dimensions. **b,** The average dark field scattering spectrum from each coloured set of coupled mode positions. **c,** Combinations of gap refractive index, NPoM gap size and facet size to provide the observed 716 nm average coupled mode position, based on a 80 nm diameter nanoparticle. Grey line indicates the nominal gap size of 4.5 nm.

A modified DNAo structure is provided that is designed to define the NPoM gap while reducing the total amount of DNA available to generate SERS. Otherwise similar to the previous design, this construct contains a central 14 nm hole termed the *pore* (Fig. 4.4a inset). NPoMs formed using this construct provide a similar dark field scattering response with the average coupled mode resonance blueshifted to ~716 nm (Fig. 4.4a,b). While the analytical

NPoM resonance model assumes a constant refractive index in the gap, this is consistent with a drop in effective refractive index as might be expected with the removal of some DNA. This is also consistent with a decrease in gap size if the DNAo is more susceptible to compression between the AuNP and mirror.

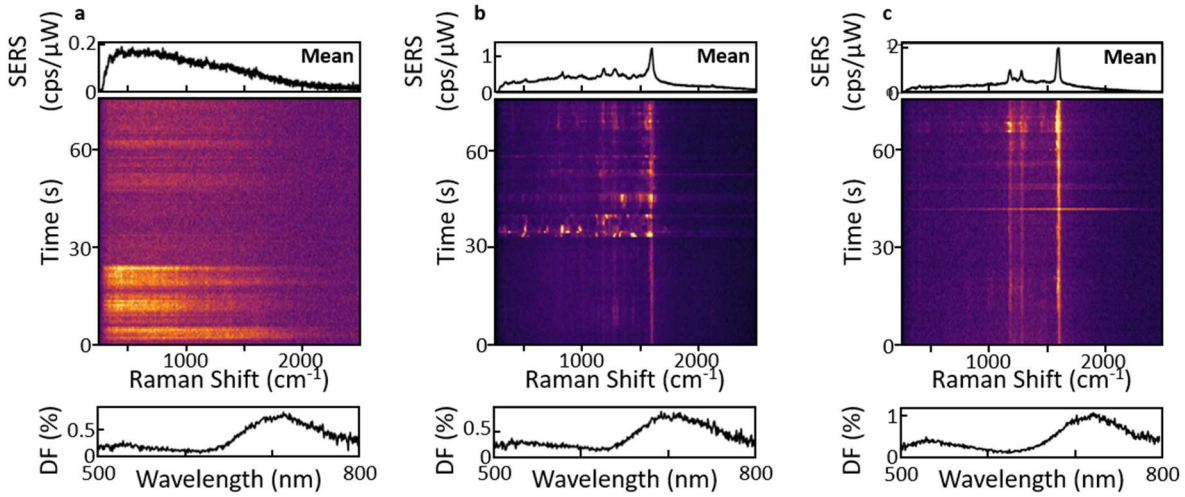

Figure 4.5 | Pore DNAo NPoM SERS. Examples series of consecutive SERS spectra from 2-layer DNAo Pore NPoMs using ~700 μW of 633 nm laser excitation with a 1 s integration time. Each time scan of spectra is shown alongside the mean SERS spectrum and the dark field scattering spectrum from each NPoM. Observed responses include **a,** a broadband but varying response and **b,c,** persistent SERS lines with additional transient and dynamic lines.

In SERS, the same categories of observed behaviour are seen including both a broadband signal and transient dynamic SERS lines (Fig. 4.5). An example is noted here (Fig. 4.5a) where the broadband response is more intense for the first ~ 25 s of the measurement with digital intensity fluctuations. Once this response ends, it can be seen to reappear at much lower intensities after ~ 20 s. As 25 s is a long timescale to be associated with any modifications to the optical response of the gold, this is possible evidence that this broadband signal does somehow result from the DNA.

The pore NPoMs do show a statistical improvement over the original DNAo design with a x4 reduction in mean average SERS signal (0.12 v 0. 45 cps/μW) (Fig. 4.6a). By removing the lowest total intensity spectrum from each scan of consecutive SERS we can crudely remove

any persistent signal and the remaining transient light shows a x2 reduction in average intensity (0.05 v. 0.1 cps/μW).

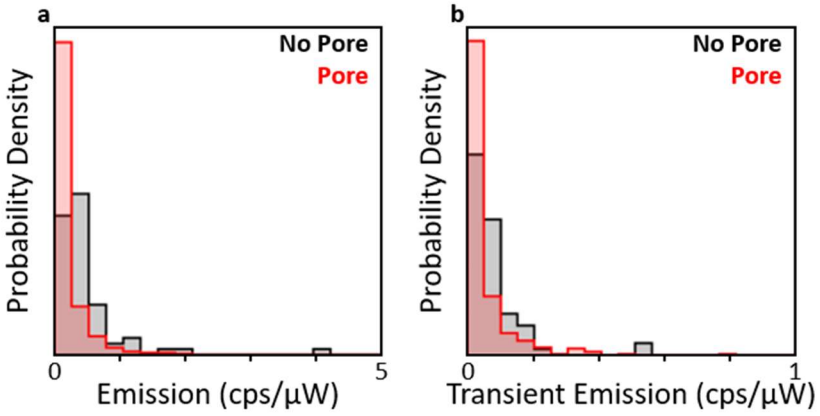

Figure 4.6| Impact of Pore on Average DNAo NPoM SERS. a, Total SERS signal from 2-layer DNAo NPoMs with and without a central pore. Each measurement aggregates 100 consecutive spectra taken using with a 1 s integration time using ~700 μW of 633nm laser power. **b,** Total SERS signal after the lowest intensity spectrum has been subtracted from each series of spectra to remove the persistent response.

4.2.3 NPoM Formed with 1-Layer DNAo Plate

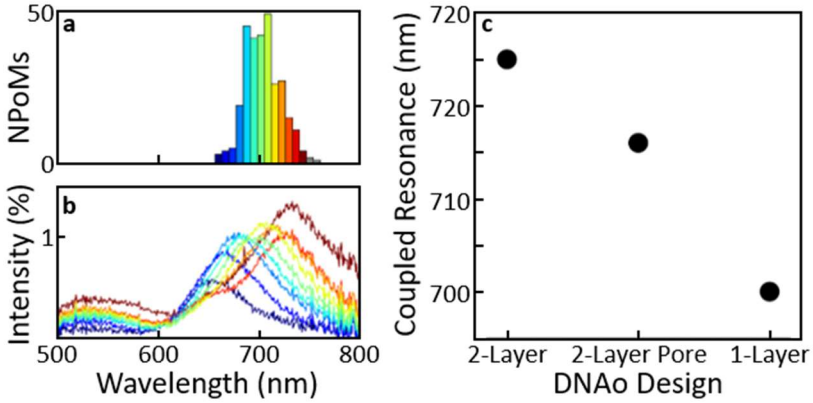

Figure 4.7 | Single Layer DNAo NPoM Dark Field. a, Extracted coupled plasmonic mode wavelengths from dark field scattering of 1-layer DNAo NPoMs. **b,** The average dark field scattering spectrum from each coloured set of coupled mode positions. **c,** Average coupled resonance wavelength for each DNAo construct.

A final DNAo design is provided consisting of a single layer of DNA with no pore. This is characterised using dark field scattering and displays a clear blue shift in average coupled mode resonance to 700 nm (Fig. 4.7). This is a counter intuitive result given that a smaller gap size is expected to redshift the plasmonic response. Speculatively, if the reduction in DNAo thickness allows for an increase in gap conductivity than this could go some way to opposing the expected redshift.

4.3 Single Molecule NPoM Cavities

The 2-layer DNAo NPoM structure (section 4.2.1) is used for single molecule SERS measurements due to the evidence provided by the work of Chikkaraddy et. al.[57] that it can successfully incorporate single molecules into the NPoM gap. As the DNAo construct shows a complex SERS response up to $\sim$1600 cm^{-1} with occasional transient modes seen up to $\sim$2000 cm^{-1} (Fig. 4.3d), a molecule is required with a SERS response at higher vibrational energies outside of this region. At the time of these measurements, the molecule dibenzoclyclooctane (DBCO, Fig. 4.1c) was available functionalised with a strand of staple DNA for incorporation into DNAo constructs. This molecule contains a high energy C≡C bond which, according to DFT calculations (Fig. 4.8a, section 3.8), provides a stretching vibrational mode $>$2000 cm^{-1}. Note that the internal approximations to DFT tend to overestimate vibrational model energies by a few percent. There are two important caveats to this calculation. First, the molecule is calculated in isolation without the complicating influence of the nearby DNAo or the gold surfaces. Second, while the experimental DBCO molecule is bound into the DNA structure the calculated molecule is instead bound to an amine group, which is a commercial form of this molecule that was purchased from Sigma Aldrich (Fig. 4.9b).

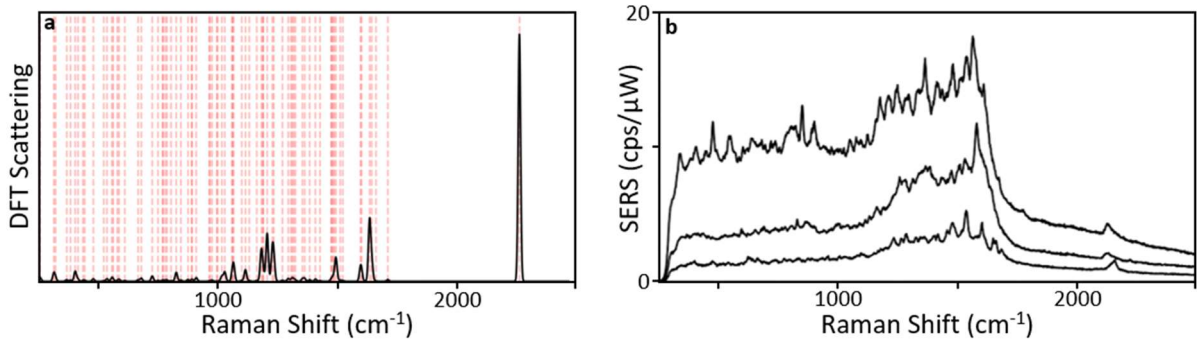

Figure 4.8 | DBCO SERS in DNAo NPoM. a, DFT SERS spectrum of DBCO. Peak heights indicate relative Raman Activity. Peak width is ad hoc. Red lines indicate the energies of all calculated vibrational modes. **b,** Example SERS spectra from 2-layer DNAo NPoMs containing single DBCO molecules. Measured using ~700 μW of 633 nm laser power. Each spectrum is the mean average of 4 consecutive spectra measured using a 1s integration time.

Despite these approximations, this calculation is sufficient to indicate that SERS from this molecule should provide a high energy SERS peak spectrally separated from the DNAo response. Experimentally, a persistent peak in this region is taken as evidence of successful molecule incorporation (Fig. 4.8b). This peak is weak in intensity, both due to being a single molecule measurement and due to a drop in the collection efficiency of the objective lens at these long wavelengths (section 3.5.4). For this reason, initial measurements are taken using ~700 μW of laser power and >1 s integration times.

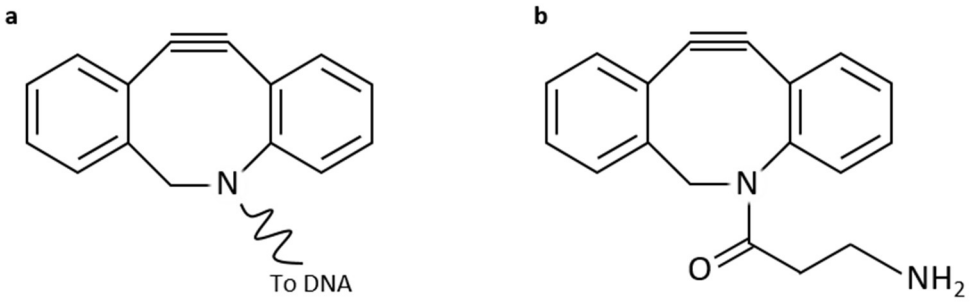

Figure 4.9 | DBCO Structure. a, Structure of DBCO incorporated into the DNAo structure. **b,** Structure of DBCO modelled in DFT and used in bulk Raman measurements with DNA attachment replaced with an amine.

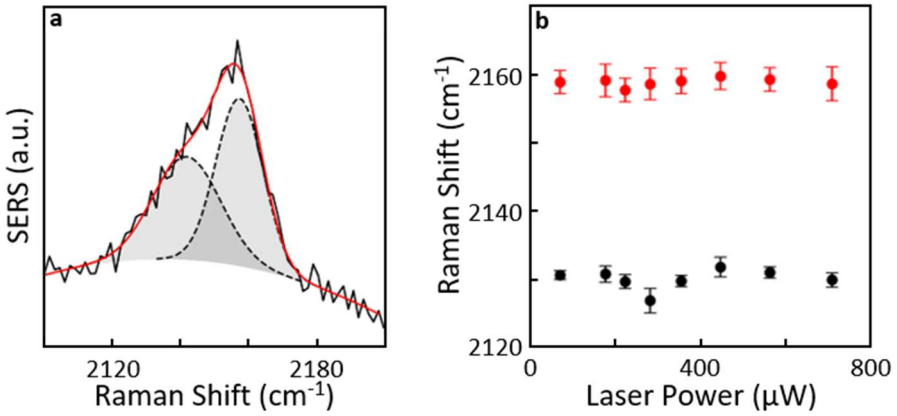

Figure 4.10 | DBCO Split SERS Peak. a, Example single molecule DBCO SERS peak from a 2-layer DNAo NPoM. SERS measured using ~700 μW of 633 nm laser power. Data shown is the mean average of 4 spectra using a 1 s integration time. The asymmetric peak is fit (red line) using two Gaussian peaks (dotted) and a quadratic background. **b,** Mean positions of split persistent DBCO SERS peaks taken from 94 NPoMs over a range of increasing 633 nm laser powers.

Experimentally, the persistent DBCO SERS peak is noted to be broad and sometimes asymmetric (Fig. 4.10a). This is indicative that it is in fact formed from multiple overlapping peaks. This suggests that an interaction between the molecule and its surroundings is splitting this high energy vibrational mode predicted by DFT. It is also possible that this unknown interaction has made the state of the molecule bi-stable and that it is switching between two states with different vibrational modes energies much faster than the >1 s spectrum integration times used here.

For 94 NPoMs showing the DBCO SERS peak, the spectrum is measured over a range of increasing laser powers from 70 to 700 μW. At each power, 4 consecutive spectra are taken in case the peak splitting shows any obvious dynamics. As these are not seen, the spectra are averaged here at each power to improve signal-to-noise. An integration time of 1 s per spectrum is used for the highest laser power which is scaled up for lower powers to counter the decrease in signal. For each given spectrum, the narrow region 2100-2200 cm^{-1} is fit to a polynomial background and either one or two Gaussian peaks (Fig. 4.10a). The most suitable model is selected using the Bayesian Information Criterion (BIC, section 3.9). In total, this

spectral region is resolvable as two SERS peaks in 40% of NPoMs measured. The average extracted line positions do not show any dependence on laser power (Fig. 4.10b), suggesting that the optical field does not play a role in this mode splitting.

Collating all the detected peak positions over all powers into a single histogram (Fig. 4.11a), each peak forms a distribution centred at around ~2130 cm^{-1} and ~2160 cm^{-1} respectively. The widths of these distributions suggests that there is a variation in the line splitting interaction between NPoM constructs. The energies of the two modes are positively correlated with a spearman coefficient of 0.54. This coefficient, bounded between -1 and 1, tests whether two quantities are monotonically related. To test the significance of this value, the data is randomly permuted and the coefficient recalculated. In 10^4 random permutations, this correlation value is never reached and, modelling the permutation results as drawn from a normal distribution, this value is over 8.5 standard deviations above the mean. Therefore, the probability that this correlation is spurious is negligible. The dominant peak in terms of total scattered intensity varies with the lower energy peak more often dominant (Fig. 4.11b). The spectra in which two peaks cannot be resolved show a single peak with average vibrational energy much closer to the 2130 cm^{-1} position (Fig. 4.11c). However, even these show a variation in vibrational energy with a standard deviation on a 10 cm^{-1} scale.

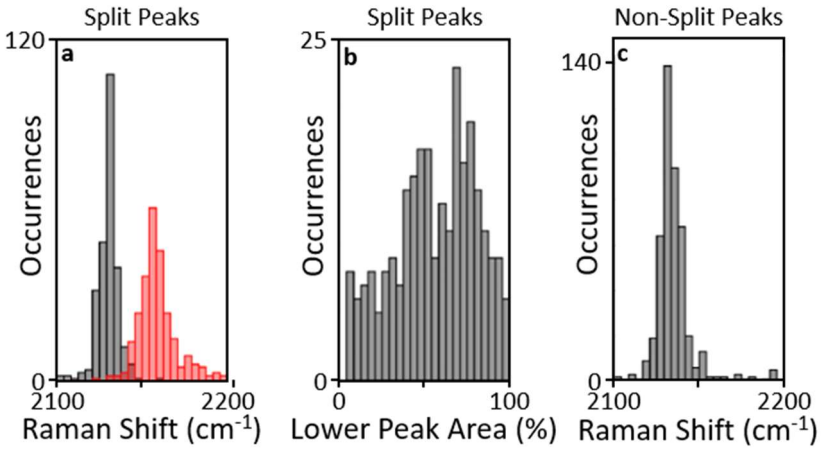

Figure 4.11 | Split DBCO Peak Distribution. a, Distribution of all DBCO split persistent peaks over all powers shown in figure 4.10. **b,** Fraction of asymmetric peak area provided by the lower energy split peak. **c,** Distribution of all peak energies which are not split within experimental resolution.

Given that the DFT calculation does not predict multiple peaks in this spectral region, bulk (non-plasmonically enhanced) Raman is measured from DBCO crystals. This averages over the Raman response of many molecules within a crystal. These molecules have the same amine function group as the molecule calculated in DFT (Fig. 4.9b). This bulk measurement shows a clear set of peaks with four peaks manually identified at 2132, 2161, 2190 and 2203 cm^{-1} (Fig. 4.12). Two of these agree well with the overlapping SERS peaks discussed while the two higher energy peaks are not seen in the persistent SERS spectrum. It is unknown exactly what interaction between DBCO molecules in the bulk crystal is causing the single vibrational mode predicted by DFT to become hybridised and split into the four modes seen here. However, it seems likely that a similar interaction is occurring with the single DBCO molecule in NPoM and the surrounding DNA / gold surfaces. This could be studied further in DFT by calculating more complex systems of multiple DBCO molecules although this get increasingly more computationally expensive as more molecules are considered.

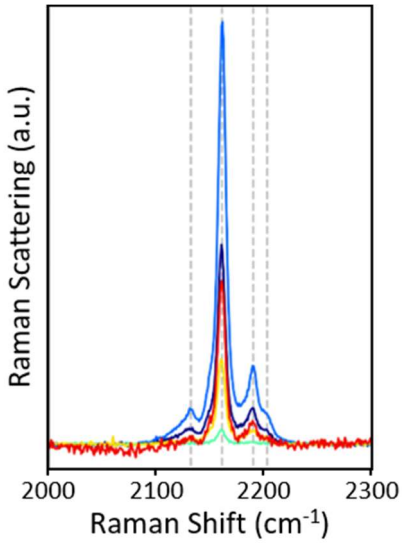

Figure 4.12 | Bulk DBCO Raman. Bulk Raman scattering of DBCO crystals. Each colour indicates a separate measured crystal. Grey lines indicate manually extracted peak positions.

Measuring consecutive SERS spectra using ~700 µW of laser power and a 1 s integration time, additional transient SERS lines are also occasionally observed in this spectral region (Fig. 4.13). These display a range of dynamic behaviour. For example, figure 4.13a shows an apparent

bifurcation with the branching peak continuously shifting in energy over 10s of seconds. Transient lines are seen both at higher and lower vibrational energies than the persistent vibration (Fig. 4.13a). The smooth changes in vibrational energy indicate a continuous change in some interaction between the DBCO molecule and its surroundings. The sudden appearance and disappearance of SERS peaks is, as previously stated for the DNAo SERS alone, reminiscent of picocavities.

In this chapter, the root cause of these smooth changes in transient vibrational mode energies is not investigated in depth. However, I here briefly foreshadow the investigations and results that will be discussed in Chapters 5 and 6. In these chapters, I will investigate transient lines in a molecule with a similar high energy -C≡N nitrile functional group in a simple molecule that forms a self-assembled monolayer (SAM, section 2.5.4). This is a simplified system compared to having DNAo in the NPoM gap. I will show that these transient events do represent picocavities and that a chemical interaction between the picocavity surface feature and functional group perturb vibrational energies in a way that that is smooth with changing relative picocavity-molecule position. Here, I conjecture both that these DBCO transient lines are generated by picocavities and that the smooth changes in transient line position is due an interaction between the molecule and low coordination number gold picocavity feature. Based on the results in this thesis, we performed preliminary DFT calculations of a low coordination number gold atom in proximity to the DBCO molecule[102]. While these calculations also do not find more than one vibrational mode in this spectral region, they do show that its energy is perturbed by the presence of the gold atom.

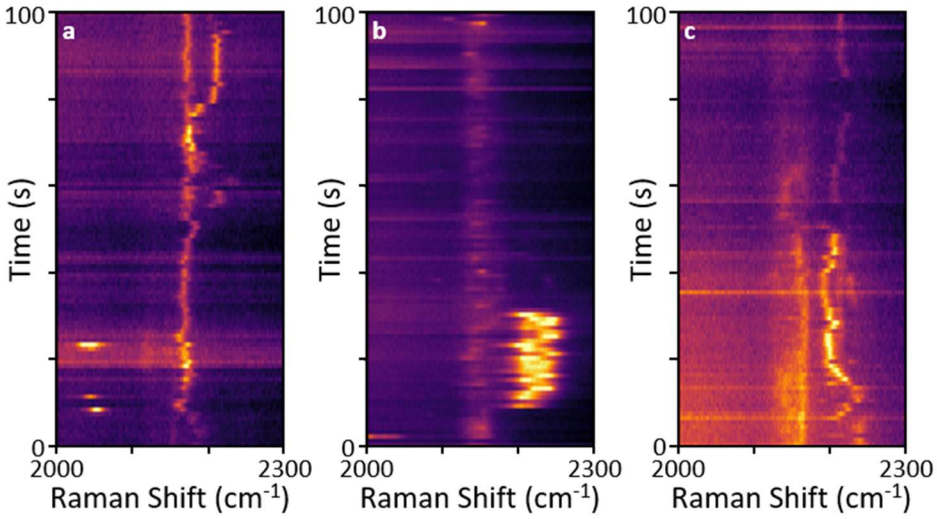

Figure 4.13 | Transient Dynamics of DBCO C≡C SERS. Examples of dynamic and transient SERS behaviour in the region of the DBCO C≡C vibrational mode. SERS taken using ~700 µW of 633 nm laser power and a 1 s integration time per spectrum.

The SERS measurements are repeated for 100 NPoMs using a 0.1 s integration time to trade signal intensity for temporal resolution. No changes in the observed dynamics, such as continuous line shifts resolving into discrete jumps or vice versa, are observed. To extract statistics, all resolvable peak positions are extracted from each of the 1000 spectra taken per NPoM. To achieve this, each spectrum is modelled over the range 2000 -2300 cm^{-1} as a polynomial background plus a set of Gaussian peaks. The optimum combination of peaks and polynomial order is set using the BIC (section 3.9). The peaks are constrained in width (standard deviation) to the range 4 – 40 cm^{-1} to prevent any possible fitting to the noise or background (although this behaviour should be suppressed by the BIC). This process was able to reproduce the observed spectra well (Fig. 4.14).

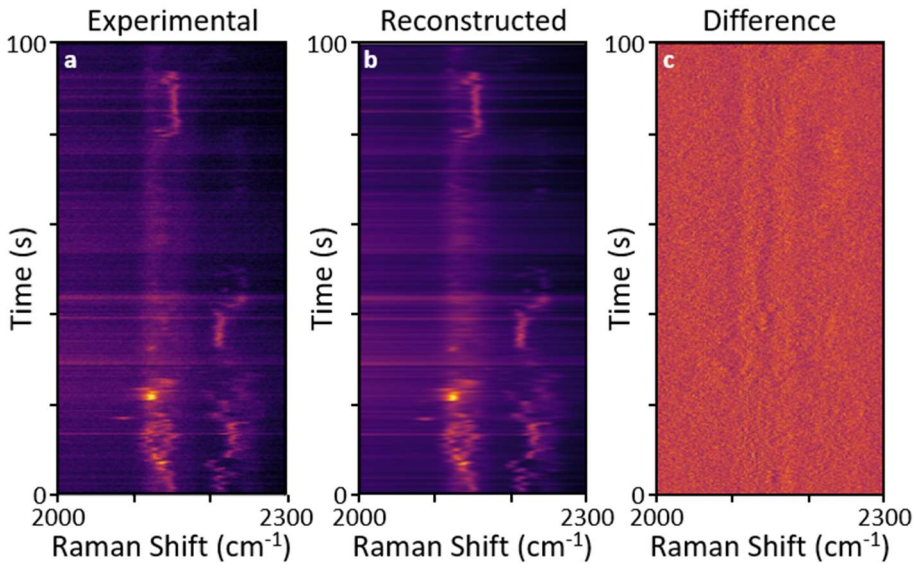

Figure 4.14 | Extracting SERS Peaks from Dynamic Spectra a, Example of dynamic and transient SERS behaviour in the region of the DBCO C≡C vibrational mode. SERS taken using ~700 μW of 633 nm laser power and a 0.1 s integration time per spectrum. **b,** Each spectrum is reconstructed as a polynomial background and set of Gaussian peaks. **c,** Difference between the reconstructed and experimental data.

Considering all detected peak positions (Fig. 4.15), the distribution is dominated by a large broad peak encompassing the 2130/2160 cm^{-1} persistent split peak positions already discussed. It is interesting that these are not resolved in this combined histogram. Smaller peaks in the distribution are seen either side of this. This distribution is broad at higher energies with a long tail. The higher energy peak of this distribution overlaps well with the two higher energy modes observed in bulk Raman. This suggests that these transient modes are these vibrational modes enhanced in intensity by a picocavity and shifting in energy due to dynamic interactions. The lower energy transient line positions have no counterpart in the bulk Raman measurement.

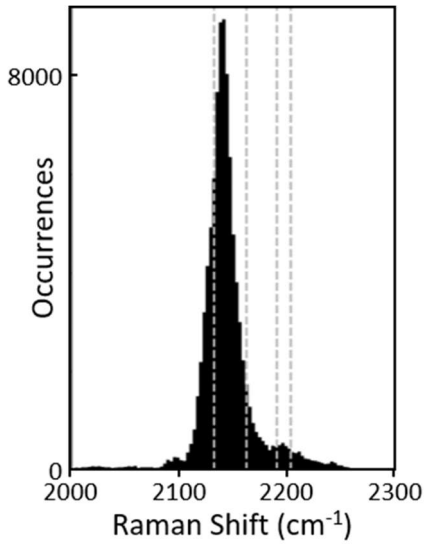

Figure 4.15 | DBCO SERS Peak Positions. All detected SERS peak positions in the region of the DBCO C≡C vibrational mode for 100 NPoMs. Each NPoM measured for 1000 consecutive spectra using 709 μW of 633 nm laser power and a 0.1 s integration time per spectrum. Grey lines indicate SERS peaks in bulk DBCO Raman.

At cryogenic temperatures, NPoM picocavities were found to be highly dependent on incident laser power[3]. Here, a preliminary experiment is carried out where the automatic detection of a transient DBCO peak lasting 10 s triggers a 30 s shuttering of the incident laser. This allows the system to evolve in the dark. In the four measured cases, the transient line is found at the same spectral position when the laser irradiation resumes. Three of these cases are shown in figure 4.16 with one omitted due to a poor signal-to-noise ratio. In one case (Fig. 4.16c), a second transient line does not survive the wait period. However, this line is only visible for a single spectrum before the wait period and may have disappeared within the spectrum integration time before the irradiation was paused.

The three events shown in figure 4.16 show an interesting relationship between the persistent and transient lines. In figure 4.16a, the transient line is not particularly spectrally dynamic and the overlapping persistent lines are stable. In figure 4.16b, changes to the energy of thetransient line (such as the sudden redshift 6 s before the wait period) have corresponding changes in the persistent lines. Such correlated effects are also seen in early times in figure 4.13c. While this effect is subtle, all of these vibrational modes result from a single molecule and an effect that changes one vibration in this spectral region would be

expected to alter the others as well. Noticing these changes is complicated by the persistent SERS peak being formed from two barely resolved vibrational modes.

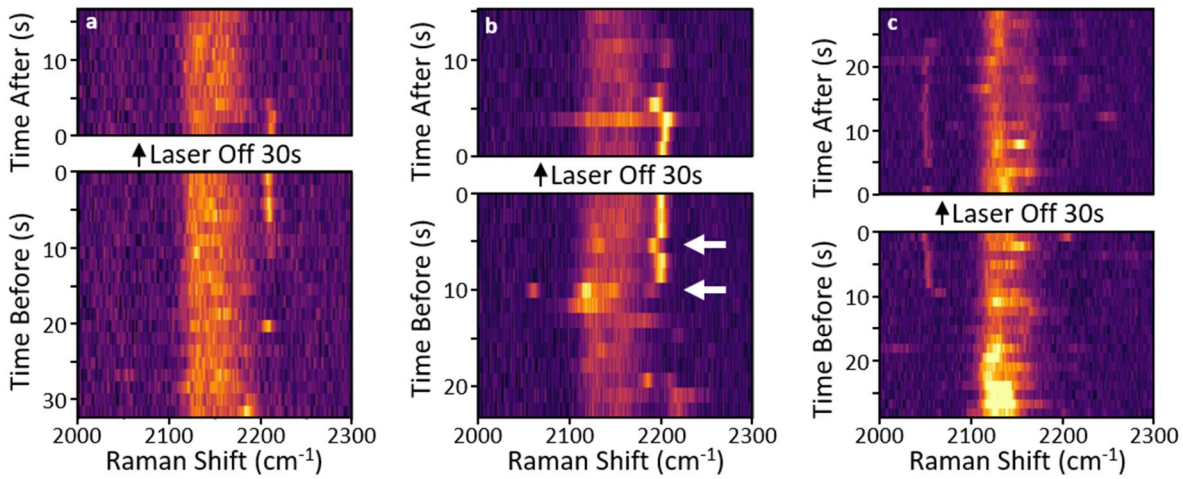

Figure 4.16 | Transient SERS in the Dark. SERS taken of DBCO DNAo NPoMs using approximately 700 μW of 633nm laser power until the automatic detection of a transient SERS line in the region of the DBCO C≡C vibrational mode. The laser is shuttered for 30s before the measurement is continued. White arrows in **b** indicate sudden red shifts in transient line energy.

4.4 Conclusion

In this chapter, I preliminarily explored the DNAo NPoM construct as a platform for measuring single molecule SERS. Measurements of dark field scattering corroborate the work of Chikkaraddy et. al.[57] suggesting a high effective refractive index for the DNAo of ~2. The refractive index of such a complex macromolecule as DNA has been found to vary depending on its sequence and conformation, meaning that this value may not be unreasonable. When the thickness of the DNAo is reduced, the coupled NPoM plasmonic mode blue shifts counter to expectation. This may be a result of changes in conductivity through the DNA which is also a complex property of this macromolecule.

Unexpectedly, the DNAo displayed dynamic SERS behaviour with the appearance of transient vibrational modes. While this is reminiscent of picocavity events measured in NPoM at

cryogenic temperatures[3], it was considered during those cryogenic measurements that room temperature picocavities would be too unstable to measure. When single molecules of DBCO are incorporated into the plasmonic cavity, the high energy C≡C stretching vibrational mode (spectrally separated from the DNAo response) is found to be split into a small set of modes. Some of these modes are transient and display continuous and directional changes in vibrational energy (in contrast to random spectral wandering around a fixed spectral position) over 10 s time scales. I conjecture that these represent picocavities where the low coordination number picocavity surface feature chemically interacts with the DBCO molecule and dynamically alters its vibrational energies. This idea will be explored further in Chapter 5 and in detail in Chapter 6. These transient lines are stable in the dark, suggesting a role of light in their formation and destruction (as with picocavities).

Here, this complex SERS behaviour is noted but further work is not carried out to explore the system systemically by varying either the incident laser power or the DNAo structure. This is primarily due to complexity of the large DNAo construct. Instead, these observations inspired a search for picocavities in NPoM with SAM spacers which are more easily modelled and explored computationally using methods such as DFT (Chapter 5). This work could not be returned to over the time period of this thesis due to the departure of collaborator Dr. Vladamir Turuk from the research group who designed and synthesised these DNAo structures.

In a future study of DNAo SERS dynamics, large datasets of DNAo SERS should be taken over a range of incident laser powers. This will allow distributions for the occurrence frequency and lifetime of transient events to be extracted. The positions of transient peaks should, when possible, also be extracted. It is noted that sometimes the DNAo can generate such a large density of vibrational modes that one mode can no longer be resolved from another (Fig. 4.8b, for example). These forms of analysis are similar to those that are applied to SAM NPoM systems in Chapter 5 and Chapter 7. This would allow the dependence of these transient modes on optical power and DNAo synthesis parameters to be extracted. The vibrational energies of the most common DNAo SERS lines could provide some insight into how the DNAo is interacting with the gold surfaces and possibly generating or stabilising picocavities.

Continuing from this preliminary work, new DNAo constructs could be continued to be designed with the aim of a more robust NPoM gap structure that minimises the amount of

DNA in regions of high optical field intensity. It should be noted that, even if not ideal as a SERS platform, the DNAo NPoM remains a useful structure for other non-Raman experiments such as studying the photoluminescence of dyes in a plasmonic cavity as an extension of the work of Chikkaraddy et. al.[57]. The observed broadband light from this system would have to be considered in such measurements.

Chapter 5: Single Molecule Scattering from Room Temperature Picocavities

5.1 Introduction

In Chapter 4, preliminary room temperature SERS measurements of Nanoparticle-on-Mirror (NPoM) constructs with a DNA Origami (DNAo) spacer showed the transient appearance of spectrally dynamic vibrational modes. The transient appearance of SERS modes is suggestive of the formation of picocavities. As discussed in section 2.8, picocavities describe the transient stochastic formation of atomic scale features on the surfaces of the NPoM gap during laser irradiation. The resulting strong optical field gradient around this feature extends over the scale of a single molecule, locally changing the SERS selection rules by efficiently generating Gradient Raman (section 2.6.3). Before the time frame of this work (2018), picocavities in NPoM had been characterised by Benz et. al.[3] at cryogenic temperatures using a Self-Assembled Monolayer (SAM, section 2.5.4) of biphenyl-4-thiol (BPT, Fig. 5.1a) as the NPoM gap spacer. In that work, picocavity events were observed to last for ~1 s with decreased stability with increasing laser power. In this chapter, I will show the detection of room temperature BPT picocavities by increasing the temporal resolution of the SERS measurements[†]. At a similar time to this work, room temperature NPoM picocavities were also reported by Shin et. al. using a similar biphenyl molecule[113].

In an NPoM system with a SAM spacer, the modified picocavity SERS is expected to result from a single molecule meaningfully experiencing a strong optical field gradient. For that reason, the transient SERS modes display random spectral wandering around a central vibrational frequency due to fluctuations in the molecule's local environment. These changes quickly average out when measuring multiple molecules simultaneously. In Chapter 4, DNAo was used to measure SERS from a single molecule with a high energy C≡C bond. This provided

[†] This work was carried out in collaboration with Cloudy Carnegie at the University of Cambridge, who provided experimental measurements of BPT and extracted initial effective molecular temperatures from this data. All other experimental measurements and data analysis carried out by me.

a vibrational mode at higher energies than the SERS response from the DNAo itself. Transient lines in the spectral region of this bond displayed continuous and directed changes in vibrational energy as well as the expected random wandering. Because of these observations, another SAM molecule is investigated in this chapter similar to BPT with an additional high energy -C≡N nitrile functional group. This is known as 4'-cyanobiphenyl-4-thiol (NC-BPT, Fig. 5.1d). Although BPT and NC-BPT are chemically similar, this change is found to extend picocavity lifetimes by a factor ~ x3. The nitrile group provides a single high energy vibrational mode that is spectrally well separated from the other vibrational modes of this molecule. In this chapter, I will explain how transient SERS lines in the spectral region of this mode are initial evidence of chemical interactions between the picocavity feature and this nitrile group. This interaction allows picocavities formed from the mirror or nanoparticle (AuNP) facet to be distinguished. A 1:9 asymmetry in picocavity generation is observed in favour of the mirror surface that reduces with incident laser power, suggesting a difference in picocavity generation energy barrier of ~ 3 k_BT between the two surfaces. These results underline the importance of the nearby chemical environment in the undetermined mechanism of picocavity formation.

The main results presented here have been published in JPCL[114], although the data has been reanalysed here to allow for a more elegant picocavity detection algorithm to be presented. This algorithm reduces the number of internal hyper-parameters that must be manually optimised, making the system more robust. This reanalysis allows the work to be extended in places but corroborates the published results.

5.2 BPT and NC-BPT Nanoparticle-on-Mirror

NPoM constructs are formed using 80 nm diameter AuNPs separated from a template-stripped gold mirror by a BPT SAM, as outlined in section 3.2. It is worthwhile reiterating here that as the thiol group binds strongly to gold during SAM formation before the AuNPs are deposited, the BPT molecules are oriented with the thiol group towards the mirror. NPoM formation can be checked using dark field scattering (Fig. 5.1b,c) which displays the expected transverse and coupled modes (section 2.5) with a clear coupled plasmonic mode at

~800 nm. The range of coupled mode resonance wavelengths results from the polydispersity in AuNP size and crystal shape and agrees with the scale of previous measurements[33,35]. As discussed in section 2.5, peaks in the coupled region of the spectrum (>700 nm) correspond to NPoM plasmonic modes where the resonantly enhanced field of the nanoparticle and its charge image couple. These modes are delocalised across the nanoparticle and its image. The transverse spectral region (< 700 nm) corresponds to modes excited by the perpendicular field polarisation where the enhanced field of the nanoparticle is rotated and coupling is largely reduced. These modes are more strongly localised to the nanoparticle only.

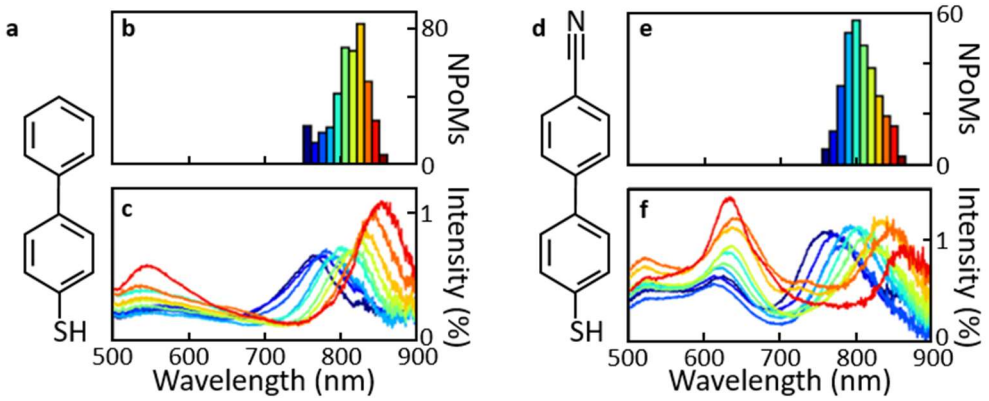

Figure 5.1 | NPoM Dark Field Scattering a, The structure of biphenyl-4-thiol (BPT) used to form a SAM. **b,** Extracted coupled plasmonic mode wavelengths from dark field scattering of 419 BPT NPoMs **c,** The average dark field scattering spectrum from each coloured set of coupled mode positions. **d,** The structure of 4'-cyanobiphenyl-4-thiol (NC-BPT) also used to form a SAM. **e,** Extracted coupled plasmonic mode wavelengths from dark field scattering of 309 NC-BPT NPoMs. **f,** The average dark field scattering spectrum from each coloured set of coupled mode positions.

As NC-BPT is chemically similar to BPT, it is also expected to form a similar closely packed SAM[115]. Indeed, NC-BPT NPoM dark field spectra display a similar range of coupled mode positions (Fig. 5.1e,f). However, there is a key difference between the spectra from each NPoM type. For NC-BPT, the transverse region of the spectrum (< 700 nm) is clearly formed from two strong modes with one (~ 625 nm) more intense than the other (~ 525 nm). For constructs with a longer wavelength coupled mode (larger AuNP), this 625 nm transverse mode is higher in intensity than the usually dominating coupled mode. In BPT, the transverse

peak is highly asymmetric suggesting that it could also be composed from these two modes with the 625 nm mode considerably reduced in intensity. While it is unclear if the change in the intensity of this mode could be the result of a simple difference in SAM packing density or optical response due to the polar C≡N bond, it does identify a difference between these systems as a result of the only this additional functional group.

5.3 Room-Temperature BPT Picocavities

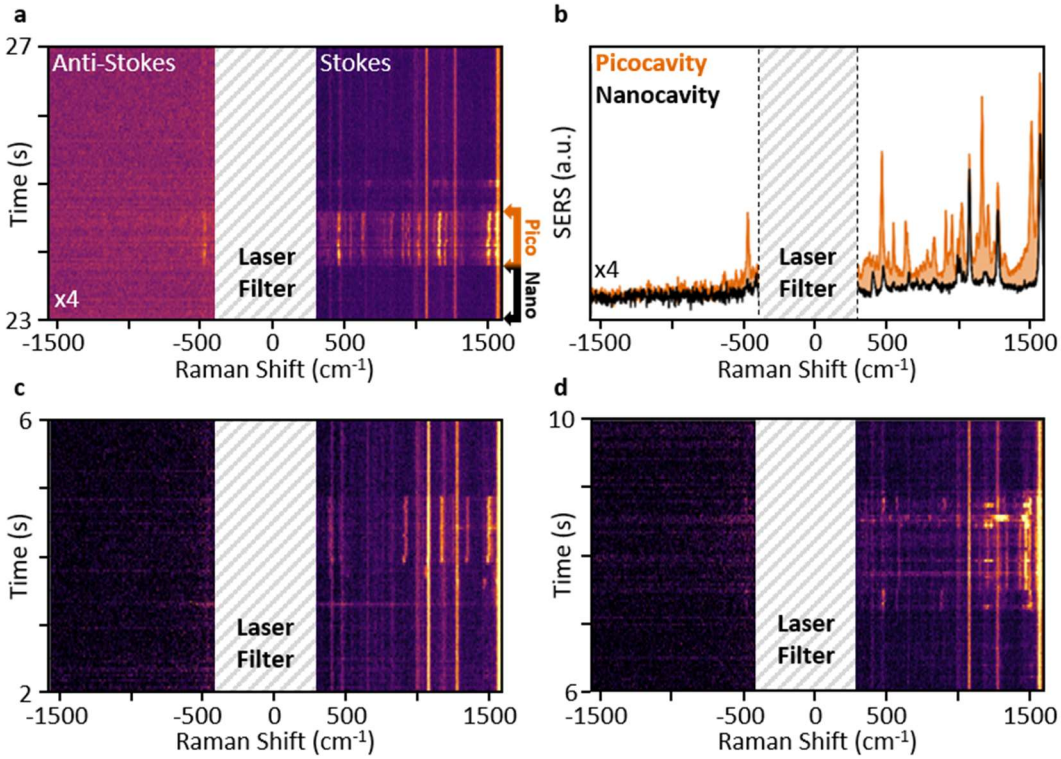

Figure 5.2 | BPT SERS Scattering. a, Example series of BPT NPoM SERS spectra (600 µW 633 nm incident irradiation, 10 ms integration time) displaying sub-second transient SERS lines at room temperature. Anti-Stokes SERS is multiplied by x4. **b,** Average SERS emission during this transient event (picocavity) compared with the average over a time window directly preceding the event (nanocavity). Anti-Stokes SERS is multiplied by x4. **c,d,** Further examples of transient BPT SERS events.

BPT NPoM SERS is measured using 633 nm laser light and experimental set up A (section 3.5). To search for transient events, the integration time per spectrum is decreased two orders of

magnitude to 10 ms in comparison to measurements of Benz et. al. at cryogenic temperatures[3]. To compensate for the decreased signal per spectrum, a laser power of 600 μW is used focussed to a diffraction limited spot. A total of 1000 consecutive spectra are taken per NPoM. The observed spectrum, as the averaged SERS from many molecules (although orders of magnitude fewer than in bulk Raman measurements), is typically stable over long periods of time (Fig. 5.2a,c,d persistent lines). This persistent vibrational response is denoted as the *nanocavity* spectrum. For example, nanocavity peak positions at >1000 cm^{-1} in figure 5.2a vary in spectral position with a standard deviation of only ~0.4 cm^{-1}. This measured deviation is dominated by the peak position uncertainty due to noise from sources like photon shot noise and electronic noise from the cooled CCD used to capture the spectrum. To minimise this electronic noise, each spectrum is read from the camera at the slowest possible read out speed (50 kHz), increasing the total cycle time per spectrum to 34 ms. Figure 5.3 shows an example dark field spectrum before and after a SERS measurement, showing no significant change to the NPoM due to the laser irradiation.

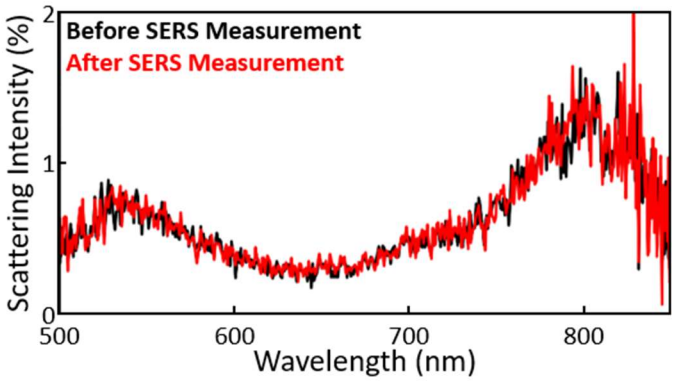

Figure 5.3 | Dark Field After Laser Irradiation. Example BPT NPoM dark field scattering spectrum before and after a 34 s SERS measurement with 600 μW of 633 nm irradiation.

Occasionally, transient sub-second SERS peaks are observed (occurrence frequency discussed in detail in section 5.6). Qualitatively, this is similar to the picocavity SERS measured by Benz et. al.[3] at 10 K (Fig. 5.2, section 2.8). Two characteristic properties of picocavity spectra can be tested here. As discussed, single molecule picocavity SERS exhibits spectral wandering due to changes in the molecular local environment (such as the proximity of ions) that is not

ensemble averaged. In figure 5.2a, the transient lines display standard deviations in mode energy of 2-4 cm^{-1} – an order of magnitude larger than the corresponding nanocavity SERS.

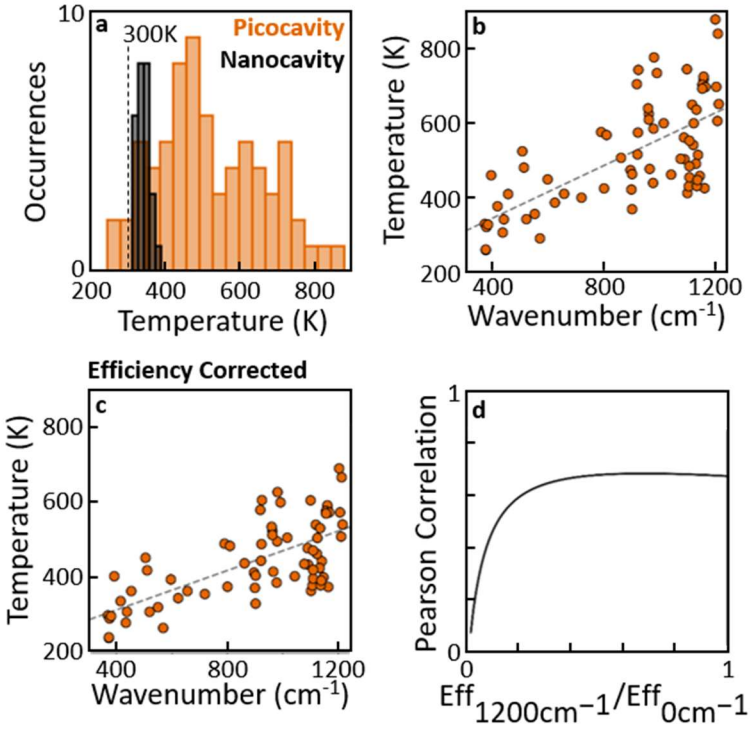

Figure 5.4 | BPT Effective Temperatures. a, Effective temperatures of BPT vibrational modes using ratios of Stokes and anti-Stokes SERS scattering. Nanocavity temperatures extracted from persistent SERS lines averaged over 30s time periods. Picocavity temperatures extracted from transient SERS lines averaged over their lifetimes. **b,** The positive correlation between transient mode wavenumber and extracted effective temperature. **c,** Transient effective temperatures are supressed if the SERS intensity ratios are corrected for experimental collection efficiency. This graph assumes that the collection efficiency drops linearly in wavelength space 27% between 0 and 1200 cm^{-1}. **d,** This efficiency drop against the Pearson correlation between mode wavenumber and corrected effective temperature.

Due to the small effective volume of a plasmonic picocavity, the coupling between it and the vibrational modes of the molecule is large enough to induce optomechnical pumping of the vibration modes above their thermal phonon occupancy (section 2.8). As discussed in section 2.6.2, the ratio of anti-Stokes to Stokes scattering provides an effective temperature (phonon

population) T for the corresponding vibrational mode. In order to simultaneously measure anti-Stokes and Stokes SERS with a finite spectral measurement range, the highest wavenumber collected is chosen to be ~1600 cm^{-1}. This encompasses the Stokes peaks of all BPT vibrational modes bar some very high energy (~3000 cm^{-1}) stretching modes of the C-H bonds. By averaging spectra during a picocavity event, the transient anti-Stokes lines can become visible above noise (Fig. 5.2b). Anti-Stokes lines from the nanocavity spectra can also become resolvable if spectra are averaged over periods of 30 s.

As expected for a system in thermal equilibrium, nanocavity SERS from a set of NPoM constructs provide a narrow distribution for T averaged at 341 K (Fig. 5.4a). In contrast, transient modes display temperatures over a large range up to 800 K. In this case, this is an effective temperature characterising the optomechnical pumping of each vibrational mode. A correlation (Pearson Correlation = 0.7) is noted between vibrational energy and effective temperature (Fig. 5.4b). This suggests that the higher energy vibrational modes overlap better in energy with the plasmonic cavity leading to greater coupling and more effective vibrational pumping. It is important to note that the effective temperatures observed here (<800 K) are lower than those observed at cryogenic temperatures (>1000 K). This is expected, with the greater ambient temperature providing a greater rate of thermal depopulation of excited vibrational states through non-linear phonon-phonon scattering.

It should be noted that these effective temperatures utilise the SERS intensity ratios as experimentally measured. However, due to a spectral dependence to both the out-coupling efficiency of light from an NPoM gap and the efficiency with which light is experimentally detected, this differs from the actual ratio of scattered light generated by the molecule. The collection efficiency in this experimental system is known to decrease with increasing wavelength. This supresses the effective intensity of Stoke modes relative to their anti-Stoke counterparts and increases calculated effective temperatures. As this is a more pronounced effect for higher wavenumber modes, it is important to check that it is not the source of the observed correlation between wavenumber and effective temperature. Unfortunately, a spectral collection efficiency curve was not collected for this experimental set up at the time of these measurements. However, this was collected for another experimental set up (set up D, section 3.5) that can be used for a rough estimate. This shows an approximately linear drop of 27% in collection efficiency between 633 nm (0 cm^{-1}) and 685 nm (1200 cm^{-1}). Taking this

linear efficiency curve with wavelength, the effective temperatures can be corrected (Fig. 5.4c). This lowers the effective temperature of the highest wavenumber modes to ~600 K which is still pumped above room temperature. The strong 0.7 Pearson correlation between wavenumber and effective temperature persists. The 27% drop in collection efficiency can be varied to investigate the effect on the observed correlation. As shown in figure 5.4d, a high ≥80% drop in efficiency is needed to supress this correlation. Therefore, we can be confident that the observed optomechnical pumping and the correlation with vibrational energy is not a collection efficiency artefact.

In summary, the transient lines observed here satisfy the two characteristic features of BPT picocavities set out in Benz et. al.[33]. These observations support the conclusion that the transient SERS is the result of picocavities at room temperature.

5.4 Room-Temperature NC-BPT Picocavities

Picocavity events are also seen in SERS measurements of NC-BPT NPoMs. This data is collected using 300 μW of 633 nm light using experimental set up B (section 3.5). Figure 5.5 demonstrates such events lasting much longer than was seen for BPT events above. As will be shown, this longer picocavity lifetime is characteristic of the NC-BPT system. Therefore, the integration time per spectrum is increased compared to BPT measurements to 100 ms. According to Density Function Theory calculations[†] (DFT, section 3.8), the SERS from NC-BPT and BPT should very similar as a reflection of their similar chemical structures. This is verified experimentally (Fig. 5.5a). The exception to this is an additional high energy C≡N stretching vibration at ~2250 cm^{-1} displayed by NC-BPT. To include this SERS mode in our spectral measurement window, anti-Stokes wavenumbers are not included in the NC-BPT spectra. As this high energy mode is well separated energetically from other vibrational modes in the molecule (Fig. 5.5d), any modifications to the energy of this vibrational mode during a picocavity event should be easily discernible.

[†]This DFT was carried out by Tamas Földes of University College London

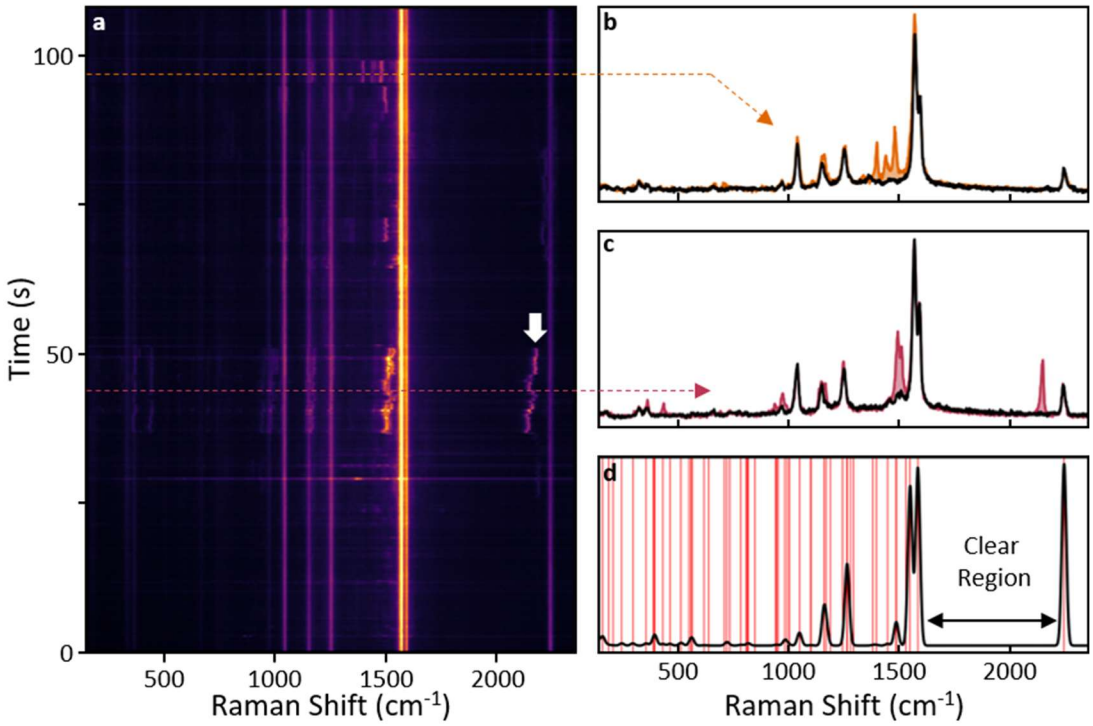

Figure 5.5 | NC-BPT SERS Scattering. a, Example series of NC-BPT NPoM SERS spectra (300 µW 633 nm incident irradiation, 100 ms integration time) displaying transient SERS lines at room temperature. Arrow indicates picocavity line near the C≡N vibrational mode. **b,** Average SERS emission during an event with no transient line near 2000 cm^{-1}. **c,** Average SERS emission during an event with transient line near 2000 cm^{-1}. Nanocavity spectrum shown in black. **d,** DFT calculated spectrum of NC-BPT. Peak heights indicate relative Raman activity. Red lines indicate all vibration mode energies. DFT vibrational energies empirically scaled to match experimental positions (x0.975 for <1700 cm^{-1} and x0.957 for >1700 cm^{-1}).

During some picocavity events, the CN vibration is unaffected and the spectral response is very similar to picocavities observed in BPT (Fig. 5.5b). In others, a transient SERS line is observed below the C≡N stretching vibration (Fig. 5.5a white arrow, 5.5c). As there are no dark vibrational modes in this spectral region to be made visible by the picocavity (Fig. 5.5d), this cannot just be the result of altered scattering cross sections due to Gradient Raman (section 2.6.3). It should also be noted that picocavity events containing this transient mode can qualitatively also exhibit increased spectral dynamics (Fig. 5.5a). When discussing BPT (section 5.3), this was quantified in terms of a standard deviation in the randomly fluctuating mode energy. Here, the change in energy is noted to be continuous and smooth over a

seconds timescale (similar to the high energy transient modes observed with DBCO in Chapter 4).

If the picocavity surface feature interacts with the nitrile functional group, this could alter the vibrational energy of the C≡N stretching mode to generate the observed transient peak. If this interaction were especially sensitive to the relative molecule-adatom position, this would convert any thermal sub-angstrom fluctuations in this position to changes in molecular vibrational energies. Any directed relative adatom-molecule motion would lead to continuous shifts in the modified vibrational energies. To preliminarily probe this hypothesis, a single NC-BPT molecule is modelled between two slabs of gold atoms using the program SIESTA[116†]. No significant partial bond formation is noted between the nitrile functional group and any atoms of the gold slab. Note that the nitrile −C≡N group should not be confused with the isocyanide −N≡C group, which does bind to gold surfaces[117,118]. An adatom is placed on the surface of the gold nearest the nitrile group (Fig. 5.6a). The system is initialised at a temperature of 100 K and simulated forward in time using a microcanonical ensemble (NVE) molecular dynamics simulation, allowing a stochastically exploration of its energy landscape. Over the course of the simulation, the distance from the adatom to the nitrogen atom (d_{NAu}) decreases until a partial bond is formed (Fig 5.6b,c). This results in a 0.63 eV ≈ 25 k_BT reduction in energy, indicating that an interaction between the low coordination number picocavity feature and nitrile group is very energetically favourable. This is consistent with previous reports that nitrile groups can bond with low coordination number gold (like a gold tip)[119]. While this computational simulation cannot provide perturbed vibrational mode energies for the system, a detailed investigation into this interaction using Density Functional Theory is carried out in Chapter 6. Here, the presence of this modified C≡N mode in a picocavity spectrum is taken as a marker for adatom formation from the AuNP facet.

†This calculation was carried out by Istvan Szabo of Kings College London.

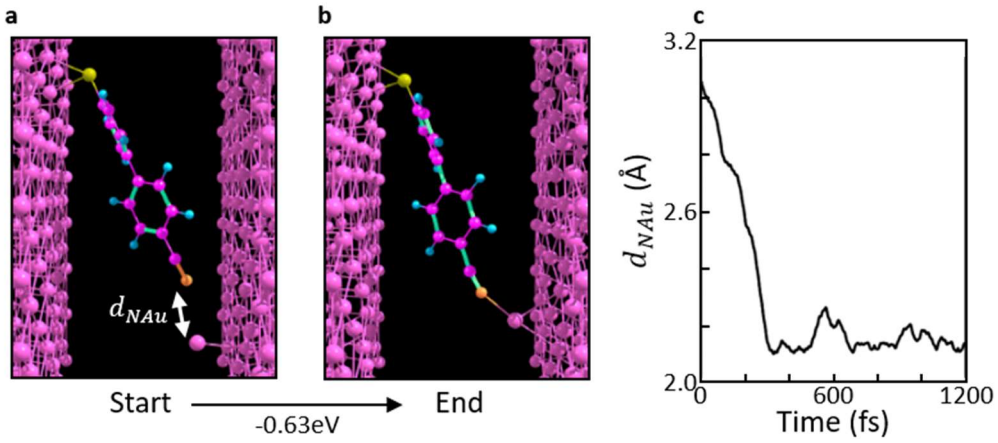

Figure 5.6 | Au-NC Interaction. a, Start and **b,** end frames from a SIESTA energy minimisation calculation with a single NC-BPT molecule placed between two slabs of gold with a nearby adatom. **c**, The nitrogen-gold distance over the course of the simulation.

5.5 Automated Picocavity Detection for Large Datasets

5.5.1 Picocavity Detection Metric Generation

Using automated data collection (section 3.6), SERS spectra are collected from 1415 BPT and 1183 NC-BPT NPoMs with 1000 consecutive spectra taken per NPoM. This results in over 2 million total SERS spectra collected over a range of incident laser powers. These will used here to compare and contrast the formation rates and lifetimes of picocavities in each system. Due to the large dataset, a method must be defined to automate picocavity detection. I will describe here a method for this with a focus on minimising computational complexity to maximise analysis throughput.

As total SERS emission increases digitally during a picocavity event, a simple SERS intensity threshold can be used to detect and define picocavities. However, this is complicated by other sudden intensity increases due to broadband processes (section 2.7). Therefore, the effects of narrow and broadband spectral features must first be separated. This is accomplished using a Continuous Wavelet Transform (CWT) $W(\mu, \sigma)$. The Ricker wavelet is given by

$$\varphi(x;\mu,\sigma) \propto \frac{1}{\sigma}\left(1-\left(\frac{x-\mu}{\sigma}\right)^2\right)e^{-\frac{(x-\mu)^2}{2\sigma^2}}. \quad (5.1)$$

which is proportional to the second derivate of a Gaussian function. This means that the overlap integral with the arbitrary function $f(x)$

$$W(\mu,\sigma) = \int_{-\infty}^{\infty} f(t)\ \varphi(t;\mu,\sigma)\ dt \tag{5.2}$$

is large whenever f locally approximates a peak-like structure of scale σ at $x = \mu$. By applying this overlap integral to a SERS spectrum with the correct characteristic width, a response is provided only by the peaks (with large positive values at the peak positions and negative values either side). Here, this width is set 20 cm^{-1} (Fig. 5.7a,b). Applying this integral over a finite spectral region generates large features at the spectrum edges due to zero-padding, so a linear background is first removed from each spectrum such that the spectrum edges are set to zero.

Over the timeframe of a series of SERS spectra, it is possible for the scattered intensity to slowly change due mostly to physical drift in the experimental system. For simplicity, we will consider these changes to have no spectral dependence. To account for this, the intensities at known nanocavity peak positions are extracted over time relative to their median values. These are averaged into a single estimate for spectrum intensity drift (Fig. 5.7c). To remove noise from this estimate, it is replaced with a polynomial approximation. The order of this polynomial is automatically determined using the Bayesian Information Criterion (BIC), a statistical metric for how well a set of data is described by a given model (section 3.9). We consider samples $\{x_i, y_i\}$ to be modelled with a polynomial $P(x_i)$ of order N. We assume that the sample noise is normally distributed with standard deviation σ. The BIC is given by

$$\mathrm{BIC} = (N+2)\ln\left(\sum_i 1\right) + \sum_i \left(\ln(2\pi\sigma^2) + \frac{(P(x_i)-y_i)^2}{\sigma^2}\right) \tag{5.3}$$

which is minimised at the polynomial order that best describes the samples without overfitting. This drift estimate (Fig. 5.7c, red) is used to normalise the SERS response over time (Fig. 5.7d). Once the median spectrum is removed, what is left is mostly noise with additional features during picocavity events (Fig. 5.7e). This is converted into a picocavity detection metric by taking the root-mean-square (RMS) at each point in time (Fig. 5.7f).

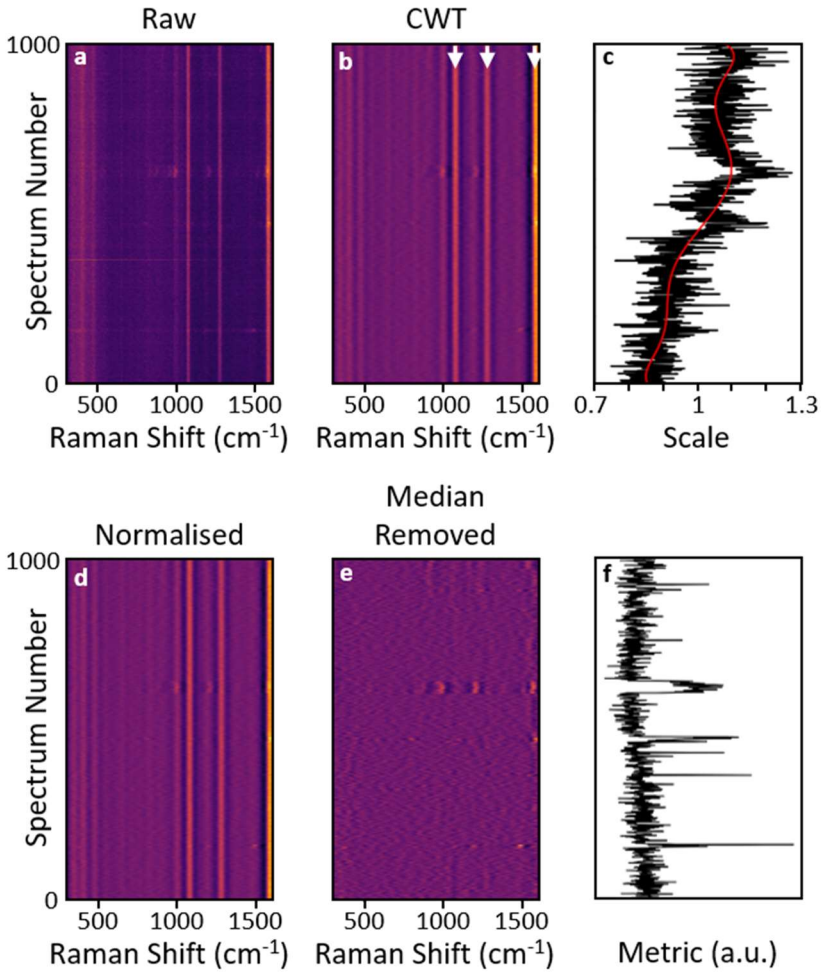

Figure 5.7 Generating the Picocavity Detection Metric. a, Example series of BPT NPoM SERS spectra is transformed using **b,** a Continuous Wavelet Transform with a Ricker wavelet of width 20 cm^{-1}. The response at known nanocavity SERS line positions (white arrows) is used to **c,** track the average drift in scattering intensity over time. This is smoothed using a polynomial approximation (red). **d,** The spectra are normalised by this drift estimation and **e,** the median spectrum is removed. **f,** The root-mean-square at each point in time forms the final picocavity detection metric.

The picocavity detection metric (Fig. 5.7f) is formed from a time varying baseline with digital increases due to picocavities. This baseline will be approximated as a polynomial and removed. The metric noise, which we will assume here to be normally distributed, is a useful internal reference for the threshold that will define a picocavity.

5.5.2 Removing a Flat Detection Metric Baseline

Fitting a polynomial estimate for the metric baseline requires any metric points that could possibly represent a picocavity to be ignored. However, determining which points to ignore requires a comparison to an estimate of the baseline. This chicken-and-egg style problem can be solved by defining an initial crude baseline that can be iteratively improved. The simplest baseline estimate is a flat line (polynomial order 0). Here, I will describe the removal of such a flat baseline estimate.

The discrete elements of the metric are denoted as M_i for index i, and the elements of the absolute derivate are $D_{i>0} \equiv |M_i - M_{i-1}|$. In this flat baseline approximation, D_i are samples drawn from a half normal distribution (due to noise) with large outliers due to the picocavities. A crude underestimate for the baseline would be one noise standard deviation above the minimum sample measured (Fig. 5.8 red), removed with transformation $M_i \rightarrow M_i - \min(\{M_i\}) - \text{median}(\{D_i\})/\sqrt{2}\,\text{erf}^{-1}(1/2)$ where erf^{-1} is the inverse error function. The true metric baseline is now slightly above zero with some metric points now guaranteed to be both positive and negative. The baseline noise level σ is approximated as the root-mean square (RMS) of all negative values of M_i as these can't be influenced by the positive picocavity outliers. We consider that values of M_i above a multiple of σ may represent possible picocavity elements. This factor is set here to two.

To iteratively improve the centring of the metric baseline on zero, the median of all points below this picocavity threshold is repeatedly removed ($M_i \rightarrow M_i - \text{median}[M_i \leq 2\sigma]$) until convergence (Fig. 5.8, orange). This is then again repeated to convergence with σ now also re-estimated each iteration as the RMS of all negative values of M_i (Fig. 5.8, green).

After the transformation $M_i \rightarrow M_i \,/\, \sigma$, the metric should now have been transformed to have a baseline approximately centred on zero with a noise level of one.

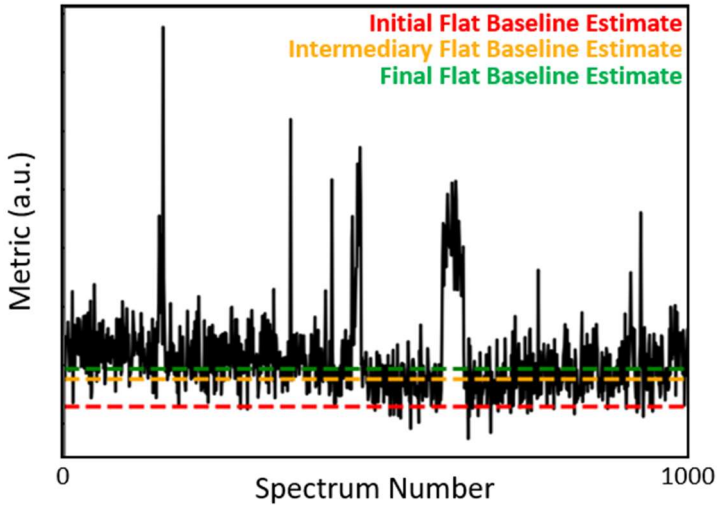

Figure 5.8 | Centring the Metric Baseline. The metric baseline is assumed flat with normally distributed noise. This baseline is initially estimated as one noise level above the minimum metric value (red). The noise level is estimated as the root-mean-square (RMS) of all metric point deviations below this baseline estimate. The baseline is repeatedly updated to the median of all points not exceeding the current baseline estimate by twice this noise level (orange). This is then repeatedly updated the same way while also re-estimating the noise level at each iteration (green).

5.5.3 Removing a Polynomial Detection Metric Baseline

In general, the metric baseline is represented by some polynomial $B_i = P(i;\theta)$ where θ are polynomial coefficients of undefined order N. There is also some unknown Gaussian noise level σ. Due to rough translation and normalisation applied to the metric in section 5.5.2, it can be initially approximated that B_i = 0 and σ = 1. This will be iteratively updated. When iterating and optimising a new polynomial estimate, we ignore any possible picocavity response by defining a threshold for possible picocavities $T_i = B_i + 2\sigma$ (which is initially 2 for all i) above which metric elements are discarded (Fig. 5.9a). The likelihood of a given estimate for the polynomial (and σ) is given by

$$L = \prod_{j\,(M_j \le T_j)} \frac{2}{\operatorname{erf}\left(\frac{T_j - P(j;\theta)}{\sqrt{2}\sigma}\right) + 1} \frac{e^{-\frac{1}{2}\frac{\left(M_j - P(j;\theta)\right)^2}{\sigma^2}}}{\sqrt{2\pi}\sigma} \tag{5.4}$$

which accounts for the removal of all samples above the threshold. For a given polynomial order, the optimum curve maximises L. The optimum polynomial order then minimises

$$\mathrm{BIC} = (N+2)\ln\left(\sum_{j\,(M_j \le T_j)} 1\right) - 2\ln L. \tag{5.5}$$

After new estimates for B_i and σ are defined, this is used to update the threshold $T_i = B_i + 2\sigma$. This process is iterated until convergence (Fig. 5.9b), at which point the metric is transformed $M_i \to \frac{M_i - B_i}{\sigma}$.

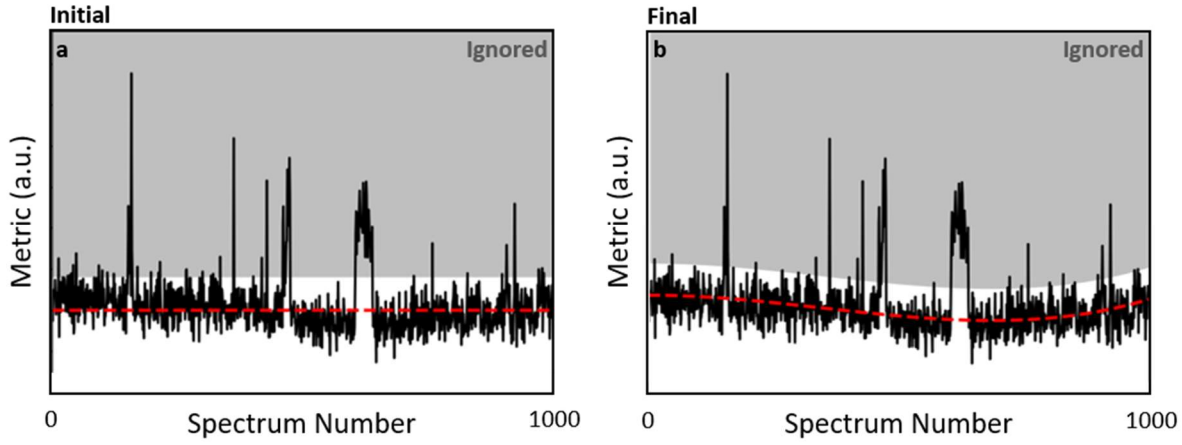

Figure 5.9 | Removing metric baseline. a, Initial metric baseline is assumed to be flat. All points exceeding this by twice the noise level are masked as possible picocavities (grey). **b,** The baseline is repeatedly re-estimated as a polynomial fit of all non-masked metric values.

At this point, the metric baseline should be well approximated as zero for all time. The metric noise level should have an average of one. The only remaining complication is the possibility that this noise level could be time varying. Again, this can be corrected by modelling the noise level with a polynomial $\sigma_i = P(i;\theta)$ of undefined order N. In this case, only negative values of M_i are considered when optimising the polynomial as these are free from the influence of picocavity events. We model these elements as drawn from a half normal distribution with varying standard deviation. The likelihood is given by

$$L = \prod_{j\,(M_j \leq 0)} \frac{2}{\sqrt{2\pi}P(j;\theta)} e^{-\frac{1}{2}\frac{{M_j}^2}{P(j;\theta)^2}} \tag{5.6}$$

with BIC

$$\mathrm{BIC} = (N+2)\ln\left(\sum_{j\,(M_j \leq 0)} 1\right) - 2\ln L. \tag{5.7}$$

Once the optimal polynomial is found, the metric is corrected using the transformation $M_i \rightarrow \frac{M_i}{\sigma_i}$.

Correcting the baseline and then noise level is iterated until convergence. This provides the final metric for the existence of a picocavity at a given point in time (Fig. 5.10).

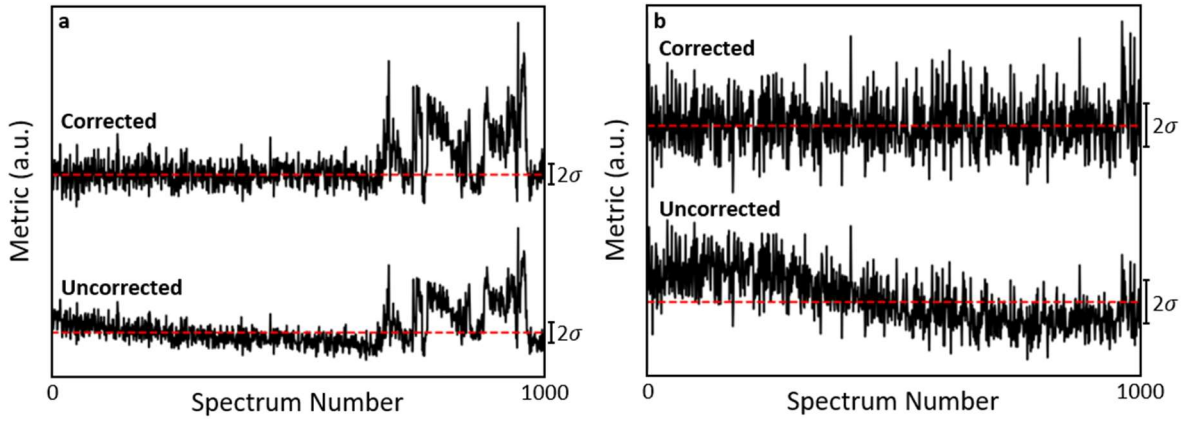

Figure 5.10 | Removing metric baseline. Example of BPT picocavity detection metrics before and after metric baseline removal and re-normalisation. Red line indicates relative zero.

5.6 Picocavity Lifetimes and Formation Rates

Picocavities are defined by the detection metric crossing an ad hoc threshold. Due to the processing in sections 5.5.2 - 5.5.3, this metric has a noise level of 1. The picocavity detection threshold must be set carefully to maximise detection sensitivity while minimising the influence of this metric noise. Even when this threshold is set optimally, events for which the

metric is close to the threshold can cross below it artificially for single spectra due to noise. To account for this here, any single spectrum crossing of the threshold (from below or above) is ignored in this analysis. This removes all single spectrum picocavity events from the dataset which must be taken into consideration when analysing and interpreting the data. It should be noted here that the computationally cheap picocavity detection metric described in this chapter is likely to display some degree of bias towards brighter picocavity events.

First, we will consider picocavities generated from BPT NPoMs using 447, 563 and 709 μW of laser power. We will investigate the picocavity detection threshold using the 709 μW dataset which displays the greatest signal-to-noise ratio. The picocavity formation rate is defined using the time between the starts of consecutive events. In figures 5.11 – 5.12, the distributions of picocavity lifetimes and formation times are shown with varying metric detection thresholds along with the same distributions generated by replacing the experimental metrics with normally distributed noise for comparison.

If the metric noise is normally distributed as assumed, a detection threshold of 1 is crossed by any given non-picocavity spectrum with 16% probability. The result of this low threshold value is a bi-exponential distribution of picocavity lifetimes with the fast component dominated by these noise-generated false picocavity detections (Fig. 5.11a, red). As the detection threshold is raised, the influence of noise rapidly falls and the picocavity lifetime distribution tends to a single exponential (Fig. 5.11). However, the smallest measureable lifetime (two integration times) remains over represented. This could suggest that the picocavity lifetimes are in fact bi-exponential but that this is poorly resolved here. In these experiments, picocavities are sometimes observed to disappear (below the resolvable detection limit) for short periods before the same transient lines reappear (Fig 5.2a). This would indeed be detected as multiple shorter lived picocavities closely spaced in time. This over representation could also be (in part or in full) a remaining analysis artefact resulting, for example, from the approximation of the metric noise as normally distributed. In Chapter 7, a BPT NPoM picocavity SERS dataset measured using two simultaneous scattering wavelengths undergoes a much more computationally expensive analysis that explicitly extracts the intensities of possible picocavity SERS peaks and compares them to the local spectral noise level. That analysis, which should be more sensitive to weaker picocavity events, shows a less ambiguous bi-exponential lifetime distribution.

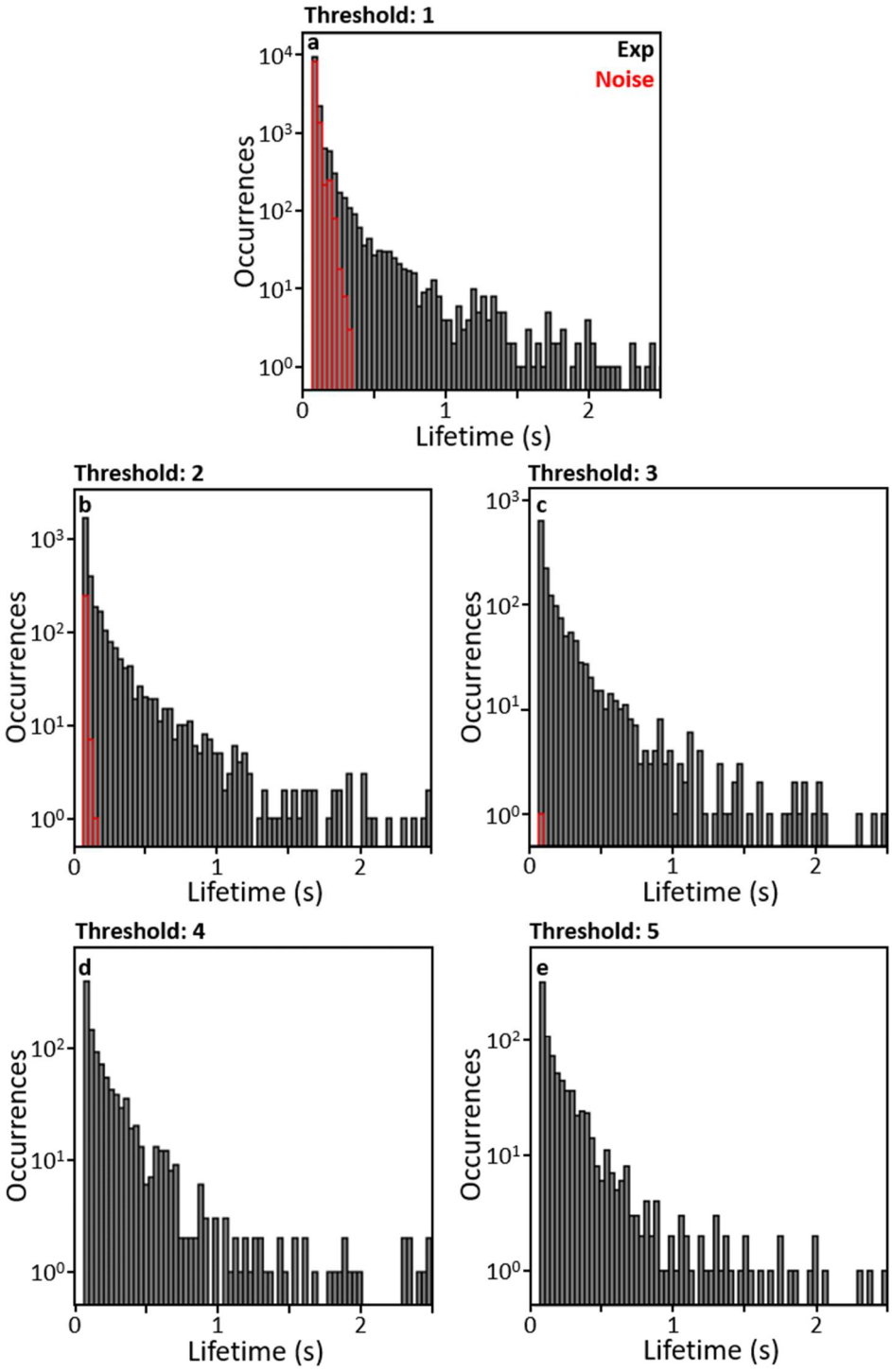

Figure 5.11 | Lifetime with Metric Threshold. For BPT NPoMs under 709 μW of 633 nm irradiation, detected distribution of picocavity lifetimes with metric detection threshold set at **a,** 1 **b,** 2 **c,** 3 **d,** 4 and **e,** 5. The distributions formed by replacing the metrics with normally distributed noise are also shown (red).

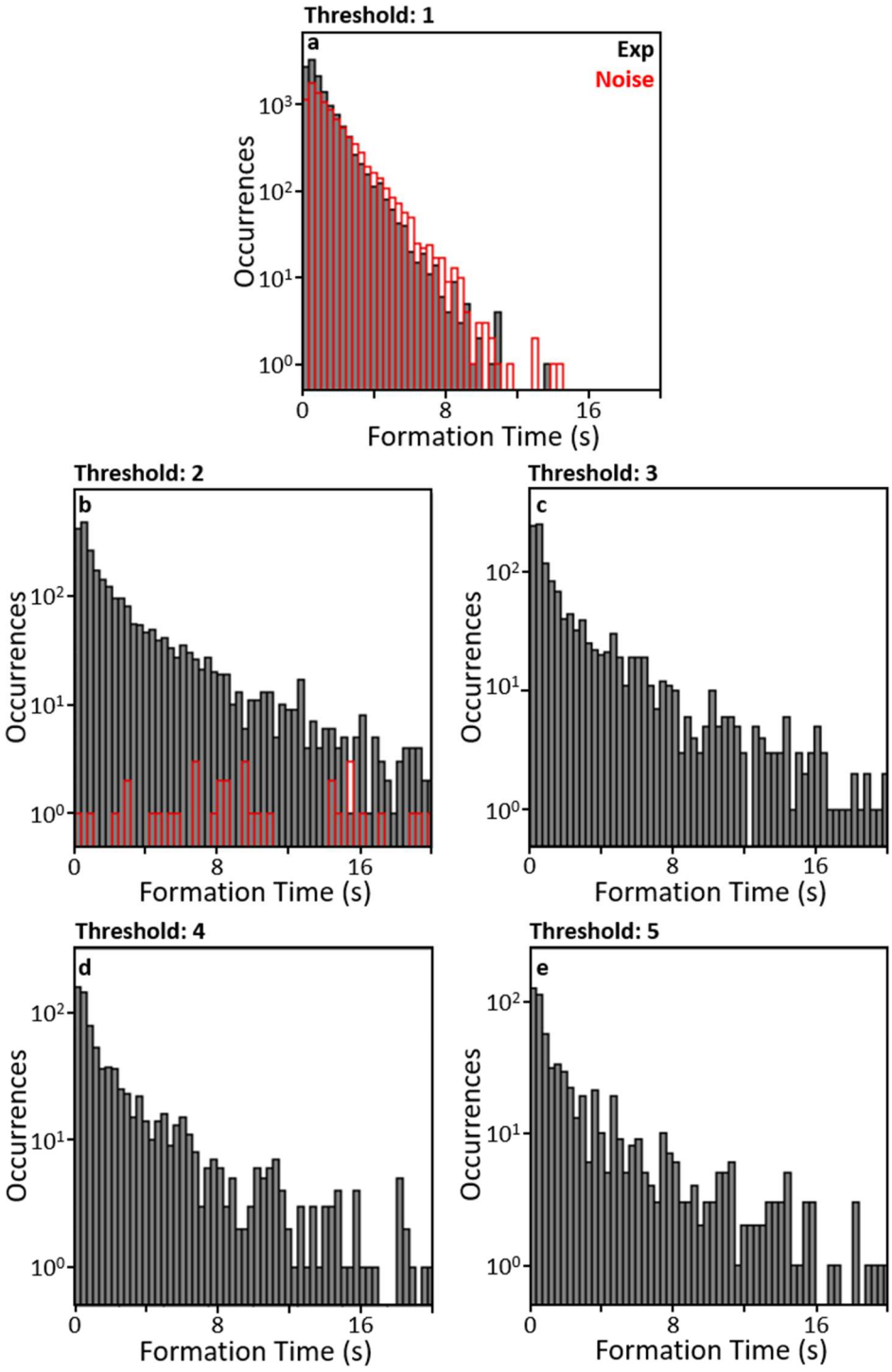

Figure 5.12 | Formation Time with Metric Threshold. For BPT NPoMs under 709 µW of 633 nm irradiation, detected distribution of times between picocavity formations with metric detection threshold set at **a,** 1 **b,** 2 **c,** 3 **d,** 4 and **e,** 5. The distributions formed by replacing the metrics with normally distributed noise are also shown (red).

If picocavities are formed mutually independently, the formational times should follow an exponential distribution. In figure 5.12, when the detection threshold is low this distribution is dominated by noise. As the threshold is raised, the distribution tends instead to a bi-exponential distribution indicating that some consecutive detected picocavities are not independent. This is likely generated from the same source as the inflated number of short lived picocavities.

Based on these distributions, a detection threshold of 4 is used here. To extract the characteristic picocavity lifetime, the lifetime distribution is modelled using an exponential probability density function (PDF) with only events lasting more than two spectra considered. The PDF is truncated to account for the artificial lack of very short lived events in the dataset. The formation times are modelled using a bi-exponential PDF similarly truncated to account for the impossibility of measuring an inter-picocavity time of less than four spectra. The longer characteristic time from the PDF is presented as the formation rate of the system.

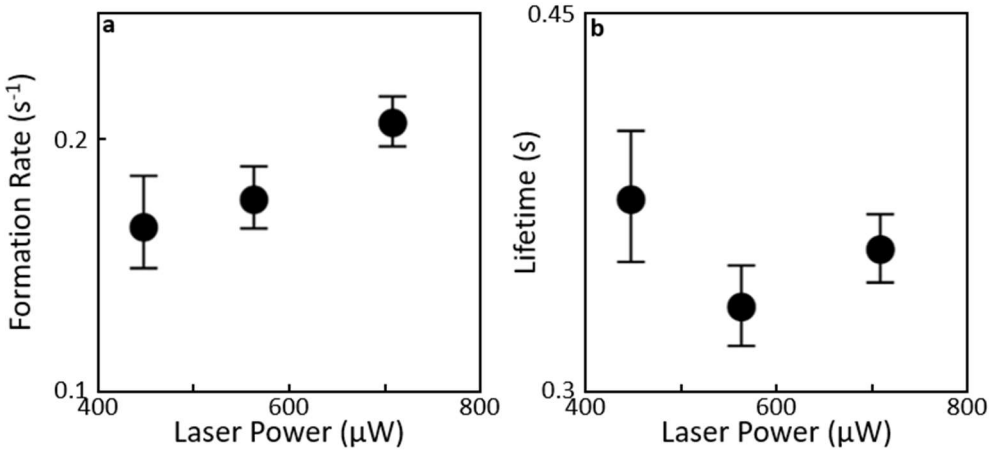

Figure 5.13 | BPT Picocavities with Laser Power. a, Characteristic formation rate and **b,** lifetime of BPT picocavities detected with varying input 633 nm laser power.

Comparing the three incident laser powers, an increase in formation rate can be seen with increasing power (Fig. 5.13a). While this aligns with a role of light in picocavity generation (either through some direct mechanism or through NPoM heating), one must be cautious when drawing conclusions based on three data points. The characteristic picocavity lifetime

shows no significant laser power dependence greater than the uncertainty on each measurement (Fig. 5.13b). This perhaps indicates that thermal energy dominates the destruction of picocavities in the BPT NPoM system at room temperature.

These values can now be compared to their counterparts from the NC-BPT system. For this data, the lifetime and formation rate distributions follow the same forms (Fig. 5.14), showing that the increase in integration time for this dataset was a reasonable change in parameter.

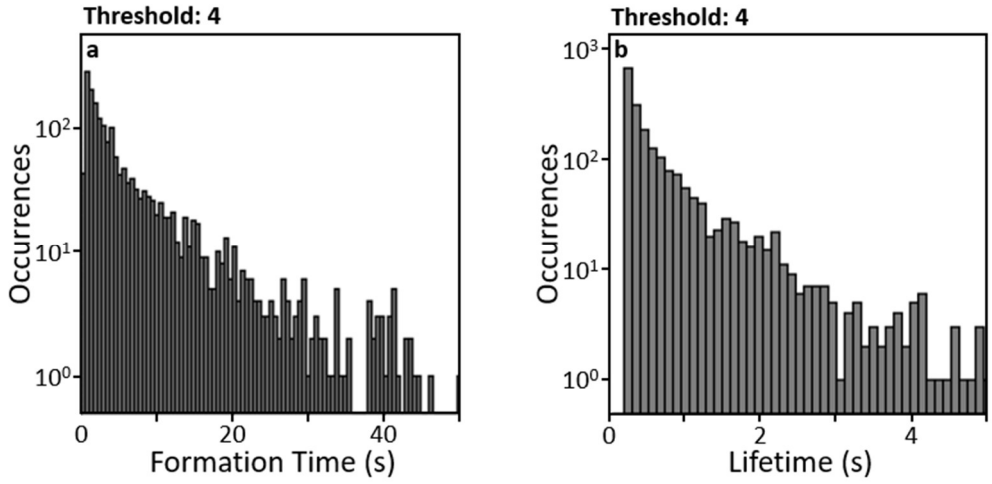

Figure 5.14 | NC-BPT Formation Times and Lifetime. Distributions of **a,** formation time and **b,** lifetime for NC-BPT picocavities generated under 705 μW of 633 nm laser irradiation.

Again, an increase in formation rate is seen with increasing laser power while the characteristic lifetime does not show a significant decrease (Fig. 5.15). This time, this is observed over 5 input laser powers. The formation rate observed is ~ 2x smaller than for BPT at equivalent powers while the lifetime is ~3x larger. This significant increase in picocavity lifetime could be due in part to a change in the properties of the SAM such as packing density. It could also be influenced by any molecule-adatom interactions (section 5.4) when picocavities form from the AuNP facet.

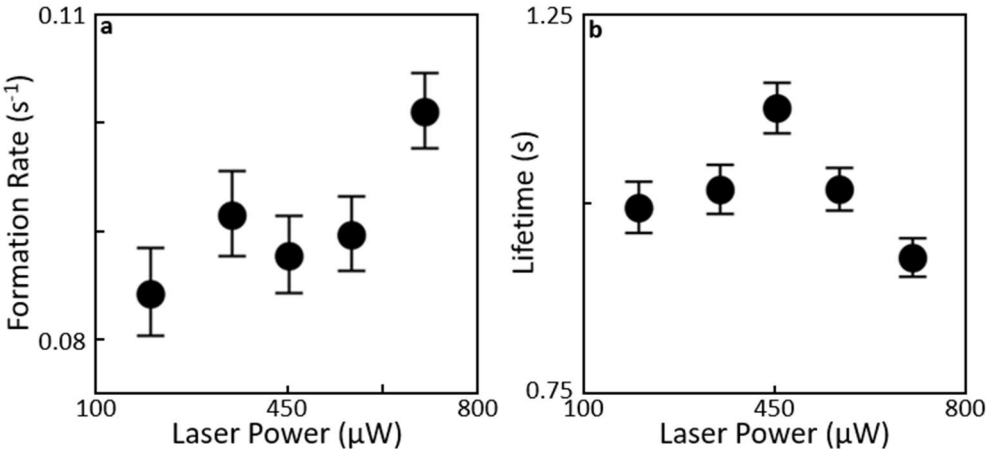

Figure 5.15 | NC-BPT Picocavities with Laser power. a, Characteristic formation rate and **b,** lifetime of NC-BPT picocavities detected with varying input 633 nm laser power.

5.7 Gap Asymmetry

At each laser power, the detected NC-BPT picocavity events are separated depending on the existence of a modified CN vibrational mode (Fig 5.16a,b). This is achieved by re-calculating the picocavity metric only on the relevant CN spectral range 1750 – 2430 cm^{-1} and cross-referencing if a given picocavity event also registers as an event in this range. As shown in figure 15.6c, this is only true for 10-15% of detected events at any given laser power. If all picocavities forming on the AuNP facet lead to this modified SERS line, which seems likely given the apparent energetic favourability of the adatom-molecule interaction, then this reveals a large asymmetry in picocavity generation between the two bulk gold surfaces. This is strong evidence that picocavity formation is modified by the local chemical environment of the gold surface, although further work should be undertaken to remove any impact from differences in gold structure between the AuNP facet and template-stripped gold mirror surface (such as attempting to repeat the SERS analysis with nanoparticle dimers rather than the NPoM structure). This asymmetry is somewhat intuitive in this case as the NC-BPT molecule binds strongly to the mirror surface via the thiol functional group while the nitrile functional group does not meaningfully interact with the bulk AuNP gold. This would be expected to lower the effective energy barrier for picocavity formation from the mirror.

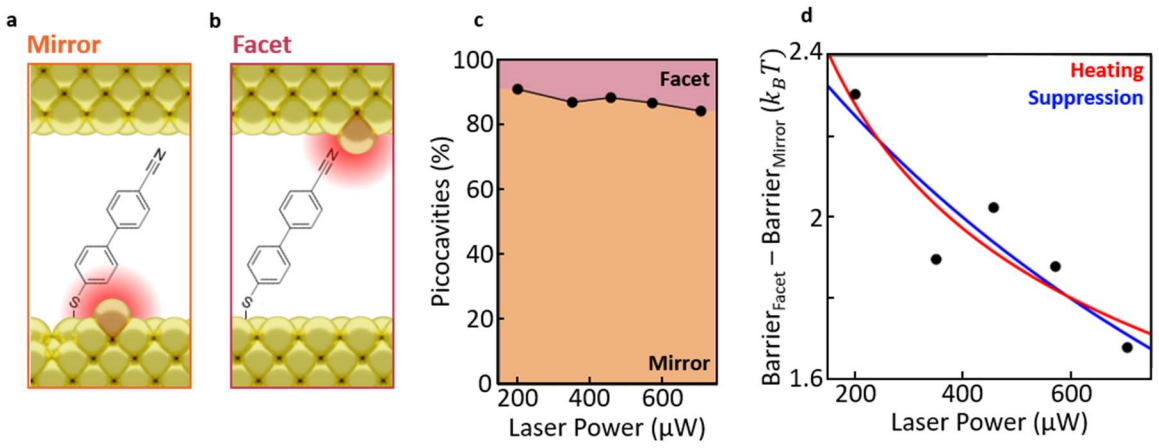

Figure 5.16 | NC-BPT Picocavity Asymmetry. Schematics of picocavities forming from the **a,** mirror and **b,** AuNP facet. **c,** The relative probabilities of formation from the mirror or facet with varying laser power. **d,** These probabilities converted to the picocavity generation barrier difference between the two surfaces, normalised to k_BT. This can be modelled either as due to heating (red) or due to an optical suppression of the energy barriers (blue).

The fraction of picocavity events measured from the AuNP facet increases with laser power (Fig. 5.16c). If we model the formation of picocavities with a thermal barrier, this fraction F can be written as

$$F = \frac{1}{1 + e^{\frac{\Delta B}{k_B T}}} \tag{5.8}$$

$$\frac{\Delta B}{k_B T} = \ln\left(\frac{1 - F}{F}\right) \tag{5.9}$$

where ΔB is the difference in energy barrier between picocavity formation from the AuNP facet and mirror, k_B is Boltzmanns constant and T is the NPoM temperature. This barrier difference (normalised to k_BT) drops with laser power (Fig. 5.16d). If the equilibrium NPoM temperature increases significantly over this power range, this would be expected simply due to increasing value of k_BT. In this case, assuming that the NPoM construct radiates away heat according to the Stefan-Boltzmann Law, the equilibrium NPoM temperature under laser irradiation I is

$$\frac{T}{T_0} = \sqrt[4]{c_1\, I + 1} \tag{5.10}$$

where c_1 is a constant and T_0 is the ambient temperature of the surroundings. This gives

$$\frac{\Delta B}{K_B T} = \frac{\Delta B / K_B T_0}{\sqrt[4]{c_1 I + 1}}. \tag{5.11}$$

This model is consistent with an idea that light drives the formation of picocavities solely through NPoM heating. Another hypothesis is that light is somehow directly involved in the picocavity formation mechanism, modelled here by a suppression of the formation energy barrier as the incident intensity is increased. For simplicity, when considering this model the system temperature is assumed to not increase significantly and is fixed as a constant. A simple linear suppression of the formation barrier has the form

$$\Delta B = \frac{\Delta B|_{I=0}}{1 + c_2 I} \tag{5.12}$$

where c_2 is a constant and the extra term in the denominator keeps the result finite as $I \rightarrow 0$. This gives instead

$$\frac{\Delta B}{K_B T} = \frac{(\Delta B / K_B T)_{|I=0}}{c_2 I + 1}. \tag{5.13}$$

Both of these optimised models are shown in figure 5.16d and both describe the trend of the data well with ΔB = 3.4 $K_B T_0$ and $\Delta B_{I=0}$ = 2.6 $K_B T$ for the heating and suppression models respectively. Therefore, these models cannot be separated using this data. Future work characterising a range of molecules generating picocavity SERS with asymmetric signatures, and collecting the required anti-Stokes SERS scattering to independently measure system temperature, could continue this form of analysis further. The suppression model of picocavity generation is investigated in greater depth in Chapter 7 where simultaneous SERS is measured from BPT NPoMs at two scattering wavelengths. This provides information on the spatial distribution of picocavities within the NPoM gap and supports a greater picocavity generation rate (lower generation energy barrier) where fields in the NPoM gap are largest.

It is important to note that the 10% prevalence of facet picocavities means that the picocavity– nitrile interaction cannot in fact be the driving force between the longer observed picocavity lifetime in NC-BPT compared to BPT. Removing this minority of events, the characteristic picocavity lifetime remains ~ 1 s. This points to more subtle differences, such as SAM packing and structure, causing this observed difference. This points back to the

differences in dark field scattering spectra observed between BPT and NC-BPT NPoMs (section 5.2).

5.8 Conclusion

In this chapter, I have showed observations of room temperature picocavities in NPoMs with SAM spacers of BPT and NC-BPT. I have preliminarily shown that a picocavity adatom in proximity to the nitrile group of the NC-BPT will energetically favourably interact with it, providing a spectral signature for picocavities forming on the AuNP facet. This interaction is characterised further using Density Function Theory in Chapter 6. Leveraging the asymmetry of this molecule and this spectral signature, I showed that only ∼10% of picocavities in this system form on the AuNP facet rather than the gold mirror. This points to the importance of the local chemical environment in picocavity formation. It is important to consider possible differences between the template stripped and AuNP gold surfaces. While these should intuitively be the same on the local scale of the picocavity, this could be tested by repeating this work while replacing the NPoM with an AuNP dimer. The experimental procedure of forming dimers with a uniform NC-BPT monolayer between them and then accessing the correct optical axis of the resulting structure could be difficult, which is why these experiments are so well suited to NPoM. Repeating these measurements using molecules where a nitrile group is opposite a different functional head group that can bind to gold (rather than the thiol) could lead to changes in the energy barrier difference between the two gold surfaces correlated to the binding affinity of the head group to gold.

I have presented a computationally lightweight picocavity detection method that expands the concept of a simple SERS intensity threshold to be robust against changes in the SERS background and drifts in experimental SERS intensity over time. This was applied to a dataset of over two million BPT and NC-BPT SERS spectra and showed that the lifetime of NC-BPT picocavities is significantly increased ∼x3 in comparison to BPT. As only 10% of the NC-BPT picocavities involve the picocavity-nitrile interaction, this cannot be the dominant effect stabilising picocavities here. Instead, this small change in the SAM molecule must be leading to more subtle changes in SAM packing density and structure. This may be related to the extra

plasmonic mode seen in the dark field scattering of NC-BPT NPoMs. I would be interested in seeing SAM behaviour in the NPoM gap modelled computationally with molecular dynamics. These simulations are used to model the formation of SAMs on a metal surface[55], and could be further increased in complexity to study SAMs between two gold surfaces applying the high pressure of an NPoM cavity.

It is interesting to contrast the picocavity detection method in this chapter to the more complex analysis that will be described in Chapter 7. This method is computationally cheap but compresses all the spectral data to a single metric value and provides no information on the picocavity peaks that it detects (i.e. How many are there? How intense are they? etc.). While the later analysis separates SERS spectra into nanocavity, background and transient components and explicitly extracts the possible picocavity peaks, it is much more computationally expensive. As with all forms of computational analysis, one method is not necessarily better than the other and different needs require different aspects of the method to be prioritised (i.e. speed v. accuracy).

Chapter 6: Picocavity-Molecule Interactions Tracked Through Transient Mode Dynamics

6.1 Introduction

In Chapter 5, we observed transient picocavity SERS events from NPoM constructs formed with a Self-Assembled Monolayer (SAM) of molecule 4'-cyanobiphenyl-4-thiol (NC-BPT). Across a range of incident laser powers, 10-15% of these events contained a transient vibrational mode downshifted from the >2000 cm^{-1} high energy C≡N bond stretching vibration of the molecule's nitrile group (Fig 6.1a, white arrow). This is a region of vibrational energies where no additional dark vibrational modes of the molecule exist to be made visible by the picocavity (see sections 2.6.3 and 2.8 for additional context). Molecular dynamics SIESTA calculations suggested that an interaction between the nitrile group and a low coordinate number picocavity adatom on the gold nanoparticle (AuNP) surface, to which this group is adjacent, would be energetically favourable. It was proposed that this would perturb the CN vibrational mode energy of this single interacting molecule which would then be enhanced in SERS intensity by the optical effects of the picocavity to be comparable to all other molecules in the NPoM gap. As metal-molecule interactions underpin key mechanisms in molecular electronics[5], catalysis[120,121], electrochemistry[122] and the formation of green technologies[123], this is considered an interesting opportunity to explore and characterise such an interaction optically and in relatively ambient conditions.

In this chapter, I present an experimental dataset of NPoM SERS measurements containing this perturbed CN picocavity mode. From this, I characterise this transient mode based on distributions of energy downshifts (relative to the unperturbed CN vibrational energy) and the rate of dynamic spectral wandering. The system is also represented in Density Functional Theory (DFT, section 3.8) which predicts the vibrational modes of a system. To be computationally tractable to calculate, this model of the picocavity-molecule interaction ignores intermolecular interactions between NC-BPT molecules and the existence of the bulk gold surfaces. It instead models a single molecule and a number of gold atoms (Fig. 6.1b,c).

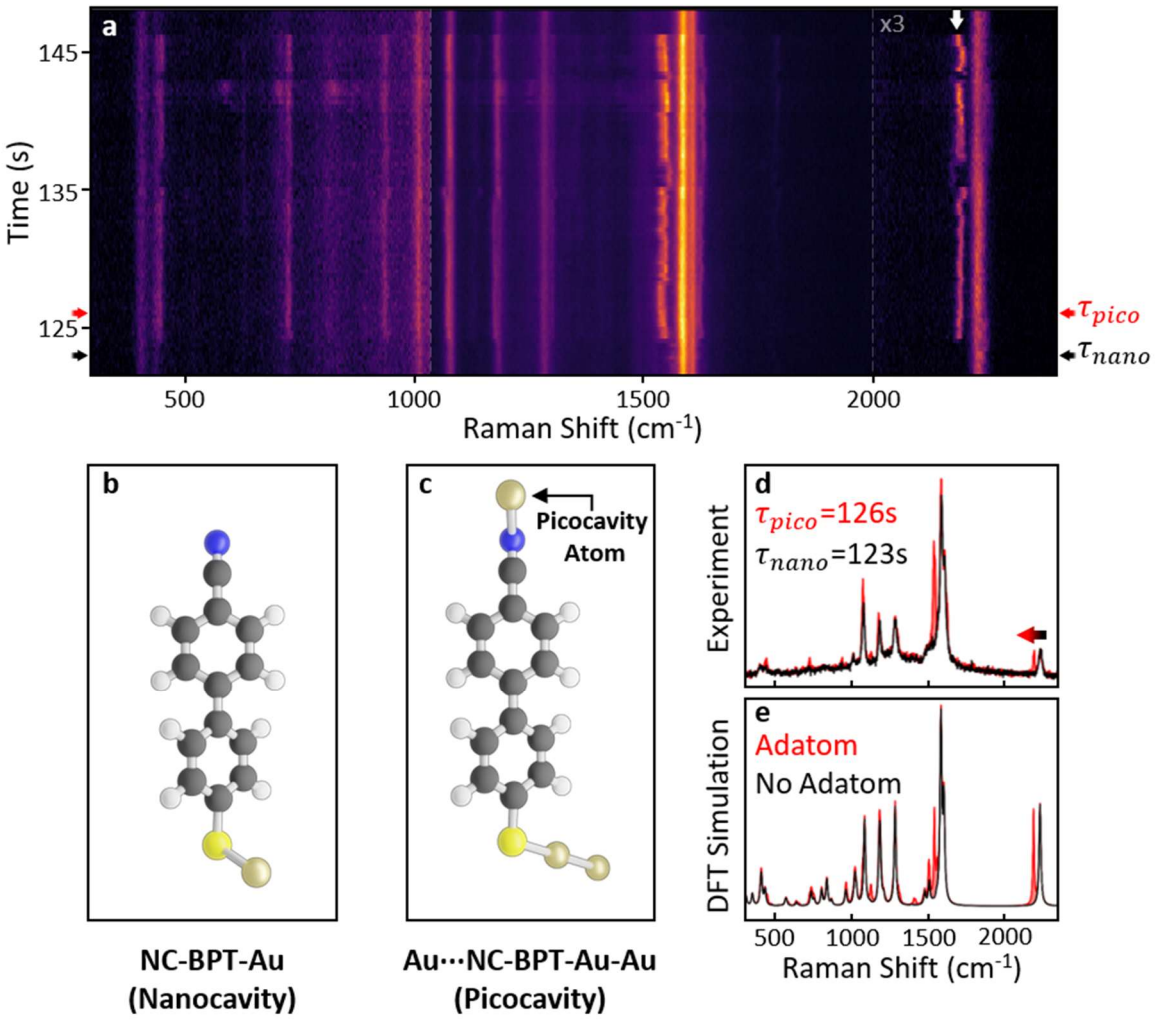

Figure 6.1 | Adatom Perturbed Transient SERS. a, Example consecutive NPoM SERS spectra using NC-BPT SAM spacer. A transient (picocavity) event displays a dynamic SERS mode (white arrow) near the CN stretch vibration. Intensity above dashed line multiplied x3. **b,** Density Functional Theory (DFT) model of NC-BPT molecule with thiol bound to gold. **c,** DFT model with a gold atom in proximity to the nitrile functional group. **d,** SERS spectra from before (τ_{nano}) and during (τ_{pico}) the picocavity event in **a**. **e**, DFT spectra with and without the gold atom. Scaling applied to match peak positions to experiment. Gold atom positioned to reproduce experimental transient peak positions. Peak ratios without adatom matched using field polarisation direction. Peak ratios with adatom are not provided by DFT during a picocavity and are ad-hoc here. The lower intensity C≡N mode in experiment is due to a reduced collection efficiency at these longer wavelengths.

Within this DFT model, the addition of a gold atom near the nitrile group does recreate the observed vibrational energy perturbations (Fig. 6.1d,e). It is important to note that while DFT provides both changes in vibrational energies and Raman activities due to the adatom

interaction, it cannot capture the effects of Gradient Raman due to the enhanced picocavity optical field (section 2.8). Therefore, the Raman peak intensity ratios provided by DFT are generally ignored throughout this chapter.

By repeating the DFT calculation while scanning the adatom position relative to the molecule (resulting in 1350 total calculations), the landscapes for system energy and vibrational perturbations are comprehensively mapped within the model. By correlating the spectral dynamics of multiple perturbed vibrational modes between an experimental measurement and theory, a 14 s picocavity event is inverted into a 133 point trajectory over time for the adatom position relative to the molecule in 3D space. Despite the available 3D domain for the adatom position, the obtained trajectory is predominantly confined to a plane and seems to map out a thermal transition of the adatom from one interstitial site of the AuNP facet to another.

The work presented in this chapter is under review at Nature Communications.

6.2 Experimental Observations of Perturbed Vibrational Dynamics

The NC-BPT NPoM system is measured using experimental set up C (section 3.5). Each NPoM is repeatedly irradiated with 100 ms bursts of 500 μW 633 nm laser light until the automatic detection of a perturbed CN picocavity mode. This short duration is selected to favour picocavity generation within a single burst without then destroying it (although the formation is still rare as discussed in Chapter 5) while collecting enough signal to detect the picocavity. Once a sudden increase in SERS within the spectrally clean zone is detected, 60 consecutive SERS spectra are collected using a lower 25 μW laser power with an increased 1 s integration time. This lower power is used in the hope of prolonging picocavity lifetimes. In total, 87 SERS time-scans are collected containing CN picocavities. Between events, the dynamics of the CN vibrational mode shows a range of behaviours. In figure 6.2, examples are shown of continuous and directed spectral drift as well as discrete switching between spectral positions.

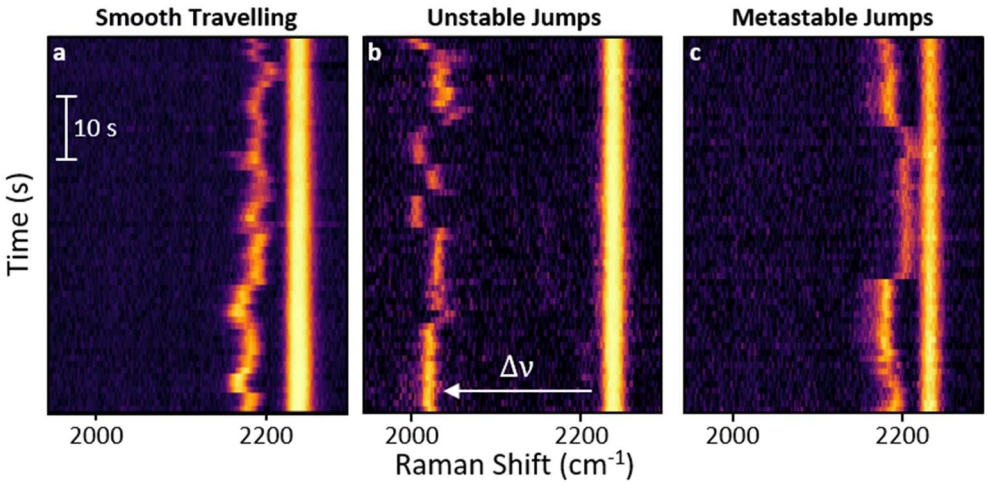

Figure 6.2 | Example Transient CN SERS dynamics. Consecutive SERS spectra during picocavity events with a transient perturbed CN vibrational line shifted from its unperturbed energy by $\Delta\nu$. Examples of dynamic behaviour for this line include **a,** continuous directed shifts on a seconds time scale **b,** repeated discrete jumps between vibrational energies and **c,** discrete jumps in vibrational energy that are stable on a 10 s timescale. Spectra taken using 25 µW of 633 nm laser power and 1 s integration times.

Extracting the downshift ($\Delta\nu$) of the CN vibration from the unperturbed frequency for all spectra over all events, the resulting distribution ranges over 400 cm^{-1} with a most frequent value of $\Delta\nu \sim 50$ cm^{-1} (Fig. 6.3a). This distribution convolves the probability of a picocavity event forming at a given downshift with the stability of that downshift value in time. The inter-spectrum change in CN mode energy (denoted 'wandering' $\partial\nu$) can also be used to form a histogram (Fig. 6.3b). This displays no characteristic dependence on downshift (not shown), and for smaller values of $\partial\nu$ follows an exponential distribution with an average wandering rate $\overline{\partial\nu} \sim (4.3\pm0.3)$ $cm^{-1}s^{-1}$ (Fig. 6.3b, dashed line). Note that if this wandering is thermally driven at a thermal sampling rate sufficiently faster than the experimental integration time, the underlying rate of thermal wandering may be supressed here by a temporal averaging over each integration time window. This is discussed further in section 6.6. The observed dynamics on a second timescale is slow compared to sub-ps molecular vibrational frequencies as well as the sub-µs acoustic frequencies of the NPoM structure itself[124]

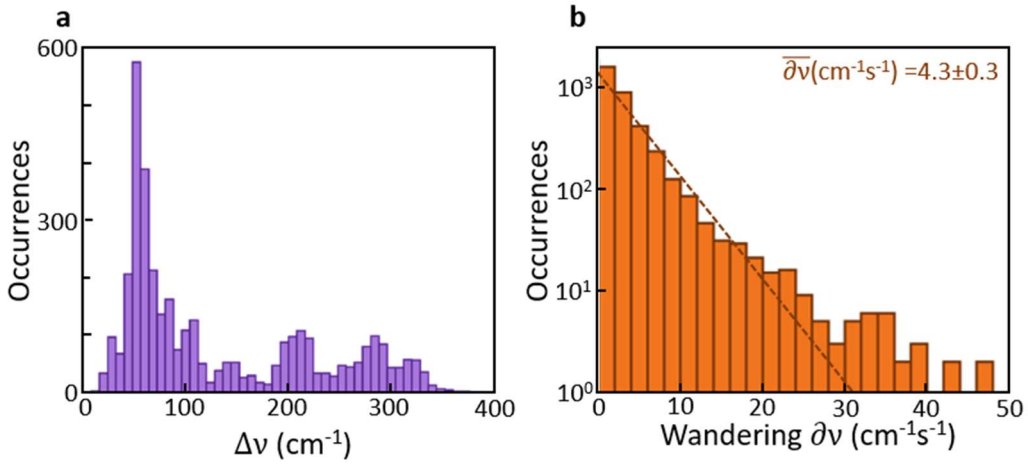

Figure 6.3 | Aggregated Transient SERS Position. b, Histogram of all experimentally observed transient CN downshifts $\Delta\nu$ from unperturbed vibrational energy. Aggregated from 87 NPoMs. Picocavity SERS taken using 25 μW laser power and 1 s integration times. **c**, Distribution of observed inter-spectrum changes in transient CN vibrational energy $\partial\nu$. Model $\propto \exp(-\partial\nu/4.3\ \mathrm{cm^{-1}s^{-1}})$ shown dashed.

6.3 Modelling the Perturbation with Density Functional Theory

6.3.1 Energetically Minimising Adatom Position

To contextualise the experimental measurements and explore the adatom-molecule interaction systematically, the system is represented using a DFT model. As the computational complexity of these models depends strongly on the size of the system being represented and the complexity of the interactions within it (the problem is complexity class NP[125]), the modelled system must be simplified here. This is done by ignoring the existence of the bulk gold surfaces and surrounding molecules in the SAM. The unperturbed (nanocavity) SERS spectrum is modelled as the response of a single NC-BPT molecule with the thiol functional group bound to single gold atom (NC-BPT-Au, Fig. 6.1b). For the perturbed (picocavity) system, a gold atom is placed in proximity to the nitrile functional group (Au···NC-BPT-Au-Au, Fig. 6.1c) to represent the picocavity. To keep an even number of electrons in the system, a second gold atom is attached to the bottom of the molecule in this case. The validity of these representations is discussed in section 6.3.2. Before vibrational mode energies can be

calculated, all atoms in the system must be arranged so that the system is in a structural energetic minimum. These can either be a global minimum or some internal system coordinates (such as the distance between a pair of atoms) can be constrained. We initially consider both nanocavity and picocavity systems in their globally energetically minimising conformations.

As discussed briefly in section 3.8, DFT contains a set of internal approximations that trade accuracy for computational complexity. The main hyper-parameters to be selected are the basis set, the hybrid exchange correlation functional and the dispersion correction[†]. The common B3LYP hybrid exchange correlation functional[91] is selected along with Grimme's D3 dispersion correction with Becke-Johnson damping[92] (B3LYP-D3BJ). The perturbed picocavity DFT spectra using the basis sets Def2-SVP, Def2-SVPD and Def2-TZVP[126–128] are compared in figure 6.4. These show some minor differences in absolute vibrational mode energies but are qualitatively very similar. In this chapter, the larger Def2-TZVP basis set is used. The impact on altering these DFT parameters on the main results of this chapter is discussed in section 6.9.4.

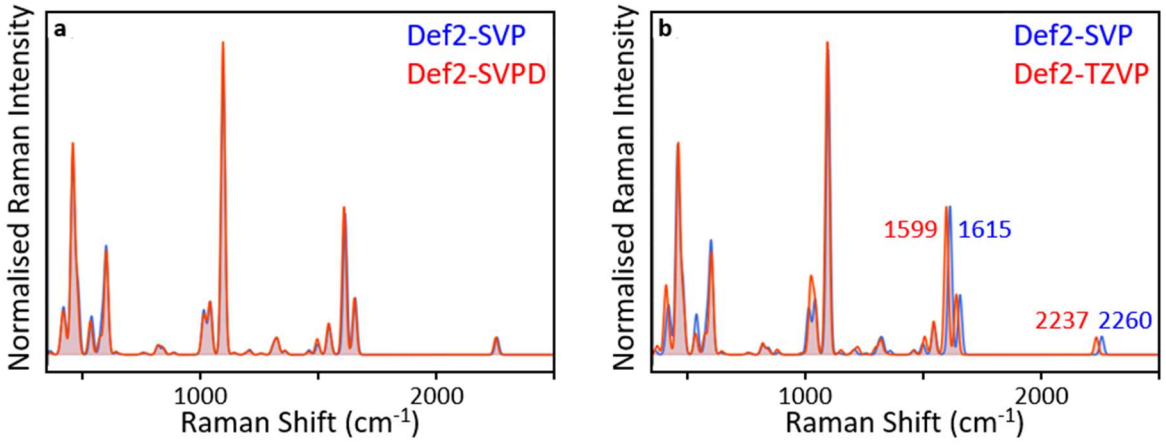

Figure 6.4 | Varying Picocavity DFT Basis Set. DFT calculated Raman spectra of the picocavity Au···NC-BPT-Au-Au structure with varying basis set. **a,** Comparison between the Def2-SVP and Def2-SVPD basis sets. **b**, Comparison between Def2-SVP and Def2-TZVP basis sets.

[†] DFT presented in this chapter provided by collaborator Tamas Földes of University College London. Analysis and application of these calculations shown here is carried out by me.

Due to the internal approximations within a DFT calculation, calculated vibrational energies normally differ a few percent from experimental values[129–131]. With the goal of improving DFT accuracy, this discrepancy is an area of study and is known to depend on the character of the vibrational mode[132] (e.g. if mode does or doesn't involve the stretching or bending of certain bond types). This can normally be mitigated by applying a single scaling factor to all vibrational energies although some disagreement still remains. Here, this scaling can only be investigated for the nanocavity calculation for which we have a fixed experimental reference. A scaling factor of 0.975 works well with the exception of the CN vibrational mode which requires a greater scaling of 0.956 (Fig. 6.5).

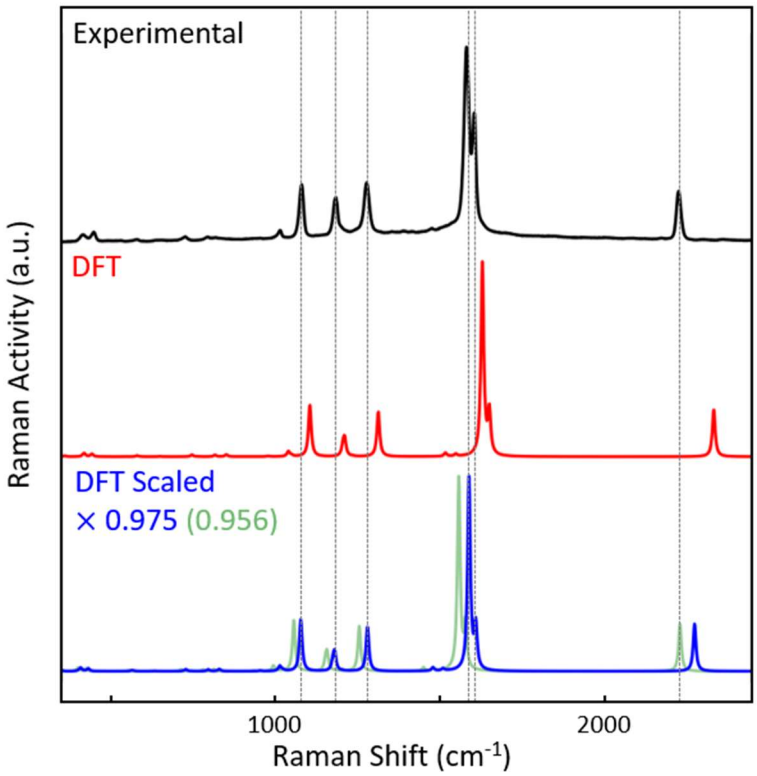

Figure 6.5 | DFT Scaling Factors. Experimental nanocavity SERS spectra and calculated DFT spectra for the nanocavity NC-BPT-Au structure disagree in vibrational mode energies. This is mitigated by scaling the DFT mode energies down, although the CN mode requires greater scaling than the other modes.

Minimising the energy of the Au···NC-BPT-Au-Au (picocavity) system, the gold adatom is placed 2.2 Å away from the N atom as the system relaxes 0.2 eV (~8 k_BT) compared to when the adatom is far from the molecule. At this position, the adatom forms a partial bond of Mayer Bond Order[133] (MBO) 0.3 with the N atom. To form this bond, electron density is

removed from the nitrile group and the CN bond order drops from 3 (triple bond) to 2.7. This reduction in the restoring force between the C and N atom leads to a downshift of ~80 cm^{-1} (scaled by 0.956) in the CN vibrational mode energy in comparison to the ~50 cm^{-1} observed most frequently in experiment. As the NC-BPT molecule is highly conjugated, this electron density reorganisation has a knock-on effect on a range of bond strengths throughout the molecule (Fig 6.6).

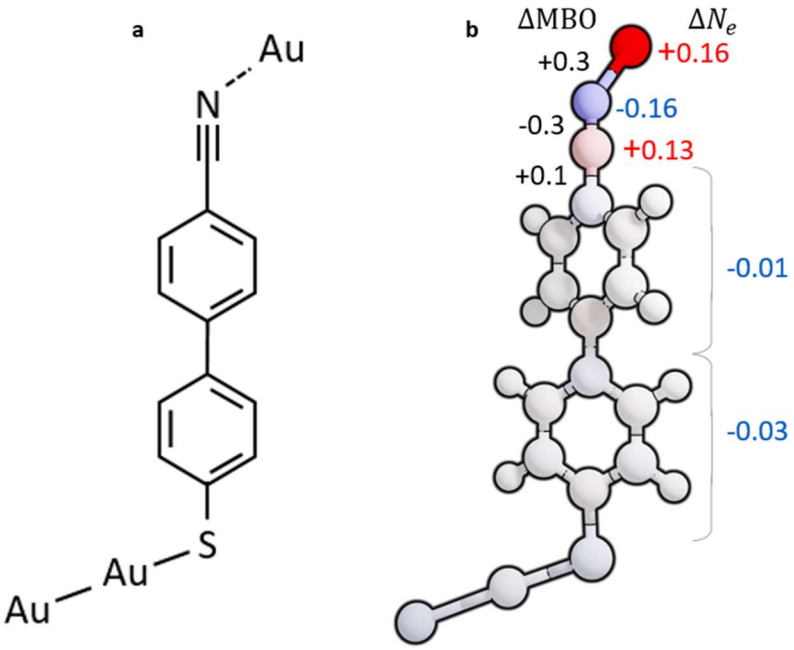

Figure 6.6 | Bond Order Perturbation. a, DFT modelled NC-BPT structure with picocavity adatom present. **b,** In the energetically minimising structural configuration, the adatom forms a partial bond of Mayer Bond Order (MBO) 0.3 with the N atom. Charge density ΔN_e is redistributed (red for increase and blue for decrease) compared to when the adatom is placed a large distance away.

6.3.2 Validity of DFT Simplifications

Before considering how the picocavity system evolves as the adatom is moved away from the energetically minimising position, we will first address the largest simplifications in the modelled system.

In DFT, the anchoring of the molecule to the bulk gold mirror is represented using either one or two gold atoms. While a single gold atom is alone comparable to the weight of the NC-BPT

molecule, it is worth investigating whether a single atom can correctly capture the influence of the delocalised electronic structure of bulk gold. For the nanocavity system, we replace the single anchoring gold atom with clusters of both five and thirteen atoms to form more computationally complex systems. The gold atoms are fixed in structure as a small cluster and flat layer respectively with inter-atomic distances set by those of a gold FCC lattice.

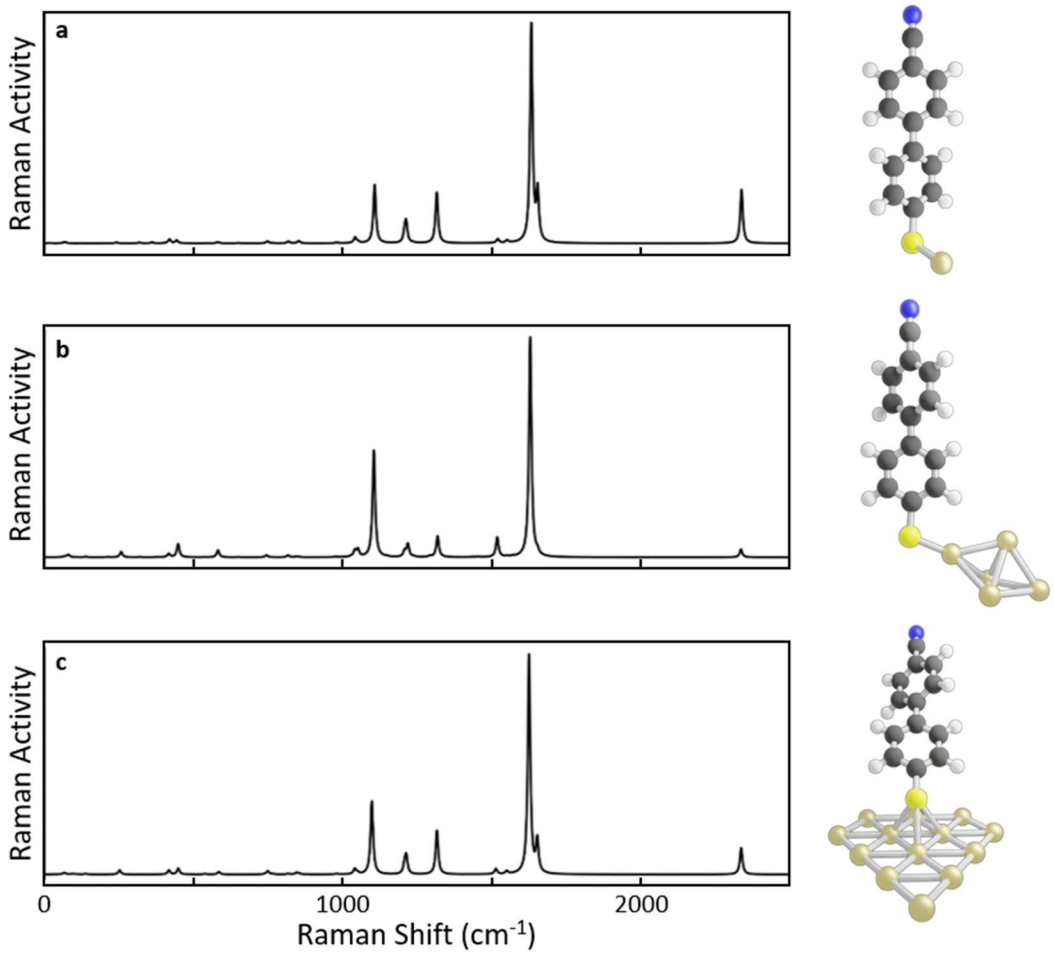

Figure 6.7 | Thiol-Gold Binding Models. DFT Raman spectra for the NC-BPT molecule attached to **a,** one, **b,** five and **c,** thirteen gold atoms via the thiol group. The angle between the molecule and layer of thirteen atoms is fixed at 45° to prevent the molecule from lying flat against the layer.

Reassuringly, this leads to very little change in the resulting vibrational energies with a root-mean square (RMS) change in peak positions between 700 and 2500 cm^{-1} (the range relevant

to the experimental measurements) of only 2.9 cm^{-1} and 2.1 cm^{-1} for these alternatives respectively (Fig. 6.7). The same comparison using the picocavity DFT provides RMS changes of 6.8 cm^{-1} and 5.8 cm^{-1} respectively (Fig. 6.8). This is larger than for the nanocavity case, but smaller than the 12.4 cm^{-1} RMS difference between the nanocavity and picocavity calculations. Changes can be seen in the Raman activity of the vibrational modes, which makes some modes seems to dis/appear between structures, but these calculated activities are not important for this work as already discussed.

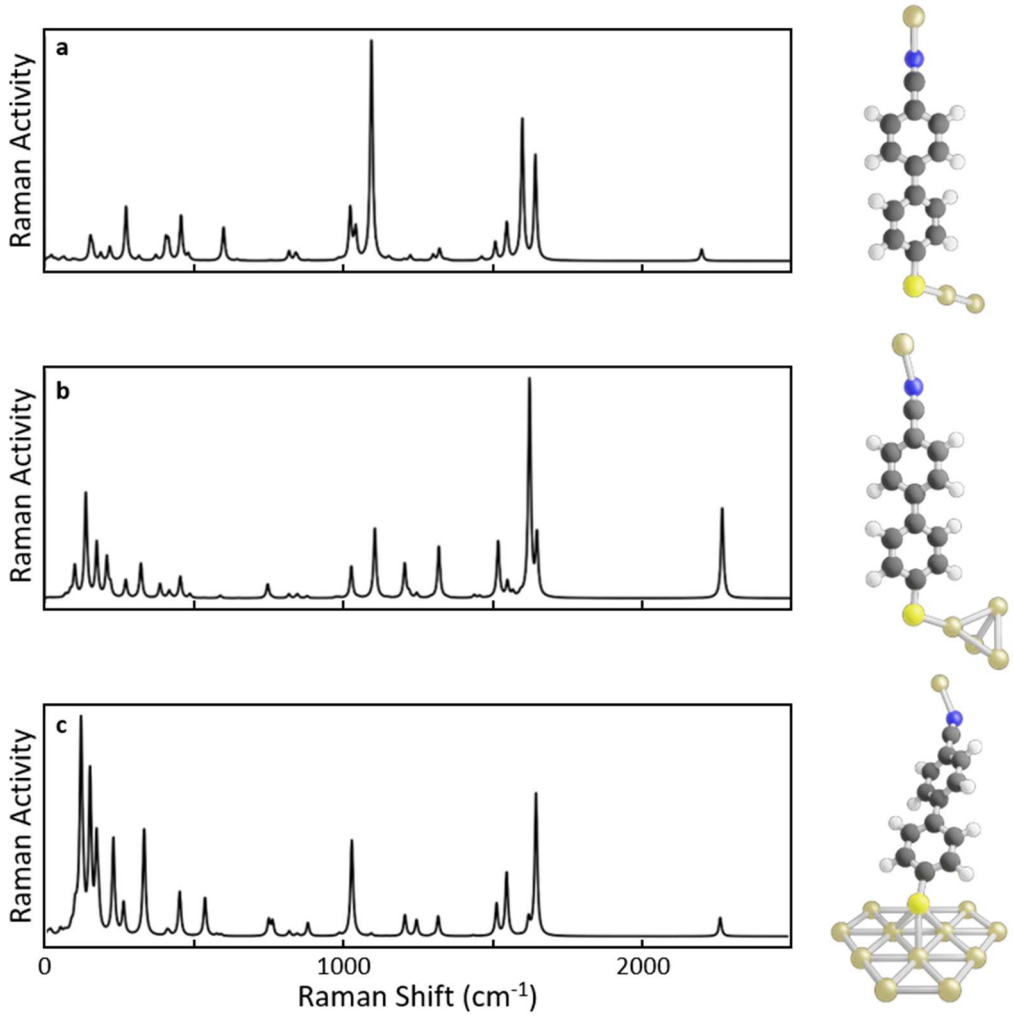

Figure 6.8 | Thiol-Gold Binding Models with Adatom. DFT Raman spectra for the adatom-interacting NC-BPT molecule attached to **a,** two, **b,** four and **c,** twelve gold atoms via the thiol group. The angle between the molecule and layer of twelve atoms is fixed at 45° to prevent the molecule from lying flat against the layer.

As these changes involve variations on to the binding between the molecule and gold through the thiol group, we may wish to compare changes to the S-C vibrational mode. Unfortunately, an isolated vibration of the S-C bond is not a normal mode of this system and changes to this bond (and indeed the Au-S bond/s) form part of multiple different low energy vibrational modes. Lower energy modes represent vibrations delocalised over the molecule such as molecular flexing. We might expect these to be more sensitive to our selection of gold binding (and to the ignored interactions with surrounding molecules) than higher energy modes representing more localised vibrations. Indeed, the RMS change in nanocavity mode energy for modes <700 cm^{-1} is higher at 6.5 cm^{-1} and 8.6 cm^{-1} when comparing the single anchoring gold atom to the clusters of five and thirteen atoms respectively. These changes are 5.4 cm^{-1} and 8.8 cm^{-1} when comparing the picocavity systems. This means that we have much lower confidence in frequencies of the lower energy calculated vibrational modes which are never directly compared to our experimental measurements.

The assertion that there is little chemical interaction between the nitrile group and the high coordination AuNP bulk gold is also observed in literature where -C≡N binding to gold is found to be highly selective to lower coordination number sites[119]. This can be reaffirmed within the DFT model by placing a layer of 12 gold atoms near the nitrile functional group (Fig. 6.9). As expected, the resulting vibrational energies are not significantly perturbed (1.2 cm^{-1} and 2.7 cm^{-1} RMS changes in mode energy for >700 cm^{-1} and <700 cm^{-1} respectively). This lack of interaction can also be seen in the resulting gold-nitrogen separation, which is much larger for the gold slab (2.83 Å) than for the gold adatom (2.16 Å).

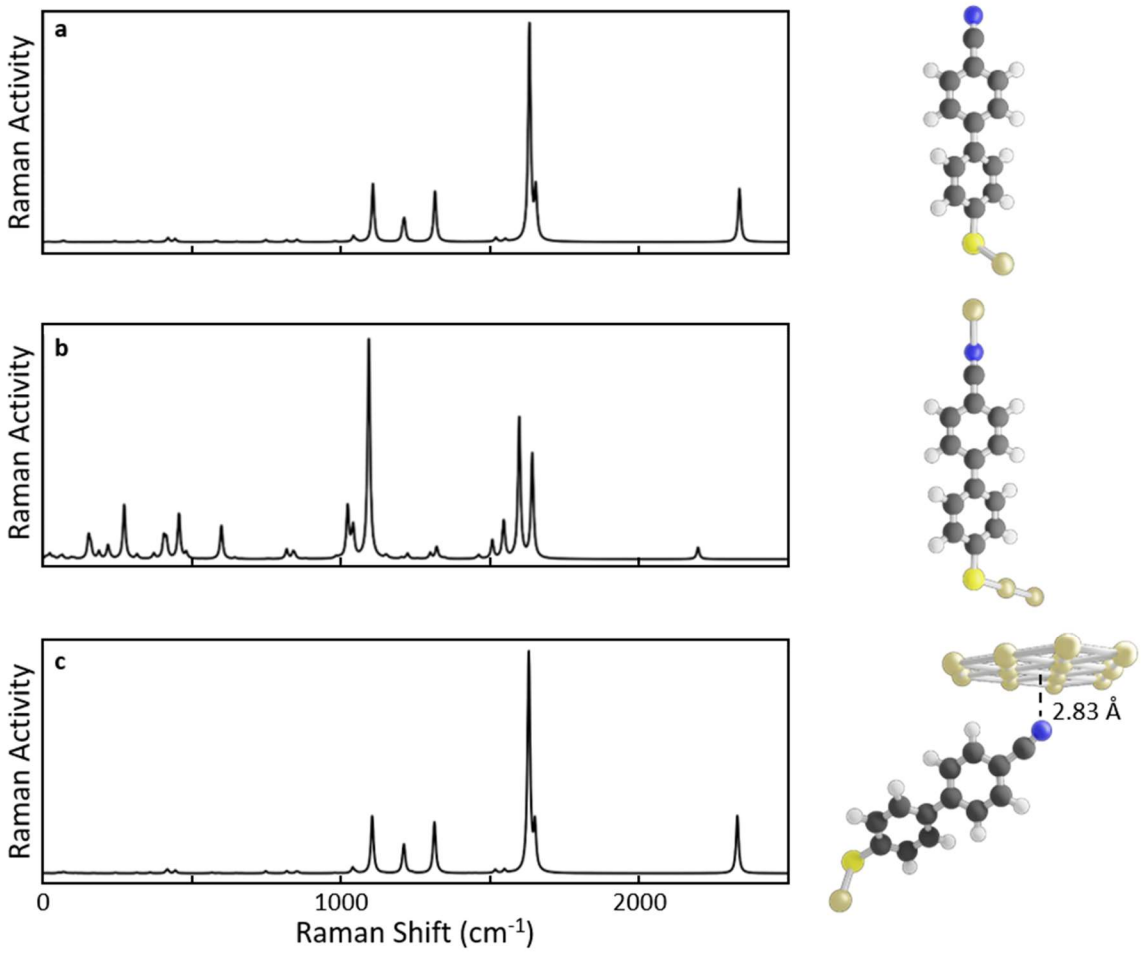

Figure 6.9 | CN-Bulk Gold Interaction. DFT Raman spectra of the modelled **a,** nanocavity and **b,** picocavity systems. **c,** Nanocavity DFT spectrum with a layer of an additional 12 gold atoms in proximity to the nitrile functional group. The angle between molecule and layer of twelve atoms is fixed at 45° to prevent the molecule from lying flat against the layer.

To briefly explore the impact of modelling a single molecule while ignoring the influence of the larger SAM, a higher complexity calculation is carried out of 7 NC-BPT molecules bound to a layer of 43 Au atoms. These gold atoms are fixed in position according to the {1,1,1} facet of a FFC gold lattice. The relative separation of molecules is defined by experimental measurements of a bi-phenyl SAM[49]. Within these constraints, the system is geometrically relaxed. The calculated SERS spectrum of this system is very similar to the single molecule calculation bar a general increase in vibrational energy for all peaks (Fig 6.10). In section 6.5, the effect of moving the picocavity adatom around the nitrile group is explored. The influence

of surrounding molecules on the picocavity DFT system is not explored here due to the computational expense of repeating this complex 7 molecule calculation with varying adatom positions.

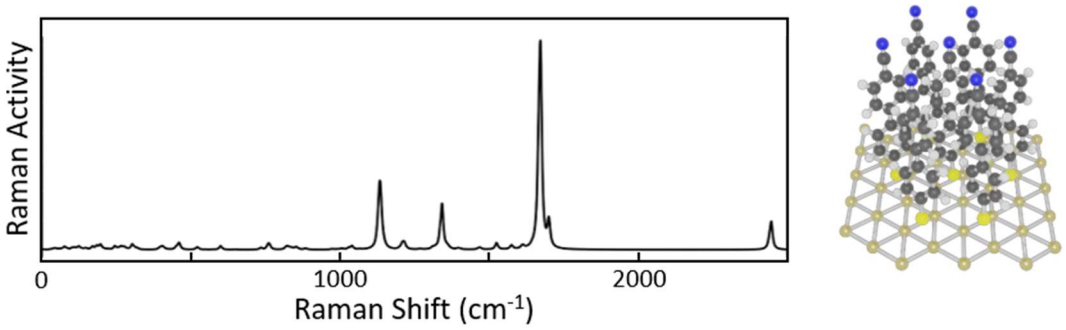

Figure 6.10 | NC-BPT Molecule Cluster. DFT Raman spectrum for 7 NC-BPT molecules bound to a layer of 43 gold atoms.

6.5 Varying the Adatom-Molecule Position

The picocavity DFT is now extended away from the energetic minimum by defining a coordination system for the relative adatom-molecule position. The position of the adatom is tracked using spherical polar coordinates ($d_{\mathrm{NAu}}, \phi, \theta$) with axes defined by the C≡N bond (z) and plane of the upper phenyl ring (xz plane) with the N atom at the origin (Fig. 6.11a). With these relations fixed, the system is otherwise allowed to geometrically relax. The separation d_{NAu} is varied from 1.8-3.2 Å in 0.1 Å steps while ϕ and θ are varied from 0-90° and 11-91° respectively in 10° steps. This results in 1350 individual DFT structures. The extent of ϕ is limited to a quarter of the full 360° range to reduce the necessary number of calculations by assuming that the other three quadrants are similar due to symmetry. As well as a perturbed set of vibrational mode energies, each calculation yields a relative system energy as well as the MBO between each pair of atoms in the system. The resulting energy landscape, as found previously (section 6.3.1), is minimised at d_{NAu}=2.2 Å (Fig 6.11b). It is important to note that these energy calculations represent the electronic energy of the calculated system and do not capture other neglected contributions from SAM intermolecular

interactions and interactions between the adatom and bulk gold. At this d_{NAu}, the system energy is minimised at ϕ=90° (Fig. 6.11c), reflecting the spatial overlap between the Au valence orbitals and the C≡N π-orbital to which they hybridise, and canted at θ~40°. The N-Au MBO increases continuously with adatom approach (Fig. 6.11d) and shows a similar angular dependence maximised at ϕ=90° and at a slightly higher value of θ (Fig. 6.11e).

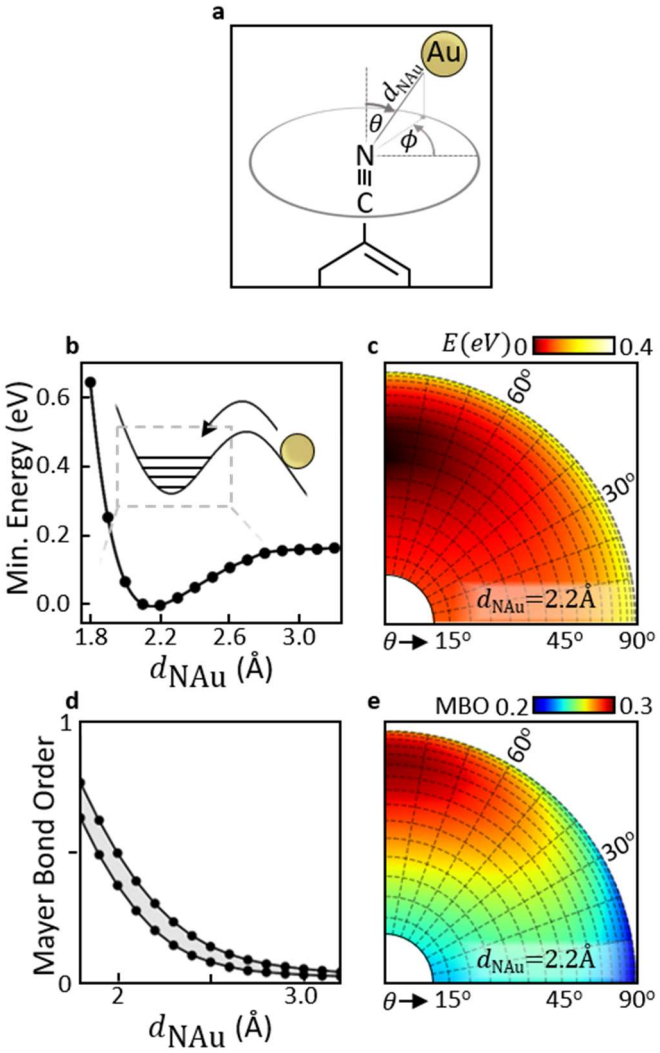

Figure 6.11 | Energy and Perturbation Landscapes. **a,** Coordinate system defining adatom position relative to NC-BPT C≡N bond and upper phenyl ring. **b,** DFT system energy *vs* d_{NAu}, optimising adatom angular position at each distance. Inset: Schematic of complete energy landscape of which this well is a component. **c,** Relative system energy with varying adatom angular position for energetically favourable d_{NAu}=2.2 Å. **d,** Range of possible N-Au MBO (with varying angular position) with d_{NAu}. **e,** N-Au MBO with varying adatom angular position for energetically favourable d_{NAu}=2.2 Å.

For completeness, figure 6.12 shows the calculated Raman spectrum at every adatom position. This is shown on a logarithmic colour scale. While projecting the 3D parameter space here onto a linear series of spectra somewhat obscures more subtle trends, it is clear that the large perturbation of the CN vibration (which can take any value over a continuous range of hundreds of wavenumbers) is matched by other perturbations across the SERS spectrum. Qualitatively, the vibrational energy changes are smooth enough at this level of resolution that interpolating between calculated adatom positions should be a good approximation for further calculations.

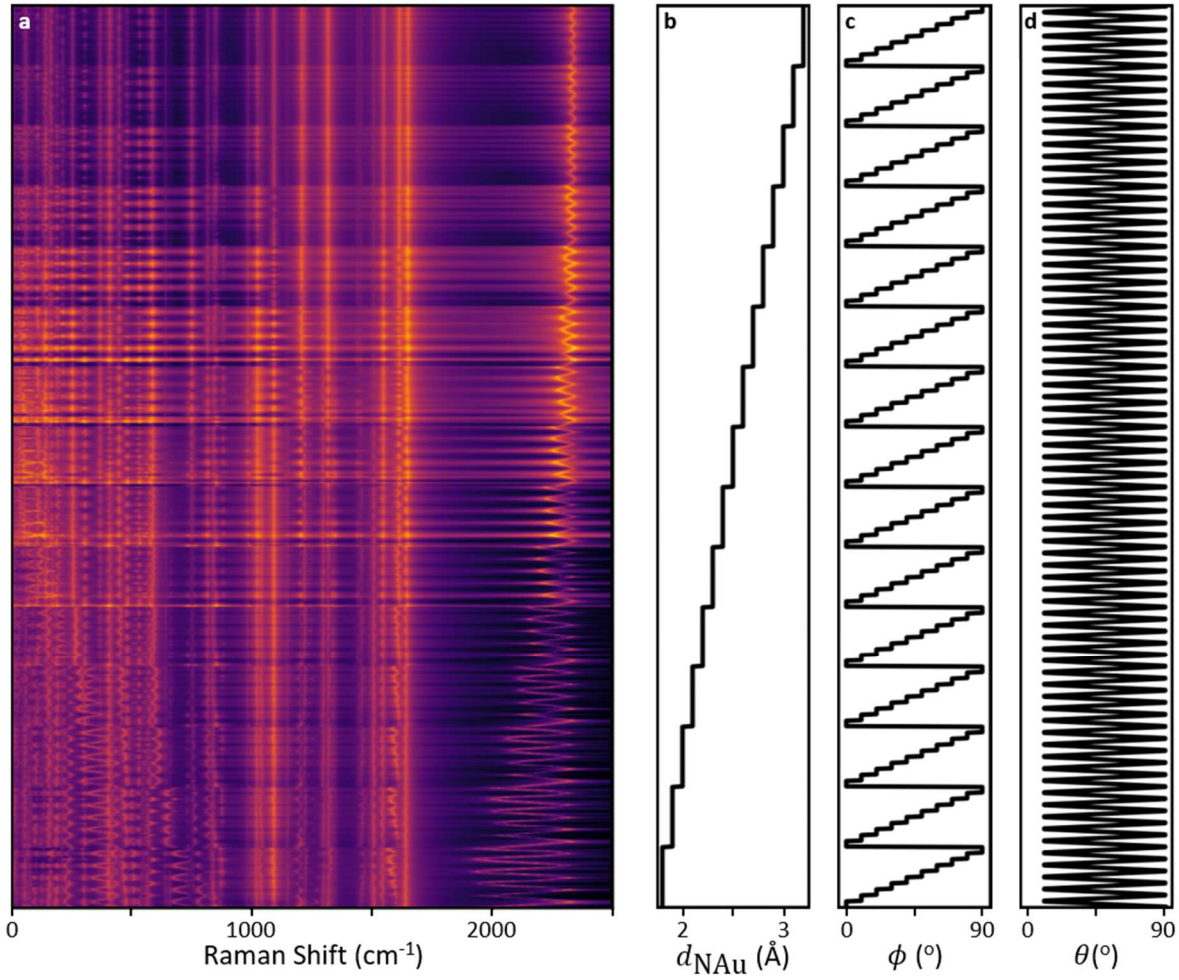

Figure 6.12 | All Perturbed DFT Spectra. a, Set of 1350 DFT picocavity Raman spectra (log colour scale) with varying **b, c, d,** adatom position coordinates.

As calculating vibrational energies involves derivatives of the energy landscape with respect to atom movement, we must discuss the impact of performing these calculations away from

the energetically minimising conformation of the simulated structure. This can introduce errors that cause the lowest energy vibrations to become unphysically negative. Across the parameter space shown, this occurs to a maximum of the three lowest energy vibrational modes. These low energy vibrations represent flexing motions of the entire molecule that will also be the most sensitive to the model simplifications regarding the representation (or lack thereof) of the bulk gold surfaces and surrounding molecules. It is important to note that this low energy region of the spectrum, of which we are less confident, is never used in direct comparison to experiment.

To simplify the discussion, we will explore the perturbation of the SERS spectra while fixing θ, ϕ = 91°, 90° for which the perturbation is strong (Fig 6.13). As the adatom approaches perpendicular to the upper phenyl ring, vibrational modes across the spectrum are perturbed while the CN vibration continuously lowers in energy as the bond order decreases. Interesting changes are observed in two dominant vibrational modes representing stretching of the lower and upper phenyl rings at $\sim$1600 cm^{-1} (Fix 6.12a,b, α and β). The trajectories of these vibrational energies appear to follow an anti-crossing with an additional translation in energy meaning that β stays approximately fixed in energy. With decreasing d_{NAu}, the vibrational motion of the top ring is increasingly influenced by the heavy gold adatom. Since the lower ring is already bound to gold, this indeed reduces the molecular asymmetry causing these vibrational modes to mix (Fig 6.13b,c). The phenyl-phenyl bond also strengthens leading to a reduced dihedral angle between the rings (Fig 6.13d), which is a relationship consistent with previous studies[134]. In experiment, this phenyl ring rotation may be sterically resisted by surrounding SAM molecules. Further perturbations are seen across the Raman spectrum, highlighting electron density reorganisation and the consequent changes in bond strengths.

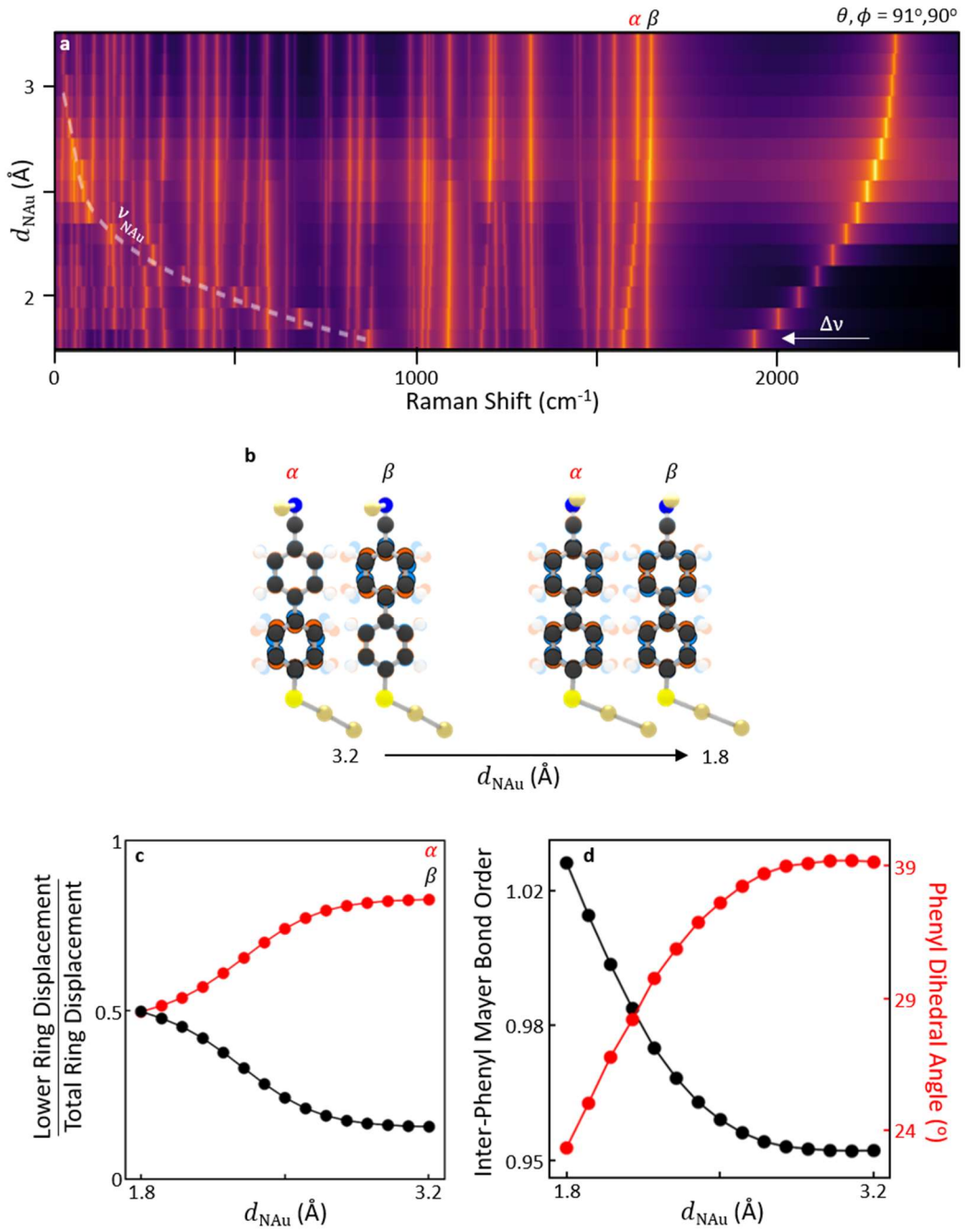

Figure 6.13 | Perturbed Vibrational Modes with Approaching Adatom. **a,** DFT spectra with varying d_{NAu} and fixed θ, ϕ = 91°, 90° (log colour scale). A series of anti-crossings increases in energy with adatom approach (ν_{NAu} dashed line). **b,** Phenyl ring stretching vibrational modes (α, β) hybridise with decreasing d_{NAu} and lowered molecular asymmetry. Orange and blue indicate opposite extrema of the vibrational motion. **c,** Mode mixing quantified by the fraction of total ring carbon atom displacement represented by a single phenyl ring. **d,** With decreasing d_{NAu}, the inter-phenyl ring bond order drops and the rings rotate to be more co-planar.

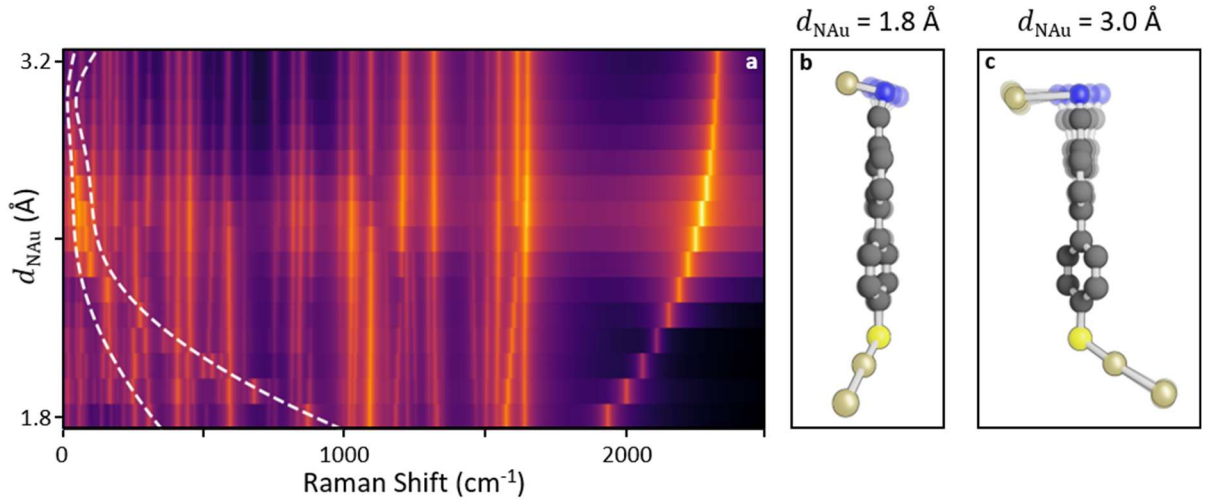

Figure 6.14 | N-Au Vibrational Mode. **a,** Observed SERS anti-crossings track the energy of the N-Au pseudo-mode. The extreme bounds of this energy (dashed lines) are estimated using effective mass estimates for the N-Au bond stretching pseudo-mode taken from vibrational modes at **b,** near and **c,** far adatom distances.

A new vibrational pseudo-mode (ν_{NAu}) rapidly increases in energy as d_{NAu} decreases, seen through a set of anti-crossings with successively higher energy vibrations (Fig 6.13a, dashed line). Here, we will demonstrate that this pseudo-mode likely arises from the N-Au interaction and tracks the strength of this partial bond. We will estimate the pseudo-mode energy considering the stretching of this partial bond (adatom movement only along the d_{NAu} coordinate). From vibrational analysis, the pseudo-mode related to partial bond stretching atom has frequency

$$\nu = \frac{1}{2\pi}\sqrt{\frac{D}{\mu}} \tag{6.1}$$

where the force constant D is the second derivative of the system energy with respect to d_{NAu} and μ is the reduced mass of the pseudo-mode. To estimate this mass, vibrational modes are selected at near and far d_{NAu}= 1.8, 3.0 Å in which the stretching motion of the N-Au partial bond is heavily involved (Fig. 6.14b,c). In both cases, the vibrational modes involve a linear translation of the Au atom. At d_{NAu}= 1.8 Å (Fig. 6.14b), all atoms in the molecule are effectively still apart from the N whose motion can be modelled as a rotation around the C atom in the nitrile group. At d_{NAu}= 3.0 Å (Fig. 6.14c), the lower molecular atoms

are again effectively still but the upper phenyl ring and nitrile group move together. This can also be modelled as a rotation with all atoms in the upper phenyl ring and nitrile group rotating around the ipso (upper) C atom of the lower phenyl ring. In both cases, the force (F) experienced by the Au atom and the section of rotating molecule due to the Au-N interaction is equal and opposite in sign so

$$F = m_{\mathrm{Au}} a_{\mathrm{Au}} = -I_{\text{NC-BPT}}\, a_{\mathrm{N}} / r_{\mathrm{N}} \tag{6.2}$$

where a_{Au} and a_{N} are the linear accelerations of the Au and nitrogen atoms respectively, m_{Au} is the mass of the gold atom, $I_{\text{NC-BPT}}$ is the moment of inertia of the rotating NC-BPT atoms and r_{N} is the distance of the N atom to the centre of rotation. The relative acceleration a_{rel} of the Au-N distance is

$$a_{\mathrm{rel}} = a_{\mathrm{Au}} - a_{\mathrm{N}} = F\, \frac{I_{\text{NC-BPT}} + m_{\mathrm{Au}} r_N}{I_{\text{NC-BPT}}\, m_{\mathrm{Au}}} \equiv \frac{F}{\mu} \tag{6.3}$$

$$\mu = \frac{I_{\text{NC-BPT}}\, m_{\mathrm{Au}}}{I_{\text{NC-BPT}} + m_{\mathrm{Au}} r_N}\,. \tag{6.4}$$

This gives effective masses of μ = 14.92, 111.38 atomic units in each d_{NAu} limit. The two limiting curves for the resulting pseudo-mode energy are shown in figure 6.14a, successfully bounding the observed series of anti-crossings that move from one bound to the other with varying adatom distance. This pseudo-mode estimation breaks down at large adatom distances where the interaction is very weak.

6.6 Thermal Fluctuations of a Quantum Harmonic Oscillator

We can use the energy landscape obtained through DFT to explore the feasibility that the observed CN mode spectral wandering (section 6.2) is thermally driven. For a simple approximation, we consider changes only in the d_{NAu} coordinate. Around the energetically favourable adatom position, this energy potential (Fig. 6.15) has an effective harmonic spring constant of $k = 2.84$ eVÅ^{-2}. To estimate a reduced mass for the vibration (m) along this coordinate, we consider the reduced masses estimated at d_{NAu} = 1.8 Å and 3 Å in section 6.5. At the energy minimising d_{NAu} = 2.2 Å, the MBO of the N-Au partial bond is 34.5% along the

values at these two limiting distances. Linearly interpolating the reduced mass by this same ratio amount provides an estimate of 48.3 atomic mass units.

The energy level spacing of a quantum harmonic oscillator (QHO) is given by

$$\hbar\omega = \hbar\sqrt{\frac{k}{m}} = 15.7 \text{ meV} \tag{6.5}$$

while the zero-point motion in the ground state is given by

$$\langle x^2\rangle^{\frac{1}{2}} = \sqrt{\frac{\hbar}{2m\omega}} = 5.25 \text{ pm.} \tag{6.6}$$

Note that this energy spacing (15.7 meV = 127 cm^{-1}) approximately matches the N-Au psuedomode energy ν_{NAu} at d_{NAu}=2.2 Å as expected (Fig. 6.13a).

Taking a thermal energy of k_BT=25 meV, this QHO exists in a thermal superposition at time t of

$$\varphi(x,t) \propto \sum_{n=0}^{\infty} e^{-\frac{\left(n+\frac{1}{2}\right)\hbar\omega}{2k_BT}} e^{-i\left(n+\frac{1}{2}\right)\omega t}\phi_n \tag{6.7}$$

where ϕ_n are the energy eigenstates of the system (Hermite functions). The root mean square displacement of the oscillator tends towards $\langle x^2\rangle^{\frac{1}{2}} = 7.1$ pm as this series is truncated at an increasing number of terms. Around the energetic minima, the energy of the CN vibration varies locally by 166.9 $cm^{-1}Å^{-1}$ (after scaling x0.956) with d_{NAu} (Fig. 6.15), giving an expected thermal variation of approximately 12 cm^{-1}. Given the harmonic approximation and coordinate restriction made here, it is likely that thermally induced relative adatom-molecule motion drives the observed spectral fluctuations. It is important to note that if the time scale at which the system thermally samples the CN mode energy is much smaller than the integration time t then we would expect the observed wandering to tend as $\propto t^{-\frac{1}{2}}$ due to temporal averaging, so it is expected that this would be an overestimate of the observed value.

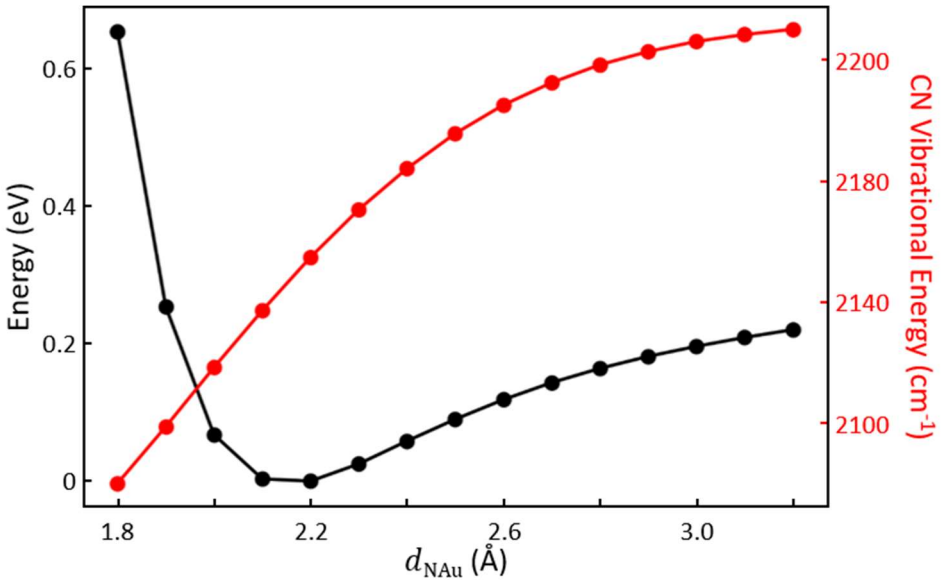

Figure 6.15 | System and CN Vibrational Energy with d_{NAu}. Relative system energy with varying d_{NAu} and fixed $\theta = 41°, \phi = 90°$ passing through the global energy minima. The energy of the CN vibrational mode is also shown along the same curve (scaled x0.956).

Considering instead motion in ϕ through the minimum energy configuration ($d_{\mathrm{NAu}} = 2.2\text{Å}, \theta = 41°$), the potential landscape can be approximated harmonically for small angle variations from the minima as

$$E = \frac{E_0 \phi^2}{2} \quad , \quad E_0 = 0.14 \text{ eV} \tag{6.8}$$

giving a smaller harmonic energy level spacing of

$$\hbar\omega = \hbar \sqrt{\frac{E_0}{m \, {d_{\mathrm{NAu}}}^2}} = 1.6 \text{ meV}. \tag{6.9}$$

6.7 Alternative Models for Perturbed Vibrational Energies

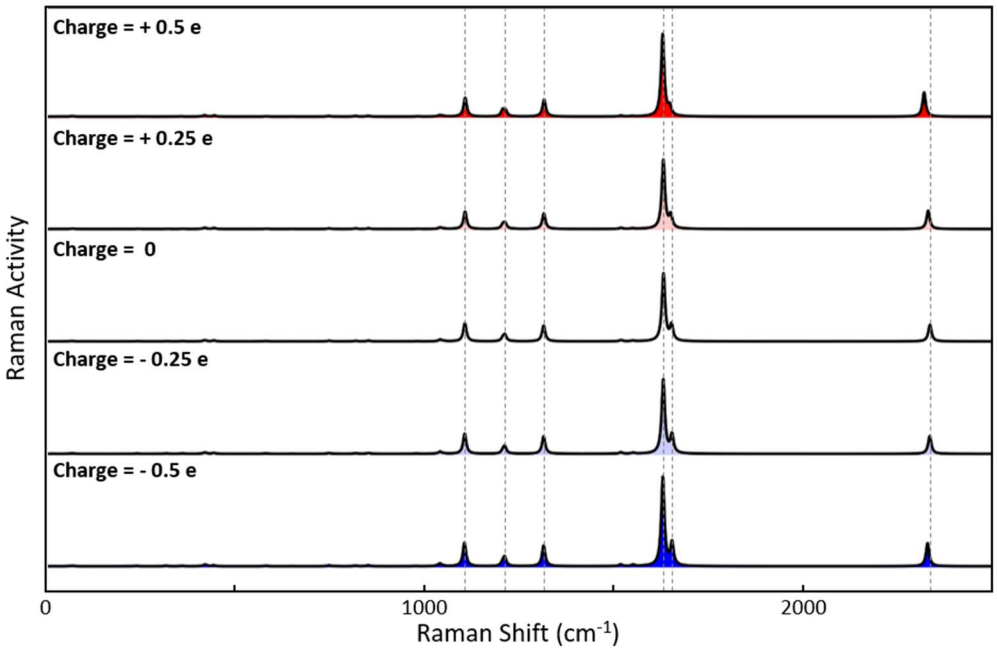

Figure 6.16 | **Replacing Adatom with Point Charge.** DFT Raman spectra of the energetically minimised picocavity system where the gold adatom replaced with a point charge of varying sign and strength.

So far, we have focussed on modelling the perturbation of vibrational energies in terms of an interaction between the molecule and picocavity. However, it is important to consider whether alternative models can also explain the observed spectral dynamics.

First, we consider changes to vibrational mode energies due to an applied field. This is known as the Stark effect. The AC Stark Effect should induce vibrational energy changes due to the picocavity field oscillating at optical frequencies. However, this effect splits vibrational energies[135] in contrast to the asymmetric shifts observed so must be experimentally unresolved here. A DC field generated through any charge accumulation at the picocavity position would modify vibrational energies through the DC Stark effect, which for the C≡N functional group goes as $(20\pm5)\ cm^{-1}V^{-1}$ [118,136] requiring large potentials to replicate experimental observations. This effect can be reproduced in DFT by replacing the adatom (in the energetically minimised position) with a point charge. Charge magnitudes as large as 0.5e

(where e is the fundamental charge) change the energy of the CN vibration by only $\leq$6 cm^{-1} (Fig. 6.16). Similarly, charging the molecule itself fails to recreate the observed scale of the perturbation (Fig. 6.17).

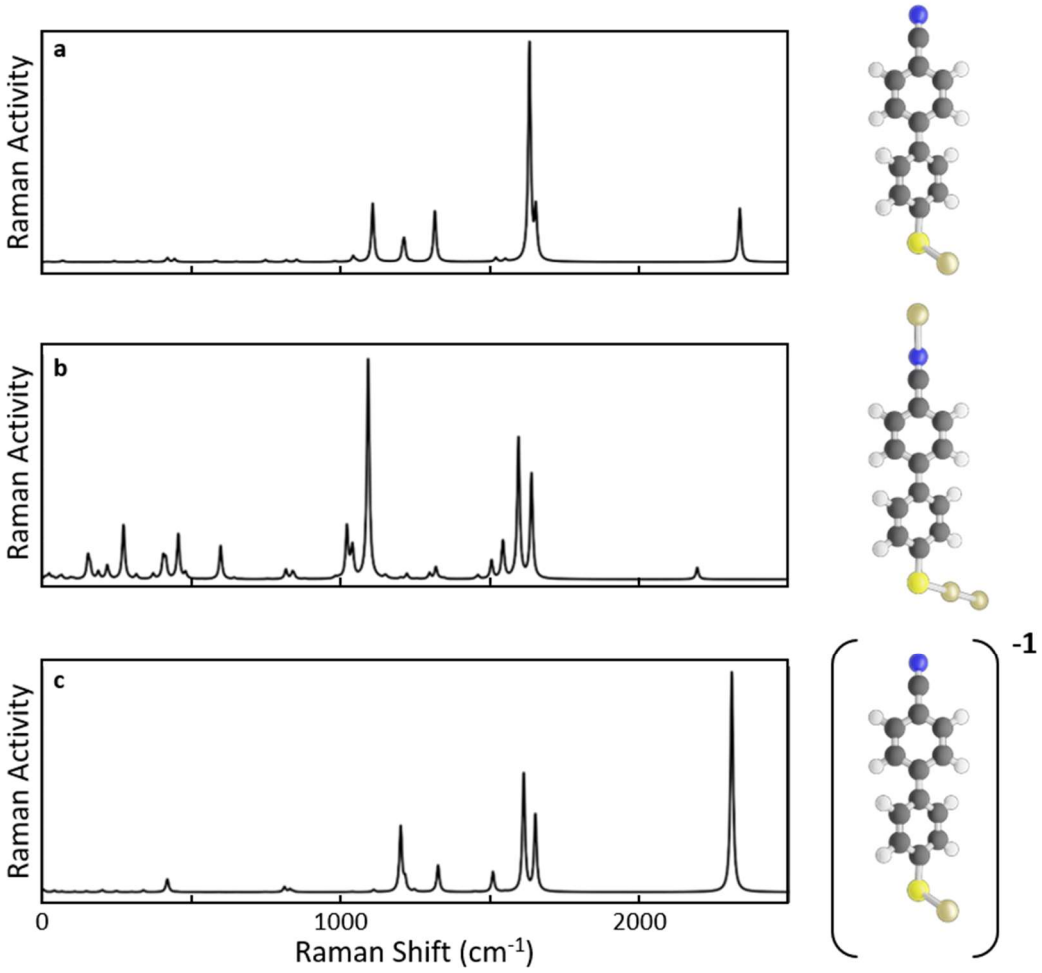

Figure 6.17 | **Molecular Charging.** DFT Raman spectra of the **a,** nanocavity and **b,** picocavity systems. **c,** DFT Raman spectrum of the nanocavity system with an additional negative charge. This modifies Raman activities but does not significantly alter vibrational energies.

If the picocavity enhances the SERS of a molecule with an ^{13}C≡N bond isotopologue, then we would indeed expect a downshift of the CN vibrational mode which has been experimentally measured as 52 cm^{-1} [36]. This rare occurrence (1.1% natural abundance[137]) is likely to explain a small fraction of our observations but is a static effect that cannot explain the spectral dynamics observed. The presence of this carbon isotope would be unlikely to have a

significant effect on the rest of the SERS spectrum which can be demonstrated with DFT (Fig. 6.18).

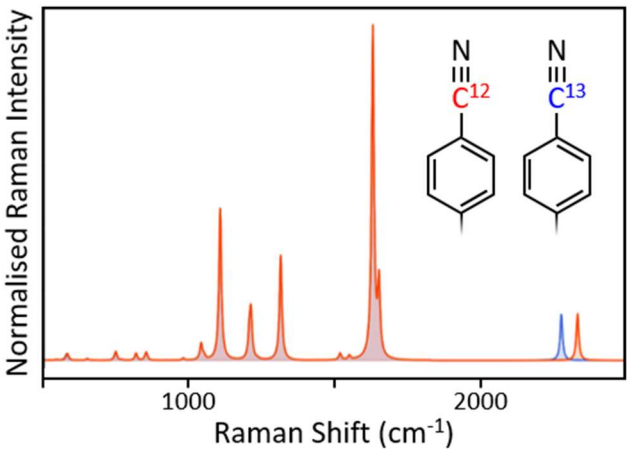

Figure 6.18 | **CN Isotopologue.** DFT Raman spectra of the nanocavity NC-BPT system with and without the nitrile carbon atom replaced with a heavier C^{13} isotope.

We now consider the assumption that a discrete change in the SERS spectrum during a picocavity event is the result of a change in relative adatom-molecule position and is not due to the picocavity switching the molecule with which it is interacting. In the DFT model, the high sensitivity of vibrational mode energies to the adatom-molecule position means that these discrete changes require only sub-angstrom atomic movements within a spectrum integration time. This must be compared to the ~6 Å intermolecular spacing in a bi-phenyl SAM[49] that would require the adatom to traverse a much larger distance in the same time. Occasionally (< 15% of observed CN picocavity events), the CN transient mode is observed to be split into two peaks. An example of this is shown in figure 6.19a where the spectrum switches repeatedly between one and two transient CN peaks. When two peaks are present, they are correlated in vibrational energy over time. Preliminary DFT suggests that this could be caused by the hybridisation the perturbed CN vibrations from 2 molecules coupling through mutual interaction with a single adatom (Fig 6.19b). This suggests that it may be

difficult for an adatom cleanly stop an interaction with a given molecule and start interacting with another without some intermediary spectral signature being detected.

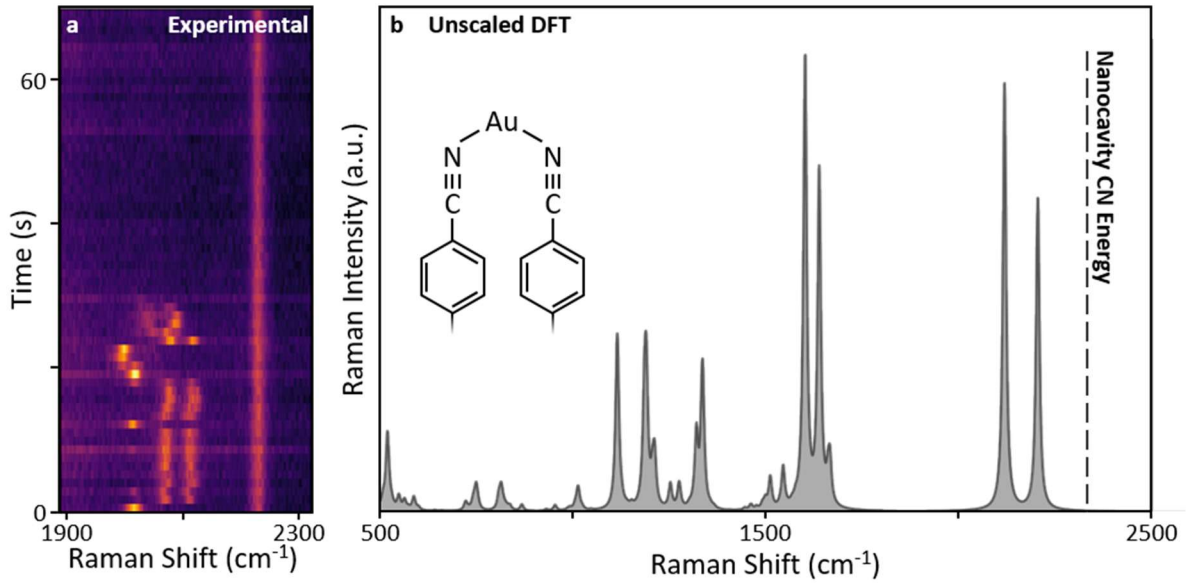

Figure 6.19 | Split CN Transient Vibration. a, Experimental picocavity spectra taken with 1 s integration times and 25 µW of 633 nm laser power displaying discrete switching between a single and spilt transient CN vibrational line. **b,** Preliminary DFT Raman from two NC-BPT molecules coupled through a mutual interaction with the same Au atom.

Of these models, a single adatom-molecule interaction per picocavity event with a varying relative adatom-molecule position over time appears to be the most reasonable explanation for the majority of observations.

6.8 Adatom - Phenyl Interactions

To briefly investigate if adatom-molecule interactions may be more general with functional groups that do not generate such clear spectral signatures as the nitrile group, we also calculate adatom perturbed spectra for biphenyl-4-thiol (BPT) in DFT. Without the CN triple

bond, the adatom is instead placed a certain distance d_{CAu} from the para (top) carbon of the upper phenyl ring at an energetically favourable angular position. Practically, this results in the adatom being perpendicular to the plane of the upper ring ($\theta, \phi \sim 90°$). Again, the vibrational modes are strongly modified by the Au adatom as its valence orbitals overlap with the π-orbitals of the ring giving a shallower 0.1 eV local energy well at d_{CAu}=2.2 Å with a MBO of 0.5 for the C-Au bond (Fig 6.20). It is therefore possible that such Au-molecule coordination bonds may be prevalent in more molecule-surface interactions with picocavities, requiring further study.

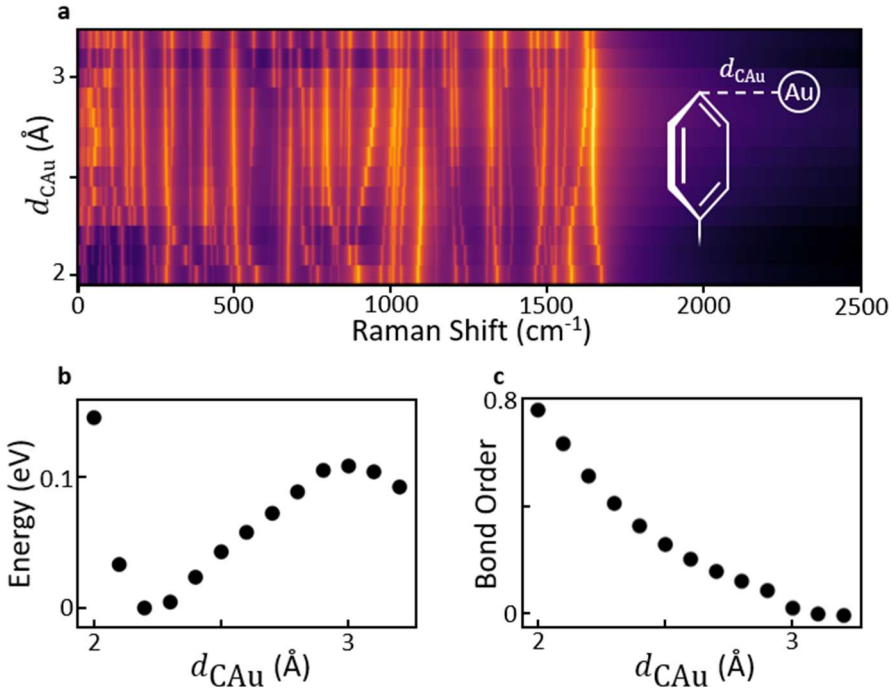

Figure 6.20 | BPT Adatom Interactions. a, DFT Raman spectra of biphenyl-4-thiol (BPT) with an Au adatom a distance d_{CAu} from the upper phenyl ring C atom at an energetically minimising angle (log colour scale). Practically, the atom is perpendicular to the plane of the upper phenyl ring. **b,** Relative system energy with d_{CAu}, **c,** MBO between Au adatom and upper carbon atom with d_{CAu}.

6.9 Extracting Adatom Trajectory from SERS Spectra

6.9.1 Inverting Adatom Position using Vibrational Mode Energies

As each relative adatom-molecule position generates a unique fingerprint of vibrational mode energies, a picocavity SERS spectrum with enough well-resolved peaks should be invertible to provide an adatom position relative to the molecule. This is explored here using a picocavity event of 133 consecutive spectra taken at a higher 300 μW laser power to allow shorter 100 ms integration times (Fig. 6.21a). Four picocavity peaks are resolvable at all times during this event which can be assigned to vibrational modes in the DFT dataset (linearly interpolating between calculated adatom positions). This peak assignment is taken as given here and will be discussed in section 6.9.5. For a given spectrum, the adatom could initially be positioned anywhere within the 3D DFT parameter space. Stipulating the energy of any perturbed vibrational mode collapses the dimensionality of the possible picocavity positions to a 2D surface. Fixing further vibrational energies collapses this to a 1D line and then a unique point in 3D space. This assumes that the vibrational modes chosen/visible do not contain redundant information. As there are uncertainties in the measured energy of any vibrational mode, the confidence with which the adatom can be localised increases with the number of vibrational modes considered. Note that this is an exact analogy to macroscopic triangulation using, for example, GPS satellite signals.

This adatom triangulation requires a high level of accuracy for the DFT vibrational mode energies. As discussed previously, DFT contains intrinsic approximations that, for NC-BPT, over-estimate these energies. This can be mitigated with ad hoc scaling factors that are known to depend on the vibrational character of the modes[132]. These internal DFT errors combine further with the representation of the experimental system with a simplified model. Note that applying either a single scaling factor to all vibrational modes or separate scaling factors to each mode provides additional model parameters that must be specified or optimised in order to extract the adatom position. Within the DFT model, the range of adatom-molecule positions provides a corresponding range of possible energies for each vibrational mode. For each experimental spectrum, figure 6.21b shows the range of scaling factors that could be applied to the each DFT mode for this range to overlap with the experimentally observed

energy. For two of the vibrational modes (1521 and 1537 cm^{-1}), there are no constant scaling factors available that place the experimental measurements inside the range permitted by DFT for every spectrum. These represent modes that stretch the phenyl rings. Just like the phenyl ring stretch modes discussed in figure 6.13, these are vibrations initially localised on a single phenyl ring that become delocalised across both rings with increasing adatom interaction. Due to this strong change in vibrational character, we therefore may expect the scaling factor for these modes to be dependent on the adatom-molecule position. In experiment, we may expect the strength by which these modes are perturbed by the adatom to be sensitive to the intermolecular SAM interactions neglected in the DFT model. Therefore, direct adatom triangulation from individual spectra is not possible here.

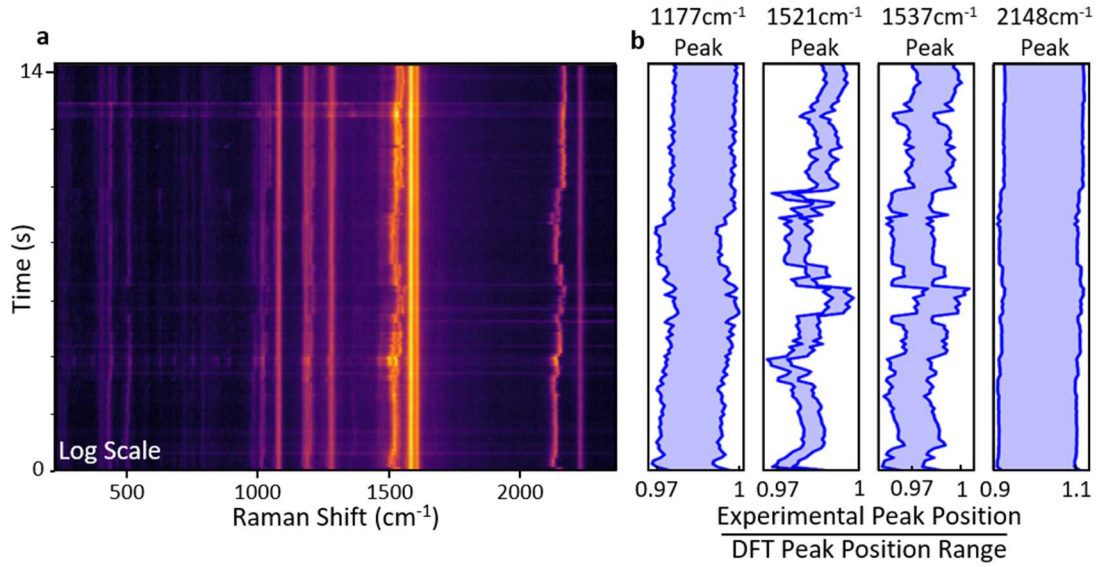

Figure 6.21 | SERS Scan for Adatom Trajectory Inversion. a, Experimental picocavity spectra taken with 300 µW 633 nm laser power using 100 ms integration times (log colour scale). Time starts when picocavity first forms. **b,** Range of possible scaling factors that could be applied to the DFT vibrational energies to overlap experimental transient SERS peaks with the ranges provided within the DFT model.

A number of possible ad hoc solutions for this problem were attempted, including a DFT scaling factor that varied smoothly with vibrational energy and scaling factors that changed linearly with vibrational mode delocalisation across the two phenyl rings. These are not discussed in detail here as the additional free parameters allowed the resulting adatom

trajectory to be arbitrarily moved within the parameter space. With improvements in theory, computational power and resources over time, a more complex and accurate model of the system should make it possible to directly triangulate the adatom position from any given experimental spectrum. This is considered here as an end goal of this style of study but is currently unfeasible.

6.9.2 Inverting Adatom Trajectory using Vibrational Mode Dynamics

The picocavity vibrational modes in this experimental scan (Fig. 6.21a) change energy dynamically over time. Although direct adatom triangulation within the DFT model from any given spectrum is not possible (section 6.9.1), these dynamic changes between spectra can be leveraged as an alternative source of information. Here, we will not assume that the DFT is able to perfectly predict perturbed vibrational energies. Instead, we will use the weaker assumption that the DFT correctly captures the trends of how the vibration energies are perturbed by the adatom. This means that if a change in relative adatom location causes a vibrational mode to increase in energy in the experimental system, then the same mode should increase in energy in the DFT model. A different adatom movement that causes a larger energy increase should again be reflected by a larger increase within the model. Importantly, we will not assume that the relationship between the size of the energy perturbations between experiment and DFT are linear.

To apply these assumptions, we will define an adatom trajectory as a series of relative adatom-molecule positions over the course of the experimental measurement. We score any given trajectory by comparing the energy of each transient picocavity mode over time between DFT and experiment using a Spearman correlation (high Spearman correlation between two sets of values indicates a monotonic relationship). The optimum adatom trajectory to describe the experimental observations provides the highest averaged Spearman correlation between the four transient picocavity peaks. Note that if the correlation function used was instead linear (such as the Pearson correlation) then this would be mostly equivalent to scaling DFT peak energies and matching them directly to experimental values as discussed in section 6.9.1 which we determined does not work here.

The adatom trajectory has three parameters ($d_{\mathrm{NAu}}, \phi, \theta$) per spectrum for a total of 399 parameters that cannot practically be systematically scanned to identify the optimal solution. Instead, the trajectory is optimised from an initial state consisting of a random adatom location in the DFT parameter space at each point in time. To ensure that the final result represents a global solution, this optimisation is carried out from 5 independent random starting trajectories.

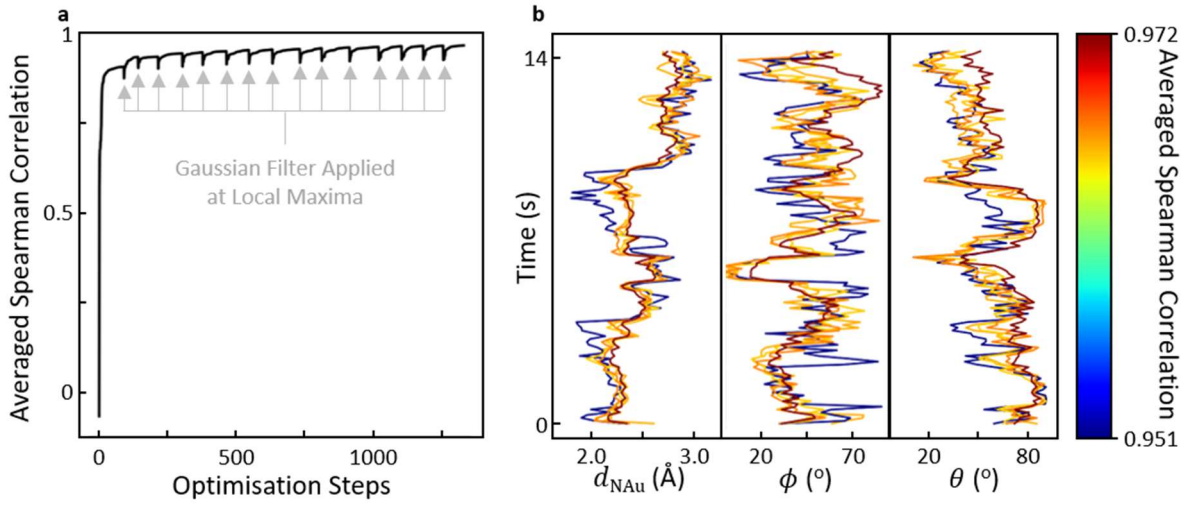

Figure 6.22 | Adatom Trajectory Optimisation. Adatom trajectory is optimised by maximising the averaged spearman correlation between transient SERS peak energies in experiment and DFT. **a,** Representative trajectory score with optimisation steps. The trajectory is initialised randomly. Adatom positions at each point in time are optimised through a random walk followed by gradient ascent. At each local maximum, a Gaussian smoothing of adatom positions (std = 1 time step) is applied and the system attempts to optimise to an improved maximum. **b,** Five independently initialised and optimised adatom trajectories to describe the observed transient SERS line dynamics.

A random trajectory provides an expectedly low average correlation between the experimental and theoretical peak positions (Fig. 6.22a). This is improved using a random walk process. When this fails to improve the trajectory further, a gradient ascent algorithm is applied to generate a trajectory that is locally optimised (i.e. no small change to the adatom position at any point in time can improve the trajectory). Due to the random initialisation, this trajectory is likely to still contain sudden changes in adatom position that act as a barrier to further optimisation. The application of Gaussian smoothing (standard deviation = 1 time

step) to the adatom position over time supresses these sudden changes at the cost of lowering the averaged correlation score. Away from the previous local maximum, the system now has the potential to re-optimise to an improved locally optimised solution. If it cannot improve, the system instead returns to the previous local maximum. This re-optimisation process is repeated until the system cannot, after 2 attempts, improve upon the local maximum found. An illustrative example of the average correlation during optimisation is shown in figure 6.22a. It should be noted that the averaged Spearman correlation here is a highly non-linear score function with greater improvements needed for a given increase in score as it approaches the maximum of 1.

The five independently optimised solutions provide final averaged correlations ranging from 0.952 to 0.971. As these solutions are similar (Fig 6.22b), they represent closely spaced local maxima in the parameter space and strongly suggest the existence of a nearby global maximum. The lowest scoring trajectory (0.952) is noticeably less similar to the other four then they are to each other. This trajectory is therefore an outlier, further justifying the independent optimisation of multiple trajectories. Without a full parameter sweep, it is not possible to be certain if we have found the globally maximising solution or if a small (but non-continuous) alteration may still lead to a small improvement. A genetic algorithm is a possible method through which the independently optimised trajectories could be combined to efficiently search further for a global maximum[138], although this is not attempted here. Note that ϕ is the noisiest coordinate that varies the most between trajectories, representative of this coordinate's generally softer energy landscape and correspondingly weaker influence on the vibrational mode energies.

6.9.3 Projecting the Adatom Trajectory onto the AuNP Facet

Currently, the optimised adatom trajectories are represented in a reference frame relative to the NC-BPT N atom. To instead move to a reference frame more representative of the NPoM gap, we instead fix the bottom of the NC-BPT molecule by fixing the lower sulphur-bound gold atom at the origin and fixing the plane defined by this lower Au-S-C junction in orientation. Considering the optimised solutions in order of increasing averaged correlation, the

trajectories in this frame become increasing well confined to linear planes (Fig. 6.23a,b, ±0.17 Å deviation from plane for maximum correlation). Projected into these planes, the trajectories generate two clusters of adatom positions that become increasingly resolved with correlation which approximately represent early and late times. This can be quantified by clustering the adatom positions using a Gaussian Mixture Model with either 1 or 2 clusters. These two descriptions are compared using the Bayesian Information Criterion (BIC, section 3.9) which, for all but the lowest correlation trajectory, describes two clusters as the better description (Fig 6.23c). A cluster resolution figure-of-merit, defined by the separation in cluster centres divided by the cluster widths along the line between them, increases with averaged correlation (Fig. 6.23d). This suggests that the convergent global solution is a trajectory confined close to a flat plane and containing an early-time and late-time cluster of adatom positons.

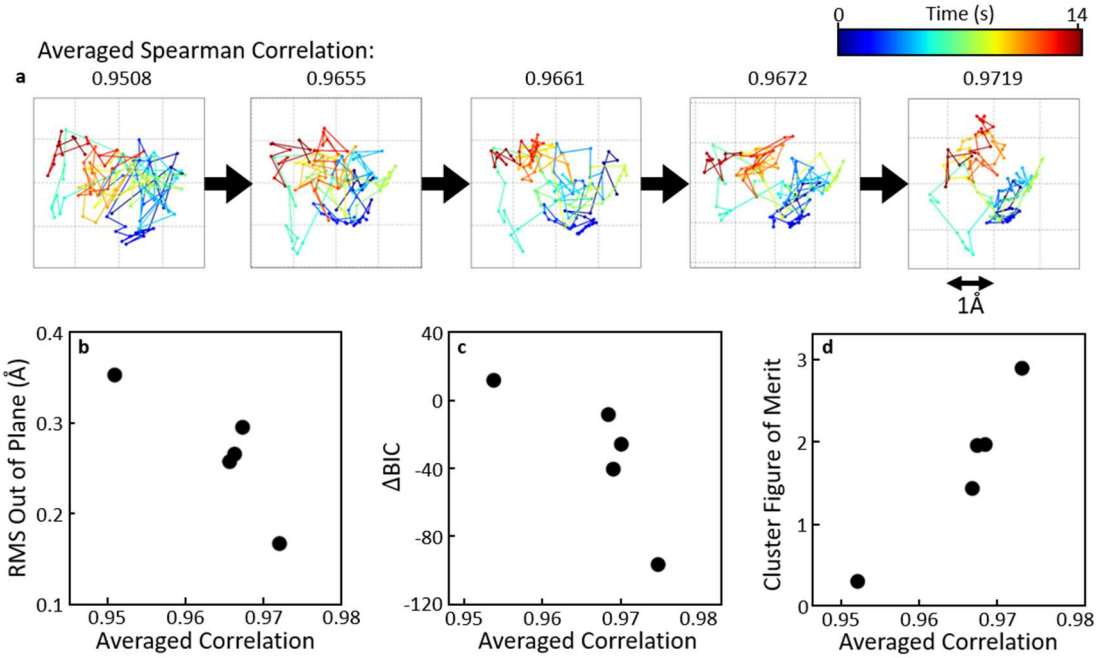

Figure 6.23 | 2D Trajectory Projection. a, Each independently optimised trajectory projected onto 2D planes in order of increasing averaged Spearman correlation **b,** Root Mean Square (RMS) deviation from the plane with increasing averaged correlation. **c,** Difference in Bayesian Information Criterion (BIC) describing the 2D trajectory positions using a 2-part Gaussian Mixture Model rather than a single Gaussian cluster. ΔBIC < 0 denotes two clusters as the better description **d,** Figure of merit for cluster resolution given by the cluster separation divided by the sum of the cluster widths.

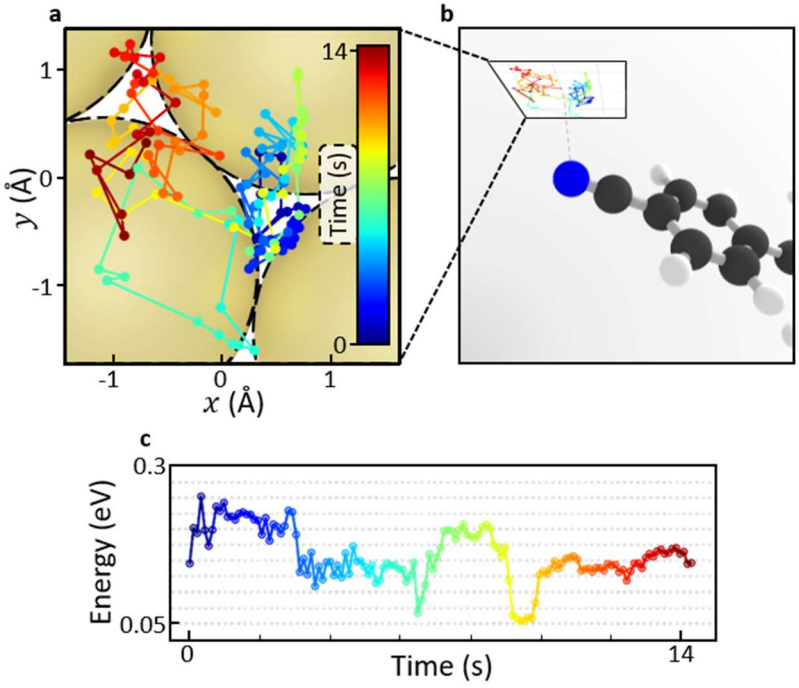

Figure 6.24 | Adatom Trajectory on the AuNP Facet. a, Trajectory with highest averaged correlation projected onto a plane with the {1,1,1} FCC lattice of the underlying nanoparticle facet added so that the trajectory clusters overlay interstitial sites. **b,** The positions of this plane relative to the NC-BPT molecule in 3D space. **c,** DFT energy along adatom trajectory**.**

We will now only consider the maximally optimised trajectory found here (averaged correlation 0.972). If the movement of the molecule relative to the bulk gold is assumed negligible compared to the movement of the adatom, the plane of the trajectory can be interpreted as the plane of the nanoparticle facet with the trajectory clusters separated by approximately the 1.7 Å minimum distance between energetically-favourable interstitial sites on a {111} gold surface. This allows the atoms of the nanoparticle facet to be tentatively overlaid over the adatom trajectory (Fig. 6.24a, dashed). Any ignored molecular motion would add additional noise to this trajectory. Note that the trajectory should not be affected by any net nanoparticle motion as this would lead to unseen changes in the SERS from all other molecules in the NPoM gap.

The adatom-molecule interaction, as described by the DFT, relaxes in energy over time (Fig. 6.24c) with transient excitation and relaxation likely due to transfers with hidden (un-modelled) energy reservoirs in the system (such as intermolecular interactions). A discrete drop in energy of 100 meV at 3 s corresponds to when the adatom first leaves the

well of the initial interstitial site. This energy is indeed of the order required for an adatom to move away from an interstitial site (Fig. 6.25).

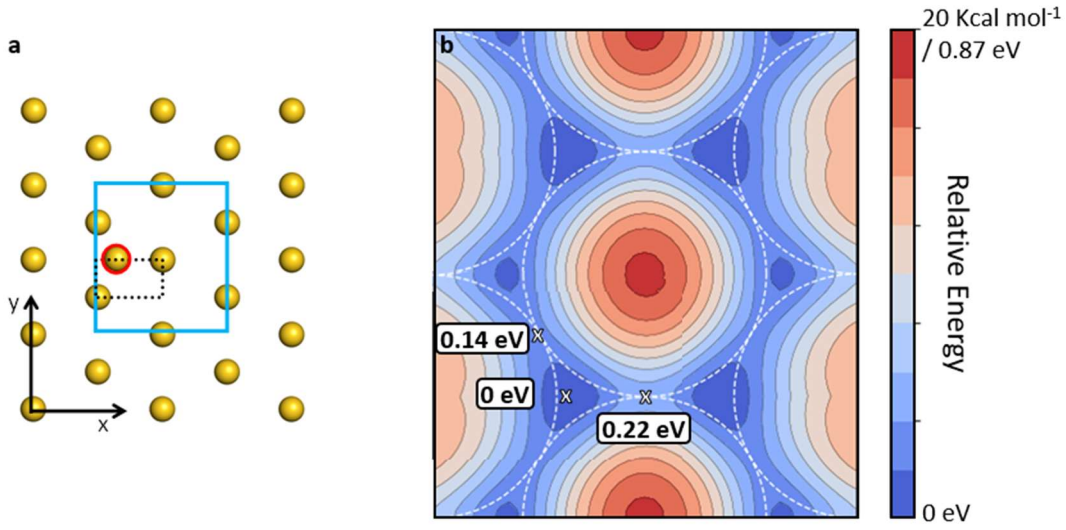

Figure 6.25 | Interstitial Site Energy Barrier. a, Layer of gold atoms modelled using DFT, spaced according to the {1,1,1} facet of a gold crystal. System energy calculated with additional adatom (red outline) scanned in lateral position above the array. Black dotted region is where the adatom is scanned. Blue region is extrapolated area formed from reflecting the calculated region. **b,** Relative energy over the extrapolated area, with energy barriers between interstitial sites labelled. These barriers are not identical as the small array of atoms calculated has broken the system symmetry.

Over short timescales where the bounded nature of the adatom confinement has reduced effect, the adatom dynamics follow anomalous sub-diffusion (Fig. 6.26) with a mean square displacement $\mathrm{MSD} = \Gamma \Delta t^{\alpha}$ (over time window Δt) giving α=0.87±0.03 and Γ=(0.92±0.03) $Å^2 s^{-1}$. This is consistent with thermally diffusive motion hindered by the energy landscape. Crudely ignoring the anomalous nature of this diffusion gives an order of magnitude for the diffusion coefficient $D \sim \Gamma/2 \sim 5\text{x}10^{-21}\ m^2 s^{-1}$ which agrees with previously extracted values for copper adatoms on gold nanocrystals using x-ray diffraction[139].

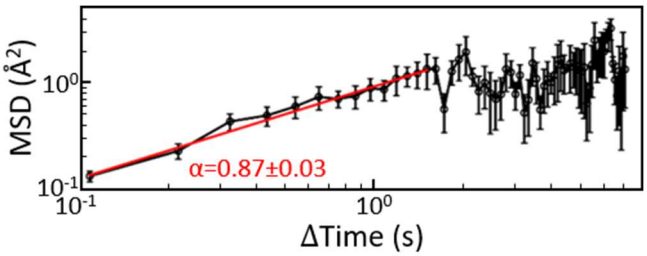

Figure 6.26 | Adatom Diffusion. Average mean square displacement (MSD) of the adatom with varying time window along the 3D trajectory. For smaller time windows, this is well modelled by anomalous diffusion (red line).

Projecting the trajectory instead to a more complex quadratic 2D surface provides surface curvatures of -1.25Å^{-1} and -0.15Å^{-1} in two orthogonal directions (not shown). Despite the significant increase in complexity (this surface is described by 6 parameters increased from 3 for the linear surface), this only reduces the root-mean-square deviation of the trajectory from the surface from ±0.17Å to ±0.11 Å. Given this, the linear plane is taken as a valid projection. This facet plane defines the molecule as tilted 73° from the vertical, in agreement with the energy minimising angle for the thiol bond found in DFT (Fig. 6.27). This is similar to a value of 61° found previously using a X-ray absorption fine structure measurement[140].

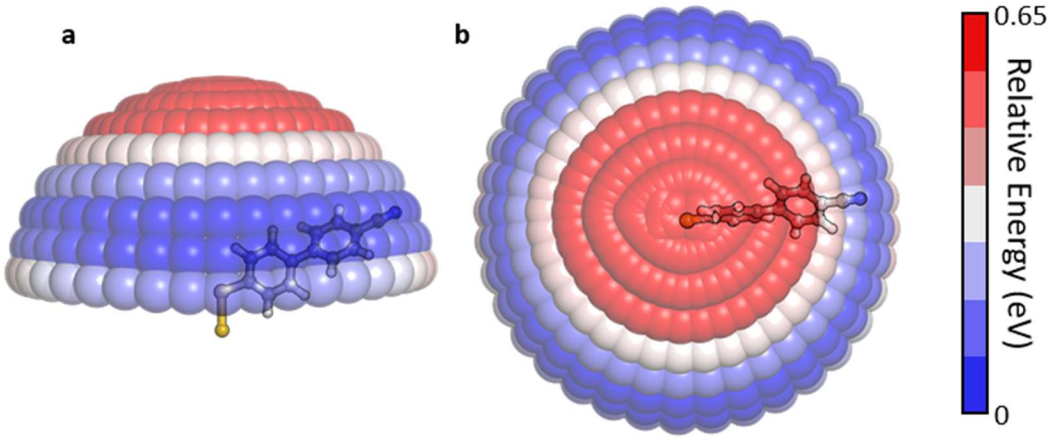

Figure 6.27 | Relative Electronic Energy of Titled Molecule. Relative DFT energy when the NC-BPT molecule is tilted with the S-Au bond defined as vertical, shown **a,** from the side and **b,** from above.

Maximising the averaged Spearman correlation is ambivalent to the relative size of the frequency shifts between theory and experiment. We find that the average difference in the scale of the vibrational perturbations between DFT and experiment varies between vibrational lines. While the shifts in CN peak position are x3 larger in DFT than experiment, the perturbations of the two phenyl vibrational modes at ~1500 cm^{-1} are instead x4-10 smaller (Fig. 6.28). This suggests that while the DFT model captures the trend of the peaks, the absence of the bulk gold surfaces and surrounding molecules likely has an impact on the scale of these perturbations. With changes to the relative adatom-molecule position, the energetically minimising molecular conformation also changes (for example, the phenyl rings change dihedral angle) as electron density is reorganised. The un-modelled interactions are ignored components of the energy landscape that will influence the true energetic minimum and may supress or exacerbate the sensitivity of the vibrational mode energies to the relative adatom position in reality in comparison to the model. For example, it appears here that these un-modelled interactions increase the sensitivity of the phenyl ring vibrations to the adatom position as the scale of the DFT predictions must be increased to match experiment.

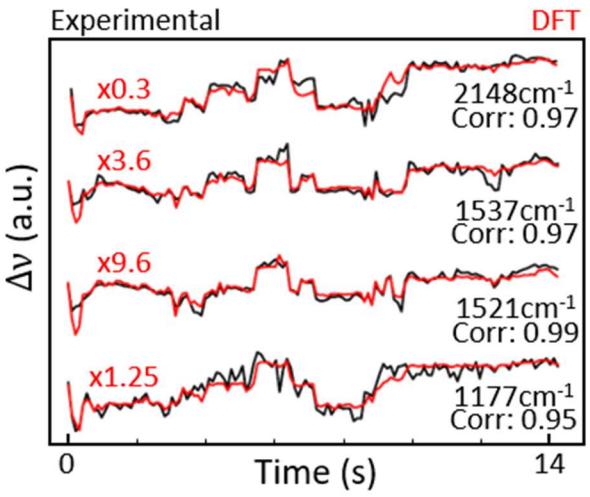

Figure 6.28 | Experimental and DFT Transient Peak Dynamics. Experimental picocavity peak dynamics over time, each shown on an individual scale to emphasise the shapes of the peak trajectories rather than their magnitudes. DFT calculated peak trajectories are overlaid (red). There are scaled and shifted to line up with the experimental lines. Each DFT peak trajectory requires a different scaling factor (red) to match experimental perturbation scale.

A fifth experimental peak, not resolvable for all time, shows predicated dynamics from DFT anti-correlated to what is observed experimentally (Fig. 6.29). If this was strongly correlated, this would be strong validation within the model for the extracted trajectory. If the absolute correlation was near zero, this would have brought into doubt the validity of the extracted trajectory within the model as it would be incapable of reproducing the spectral behaviour of a peaks not used in its optimisation. The observed anti-correlation suggests that the trajectory is correctly capturing the structure of the spectral dynamics for this mode but the negative sign cannot be ignored. It is possible that this inconsistency is the result of incorrect predictions for this mode (and/or others) in the DFT model due to the un-modelled system interactions such as between SAM molecules and between the molecule and the bulk gold surfaces. In any extension to this work using more complex models to capture these interactions, such comparisons between the experimental and predicted peak dynamics for peaks not used in the optimisation process should be prioritised.

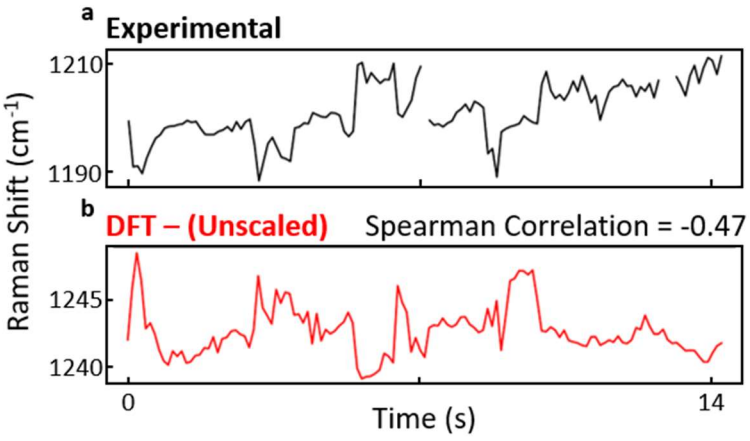

Figure 6.29 | Additional Peak. a, An experimental peak is not resolvable for all time and is not used in the trajectory optimisation. **b,** The predicted DFT dynamics from the optimised adatom trajectory is anti-correlated to the measurement.

6.9.4 Influence of Noise and DFT Hyper-parameters

To probe the robustness of the extracted trajectory, further trajectories are optimised with artificial noise added to each experimental vibrational mode energy. This noise is drawn from a normal distribution $N(\mu = 0, \sigma = 0.5\ \text{cm}^{-1})$. While the final Spearman correlation degrades as expected, the two cluster feature persists (Fig. 6.30).

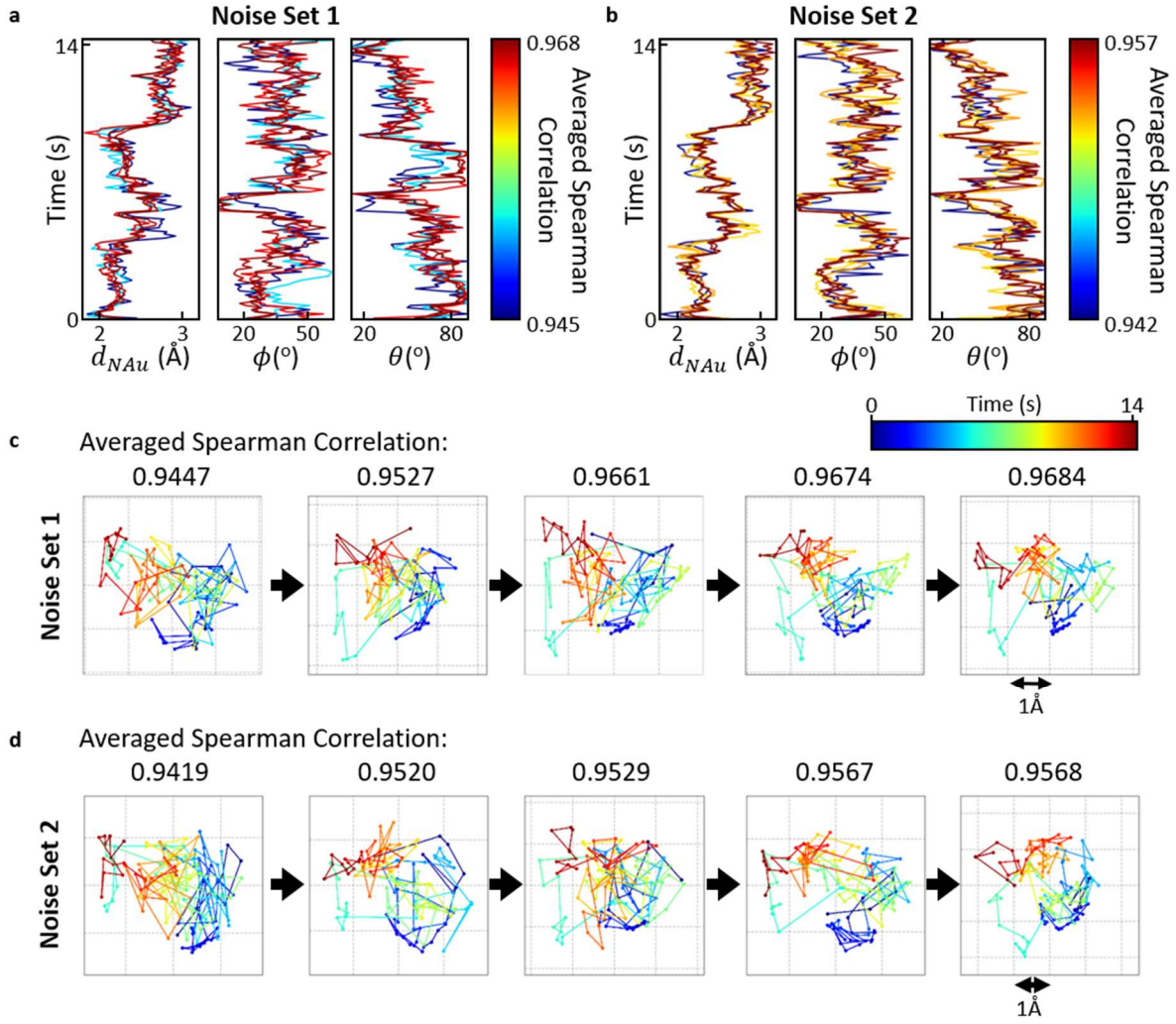

Figure 6.30 | Applying Artificial Noise. a,b, Sets of five optimised adatom trajectories after artificial normally distributed noise (standard deviation = 0.5 cm^{-1}) is added to each experimental peak energy. This is repeated with two independent sets of noise. **c,d,** The trajectories projected onto linear planes.

One of the main advantages discussed for this correlation method is that it is robust to some forms of DFT error. To test this, the entire DFT parameter space is recalculated with changes to the DFT basis set and functional (section 3.8). First, the basis set is changed from def2-TZVP to def2-SVP[126], a smaller basis set providing faster calculations that are nominally less accurate. The more complex def2-QZVP[126] basis set is calculated at the energetically minimising adatom position but shows insignificant changes to the resulting DFT spectrum (not shown) that do not justify the computational expense of a full parameter space re-calculation. Second, the DFT functional is swapped from B3LYP to the B3PW91-D3BJ[91] hybrid and the M06-L-D3[141] meta-GGA functionals. These alter the vibrational frequencies more than the change in basis set and the M06-L-D3 functional increases computation times an order of magnitude in this case. None of these DFT alterations lead to sudden significant changes in the forms of optimised adatom trajectories (Fig. 6.31).

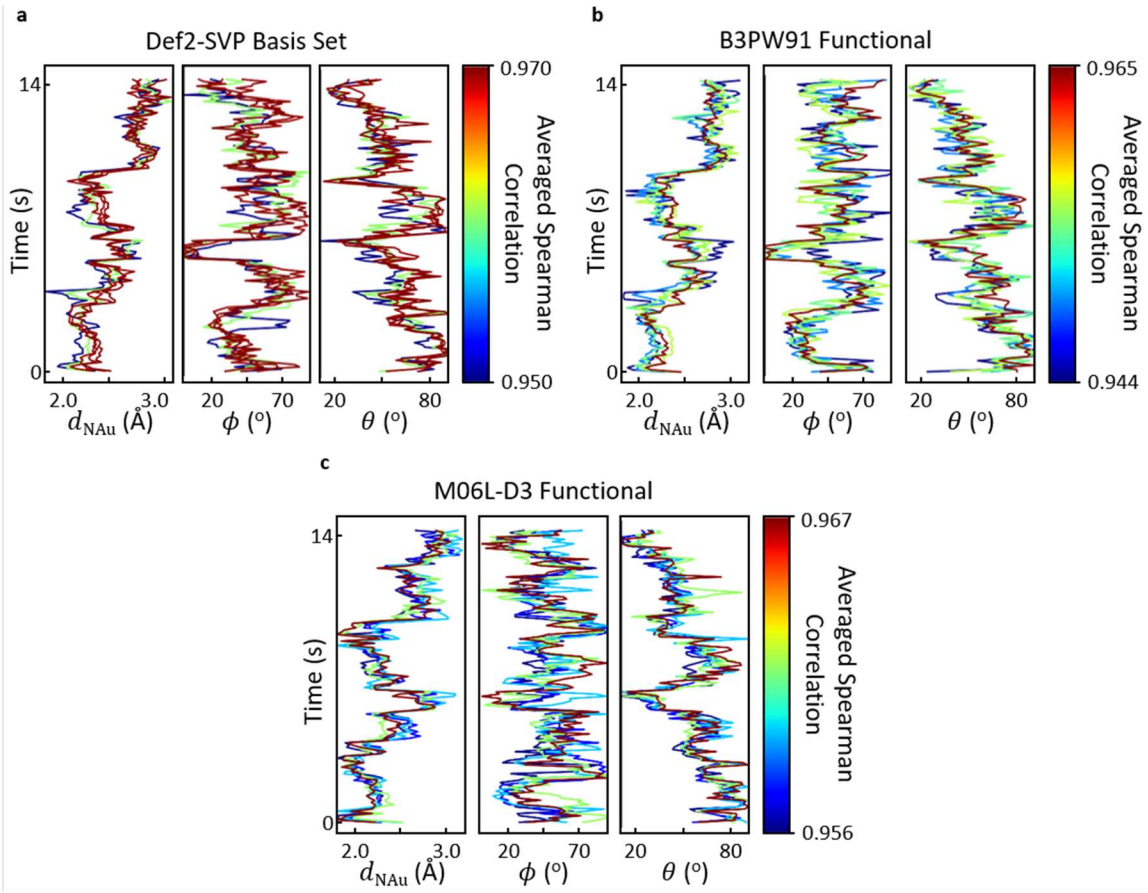

Figure 6.31 | Altering DFT Hyper-parameters. Sets of five optimised adatom trajectories where the DFT calculations are repeated while changing **a,** the basis set to def2-SVP or the hybrid exchange correlation functional to **b,** B3PW91 **c,** MO6L-D3.

6.9.5 Assignment of Vibrational Peaks to DFT

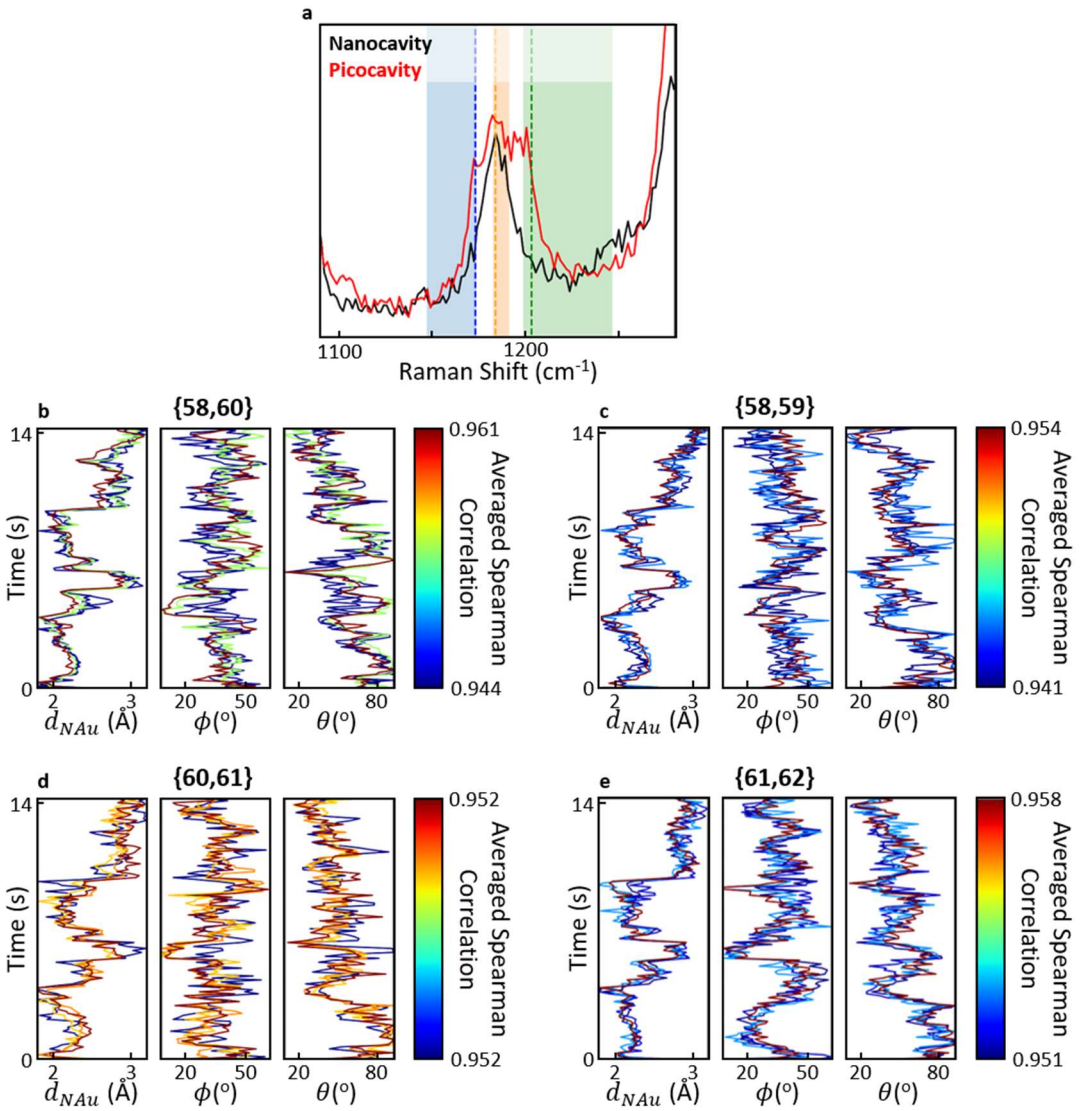

Figure 6.32 | DFT Mode Assignments. a, Experimental nanocavity and picocavity spectra near 1200 cm^{-1}. A single peak is replaced by a triplet of peaks in the picocavity case. Scaling DFT vibrational energies by 0.971 places a triplet of modes in this region. Dashed lines indicate DFT nanocavity mode energies. Shaded regions indicate the range of perturbed energies available within the picocavity DFT dataset. **b,** Set of five adatom trajectories where the transient modes at 1521 cm^{-1} and 1537 cm^{-1} are reassigned to DFT modes 58 and 60 (zero indexing the modes in order of increasing nanocavity energy). This is repeated using indexes **c,** 58 and 59, **d,** 60 and 61 and **e,** 61 and 62.

Here, we will discuss how the experimental picocavity SERS peaks were assigned to DFT vibrational modes which is essential to defining the resulting adatom trajectory discussed. The four picocavity peaks have average experimental energies of 1177 cm^{-1}, 1521 cm^{-1}, 1537 cm^{-1} and 2148 cm^{-1}. As there are no other vibrational modes in the ∼2000 cm^{-1} region, the 2148 cm^{-1} peak can be unambiguously assigned to the CN vibrational mode. During the picocavity event, an experimental nanocavity SERS peak at 1184 cm^{-1} becomes three closely spaced modes (Fig. 6.32a) The lowest energy mode is the 1177 cm^{-1} peak. In the nanocavity (NC-BPT-Au) DFT spectrum, a reasonable scaling factor of ∼x0.971 aligns a close triplet of peaks to this experimental region (Fig. 6.32a). While the central bright mode is not influenced by the adatom in DFT, it is flanked by two dark modes that are more strongly perturbed (Fig. 6.32a, coloured regions). Therefore, the 1177 cm^{-1} mode is assigned to the lowest energy DFT mode of this triplet. The highest energy experimental mode, which is not resolvable for all time, is the additional peak shown in figure 6.29 and is assigned to the higher energy mode of this DFT triplet.

The vibrations at 1521 cm^{-1} and 1537 cm^{-1} exist in a region of the spectrum containing phenyl ring stretch vibrations. Labelling each DFT vibrational mode in order of increasing nanocavity energy (starting with vibration 0), there are 8 such phenyl ring vibrations in this region indexed 55-62 (inclusive) consisting of 4 sets of symmetric/anti-symmetric pairs. Vibrations 61/62 represent the two bright modes in the nanocavity spectrum. Some modes are excluded from being our picocavity modes as they require the DFT vibrational energies to be scaled up (rather than down) to match the experimental range. This would disagree with all other visible vibrational modes which are overestimated in energy by the DFT. With these removed, some ambiguity to peak assignment remains. In the trajectory presented in this chapter, the picocavity modes are assigned to vibrations 59 and 60. These require an approximate scaling of 0.97 to 0.98 to overlap with the region seen in experiment and represent the next pair of modes down in energy from those bright in the nanocavity spectrum. Here, we briefly explore alternative peak assignments to vibrations 58/60, 58/59, 60/61 and 61/62 (Fig. 6.32b-e). The resulting trajectories are similar to those found with our assignment, suggesting some redundancy in the information contained in these phenyl ring vibrations. However, the resulting averaged Spearman correlations are worse and are in some cases only as high as the lowest Spearman correlation found with our assignment. Each of these alternative

assignments still predicts the validation peak as anti-correlated to what is observed experimentally.

6.11 Conclusion

In this chapter, I have explored the dynamic transient SERS modes of the molecule NC-BPT during a picocavity event. In particular, I have focussed on the high energy CN vibrational mode which varies in vibrational energy between transient events by hundreds of wavenumbers. By comparison to a comprehensive DFT model, I have suggested that this perturbation is due to an energetically favourable partial bond between the picocavity and the nitrile group of the molecule. Within this model, the dynamics observed is due to thermally driven sub-angstrom changes in the relative adatom-molecule position. The partial bonding strength tracks the orbital overlap of the adatom and nitrile group and leads to a perturbation of the molecule's electronic structure and changes in bond orders that are highly sensitive to this position. A smaller preliminary model with the molecule BPT suggests that these adatom interactions may be prevalent in systems without the clear spectral signature that is provided by the NC-BPT nitrile group. Due to the prevalence of metal atom – molecule interactions in catalytic chemistry[121] and molecular electronics[5], the possibility of characterising these interactions optically using this method is intriguing. However, a considerable amount of development would have to be accomplished before this preliminary work could be used as a tool for characterisation. It is interesting to recontextualise the transient SERS observed in Chapter 4 in context of this work. There, transient lines seemingly related to vibrations involving the high energy C≡C bond of a single molecule showed dynamic behaviour over multi-second timescales that was qualitatively very similar to that presented in this chapter. While I would not recommend that that system be studied in DFT in this way due to the complicating influence of the DNAo macromolecule present, I would suggest that the results observed there were due in part to a dynamic chemical interaction with the picocavity.

The DFT model presented in this chapter simplifies the experimental system by neglecting the presence of surrounding molecules in the SAM and the nearby bulk gold surfaces. While I

expect this model to mostly capture the trends of the vibrational mode energy perturbations due to the picocavity, it does not accurately predict exact vibrational energies. By instead utilising the information contained within the dynamics of transient lines over time, rather than their absolute energies, a picocavity event is inverted to provide a 3D trajectory for the adatom position relative to the molecule. This trajectory appears to trace out the movement of the adatom from one energetically favourable interstitial site on the nanoparticle facet to another. This suggests that the adatom is fully protruded from the bulk gold and free to move upon the gold surface. The local gold structure around a picocavity protrusion is unclear, and I would not expect a picocavity to be represented by a fully protruded adatom on the gold surface in general. This is explored further in Chapter 7 where the optical properties of a picocavity seems to suggest that they involve, on average, a gold atom 'semi-protruded' from the bulk metal. Again, this simplifies and ignores the unknown atomic scale structure of the gold surface around the protrusion. The picocavity event converted to an adatom trajectory here is likely self-selecting as an adatom free to move on the gold surface would lead to the most dynamic SERS perturbations. This trajectory inversion technique is not generalised as it requires a minimum of 3 (although ideally more) transient SERS modes that can be easily assigned to DFT vibrations and which show dynamic behaviour over the course of the entire picocavity event. For this technique to become more general, the accuracy of the DFT vibrational mode energy predictions will have to be improved such that an adatom position can be inverted from any single spectrum based on the transient mode energies alone.

Further development of this work will benefit greatly from the continued development of Density Functional Theory and High Performance Computing which will allow more complex systems with more accurate interactions to become tractable to model. The further theoretical understanding of SERS in a strong field gradient[80] may allow the ratio of intensities between transient modes to be used as a further source of information on the picocavity position (and orientation of the molecule relative to the NPoM gap) that is not utilised here. An extension of this work could replace the toy NC-BPT molecule with one known to undergo catalytic reactions on a gold surface. This would push this preliminary work closer to a practical application. This would likely require a greater parameter space for the relative picocavity position to be explored in DFT for comparison to experimental measurements as it

is unlikely that it would have such a key signature of the rough adatom position as the perturbed CN mode of NC-BPT.

Chapter 7: Extracting the Spatial Distribution of Picocavities using Multi-Wavelength SERS

7.1 Introduction

In Chapter 5, picocavities within NPoMs using a Self-Assembled Monolayer (SAM) of 4'-cyanobiphenyl-4-thiol (NC-BPT) as the gap spacer were catagorised based on whether they formed from the gold nanoparticle (AuNP) facet or gold mirror surface. The difference in picocavity generation rate between these two surfaces was found to reduce with incident laser power. We considered two general models for the role of light in the formation of picocavities. In a *Thermal Model*, the incident laser drives picocavity generation by heating the system. In an *Optical Model*, light is directly involved in picocavity formation through some undefined mechanism and the effective thermal energy barrier for picocavity generation is lower at regions of higher field intensity. As it was found that the generation asymmetry between the two surfaces decreases with incident laser power within both models, this observation could not be used to distinguish them. A key distinction between these models would be the lateral spatial distribution of picocavity formation within the NPoM gap which could not be accessed in the work presented in Chapter 5. Due to rapid thermal diffusion in gold[142], the Thermal Model would provide a uniform probability of picocavity generation everywhere in the NPoM gap although this generation probability could feasibly increase near the AuNP facet edge where the average surface gold atom coordination number is reduced. In contrast, an Optical Model increases the picocavity generation rate where field intensities are largest.

Light couples into the NPoM gap by exciting a linear combination of plasmonic modes[29,30]. As the excitation of a given mode is a resonant process, the final spatial profile of optical intensity in the gap (the nanocavity) depends on the wavelength of the incident light (Fig. 7.1a,b). The final enhanced field intensity around a picocavity protrusion depends on the strength of the nanocavity field at its location that is available to enhance. This leads to the hypothesis that transient SERS from the same picocavity protrusion should differ in intensity depending on

incident laser wavelength. Indeed, studies published by N. Lindquist et. al. in 2019 showed that transient SERS excited using 543 nm and 633 nm scattering wavelengths from silver nanoshells (a different plasmonic structure formed from a SiO_2 sphere coated in a silver layer) varied in relative SERS intensity between wavelengths and events[143,144]. This SERS was collected onto a set of photodiodes, allowing the origin of the SERS emission to be super-resolved (and shown to be highly localised as expected from a picocavity event) at the expense of spectral information.

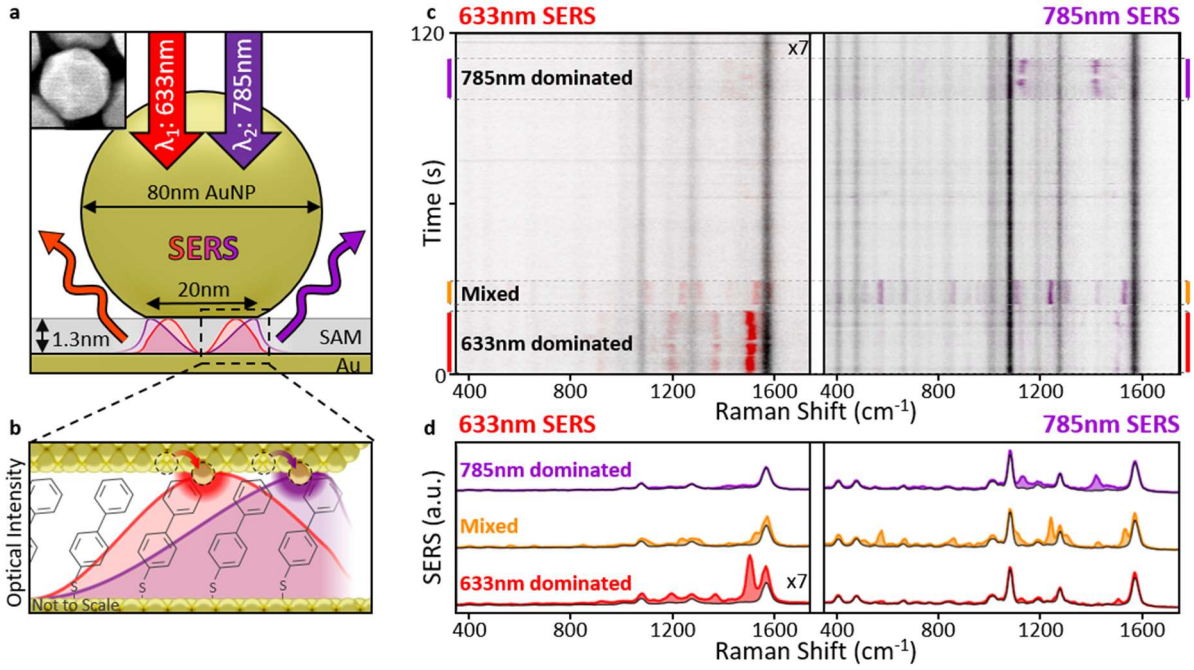

Figure 7.1 | Wavelength-Dependant Picocavity SERS. a, The NPoM structure is modelled in this chapter as a spherical AuNP truncated to create a 20 nm diameter facet. Inset: SEM shows an example of the AuNP facets[†]. **b,** The NPoM gap is defined by a BPT SAM. Near field intensities excited at 633 nm and 785 nm differ in spatial profile (shown for normal incidence from FDTD simulations). **c,d,** NPoM SERS spectra collected simultaneously with 633 nm and 785 nm excitation (100 µW and 300 µW respectively). 633 nm SERS multiplied x7 to make visible. Transient SERS scattering (coloured) differs in relative intensity and can be dominant (relative to the persistent nanocavity SERS) in the 633 nm or 785 nm spectra (corrected for experimental relative collection efficiency).

[†] SEM provided by Bart de Nijs of University of Cambridge

In this chapter, picocavity SERS is collected from NPoM nanostructures formed from 80 nm diameter gold nanoparticles (AuNPs) and the bi-phenyl-4-thiol (BPT) spacer (section 3.2) using two excitation wavelengths (2-λ SERS)*. Using 633 nm and 785 nm co-polarised incident lasers provides enough spectral separation for the resulting SERS spectra to not overlap with one another. These measurements use experimental set up D (section 3.5). As expected, transient SERS peaks are observed at the same energies in both sets of spectra. However, the relative transient SERS intensity (normalised by the persistent nanocavity SERS) varies between events even from the same NPoM structure. An example of this is shown in figure 7.1c,d, showing three sets of picocavity events that are dominant (much brighter) in either 633 nm SERS, 785 nm SERS or mixed between both wavelengths. As this intensity ratio results from the difference in the spatial field profiles for the two wavelengths, this is a probe of the picocavity adatom location with the NPoM gap.

In this chapter, I will describe methods for robustly separating scans of consecutive SERS spectra into background, persistent nanocavity and transient components. This will account for dynamic changes in broadband background signal and for wavenumber dependant drift in the persistent SERS intensities. This is used to extract the relative picocavity intensity ratio in 2-λ SERS for >2000 events. An analytical model is presented for the expected distribution of this ratio which combines nanocavity field profiles from Finite Difference Time Domain (FDTD) simulations with a probability density function (PDF) describing the picocavity formation mechanism (Thermal or Optical Model). Comparing PDF models, the data does not support the Thermal Model. Instead, the data is well described by higher rates of picocavity formation at regions of greater optical field intensity. This is useful information for the future development of picocavity generation models.

The data within this chapter also suggests that the picocavities enhance the local field at 633 nm more than at 785 nm. This is corroborated by FDTD simulations and is experimental evidence supporting the recent work of Wu et. al.[77] predicting that picocavity enhancement displays resonant behaviour in contrast to the spectrally uniform ‘lightening rod’ enhancement considered previously.

* The experimental data presented in this chapter is collected by Bart de Nijs of University of Cambridge. All analysis, model development and model optimisation carried out by me.

Throughout this chapter, the AuNP is modelled as an 80 nm diameter sphere truncated to reveal a 20 nm diameter circular facet (Fig. 7.1a). This is arguably the simplest model of a faceted nanoparticle that averages over the range of AuNP crystal shapes forming the NPoM structure[29–31] (section 2.5.3). The models presented in this chapter are extendable to more complex AuNP representations.

This work contained within this chapter is accepted for publication at ACS Photonics.

7.2 Finite Difference Time Domain Simulations

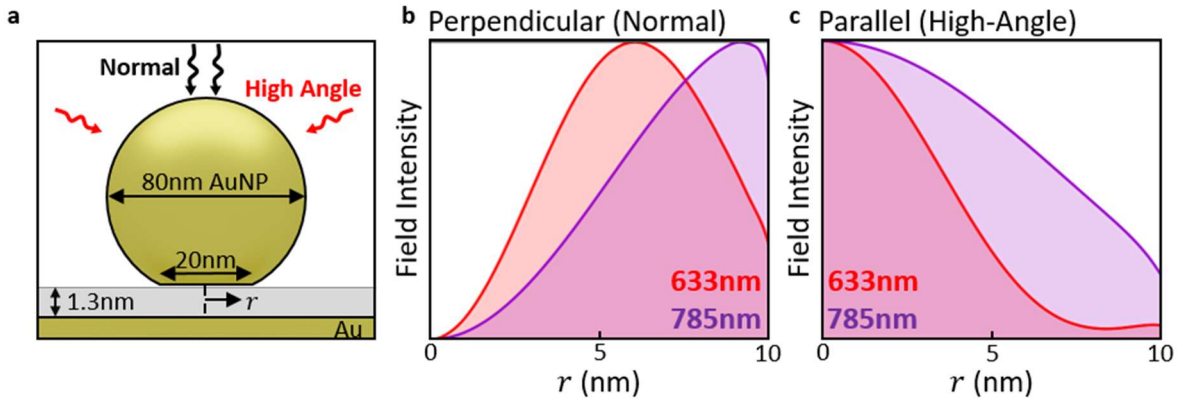

Figure 7.2 | FDTD Nanocavity Field. a, Normalised NPoM gap optical intensity distributions are calculated according to radial distance (r) from the AuNP facet centre. 633 nm and 785 nm fields are calculated under illumination **a,** perpendicular and **b,** parallel to the NPoM gap representing possible perpendicular and high angle experimental NPoM illumination. These are shown here normalised to the maximum field intensity.

The near field optical response of the NPoM system with and without an atomic scale protrusion is modelled using FDTD simulations* (section 3.7). The truncated spherical AuNP is separated from the gold mirror using a 1.3 nm dielectric layer of refractive index 1.45 to represent BPT[33]. The permittivity of gold is taken from Johnson and Christy[12]. The discrete FDTD mesh resolution is set to 2 nm, 0.2 nm and 0.02 nm around the AuNP, NPoM gap and

* FDTD simulations in this chapter are carried out by Rohit Chikkaraddy of University of Cambridge.

picocavity protrusion region respectively. The NPoM is illuminated with a broadband plane wave with direction perpendicular or parallel to the NPoM gap to represent possible normal or high angle incident light in experiment (Fig. 7.2). Which of these illumination regimes better describes the experimental measurements in this chapter is discussed in section 7.6.1. Due to the symmetry of the system, the nanocavity field profile (i.e. in the absence of the protrusion) separates into independent dependences on the distance from the facet centre (r) and the polar angle on the facet. The polar angle dependence is set by the geometry and is not wavelength dependant, so is not discussed here. The resulting field profiles show field minima or maxima at the facet centre for perpendicular or high angle illumination respectively but both results show significant differences in the spatial profiles at the two wavelengths (Fig. 7.2)

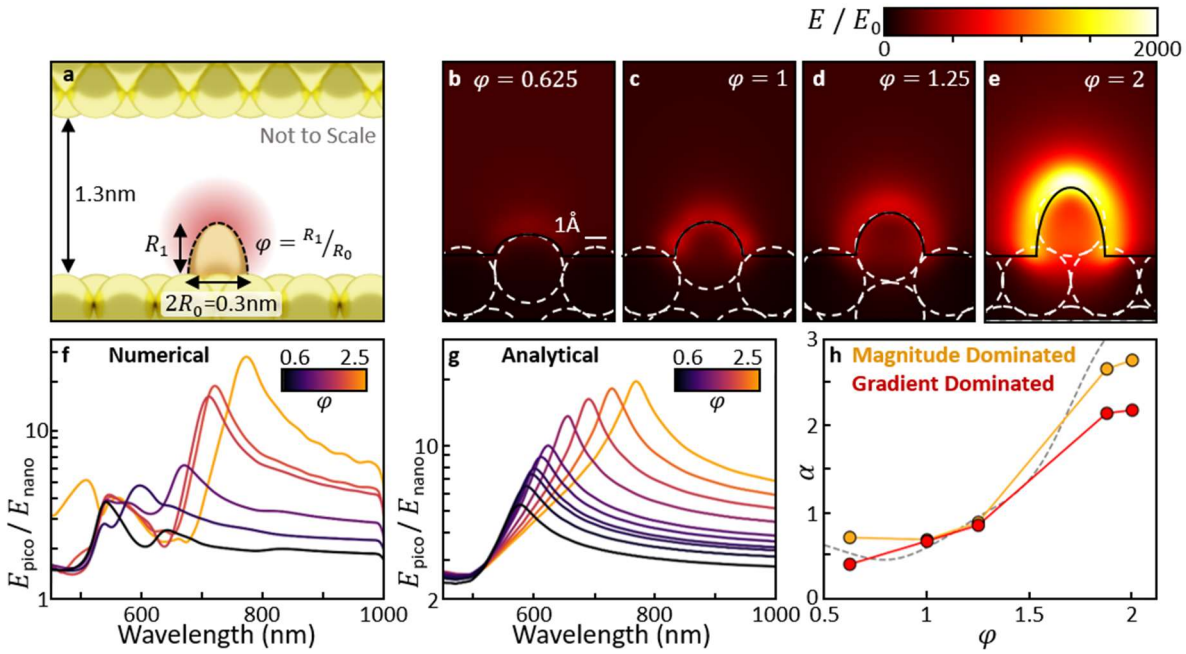

Figure 7.3 | FDTD Picocavity Simulations. a, The picocavity is modelled as a half-ellipsoid protruding from the mirror. **b-e,** Near field with ellipsoid aspect ratio (φ) normalised to field strength E_0 incident on the NPoM. Each map is shown at the wavelength of maximum field intensity. **f,** The picocavity enhanced field, normalised by the nanocavity field, with varying illumination wavelength. **g,** Analytic model of picocavity resonance using the quasi-static response of an ellipsoid in a uniform field. **h,** Ratio of effective field enhancement between 785 nm and 633 nm (α) extracted at a point 0.05 nm above the protrusion tip in FDTD in the limits of field magnitude or field gradient dominated picocavity SERS. Dashed line is analytical approximation to magnitude limit.

The picocavity protrusion is modelled using an additional half-ellipsoid protruding from the mirror below the nanoparticle centre, fixed in radius along both axes parallel to the mirror at R_0 = 0.16 nm (the size of an Au atom). The perpendicular radius R_1 is tuned to represent varying protrusions of the gold atom from the bulk gold (Fig. 7.3a). This is parameterised by the ratio $\varphi = R_1 / R_0$. This geometry is chosen to avoid the complexity of sub-atomic crevices that would be formed if the protrusion was modelled as a sphere translating out of the bulk gold. These would dominate the classical response but are not important in full quantum simulations where there is not an infinitely sharp metal-dielectric boundary around the atom. Such classical simulations of atomic scale features have held up well in a previous comparison to full quantum calculations[75]. The picocavity near-field spectrum is extracted at a point 0.5 Å above the ellipsoid tip and normalised with the nanocavity field. Note that for simulations with and without the protrusion, the simulation mesh and boundary conditions are held constant. Note that calculations with the picocavity instead protruded from the AuNP show the same results (not shown) as the nanocavity field varies very little across the NPoM gap. These calculations are performed using high angle illumination.

As φ increases, the resulting protrusion increases in sharpness (tip curvature $\propto \varphi$ for ellipsoid) and the maximum local near-field enhancement increases accordingly (Fig.7.3b-e). A key result is that the near field picocavity enhancement ($E_{\mathrm{pico}}/E_{\mathrm{nano}}$) displays resonant peaks that tune in both magnitude and wavelength with φ (Fig. 7.3f). While the full response contains multiple features, the largest resonance of the picocavity can be described well by a quasi-static field approximation (Fig. 7.3g). We consider an ellipsoidal metallic particle within a uniform field and half embedded into a metallic space. The polarizability of such an ellipsoid in this classical approximation is given by

$$\alpha_j = V \frac{\varepsilon - \varepsilon_m}{\varepsilon_m + L_s L_j (\varepsilon - \varepsilon_m)} \quad , \quad j = \{x, y, z\} \tag{7.1}$$

where the z Cartesian coordinate points normal to the metallic space interface, ε and ε_m are the permittivity of gold and BPT respectively and V is the ellipsoid volume[145]. L_j are structure parameters capturing the anisotropy the particle which are constrained by $\sum_{j=1}^{3} L_j = 1$. In the special case of a sphere, $L_j = 1/3$. Only α_z is relevant here, for which[146]

$$L_z = \frac{R_1 R_0^2}{2}\int_0^\infty \frac{ds}{(s+R_1^2)\sqrt{(s+R_1^2)(s+R_0^2)^2}}$$

$$= \begin{cases} \dfrac{1-e^2}{e^3}(\tanh^{-1} e - e), & e = \sqrt{1 - {R_0}^2/{R_1}^2} \quad \text{if } R_1 > R_0 \\ \dfrac{1+e^2}{e^3}(e - \tan^{-1} e), & e = \sqrt{{R_1}^2/{R_0}^2 - 1} \quad \text{if } R_1 < R_0. \end{cases} \tag{7.2}$$

L_s is a structure parameter accounting for the connection of the ellipsoid to the polarising metal surface and is given by

$$L_s = 1 - 0.4\frac{(\varepsilon - \varepsilon_m)}{\varepsilon + \varepsilon_m} \tag{7.3}$$

where the constant 0.4 is tuned to match the analytical result to the FDTD simulations (Fig. 7.3g).

The near field enhancement $E_{\text{pico}}(\lambda)$ / $E_{\text{nano}}(\lambda) \equiv \Gamma(\lambda)$ at wavelength λ can be used to estimate the expected ratio of picocavity SERS enhancement at 785 nm to 633 nm. This ratio can be calculated in the limits of negligible and dominant Gradient Raman (section 2.6.3) and is denoted as α^4. By being expressed to the fourth power, α represents an effective ratio of near field enhancement at each wavelength when neglecting Gradient Raman. Note that any chemical interaction between the molecule and adatom can modify SERS scattering cross sections (Chapter 6) and would impact α. This is purposefully neglected here as it is not an optical effect and would differ between molecules although it could be included if the information was available. Although a molecule undergoing SERS scattering is an extended structure, a point dipole approximation is applied here[147]. Spatial gradients are denoted through a dash ie. $E'_{\text{pico}}(\lambda)$. If the picocavity SERS is dominated by the increase in local field strength, the SERS enhancement is given by

$$\text{SERS Enhancement} \propto \Gamma(\lambda)^4$$

$$\alpha = \frac{\Gamma(785\text{nm})}{\Gamma(633\text{nm})}. \tag{7.4}$$

In the opposing limit where Gradient SERS dominates the picocavity response, this effective enhancement is

$$\text{SERS Enhancement} \propto \Gamma(\lambda)^3 \frac{E'_{\text{pico}}(\lambda)}{E_{\text{nano}}(\lambda)} \approx \Gamma(\lambda)^3 \Gamma'(\lambda) \text{ as } E'_{\text{nano}}(\lambda) \approx 0$$

$$\alpha = \left(\frac{\Gamma(785\text{nm})}{\Gamma(633\text{nm})}\right)^{3/4} \left(\frac{\Gamma'(785\text{nm})}{\Gamma'(633\text{nm})}\right)^{1/4} \tag{7.5}$$

which uses the fact that the nanocavity field has negligible gradient over the extent of a molecule.

Both limits follow the same trend based on the field values extracted 0.5 Å above the adatom protrusion in FDTD, being below unity for $\varphi \lesssim 1.25$ and increasing to 2 - 3 for the maximum possible φ = 2 (Fig. 7.3h). A similar curve is also seen in the field magnitude limit of the analytical model.

Note that this simplified FDTD model represents the gold around the picocavity as a homogenous medium and does not capture how it must locally restructure to accommodate the protrusion.

7.3 Dataset Generation for Picocavity 2λ-SERS

To investigate picocavity intensity ratios over many events, 2-λ SERS spectra are collected from 561 NPoMs with SERS spectra taken every 200 ms for a period of two minutes. Laser powers of 100 µW and 300 µW are used for the 633 nm and 785 nm light respectively. This results in a total of >670k spectra considering both scattering wavelengths. These are manually filtered to the 168 NPoMs (30%) displaying clear BPT SERS with picocavity events (providing >200k spectra). As the experimental system does not collect and detect different wavelengths of light with uniform efficiency, the relative intensities of these spectra are corrected by the spectrally-dependent instrument response of the experimental system. This is measured using the calibrated emission from a halogen lamp and a LabSphere Reflectance Standard white scattering reference (Fig. 7.4).

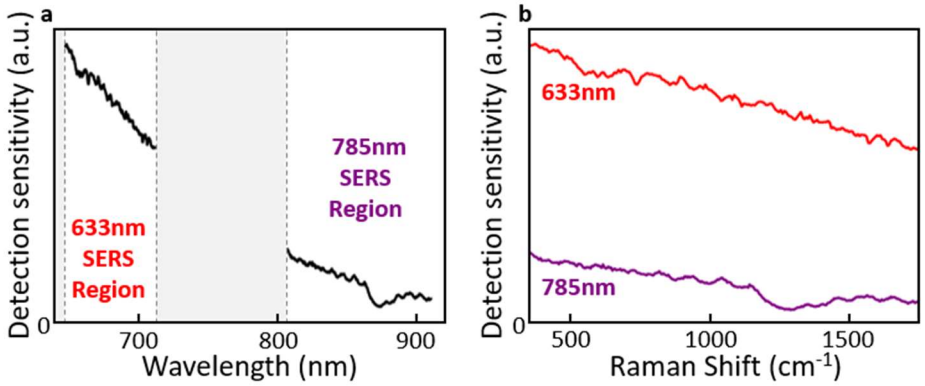

Figure 7.4 | Instrument Response Function. a, Experimentally determined instrument response function (normalised), showing the relative optical efficiency at each wavelength. This contains all optical losses resulting from lenses, optical components such as filters and gratings, and the efficiency of the CCD. **b,** Response function shown vs Raman shift for each scattering wavelength.

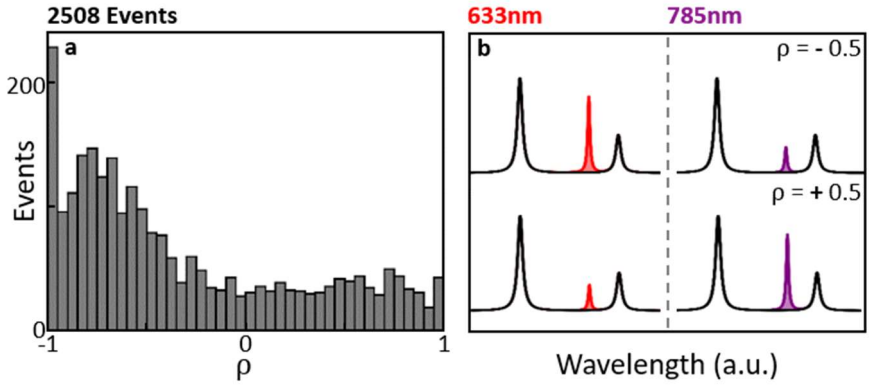

Figure 7.5 | Experimental Transient Scattering Ratios. a, Experimental transient SERS ratio over 2508 detected picocavity events. If the 633 nm : 785 nm scattering ratio is R, $\rho = (1-R)/(1+R)$ bound to the domain {-1,1} **b,** Artificial spectrum demonstrating how the sign of ρ indicates the dominant scattering wavelength.

For each time scan of SERS spectra, the transient SERS is separated from the persistent nanocavity SERS and broadband background. The transient SERS at each scattering wavelength is normalised by the persistent nanocavity SERS intensity, which corrects for all non-picocavity effects dependant on the scattering wavelength such as the different laser powers coupled into the NPoM and the different NPoM out-coupling efficiencies. These

processes are described in detail in section 7.4. After this normalisation, the 633 : 785 nm picocavity SERS ratio (R) is extracted for each event and remapped onto the finite range {-1,1} using the metric $\rho = (1 - R)/(1 + R)$ (Fig. 7.5a). Here, $\rho = 0$ represents equal normalised scattering at both wavelengths while $\rho < 0$ ($\rho > 0$) represents greater scattering at 633 nm (785 nm) respectively (Fig. 7.5b). Experimentally observed values of ρ extend over the entire available range with 72% of events showing dominant 633 nm SERS ($\rho < 0$).

7.4 Methods for Isolating Transient SERS

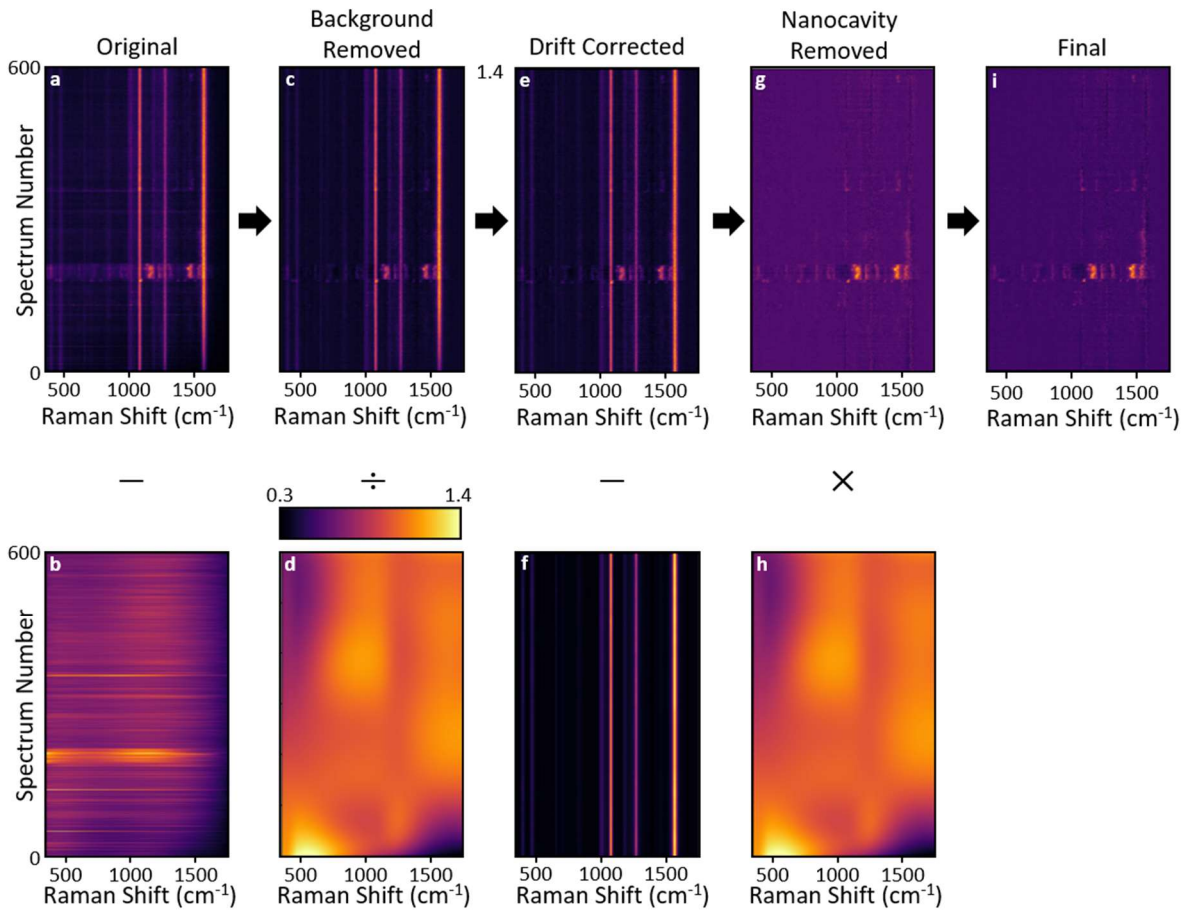

Figure 7.6 | Transient SERS Extraction. High level example of separating transient SERS from background and persistent nanocavity SERS. **a,** A scan of SERS spectra has **b,c** polynomial estimates for the background removed. **d,e,** The scan is divided by a correction map to supress drifts in persistent SERS intensity. **f,g,** This makes it simpler to estimate and remove the persistent nanocavity SERS. **h,i,** The intensity map correction is reversed for the transient SERS.

In order for transient SERS at both 633 nm and 785 nm to be compared, each spectrum must first be robustly decomposed into a background, nanocavity and transient component. Due to the large data set, this needs to be an automated process.

This decomposition is performed as a multistep process which is described in detail over the following sub-sections. This level of detail is provided here as the experimental results of this chapter depend strongly on this decomposition which may be able to be applied to future SERS analysis. Simplified high-level flow diagrams are also provided. First, the broadband background for each spectrum in a scan of consecutive SERS spectra is estimated using a polynomial function of automatically determined order. These backgrounds are removed. Next, any slow changes to the nanocavity SERS intensity over time, due to drifts in the experimental system, are corrected for by dividing through by an automatically determined correction map. The suppression of these intensity drifts allows for the persistent nanocavity SERS spectrum to be identified and isolated. With this nanocavity SERS removed, the remaining transient SERS can be re-multiplied by the correction map to reverse its application. An example of these high level processes is shown in figure 7.6.

While the execution time of these processes vary between analysed scans of SERS spectra depending of the convergence of iterative processes, each scan requires on the order of 30 minutes to complete. However, the processes described here could likely be increased significantly in efficiency by iterating the varying sub-steps of this decomposition (such as estimating the background and nanocavity SERS) concurrently rather than sequentially. The process described in this section requires the scan of SERS spectra to not be dominated by spectra containing transient SERS. While stress-tests to generate failure were not required for this work, I believe, as a qualitative metric, that if the median spectrum in time contains a significant transient to nanocavity SERS intensity ratio than this process risks incorrectly decomposing the spectra.

7.4.1 Polynomial Background Removal

Each SERS spectrum is assumed to be comprised of a broadband background, narrowband SERS and noise. The SERS peaks only exist over certain sections of the spectrum. If these

sections can be masked away then the remaining sum of background and noise can be fit to a smooth polynomial function. Here, the noise is assumed to be drawn from a normal distribution. However, this methodology is extendable to any noise distribution.

This algorithm for background removal iteratively updates the mask of possible SERS peak locations. With a given background estimate in place, a new mask is defined by all points that exceed this background by a given dynamic threshold. This process is iterated until the peak mask and corresponding background estimate converge. The inspiration for a polynomial background estimation that repeatedly updates a peak mask was provided by methods in literature[148] but the resulting algorithm was designed from scratch to remove the need for the user to define the polynomial order and to ensure stability under iteration. This is described in detail here, but the high level process is also shown using the following flow diagram for clarity (Flow Chart 7.1).

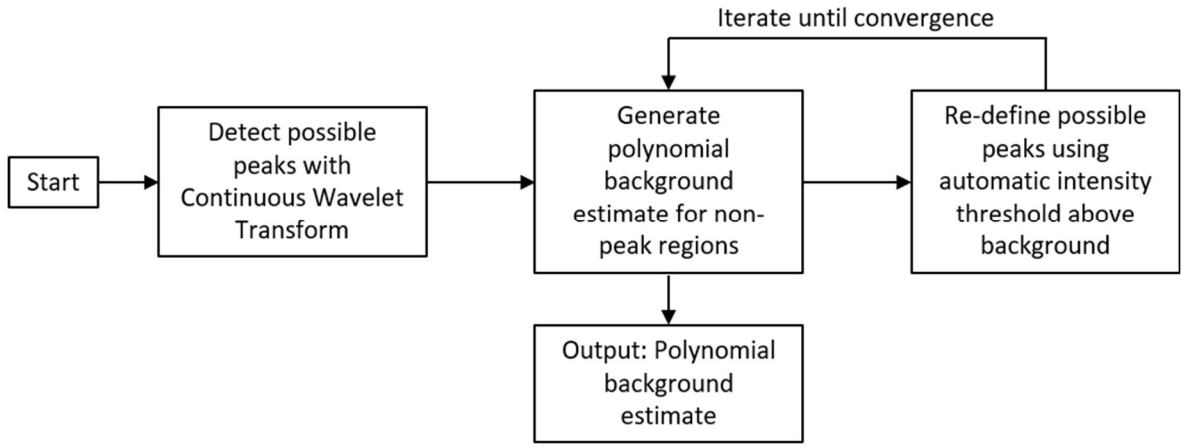

Flow Chart 7.1 | Background Removal. Process for iteratively determining a polynomial estimate for the SERS spectrum background.

The iterative process for updating the background estimate requires two sub-algorithms to be defined. The first of these automatically sets the optimum polynomial order to fit a given set of points. The second compares similar background estimates and quantitatively ranks them to select a preference. Also described here is a method for defining the initial background estimate to be iterated and the process of that iteration.

7.4.1.1 Defining the Polynomial Order

For a given set of points $\{x_i, y_i\}$ to be fit with a polynomial function, the polynomial order N must be defined. The polynomial is denoted as $P(x_i; \theta)$ where θ represents the set of polynomial coefficients. The residuals $R_i = y_i - P(\ x_i; \theta)$ are assumed to be normally distributed. The variance of these residuals is given by $\sigma^2 = \sum_i {R_i}^2 / \sum_i 1$. The Log-Likelihood of this model is

$$L = -\frac{1}{2}\sum_i \left[\ln(2\pi\sigma^2) + \left(\frac{R_i}{\sigma}\right)^2\right]. \tag{7.6}$$

The Bayesian Information criterion (BIC) is a numerical metric for model evaluation, punishing both a poor fit to the data (low L) and a large number of model parameters (section 3.9). When comparing models, a lower BIC can be considered a better description of the data. The polynomial order that minimises this metric is chosen. A key disadvantage of polynomial approximations is a tendency to generate oscillating solutions at higher polynomial orders. This behaviour can be supressed by defining a maximum number of turning points permitted over the domain of $\{x_i\}$ for a polynomial order to be considered. In this work, this is set at 3 for background estimation.

7.4.1.2 Comparing Polynomial Background Estimates

A spectrum and a polynomial background estimate are comprised of discrete elements S_i and P_i respectively. The residual between them is defined as $R_i = S_i - P_i$. Considering the distribution of all R_i, larger positive values will be dominated by SERS peaks. Near and below zero, this distribution should instead represent zero-centred noise for a good background estimate. If the distribution is correctly zero-centred, the standard deviation of this noise is given by the root mean square of the negative values. All R_i above this standard deviation estimate are discarded as possibly contaminated by SERS peaks (Fig. 7.7, dotted line).

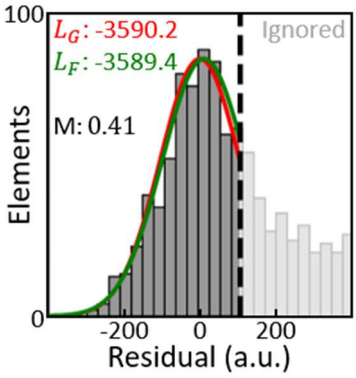

Figure 7.7 | Example Background Metric. Example histogram of residuals for a SERS spectrum with polynomial background estimate removed. Near and below zero, this distribution is near Gaussian. Above a threshold, the distribution is discarded as describing peaks and not noise. Optimising normal distributions to this data with centres fixed at zero and free to optimise provides metric M for how well the noise is represented by a zero-centred Gaussian.

The remaining R_i need to be compared to a zero-centred Gaussian truncated at this same threshold. This could be achieved by optimising a truncated Gaussian model with free centre and standard deviation parameters and consulting the optimised centre position. Instead, to make this method more generalizable to non–Gaussian noise distributions, two models are optimised and compared. The first is a truncated Gaussian fixed to be zero-centred while a second is free to translate. The second model could be increased further in complexity with the addition of a skew term but this is not done here. The log-likelihoods of the zero-centre and free-centre models are defined by L_G and $L_F \geq L_G$ respectively. Note that if the residuals perfect describe a zero-centre Gaussian then $L_F = L_G$. We define a metric

$$M \equiv \frac{2}{1 + e^{L_F - L_S}} - 1, \quad 0 \leq M \leq 1 \tag{7.7}$$

that approaches zero for polynomial backgrounds that provide normally distributed noise residuals. This is a sensitive metric, only significantly below unity in cases where the distribution is well described by a zero-centre Gaussian. When comparing similar estimates, the one with the lowest metric score can be taken (Fig. 7.7).

7.4.1.3 Defining an Initial Background Estimate

For any iterative method, an initial background estimate must be defined. Here, this could be a simple low order polynomial fit to the entire spectrum. A more robust but computationally expensive estimate attempts to ignore possible SERS peaks by detecting them using a continuous wavelet transform (CWT). The Ricker wavelet (Fig. 7.8a) is defined as

$$\varphi(x;\mu,\sigma) \propto \frac{1}{\sigma}\left(1-\left(\frac{x-\mu}{\sigma}\right)^2\right)e^{-\frac{(x-\mu)^2}{2\sigma^2}}. \tag{7.8}$$

As this is related to the second derivative of a Gaussian function, the overlap integral

$$W(\mu,\sigma) = \int_{-\infty}^{\infty} x(t)\ \varphi(t;\mu,\sigma)\,dt \tag{7.9}$$

is large when the function $x(t)$ locally approximates a peak-like structure of scale σ at $t=\mu$. This is the same peak detection technique used in Chapter 5. By integrating over all wavelet centres

$$P(\sigma) = \int \left(\frac{W(\mu,\sigma)}{\sigma}\right)^2 d\mu \tag{7.10}$$

is maximised when σ matches the characteristic scale of peak-like structures in $x(t)$ (Fig. 7.8b). This can be applied to a SERS spectrum to estimate the characteristic peak width and detect possible peak positions as maxima in $W(\mu,\sigma)$ at that width. For efficiency, this can be applied to a scan of spectra rather than each spectrum individually.

To prevent the possible domination of noise in $P(\sigma)$, an initial peak width estimate is defined (here 15 cm^{-1}). The spectra are smoothed using a quadratic order Savitzky-Golay filter of window size 2σ to supress noise while retaining pertinent spectral features. By maximising $P(\sigma)$ on these smoothed spectra, a new estimate for σ is defined. This is repeated until convergence. With this optimised width, possible peak positions are given by positive local maxima of function $W(\mu,\sigma)$ with respect to μ. Regions within 2σ of possible peak positions are masked and the remainder is fit to a polynomial as described in section 7.4.1.1. Possible peaks below a given $W(\mu,\sigma)$ threshold can be discarded so that only truly resolved SERS peaks are masked and ignored. Different thresholds for discarding possible peaks are tested

and the resulting background with the lowest metric M (section 7.4.1.2) is taken as the initial estimate (Fig. 7.8c,e).

7.4.1.4 Iterating the Background Estimate

At each iteration step, the new mask of points representing possible SERS peaks is defined as all points exceeding the current background estimate by a given threshold. This threshold is scanned and the resulting background estimate providing the lowest metric M is taken as the updated background estimate (Fig. 7.8d). This process is iterated until convergence (Fig. 7.8e).

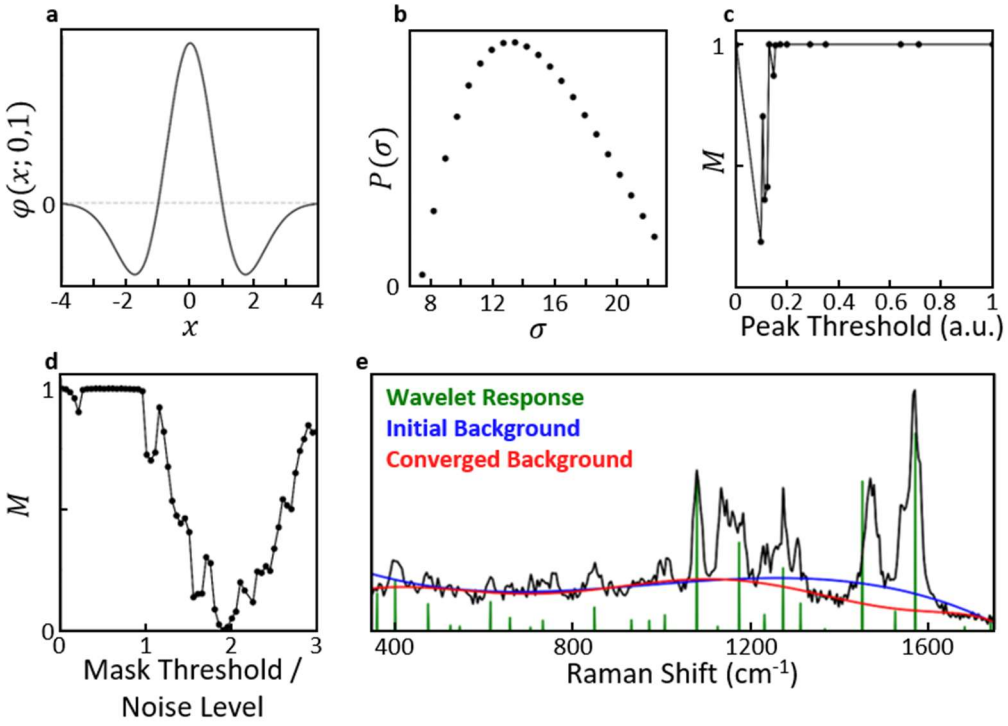

Figure 7.8 | Example Background Estimation. a, The Ricker wavelet. **b,** A CWT applied to a spectrum with varying scale σ scores how well the spectrum is represented by peak like structures of that width. **c,** Possible peaks detected by CWT can be masked away from the initial background estimate. The masking threshold modifies the metric M for the resulting background. The lowest M background is taken. **d,** To iterate a background estimate, all points exceeding the current estimate by a threshold are masked away. This threshold can be scanned to find the estimate that minimises M. **e,** An example SERS spectrum, with possible peaks detected via wavelet analysis (green) defining an initial background estimate (blue). This is iterated to generate the converged estimate (red).

7.4.2 Removing Spectral Intensity Drifts

The persistent SERS peak intensities, with backgrounds removed, can change slowly over time due mostly to drift in the experimental system. Estimation and correction of these changes makes the separation of persistent and transient SERS much simpler. This correction is defined by a map of values by which the scan of spectra is divided. This map does not have to be perfect, as its application will be reversed once the persistent SERS is estimated. The process of generating this map is described in detail here, but the high level process is also shown using the following flow diagram for clarity (Flow Chart 7.2).

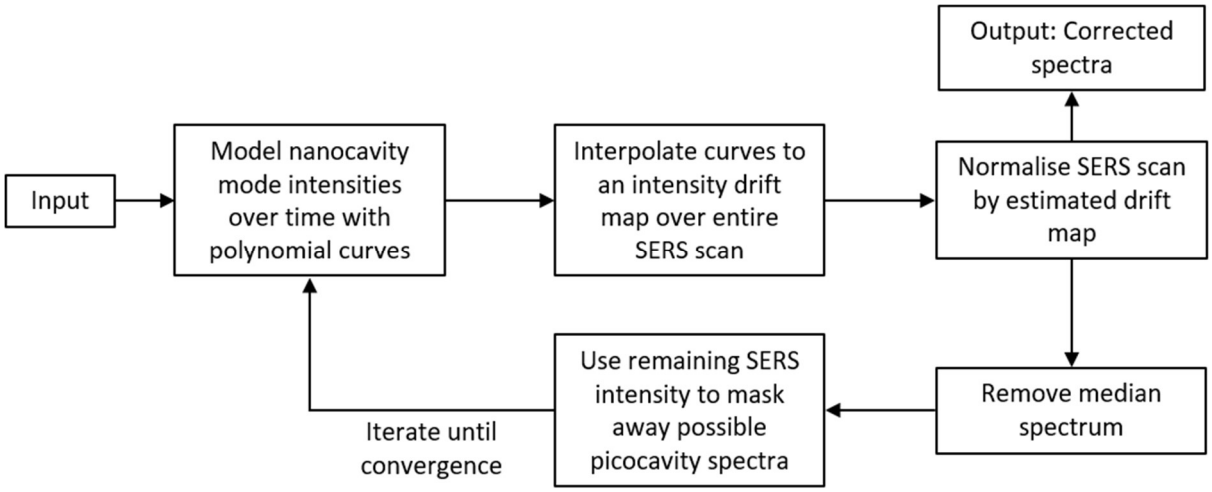

Flow Chart 7.2 | Correcting SERS Drifts. Process for normalising wavenumber dependent SERS intensity drifts while ignoring the influence of transient SERS.

The map is defined by the intensities of known nanocavity peaks over time (approximated with smooth polynomials) and is spectrally interpolated between these known spectral positions using cubic splines. As the SERS at nanocavity peak positions can increase during a picocavity event, such spectra must be masked away with high sensitivity and ignored when defining this map. This mask is initialised with no spectra labelled as possible picocavity spectra and is updated in an iterative process.

During this iterative process, a correction map is generated by fitting the integrated SERS from known nanocavity lines to polynomial curves of some given order while ignoring masked spectra. Different maps are generated depending on the polynomial order that is set. To

select an optimal order without overfitting, a loss for the drift correction quality is defined by comparing the similarity of the corrected (masked) nanocavity spectra to their median. In general, this loss drops with increasing polynomial order. The point of highest curvature in the loss-order curve represents the threshold of diminishing returns and is selected as the polynomial order used. Requiring the same polynomial order for each nanocavity line is done for stability during early iterations where picocavities will be poorly masked away. This correction map is used to normalise away the intensity drifts from the scan of spectra and the median non-masked spectrum is removed.

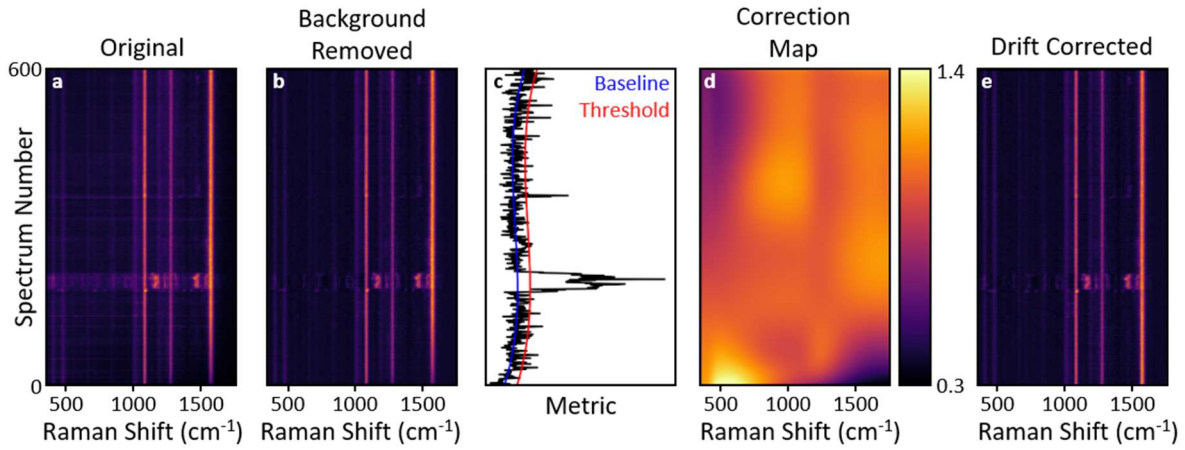

Figure 7.9 | Example Drift Estimation. a An example scan of consecutive SERS spectra. **b,** The SERS backgrounds are estimated and removed. **c,** The total SERS forms a metric that detects digital changes in the scattering intensity while ignoring slow changes in the nanocavity scattering. This labels spectra as possibly containing picocavity scattering. **d,** The intensity of known nanocavity lines, with picocavity spectra masked, form an estimated map of SERS intensity drift. **e,** Dividing by this map flattens the nanocavity SERS response in time.

The total remaining SERS at each point in time is taken as a metric formed from a time dependent baseline that increases digitally during a picocavity event (Fig. 7.9c). This baseline is removed using the background removal technique described above (section 7.4.1). The metric noise level is defined as the root mean square of all negative metric values. A new mask of possible picocavity spectra is defined by this metric passing a defined threshold (set here as twice the noise level, Fig. 7.9c red line). This can lead to a number of false single spectrum picocavity event identifications. As a single spectrum picocavity event is unlikely to

have any significant effect on the resulting correction map, all single spectrum events are removed from the mask. This process is iterated until either the mask converges or a maximum iteration number is reached (here: 10 iterations). With possible transient SERS masked away, the integrated SERS from each nanocavity line over time can be fit using polynomial functions. The polynomial order for each line is now allowed to differ and is set by minimising the BIC (section 3.9). This defines the final correction map (Fig 7.9d).

7.4.3 Nanocavity SERS Removal

Once any drifts in SERS intensity are supressed, the persistent nanocavity SERS is fairly static in time although some smaller time scale variations can remain. To estimate this persistent nanocavity SERS, possible picocavity spectra must again be masked from the scan with a required sensitivity higher than during the definition of the intensity correction map (section 7.4.2). Once the possible picocavity spectra are removed, the remaining spectra are smoothed and linearly interpolated in time to estimate the persistent SERS during the entire scan. The processes of both generating a nanocavity SERS estimate from a given picocavity mask and generating the picocavity mask itself are described in detail here, but the high level processes are also shown using the following flow diagrams for clarity (Flow Charts 7.3, 7.4).

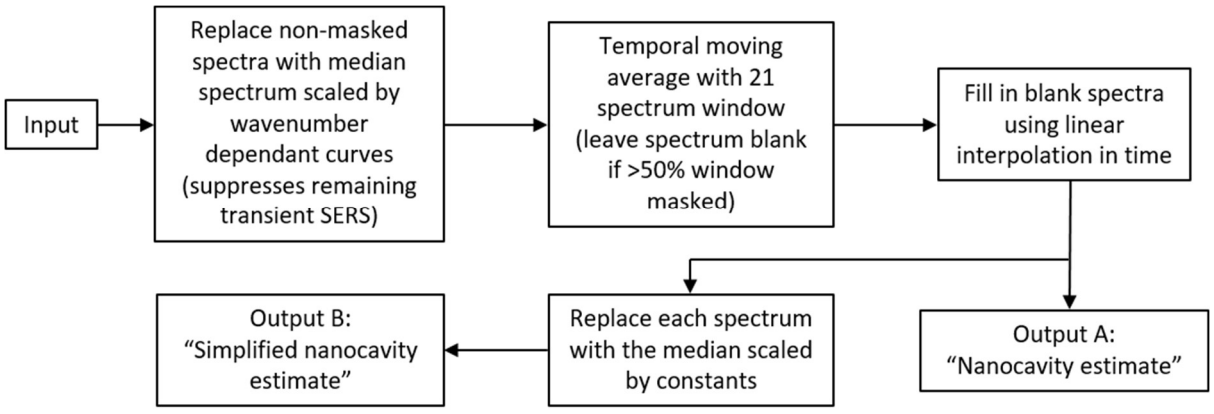

Flow Chart 7.3 | Generating a Nanocavity Estimate from Picocavity Spectrum Mask. Process for generating a nanocavity estimate for a scan of sequential SERS spectra given a mask of which spectra possibly contain transient SERS.

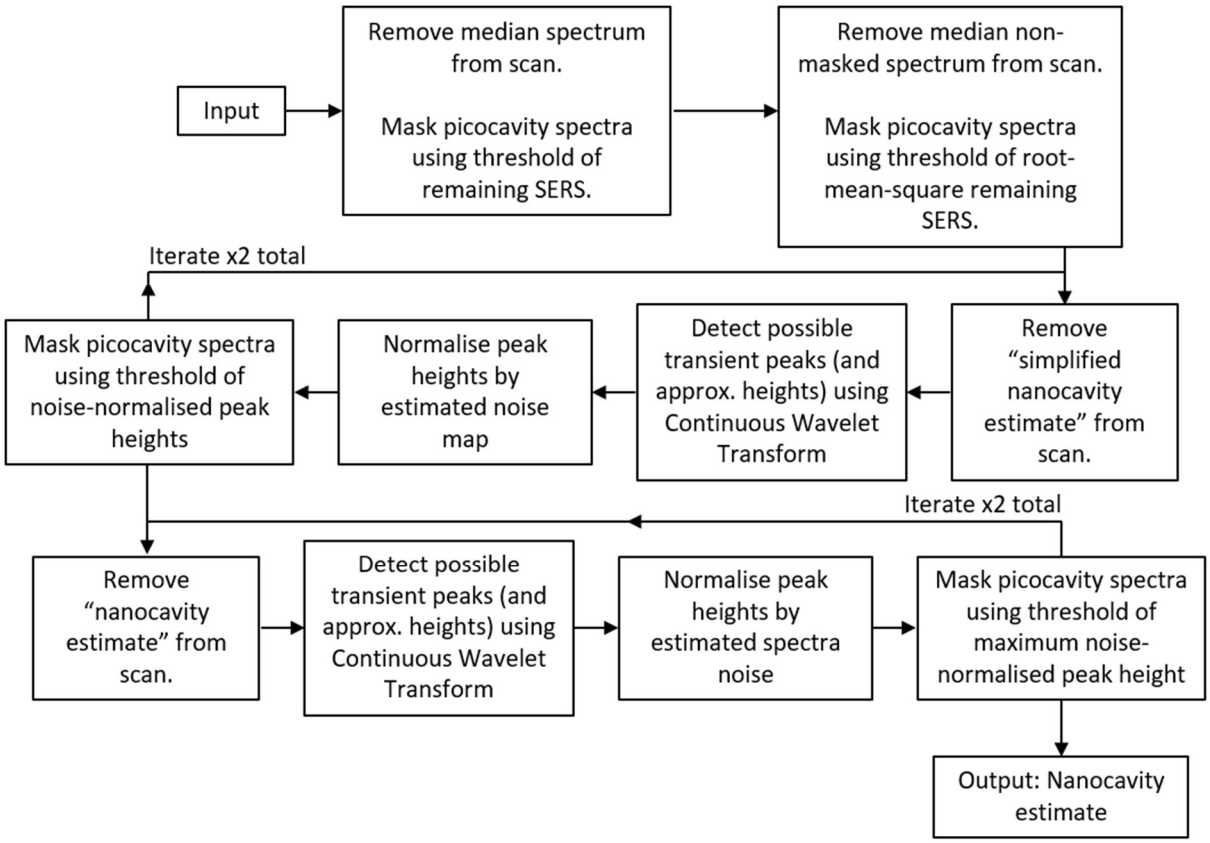

Flow Chart 7.4 | Generating a Nanocavity Estimate while Masking Picocavities. Process for estimating the nanocavity persistent SERS while ignoring spectra possibly containing transient SERS.

7.4.3.1 Generating a Nanocavity SERS Estimate from a Picocavity Mask

We consider that a mask is provided that labels which spectra may contain picocavities. This must be converted into an estimate for the persistent SERS over all time. Again, we note that this persistent SERS should be fairly static in time. First, a moving average is applied to the non-masked spectra to smooth the persistent response before linear interpolation in time is used to fill in any gaps caused by the picocavity mask.

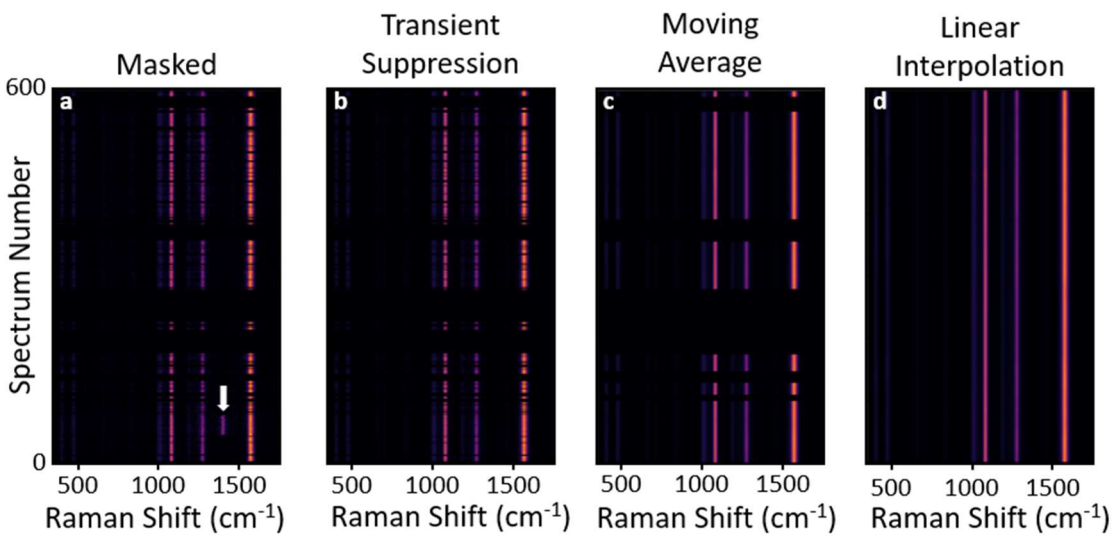

Fig 7.10 | Example Nanocavity Estimation. a Example drift corrected scan of sequential SERS spectra with spectra masked out if possibly containing transient SERS. A synthetic transient peak (white arrow) is added for demonstration. **b,** Each spectrum is replaced by their median multiplied by a spectrally dependant curve, recreating the original spectra while supressing any remaining transient peaks. **c,** A moving average is applied in time with a window size of 21 spectra. If this window is less than 50% filled with spectra than the spectrum is left blank. **d,** Blank spectra are constructed using linear interpolation in time.

If the provided mask happens to miss a weak but long lived picocavity event, this process would incorporate this transient SERS into the nanocavity estimate. This is an unacceptable possibility that we must mitigate. As each nanocavity spectrum should be very similar to their median, they can each be replaced by this median multiplied by a spectrally-dependent intensity scaling curve (a cubic spline with anchor points at known nanocavity SERS peak positions) that recreates the small differences in peak intensities between spectra. This process cannot reproduce any transient peaks that might have been missed by the mask and therefore successfully supresses them. This is shown using an artificially simulated missed transient peak in figure 7.10.

With any possible transient peaks supressed, the moving average is applied. Here, a window size of 21 spectra is used. To prevent averaging an arbitrarily small number of spectra, if >50% of the spectra within an averaging window are masked then the average is not carried out

and that spectrum is left blank (Fig 7.10c). All of these blank spectra are then reconstructed using linear interpolation in time (Fig 7.10d).

Note that if the mask is in an initial and crude state that does not remove transient SERS spectra well, this nanocavity estimate may still contain some undesirable features. To be additionally cautious, a "simplified nanocavity estimate" is also defined where each nanocavity estimate spectrum is replaced with a scaled version of their median.

7.4.3.2 Initialising the Picocavity Mask

The mask of spectra that may contain picocavities is initialised using an intensity threshold. The median spectrum is removed from the scan and the remaining SERS is summed at each point in time to generate a metric. The median removal is mostly done for visualisation purposes here as this only translates the metric a fixed amount. In the example shown in Fig. 7.11, this median is already a good estimate for the nanocavity SERS but this is not true in general. This metric is modelled as drawn from a Gaussian distribution with positive outliers due to picocavity events. For an initial high sensitivity mask, all spectra with a metric above the centre of this Gaussian are labelled as containing a picocavity (Fig. 7.11c).

The median of the non-masked spectra is now much less likely to be meaningfully influenced by picocavities. This is removed from the scan instead (Fig. 7.11d) and the metric is altered to the root mean square (RMS) of the remaining SERS at each point in time. This change in the metric definition is more sensitive to weaker picocavities. A mask threshold is now set at twice the standard deviation above the centre of the Gaussian represented by the metric baseline (Fig. 7.11e). This process could be iterated as many times as required, but is only applied once more here. This mask initialisation is crude but computationally inexpensive.

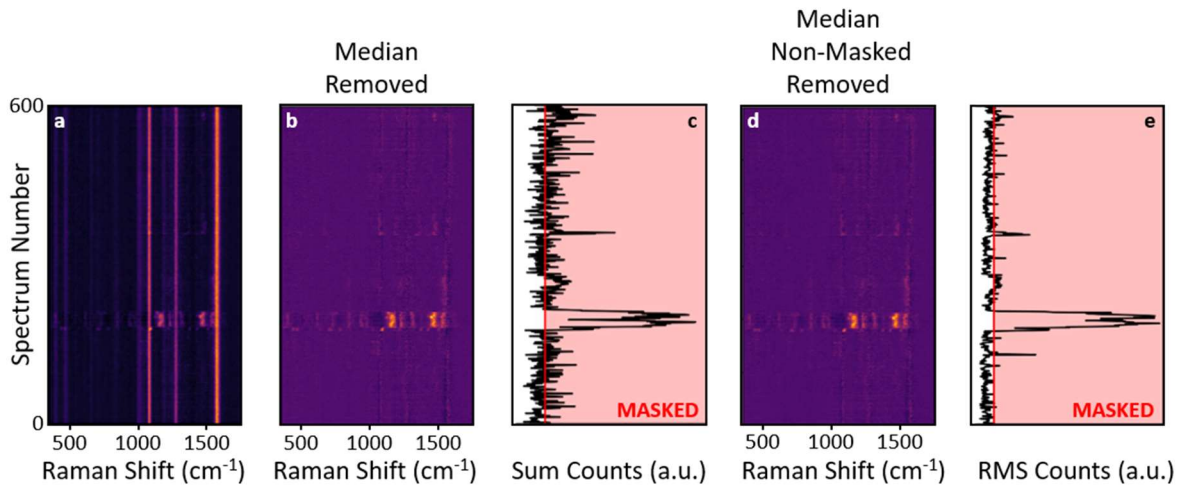

Figure 7.11 | Mask Initialisation. a Example (background removed and intensity drift corrected) scan of sequential SERS spectra. **b,** The median spectrum is removed. **c,** The summed remaining SERS forms a picocavity metric. Any spectrum above the baseline of this metric is masked as a possible picocavity. **d,** The median un-masked spectrum is instead removed from the SERS scan. **e,** The root mean square (RMS) of the remaining SERS forms a picocavity metric. Any spectrum more than two noise levels above the baseline of this metric is masked as a possible picocavity.

7.4.3.3 Iterating the Picocavity Mask

To iterate the mask of possible picocavity spectra, the current nanocavity estimate is removed from the scan (Fig 7.12a). For early iterations, this is the "simplified" estimate rather than the full estimate (section 7.4.3.1). Using a simple intensity threshold to mask possible picocavity spectra risks missing weak events. Instead, we here use a CWT to pick out peaks in the remaining SERS. This uses the Ricker wavelet (Fig. 7.8a) and is applied using the characteristic width of SERS peaks in the nanocavity estimate. This extracts the positions and approximate intensities of possible picocavity peaks.

With estimates for the background, nanocavity and transient components of the scan of SERS spectra and prior knowledge of the instrument response correction and the drift correction map applied, a noise map for the scan of spectra can be defined (Fig. 7.12b). This map assumes that both the photon counts at the detector and the spectrally uniform dark (electronic) counts follow Poisson distributions. The increased noise at the spectral positions

of removed persistent nanocavity peaks makes it more likely to incorrectly assign noise here as possible picocavity peaks. Dividing the estimated heights of all possible detected picocavity peaks (as provided by the CWT) by the noise map corrects for this bias. A picocavity metric is defined as the largest (noise normalised) estimated transient peak height at each point in time. Compared to the sum of transient SERS scattering, this metric is more sensitive to weaker picocavity events (Fig. 7.12c). Again, this metric is modelled as a Gaussian distribution with positive outliers and picocavity events are defined using a threshold one standard deviation above the distribution centre. Note that this high sensitivity threshold also captures many spectra that do not contain picocavities but this is not important here. All single spectrum picocavity events are relabelled as nanocavity spectra.

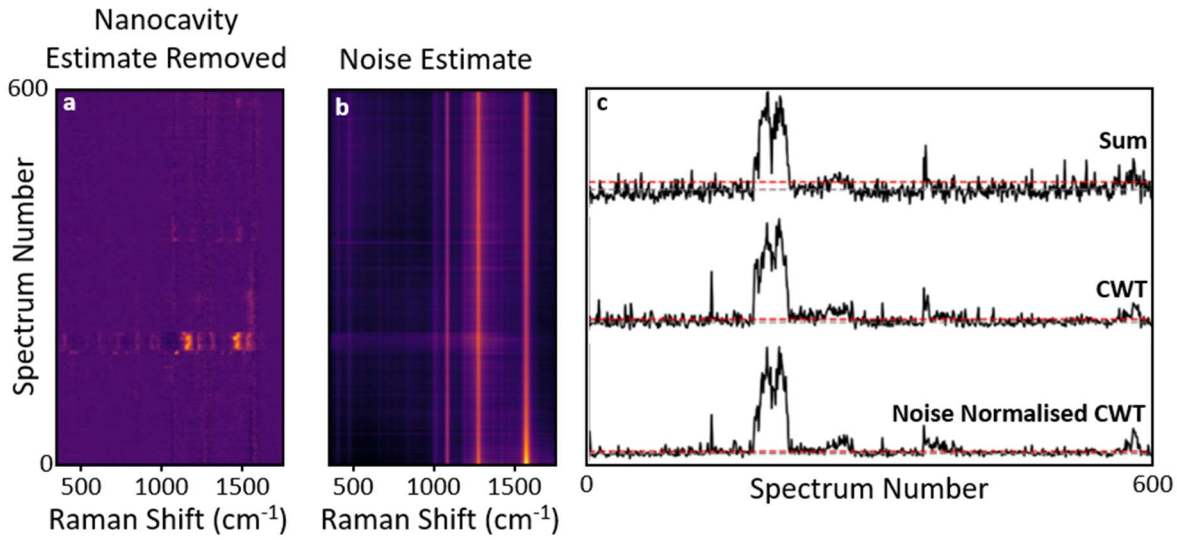

Figure 7.12 | Picocavity Mask Metrics. a, The current nanocavity SERS estimate is removed from a scan of spectra. **b,** An estimate for the scan noise profile in absence of the transient SERS. **c,** A comparison of metrics for defining possible picocavities. These include the sum of remaining SERS, the maximum response after a Continuous Wavelet Transform (CWT), and the maximum CWT response after normalisation by the noise estimate. The Normalised CWT is used here, which is more sensitive to weak events and less sensitive to noise. Red lines indicate one noise level above the metric baseline.

A simple and computationally inexpensive method to check and correct any glaring errors (if they were to arise) in the picocavity mask is to compare the spectra during a picocavity event

with the spectra before and after. If the spectra during the event are more similar to the spectra before and after the event than they are to their own average, this picocavity detection is clearly in error and the mask is updated. This will only catch a certain fraction of nanocavity spectra labelled incorrectly as picocavity events but is very inexpensive to compute as a redundancy backup and can only improve the mask.

Once the picocavity mask is initialised, it is iterated using the "simplified nanocavity estimate" twice. It is iterated twice more using the full nanocavity estimate. Re-multiplying the final result by the correction map (Fig. 7.13c) provides the final estimate for the persistent nanocavity SERS.

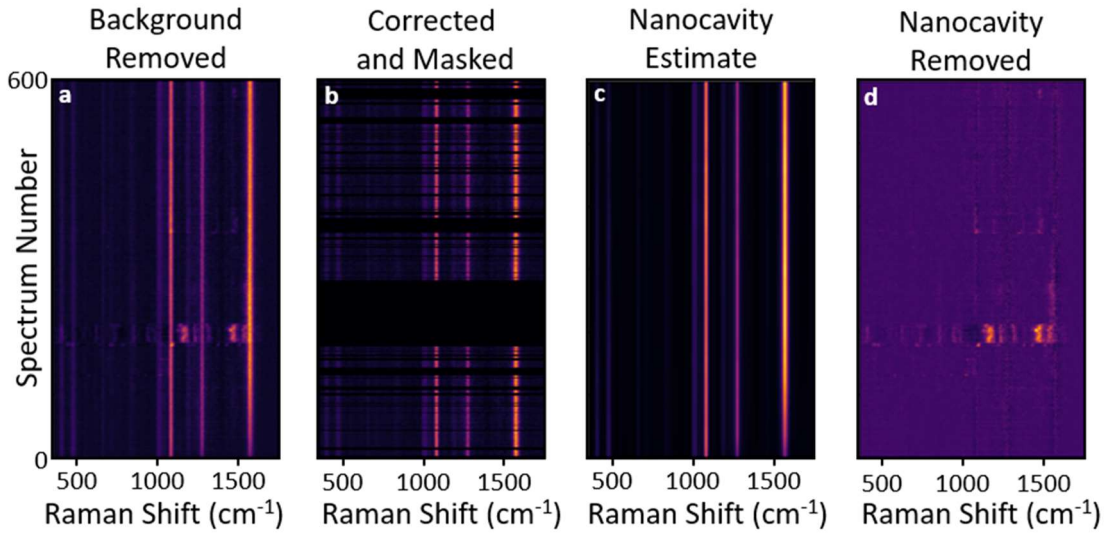

Figure 7.13 | Example Full Nanocavity Estimation. a, An example scan of sequential SERS spectra with background estimates removed. **b,** This is divided by an intensity drift correction map and possible picocavity containing spectra are masked away. **c,** A moving average is used to estimate the nanocavity spectra over time with gaps filled in using linear interpolation. The correction map application is reversed to give the final nanocavity SERS estimate. **d,** This is removed from the scan of spectra leaving only transient SERS.

7.4.4 Defining Picocavity Events

With estimates of the background and persistent nanocavity SERS removed from a scan of spectra, only 'transient scattering' remains. Picocavity events must be defined as sets of consecutive 'transient scattering' spectra. A robust way to achieve this is by attempting to extract the picocavity peaks from the spectra. This is described in detail here, but the high level process is also shown using the following flow diagram (Flow Chart 7.5).

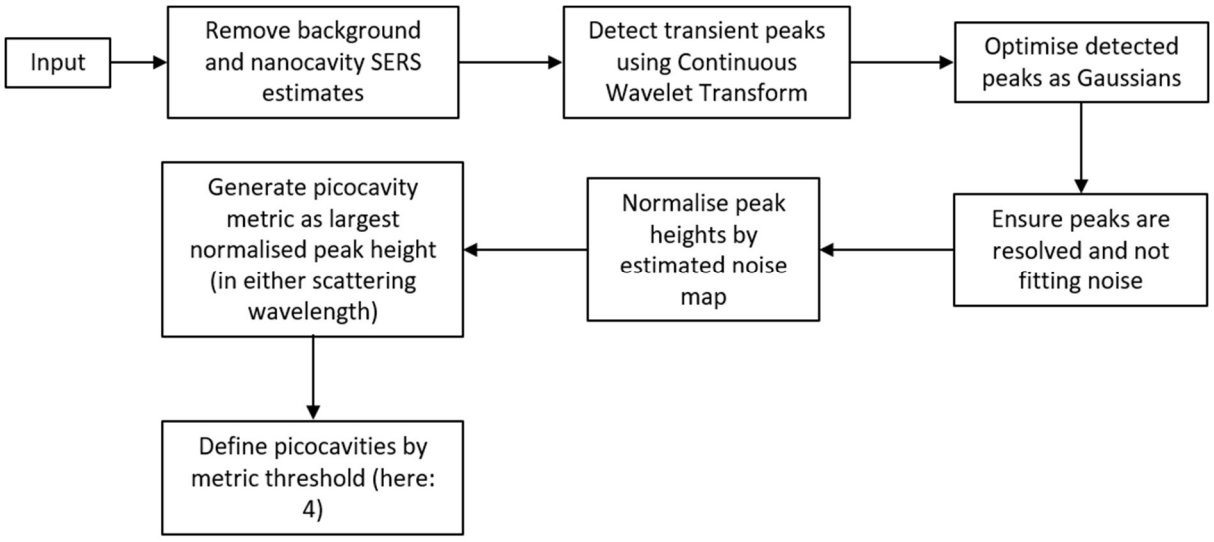

Flow Chart 7.5 | Picocavity Detection. Process for defining which spectra contain picocavity SERS.

To reduce computational complexity, possible peak energies are restricted to the discrete Raman shift values making up each spectrum. Peaks are initially estimated using a CWT (like in section 7.4.3.3) and are modelled as Gaussian peaks to reconstruct the scan of spectra (Fig. 7.14b). A second CWT on the scan with these optimised peaks removed is done as a precaution to uncover any peaks that may have been initially missed. Simple rules are implemented to guide peak optimisation. Optimised peaks must be resolved (not closer together than the sum of their widths). The region being described by a given peak must resemble a peak more than it resembles a polynomial of order ≤ 2 (as defined by the BIC, section 3.9). This prevents small remaining variations in the background being described as weak and broad peaks. With a given set of optimised picocavity peaks, a noise map for the

scan can be defined (again, like in section 7.4.3.3). This is important as the noise increases at the spectral positions of the removed large nanocavity peaks which generates narrow 'phantom' peaks in the transient spectra. To mitigate these, any peak with a height below the noise level at its location can be safely discarded. By removing the optimised picocavity peaks from the transient scan and dividing by the noise map, what remains is normalised noise. Using CWT analysis, the characteristic spectral scale of this noise can be extracted. Any optimised peak with a width comparable to this can be removed as an example of fitting the noise. This cycle of the removing peaks that do not fit these criteria and re-optimising those that remain can be iterated to convergence (Fig. 7.14).

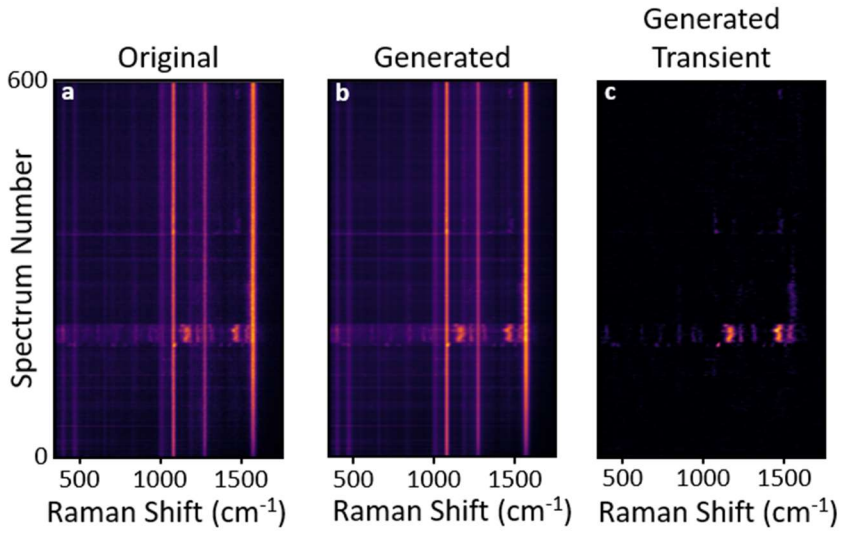

Figure 7.14 | Transient Peak Extraction. a, Example time series of SERS spectra. **b,** Reconstruction of this series as a sum of estimated background and persistent nanocavity components with additional transient SERS peaks modelled with Gaussian functions. **c,** These modelled transient peaks in isolation.

A spectrum is defined as containing a picocavity if it contains any detected peak with a height (normalised by the noise map) exceeding a given threshold. Here, we will consider the impact of varying this normalised detection threshold. In analysing the experimental results, we are comparing SERS scattering taken at 633 nm and 785 nm simultaneously. A point in time is taken to be part of a picocavity event if the threshold is met in either wavelength. A set of consecutive points in time that all trigger the threshold define a picocavity event.

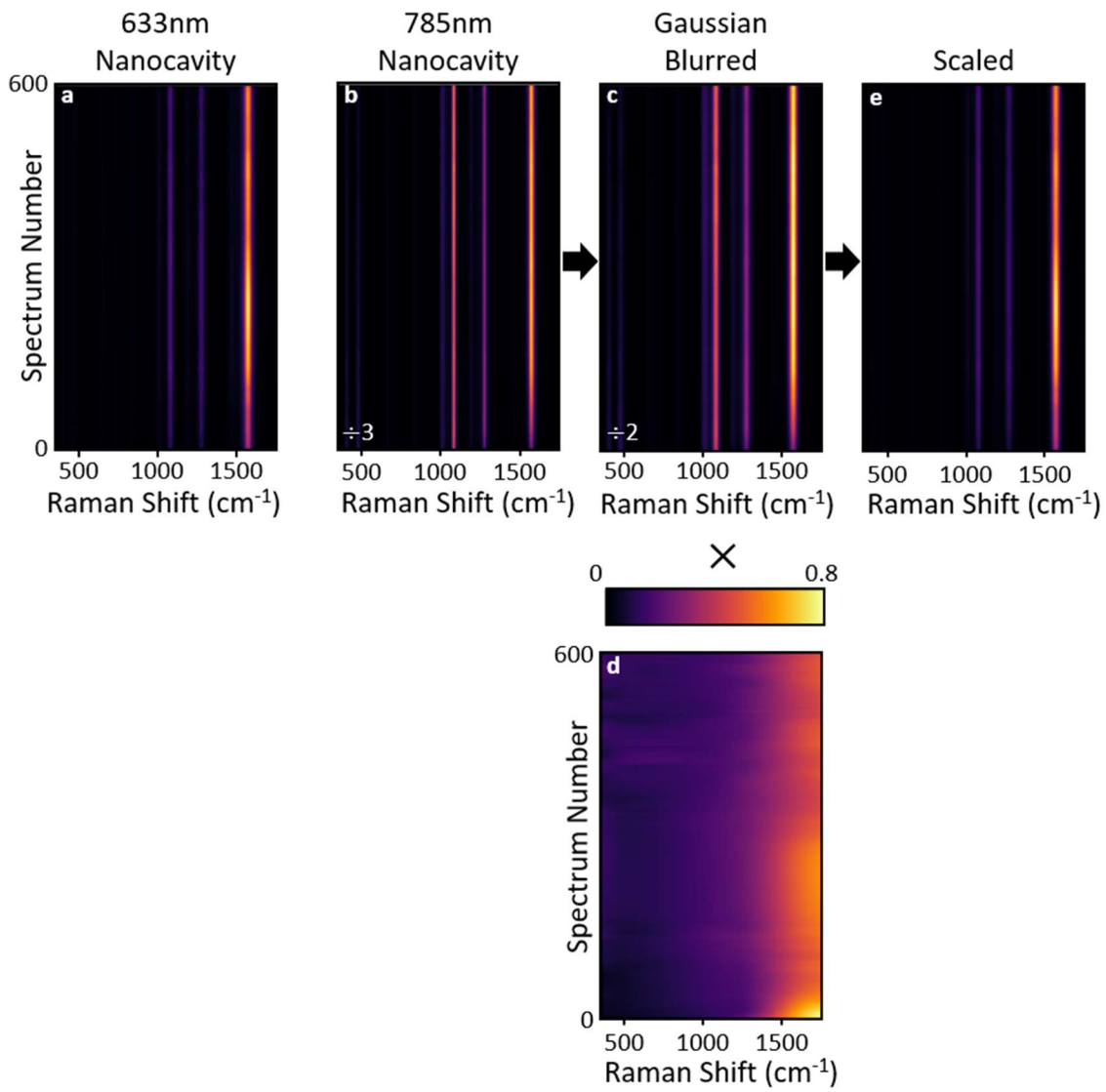

Figure 7.15 | Normalising Nanocavity SERS. a, 633 nm nanocavity and **b,** 785 nm nanocavity SERS estimates differ in peaks widths and intensities. **c,** A Gaussian blur corrects the difference in peak width. **d**, An intensity scaling map, formed from cubic splines with anchor points at nanocavity peak positions corrects for the peak intensity differences. **e,** The 785 nm SERS modified to match the 633 nm as closely as possible.

To compare scattering in both wavelengths, the transient SERS must first be normalised by using the nanocavity SERS as an internal reference. The SERS in the two wavelengths varies for a number of reasons including the difference in optical power coupled into the cavity and the wavelength dependence of the NPoM out-coupling efficiency. In addition, chromatic aberration means that the spectral widths of the 633 nm SERS lines are broadened with

respect to those at 785 nm. To match the nanocavity SERS at each wavelength, the 785 nm SERS is artificially broadened using a Gaussian kernel (Fig. 7.15c). The resulting broadened spectra are then scaled in intensity by cubic splines with control points at the positions of known nanocavity lines (Fig. 7.15d). This broadening and scaling is optimised so that the nanocavity SERS at 785 nm matches that at 633 nm as closely as possible (Fig. 7.15e). This same broadening and scaling can then be applied to the transient 785 nm SERS, normalising any differences between the two wavelengths that are not generated by the picocavity.

If the transient SERS is very small or non-existent, noise can render the summed scattering negative. In these cases, this sum is set to zero. Now, the total scattering during a picocavity event can be extracted for both 633 nm (S_{633}) and 785 nm (S_{785}). For each event, the final emission ratio metrics can be defined as

$$R \equiv \frac{S_{633}}{S_{785}}, \quad \rho \equiv \frac{S_{785} - S_{633}}{S_{785} + S_{633}} = \frac{1 - R}{1 + R}. \tag{7.11}$$

For events that are weak in absolute scattering intensity, the uncertainty due to noise dominates these metrics. For this reason, the values from these low intensity events are likely to obscure any underlying distribution for ρ. Therefore, a threshold of detected picocavity event intensity must be implemented. An example of this process is shown in figure 7.16 with the picocavity detection threshold set to 4. For all spectra within the dataset, the ratio of transient to total scattering can be calculated. At each point in time, the largest value for this ratio between the two wavelengths is taken. Separate distributions can be constructed for spectra labelled as containing or not containing a picocavity (Fig. 7.16a). While it is initially counter-intuitive that the distribution for non-picocavity spectra is not maximised at zero, this is a direct result of taking the maximum ratio from each wavelength. These distributions overlap, and can be combined to generate a curve of event intensity versus confidence that the event can be resolved from noise (Fig. 7.16b). As this confidence is increased, more picocavity events are discarded. Without discarding any events, the distribution of ρ is rather flat as the high uncertainty associated with weak events masks the true distribution (Fig. 7.16c). As the confidence threshold is raised, a resolvable distribution shape for ρ emerges (Fig. 7.16d-f). In this work, a confidence threshold of 90% is used.

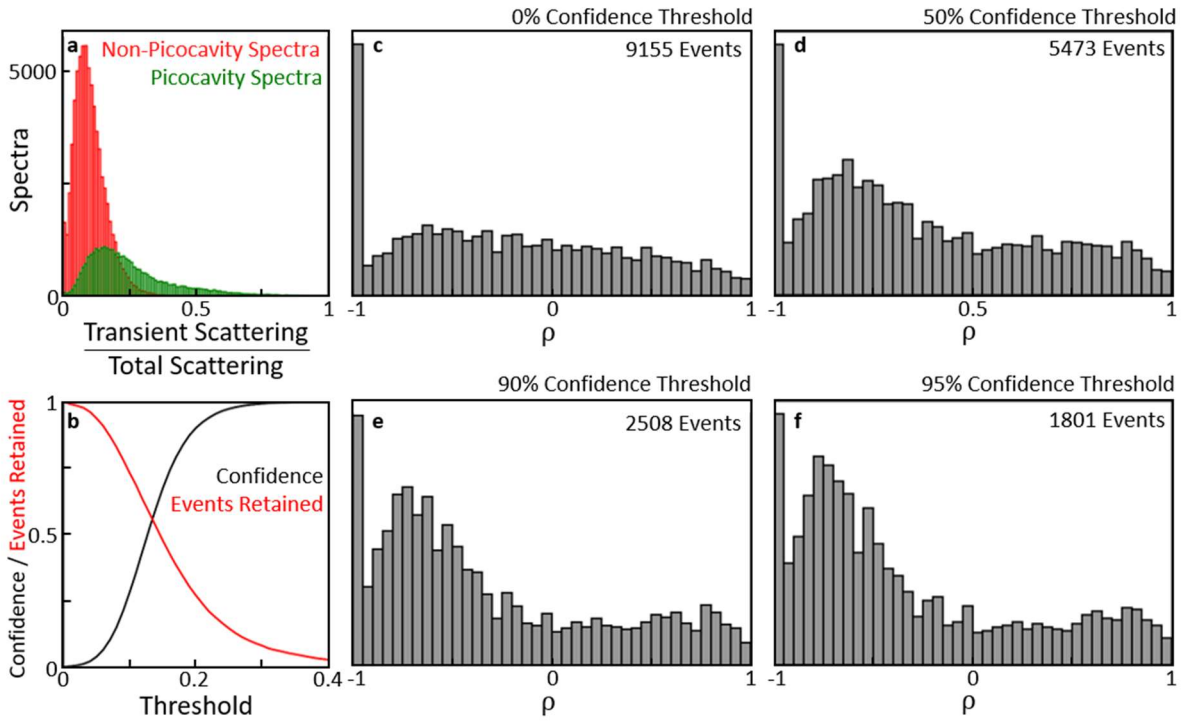

Figure 7.16 | Setting a Picocavity Intensity Threshold. a, For all SERS spectra over all NPoMs, the distributions of transient to total SERS for spectra labelled as containing and not-containing a picocavity. Picocavity detection uses a metric threshold of 4 here. **b,** The distributions overlap, defining the confidence that a picocavity event is resolvable from the noise depending on the picocavity intensity. Discarding events based on this confidence generates different histograms for ρ based on a minimum of **c**, 0% **d,** 50% **e,** 90% and **f,** 95% confidence.

As the metric threshold for defining a picocavity event is varied, the resulting distributions for the picocavity formation rate and lifetime can be constructed (Fig. 7.17). If this threshold is small, long sections of non-picocavity spectra are incorrectly labelled and the result is a low number of long lived detected picocavity events. As the threshold is raised, the total number of events increases to a maximum before decreasing again when true picocavity events begin to be discarded. The distribution of times between picocavity events varies from a single to double exponential as the threshold is raised. When the threshold is too high, the double exponential character is strong as picocavity events become split into multiple events artificially closely separated in time.

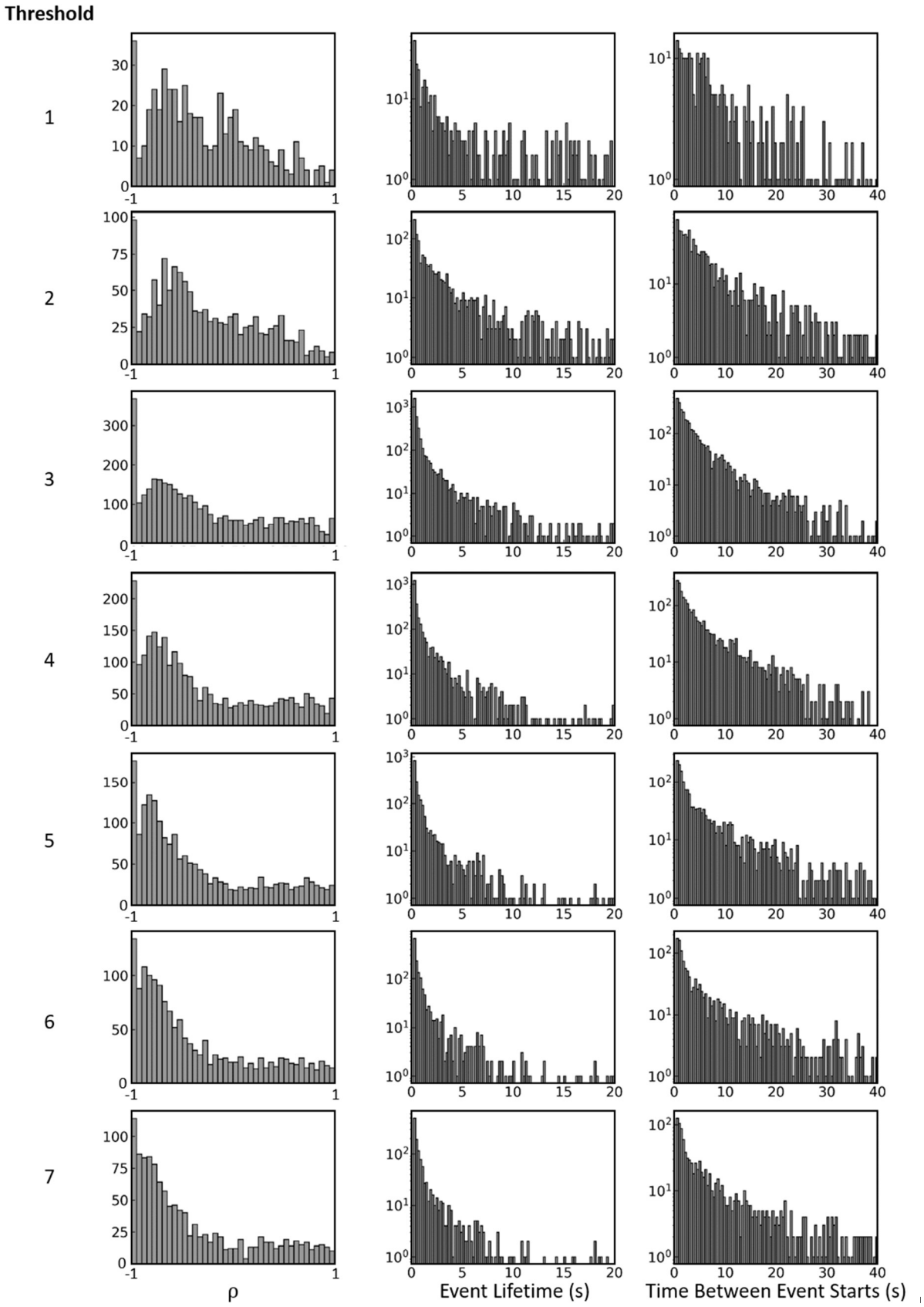

Figure 7.17 | Picocavity Properties with Detection Threshold. With varying picocavity metric thresholds for defining a picocavity spectrum, the total number of events detected (at 90% intensity confidence) varies alongside the distributions of ρ, picocavity lifetime and time between picocavities.

A metric threshold of 4 is selected, optimising the picocavity identification before the strong onset of this double exponential behaviour. The weak double exponential character that survives at this threshold is consistent with the results of the simpler BPT picocavity detection algorithm applied in Chapter 5. In that chapter, it was unclear if the observed distribution of picocavity lifetimes represented a single or double exponential. For this dataset, the more sensitive picocavity detection analysis applied here shows clear double exponential behaviour (Fig. 7.17).

7.5 A Model for SERS Ratio with Picocavity Location

Here, we will describe a model for converting a set of nanocavity NPoM field profiles from FDTD into a predicted distribution of picocavity intensity ratio R. This model will not require the structure of the picocavity to be stipulated or a picocavity near field FDTD simulation as input. The picocavity is instead only represented as a local SERS enhancement depending on the nanocavity field strength at its location. This enhancement will be allowed to favour one wavelength over another (section 7.2). The results of this optimised model will be compared to the FDTD simulations of the simple picocavity protrusion outlined in section 7.2. This model is formed from the combination of two independent sub-models. The first describes the value of R expected for a picocavity at any given position in the NPoM gap. The second is a PDF describing the relative probability of picocavity generation at that position. These will be discussed separately and the former is discussed here.

The nanocavity field strengths for wavelengths $\{\lambda_1,\lambda_2\}$ at position $\boldsymbol{x}$ of a given picocavity are provided as $E(\boldsymbol{x},\lambda) \equiv A_\lambda\, \psi(\boldsymbol{x},\lambda)$. Position $\boldsymbol{x}$ is a 2D vector describing the lateral position of the picocavity within the NPoM gap and describes picocavities forming both on the AuNP facet and gold mirror surfaces. This position can exist anywhere on the 2D surface S described by the extent of nanoparticle facet. As neither laser is resonant with the electronic absorption of BPT, the total nanocavity SERS is given by $\propto k \int_S E^4(\boldsymbol{x},\lambda) d^2\boldsymbol{x}$ where k is an undefined constant. The picocavity provides a local effective enhancement to the field magnitude α_λ for the purposes of SERS. Therefore, the picocavity SERS from this location (normalised by the total nanocavity SERS) is given by

$$\text{Picocavity Scattering} \propto \frac{k\alpha_\lambda^4 E^4(\boldsymbol{x},\lambda)}{k\int_s E^4(\boldsymbol{x},\lambda)d^2\underline{x}} \propto \frac{\alpha_\lambda^4\psi^4(\boldsymbol{x},\lambda)}{\int_s \psi^4(\boldsymbol{x},\lambda)d^2\boldsymbol{x}}. \tag{7.12}$$

While any chemical interactions between the adatom and molecule could influence the final picocavity SERS intensity (see Chapter 6), this is not optically dependent and it has not included here. This model is extendable to include this if desired. The ratio of this normalised picocavity SERS at each scattering wavelength is

$$\begin{aligned} R(\boldsymbol{x}) &= \frac{\alpha_{\lambda_1}^4\psi^4(\boldsymbol{x},\lambda_1)}{\int_s \psi^4(\boldsymbol{x},\lambda_1)d^2\boldsymbol{x}} \div \frac{\alpha_{\lambda_2}^4\psi^4(\boldsymbol{x},\lambda_2)}{\int_s \psi^4(\boldsymbol{x},\lambda_2)d^2\boldsymbol{x}} \\ &= \left(\frac{\psi(\boldsymbol{x},\lambda_1)}{\psi(\boldsymbol{x},\lambda_2)}\right)^4 \left(\frac{\alpha_{\lambda_1}}{\alpha_{\lambda_2}}\right)^4 \frac{\int_s \psi^4(\boldsymbol{x},\lambda_2)d^2\boldsymbol{x}}{\int_s \psi^4(\boldsymbol{x},\lambda_1)d^2\boldsymbol{x}} \end{aligned} \tag{7.13}$$

which separates cleanly into the product of three ratios. The ratio $\psi(\boldsymbol{x},\lambda_1)/\,\psi(\boldsymbol{x},\lambda_2)$ represents the difference in nanocavity near field strength at each wavelength. Any wavelength preference to the picocavity SERS enhancement is captured in the ratio $\alpha_{\lambda_1}/\alpha_{\lambda_2} \equiv \alpha^{-1}$. This is the same parameter α that was introduced and discussed in the context of FDTD simulations in section 7.2. The final term captures the normalisation to the nanocavity SERS and is used to define the utility function

$$\mathrm{N}_n \equiv \frac{\int_s \psi^n(\boldsymbol{x},\lambda_2)\; d^2\boldsymbol{x}}{\int_s \psi^n(\boldsymbol{x},\lambda_1)\; d^2\boldsymbol{x}} \tag{7.14}$$

resulting in the clean expression

$$R(\boldsymbol{x}) = \frac{\mathrm{N}_4}{\alpha^4}\frac{\psi^4(\boldsymbol{x},\lambda_1)}{\psi^4(\boldsymbol{x},\lambda_2)}. \tag{7.15}$$

Experimentally, this expression is complicated by the existence of noise which will dominate the response from picocavity SERS that is weak in either wavelength. As the transient SERS intensity drops significantly below the noise level, this makes it both hard to detect and also likely to be partially removed as part of the background or persistent SERS. To account for this in the model, picocavity scattering must be modified by supressing function $S(I) \leq I$ such that

$$S(I \to 0) = 0, \qquad S(I \to \infty) = I, \qquad S(I) \;/\; I \text{ is monotonic} \tag{7.16}$$

leading to the more complex expression

$$R(\boldsymbol{x}) = \left(\frac{A_{\lambda_2}}{A_{\lambda_1}}\right)^4 \frac{\int_s \psi^4(\boldsymbol{x},\lambda_2)d^2\boldsymbol{x}}{\int_s \psi^4(\boldsymbol{x},\lambda_1)d^2\boldsymbol{x}} \frac{S\left(k\alpha_{\lambda_1}^4 A_{\lambda_1}^4 \psi^4(\boldsymbol{x},\lambda_1)\right)}{S\left(k\alpha_{\lambda_2}^4 A_{\lambda_2}^4 \psi^4(\boldsymbol{x},\lambda_2)\right)}$$

$$= \left(\frac{A_{\lambda_2}}{A_{\lambda_1}}\right)^4 \mathrm{N}_4 \frac{S\left(k\alpha_{\lambda_1}^4 A_{\lambda_1}^4 \psi^4(\boldsymbol{x},\lambda_1)\right)}{S\left(k\alpha_{\lambda_2}^4 A_{\lambda_2}^4 \psi^4(\boldsymbol{x},\lambda_2)\right)}. \tag{7.17}$$

By noting that the ratio of total optical power coupled into the NPoM cavity at λ_2 compared to λ_1 is given by $L \equiv \left(\frac{A_{\lambda_2}}{A_{\lambda_1}}\right)^2 \mathrm{N}_2$, this can be re-expressed as

$$R(\boldsymbol{x}) = \frac{\mathrm{N}_4}{{\mathrm{N}_2}^2} L^2 \frac{S\left(k\alpha_{\lambda_1}^4 A_{\lambda_1}^4 \psi^4(\boldsymbol{x},\lambda_1)\right)}{S\left(k\alpha_{\lambda_2}^4 A_{\lambda_2}^4 \psi^4(\boldsymbol{x},\lambda_2)\right)}. \tag{7.18}$$

Although function S could take many ad hoc forms, the overtly simple $S(I\,;\,I_0) \equiv \max(I - I_0\,, 0)$ minimises the final number of model parameters while giving the desired behaviour. Below a threshold, this definition sets the detected scattered light to zero as it is completely dominated by experimental noise. Above this threshold, a relative suppression is applied that decreases with input magnitude. Using this definition,

$$R(\boldsymbol{x}) = \frac{\mathrm{N}_4}{{\mathrm{N}_2}^2} L^2 \frac{\max\left(k\alpha_{\lambda_1}^4 A_{\lambda_1}^4 \psi^4(\boldsymbol{x},\lambda_1) - I_0, 0\right)}{\max\left(k\alpha_{\lambda_2}^4 A_{\lambda_2}^4 \psi^4(\boldsymbol{x},\lambda_2) - I_0, 0\right)}$$

$$= \frac{\mathrm{N}_4}{{\mathrm{N}_2}^2}\, L^2 \frac{\max(\psi^4(\boldsymbol{x},\lambda_1) - \delta, 0)}{\max\left(\alpha^4 \left(\frac{L}{\mathrm{N}_2}\right)^2 \psi^4(\boldsymbol{x},\lambda_2) - \delta, 0\right)}, \quad \delta \equiv \frac{I_0}{k\alpha_{\lambda_1}^4 A_{\lambda_1}^4}. \tag{7.19}$$

This model extension has introduced 2 new parameters. First, parameter δ controls the strength of the supressing function. Optical power ratio L modifies the relative impact of the suppression on the SERS from one wavelength compared to the other. As required, this correctly returns to equation 7.15 in the limit $\delta \to 0$. This expression is not necessarily defined at all $\boldsymbol{x}$, representing positions where scattering is too weak in either wavelength to be detected experimentally.

7.6 Comparison of Picocavity Formation Models

7.6.1 Selecting FDTD Nanocavity Field Profiles

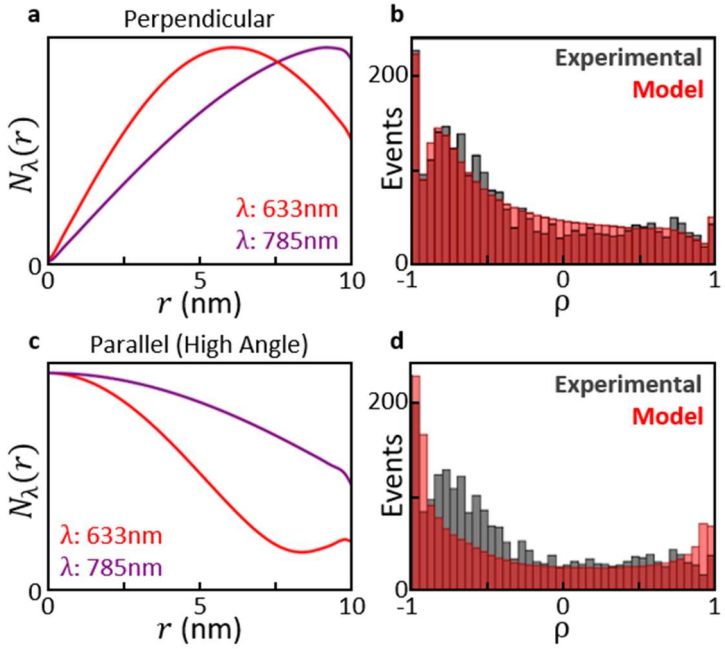

Figure 7.18 | Comparing Field Distributions. a, Normalised FDTD field strengths in the NPoM gap as a function of distance r from the AuNP facet centre for 633 nm and 785 nm incident light. Illumination is perpendicular to the NPoM gap. **b,** An optimised distribution for ρ to best match the experimental result, assuming uniform adatom generation across the NPoM gap. **c,d,** The same results shown for incident light polarised parallel to the NPoM gap.

While the model outlined in section 7.5 is applicable to any nanocavity field profiles, the FDTD field profiles outlined in section 7.2 are used here. Within the model, we define $\{\lambda_1, \lambda_2\}$ = {633 nm, 785 nm}. As discussed, only the dependence on the radial distance from the facet centre (r) is wavelength dependent for the truncated sphere NPoM and the field variation on the polar angle can be averaged over. The field profiles for 633 nm and 785 nm illumination vary depending on whether the NPoM is illuminated at normal incidence or at a high angle (section 7.2). To compare these profiles, we use a simple initial approximation that picocavities form with uniform probability anywhere within the NPoM gap. For each set of field profiles, the model parameters $\{\alpha, L, \delta\}$ are optimised to best reproduce the

experimental histogram for ρ (Fig. 7.18). By optimising a single value for α, note that we are averaging over possibly varying degrees of effective picocavity atom protrusion between events. The perpendicular (normal) field profiles are able to recreate well the general shape of the experimental histogram (Fig 7.18b) with the precise optimised parameters discussed below alongside competing PDFs. In contrast, the high angle fields are unable to reproduce the experimental observations (Fig. 7.18d). Therefore, it is taken that the perpendicular illumination FDTD calculations better represent in-coupling to the NPoM in the experimental system and these field distribution are used from here.

7.6.2 Model and Result Summary

With the FDTD field profiles selected, we can now optimise and compare PDFs describing the generation of picocavities within the NPoM gap. The relative probability of picocavity formation within a ring of infinitesimal width dr at radial position r is defined as $f(r)\, r\, dr$. As picocavity generation is known to be stochastic and temperature dependant[6] (Chapter 5), this is modelled using a generation energy barrier $B(r)$ that is overcome thermally such that $f(r) \propto e^{-B(r)/k_B T}$ where k_B is the Boltzmann constant and T is the NPoM temperature. The comparison of PDFs is therefore transformed into a comparison of different models for effective energy barrier $B(r)$. Due to rapid thermal diffusion in gold[142], note that temperature T is constant across the NPoM and is not dependent on r.

A given model, optimised to best reproduce the experimental distribution of ρ, can be compared to the experimental results in two ways. First, the distributions for ρ can be directly compared. Second, if $\rho(r)$ is defined and monotonic within the model over the full range $|\rho| < 1$ then the experimental values for ρ in this range can be inverted into radial positions for the picocavities. The distribution of these positions can be directly compared to the input $f(r)$ which should match.

The PDFs explored here will investigate the possible role of optical fields in the picocavity generation mechanism. In the Thermal Model, this is not the case and the incident laser power only drives the formation of picocavities by heating the NPoM. If the energy barrier

$B(r)$ is defined as constant then $f(r)$ is also constant. This is the model used in section 7.6.1 to select the FDTD field profiles. As the average coordination number of surface atoms on the AuNP facet drops near the facet edge, we will also consider a $B(r)$ that drops as r approaches the facet radius $R = 10$ nm. This is defined as a sigmoid centred at the facet edge allowing different values of $B(r)$ at $r = \{0, R\}$ with the rate of change between the two controlled by characteristic sigmoid width C. The Thermal Model is optimised in section 7.6.3.

For the Optical Model where local field strengths are involved in the formation of picocavities, we will retain the thermally driven description of $f(r)$ as the possible mechanism of this involvement has not yet been determined. In this case, the effective energy barrier $B^{\mathrm{OM}}(r)$ that must be thermally overcome is supressed by the local field intensity $I(r)$. This represents the optical field providing energy towards picocavity generation. In a linear model, this is defined as $B^{\mathrm{OM}}(r) = B(r)/[I(r) + \tau]$ where τ is a constant that keeps this barrier finite in the limit $I(r) \to 0$. This Optical Model was discussed briefly in Chapter 5. In the limit $I(r) \ll \tau$, this returns to the Thermal Model. We consider here the opposite limit $I(r) \gg \tau$ to neglect τ and minimise the number of model parameters. This model will be applied to both constant and sigmoidal models for $B(r)$. The expression for $I(r)$ is discussed in the relevant section 7.6.4 where the Optical Model in optimised.

In sections 7.6.3 - 7.6.5, twelve different optimisations are carried out which vary the Thermal and Optical Models. As this is a large number, they are first briefly summarised here. Both the Thermal and Optical Models can recreate the general shape of the experimental ρ distribution. The Optical Model performs better as might be expected from the higher number of optimisable parameters as will be discussed. The Optical Model requires the sigmoidal form of $B(r)$ in order to not regress back to the Thermal Model. These models disagree strongly on the value of L which can be fixed using the persistent nanocavity SERS. With this parameter no long optimisable, the Thermal Model is now unable to reproduce the experimental results while the Optical Model still performs well. Therefore, these results suggest that picocavities are more likely at regions of higher optical intensity and that fields are directly involved in the yet undetermined picocavity generation mechanism.

7.6.3 Thermal Model Optimisation

The simplest Thermal Model with constant $B(r)$ is already able to capture the main shape of the experimental ρ distribution (Fig. 7.19a). As expected from the input field distributions, $\rho(r)$ increases with r (Fig. 7.19b). Comparing the input flat $f(r)$ to that inverted from the adatom radial positions accentuates the discrepancies between the model and data (Fig. 7.19d). For example, this inverted distribution suggests an increase in adatom generation at $r \sim 6$ nm where the optical fields are strongest.

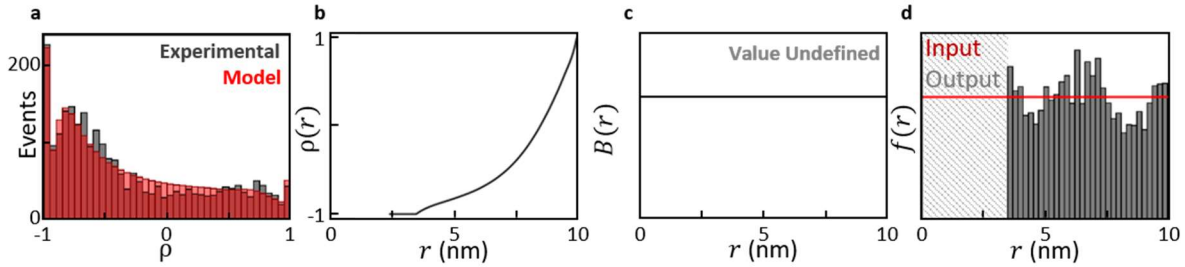

Optimised Parameters: α: 0.81, L: 2.00, δ: 0.43

Figure 7.19 | Thermal Model. $B(r)$: Constant. a, The model is optimised such that numerical distribution best matches the experimental result. **b,** The resulting ρ as a function of radial distance r from the AuNP facet centre. This is undefined where the line is missing. **c**, Optimised $B(r)$. **d,** Optimised model $f(r)$ compared to equivalent distribution of picocavity positions inverted from the optimised model. Dashed region cannot be inverted.

Surprisingly, optimising the model with the sigmoidal $B(r)$ (Fig. 7.20) provides a barrier that increases steadily by $\sim k_B T$ over the radial extent of the facet rather than decreasing close to the facet edge. This leads to only a minor improvement in the agreement between model and experiment (Fig. 7.20a).

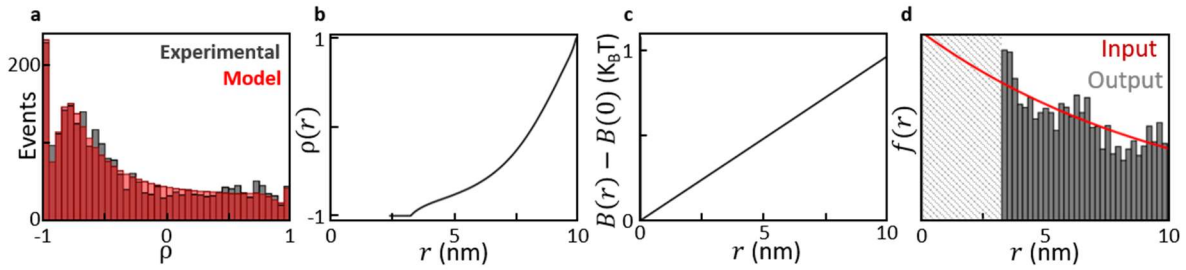

Optimised Parameters: α: 0.86, L: 1.99, δ: 0.43, $B(R) - B(0)$: 0.97K_BT, C: 61.49 nm

Figure 7.20 | Thermal Model. $B(r)$: Sigmoidal. a, The model is optimised such that numerical distribution best matches the experimental result. **b,** The resulting ρ as a function of radial distance r from the AuNP facet centre. This is undefined where the line is missing. **c**, Optimised $B(r)$. **d,** Optimised model $f(r)$ compared to equivalent distribution of picocavity positions inverted from the optimised model. Dashed region cannot be inverted.

7.6.4 Optical Model Optimisation

In the Optical Model, the effective thermal energy barrier is $B^{\mathrm{OM}}(r) = B(r)/I(r)$. As the total optical intensity (combining both pump wavelengths) increases, the local thermal barrier for adatom formation is supressed. Note that this expression does not have the correct units so some conversion factor (controlling the strength of barrier suppression for a given optical intensity) must now be wrapped into $B(r)$. This means we lose the ability to put an absolute scale on $B(r)$ within this model which is shown without units in the following figures. This causes no issues as it is the ratio $B(r)/I(r)$ and not the absolute value of $B(r)$ that is required to optimise this model.

$I(r)$ is defined as a linear sum of the two pump wavelengths

$$I(r) \propto W \frac{\psi^2(r,\lambda_1)}{\int \psi^2(r,\lambda_1)\, r\, dr} + (1-W)\frac{\psi^2(r,\lambda_2)}{\int \psi^2(r,\lambda_2)\, r\, dr}, \quad 0 \leq W \leq 1 \qquad (7.20)$$

where W is some weighting factor between the two wavelengths. Without loss of generality, the proportionality constant is set here such that $\max(I(r)) = 1$. This simply pushes the unknown true $\max(I(r))$ into $B(r)$ whose absolute scale is already undefined.

The simplest expression for W is based on the ratio of optical powers coupled into the system $W = (1 + L)^{-1}$. Defining a constant $B(r)$ causes the system to optimise $B(r) \to 0$ and the model regresses to "*Thermal Model. $B(r)$: Constant*" (Fig. 7.19). A more interesting result is found using the sigmoidal form of $B(r)$ which generates a histogram that agrees more closely with the experimental result (Fig. 7.21). This may be expected from the increased number of model parameters. The agreement between the input and inverted $f(r)$ (Fig. 7.21d) is greatly improved over the Thermal Model and is formed from two peaks. The first, at $r \sim$ 6 nm, is driven by increased optical intensity. The second, at the facet edge, is driven by the sigmoidal drop in barrier energy (Fig. 7.21c).

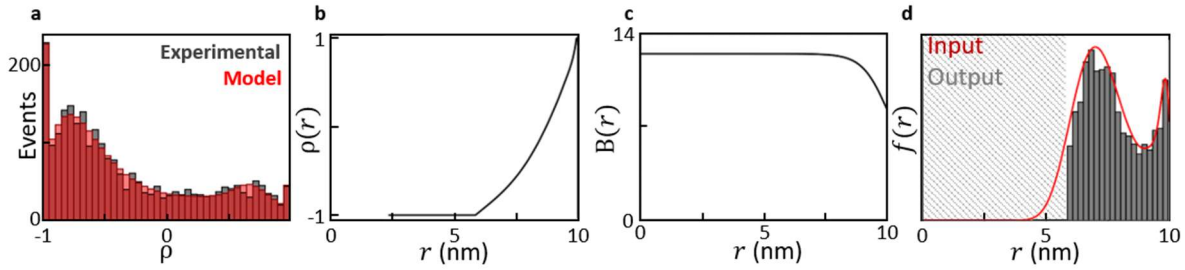

Optimised Parameters: α: 0.85, L: 0.74, δ: 0.41, $B(0)$: 12.49, $B(R)$: 8.23, C: 0.51 nm

Figure 7.21 | Optical Model. $B(r)$: Sigmoidal. W: $(1 + L)^{-1}$. a, The model is optimised such that numerical distribution best matches the experimental result. **b,** The resulting ρ as a function of radial distance r from the AuNP facet centre. This is undefined where the line is missing. **c**, Optimised $B(r)$. **d,** Optimised model $f(r)$ compared to equivalent distribution of picocavity positions inverted from the optimised model. Dashed region cannot be inverted.

For completeness, we can consider the possibility that the enhanced picocavity field is involved in picocavity formation though some feedback mechanism. This can be tested by setting $W = (1 + \alpha^2 L)^{-1}$. This again returns to the "*Thermal Model. $B(r)$: Constant*" (Fig. 7.19) when $B(r)$ is constant and gives similar final results as $W = (1 + L)^{-1}$ when using the sigmoid form of $B(r)$ (Fig. 7.22).

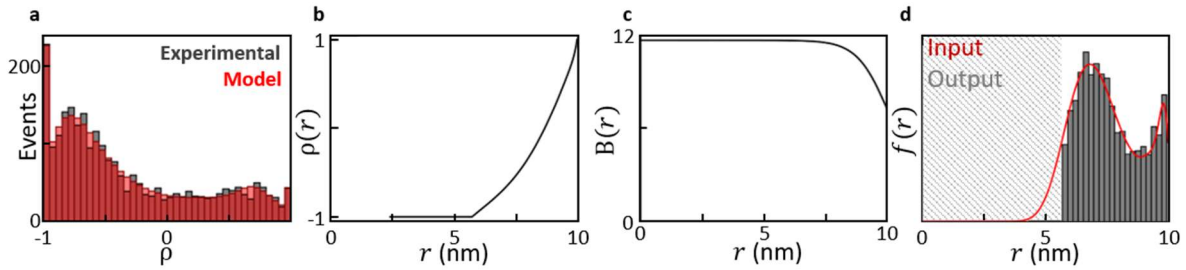

Optimised Parameters: α: 0.86, L: 0.76, δ: 0.42, $B(0)$: 11.61, $B(R)$: 7.12, C: 0.62 nm

Figure 7.22 | Optical Model. $B(r)$: Sigmoidal. W: $(1+\alpha^2 L)^{-1}$. a, The model is optimised such that numerical distribution best matches the experimental result. **b,** The resulting ρ as a function of radial distance r from the AuNP facet centre. This is undefined where the line is missing. **c**, Optimised $B(r)$. **d,** Optimised model $f(r)$ compared to equivalent distribution of picocavity positions inverted from the optimised model. Dashed region cannot be inverted.

7.6.5 Fixing Parameter L

Between "*Thermal Model. $B(r)$: Constant*" (Fig. 7.19) and *"Optical Model. $B(r)$: Sigmoidal. W: $(1+L)^{-1}$"* (Fig.7.21), a key difference is a disagreement on which incident wavelength couples more effective power into the NPoM cavity (L = 2.0 and 0.74 respectively). Fortunately, the value of L is also encoded into the nanocavity SERS. If the 785 nm : 633 nm ratio of nanocavity SERS is denoted as R_N then we note that

$$L = \left(\frac{A_{\lambda_2}}{A_{\lambda_1}}\right)^2 \mathrm{N}_2 \tag{7.21}$$

$$R_N = \left(\frac{A_{\lambda_2}}{A_{\lambda_1}}\right)^4 \mathrm{N}_4 \tag{7.22}$$

$$\therefore\ L = \sqrt{\frac{{\mathrm{N}_2}^2}{\mathrm{N}_4} R_N}. \tag{7.23}$$

Note that the ratio R_N here refers to SERS emitted directly by the molecules. Experimentally, the measured ratio is modified by the spectrally dependant out-coupling efficiency of this light from the NPoM gap. The measured SERS can be corrected by a relative out-coupling curve. SERS produced from a point source within an NPoM cavity is known to out-couple at

high angles[29,42]. Therefore, the relative out-coupling curve is generated using the square roots of the high angle NPoM scattering spectra generated in FDTD (Fig. 7.23a).

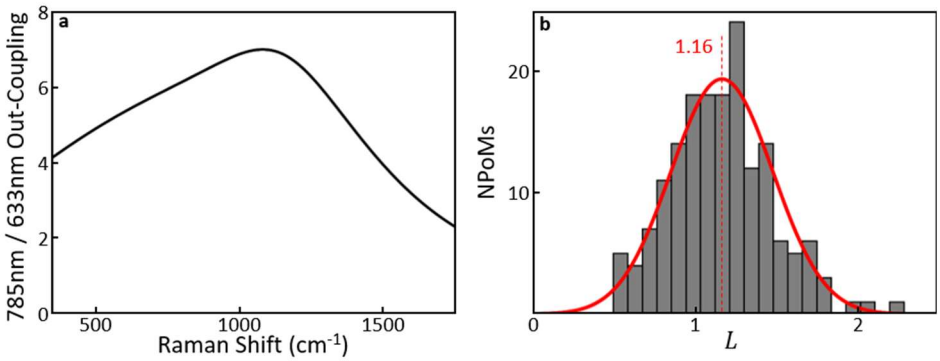

Figure 7.23 | Fixing L. a, Relative out-coupling efficiencies for SERS generated at the same Raman shift from each scattering wavelength. This is generated using the square root of the FDTD NPoM scattering cross section with high angle illumination. **b,** Post out-coupling correction, the nanocavity SERS ratio is converted to the effective optical power ratio (785 nm : 633 nm) coupled into the cavity L. Value spread due to variation in AuNP size and shape compared to truncated sphere mode. Distribution is normally distributed (red line) with a mean of L = 1.16.

Initially, it seems that a key factor missing from this calculation of L is that the Raman cross section of a vibrational mode varies depending on the scattering wavelength (section 2.6.3). For the same laser powers coupled in to the NPoM cavity at each wavelength, this could make 785 nm SERS approximately 60% less intense than 633 nm SERS. However, this just makes L throughout this model an effective optical power ratio that is the physical ratio of laser powers coupled into the NPoM multiplied by this cross section correction factor.

The resulting L follows a normal distribution due to the variations in AuNP size and shape (Fig 7.23b). By fixing L at the mean value of 1.16, the Thermal and Optical models can be re-optimised with one less free parameter.

With L fixed, the Thermal Model (with constant or sigmoidal $B(r)$) optimises to not cover the full {-1,1} domain of ρ (Fig. 7.24 ,7.25).

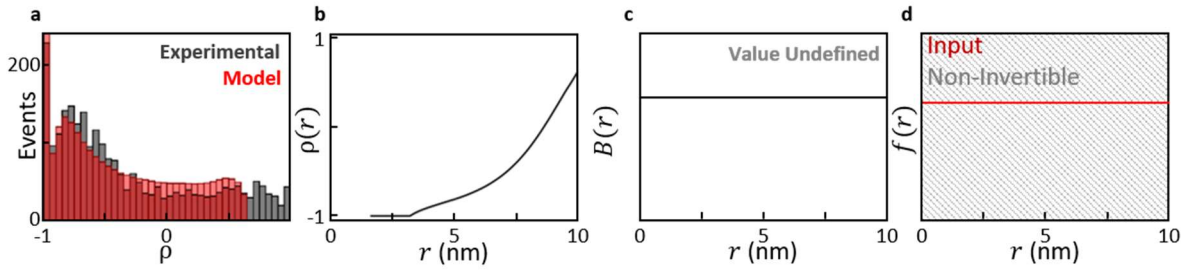

Optimised Parameters: α: 0.82, L: 1.16, δ: 0.12

Figure 7.24 | Thermal Model. $B(r)$: Constant. Fixed L. a, The model is optimised such that numerical distribution best matches the experimental result. **b,** The resulting ρ as a function of radial distance r from the AuNP facet centre. This is undefined where the line is missing. **c**, Optimised $B(r)$. **d,** Optimised model $f(r)$. The equivalent distribution of picocavity positions cannot be inverted from the optimised model here.

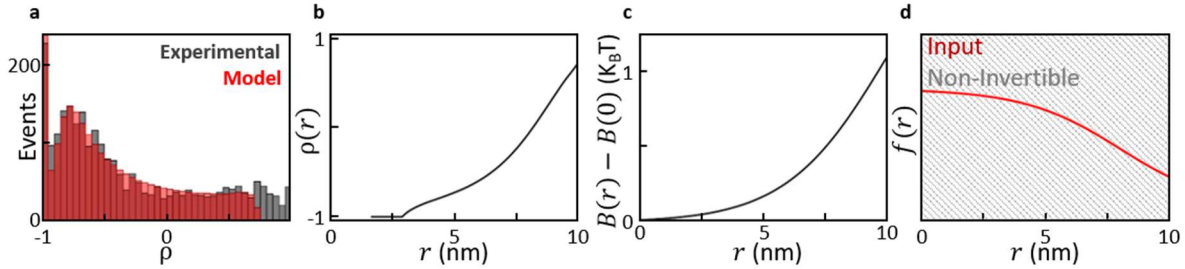

Optimised Parameters: α: 0.90, L: 1.16, δ: 0.11, $B(R) - B(0)$: 1.10K_BT, C: 2.04 nm

Figure 7.25 Thermal Model. $B(r)$: Sigmoidal. Fixed L. a, The model is optimised such that numerical distribution best matches the experimental result. **b,** The resulting ρ as a function of radial distance r from the AuNP facet centre. This is undefined where the line is missing. **c**, Optimised $B(r)$. **d,** Optimised model $f(r)$. The equivalent distribution of picocavity positions cannot be inverted from the optimised model here.

In comparison, the Optical Model (with any combination of $B(r)$ and W) does cover the full domain of ρ. The experimental distribution is only well reproduced when using the sigmoidal form of $B(r)$ (Fig. 7.26-7.29).

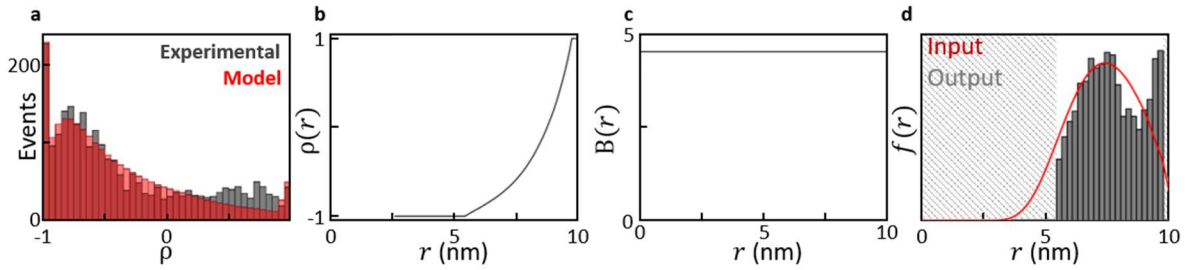

Optimised Parameters: α: 0.78, L: 1.16, δ: 0.58, $B(r)$: 4.5

Figure 7.26 | Optical Model. $B(r)$: Constant. W: $(1 + L)^{-1}$. Fixed L. a, The model is optimised such that numerical distribution best matches the experimental result. **b,** The resulting ρ as a function of radial distance r from the AuNP facet centre. This is undefined where the line is missing. **c**, Optimised $B(r)$. **d,** Optimised model $f(r)$ compared to equivalent distribution of picocavity positions inverted from the optimised model. Dashed region cannot be inverted.

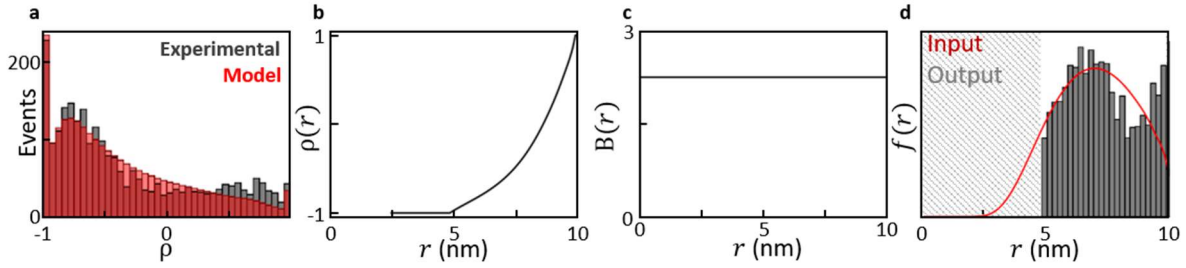

Optimised Parameters: α: 0.81, L: 1.16, δ: 0.47, $B(r)$: 2.26

Figure 7.27 | Optical Model. $B(r)$: Constant. W: $\left(1 + \alpha^2 L\right)^{-1}$. Fixed L. a, The model is optimised such that numerical distribution best matches the experimental result. **b,** The resulting ρ as a function of radial distance r from the AuNP facet centre. This is undefined where the line is missing. **c**, Optimised $B(r)$. **d,** Optimised model $f(r)$ compared to equivalent distribution of picocavity positions inverted from the optimised model. Dashed region cannot be inverted.

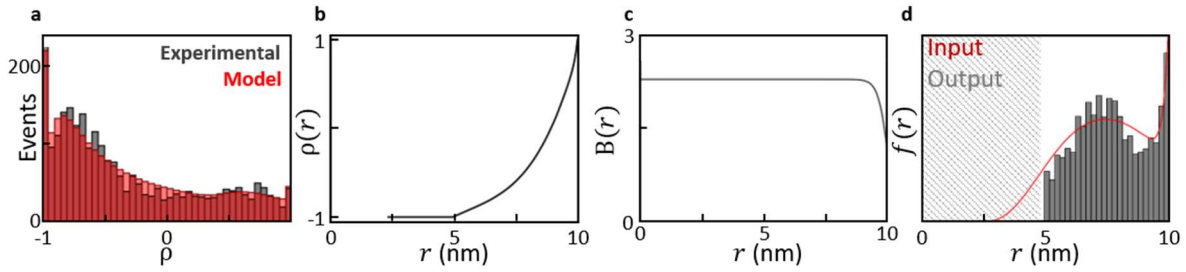

Optimised Parameters: α: 0.76, L: 1.16, δ: 0.39, $B(0)$: 2.29, $B(R)$: 1.07, C: 0.20 nm

Figure 7.28 | Optical Model. $B(r)$: Sigmoidal. W: $(1 + L)^{-1}$. Fixed L. a, The model is optimised such that numerical distribution best matches the experimental result. **b,** The resulting ρ as a function of radial distance r from the AuNP facet centre. This is undefined where the line is missing. **c**, Optimised $B(r)$. **d,** Optimised model $f(r)$ compared to equivalent distribution of picocavity positions inverted from the optimised modelDashed region cannot be inverted.

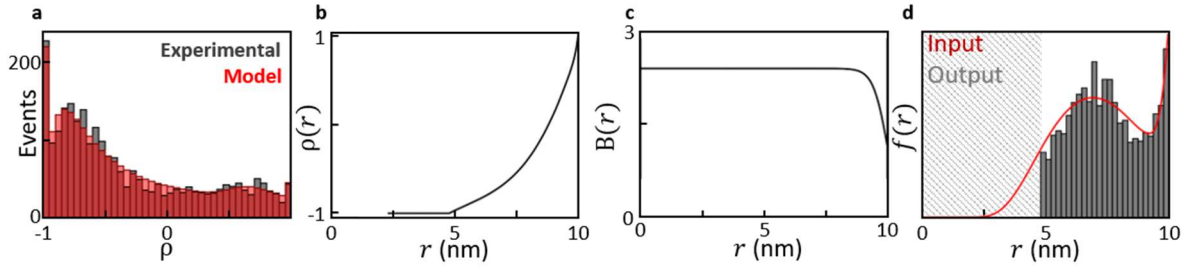

Optimised Parameters: α: 0.78, L: 1.16, δ: 0.39, $B(0)$: 2.40, $B(R)$: 1.18, C: 0.29 nm

Figure 7.29 | Optical Model. $B(r)$: Sigmoidal. W: $(1 + \alpha^2 L)^{-1}$. Fixed L. a, The model is optimised such that numerical distribution best matches the experimental result. **b,** The resulting ρ as a function of radial distance r from the AuNP facet centre. This is undefined where the line is missing. **c**, Optimised $B(r)$. **d,** Optimised model $f(r)$ compared to equivalent distribution of picocavity positions inverted from the optimised model. Dashed region cannot be inverted.

These results suggest that picocavity generation is more common at locations of higher optical intensity. To speculate, the undefined mechanism for the optically induced suppression of the picocavity generation energy barrier could be something like low probability momentum transfers from inelastic electronic scattering of light within the bulk gold to individual surface atoms providing a source of non-thermal energy.

6.7.6 Interpreting the Optimised Optical Model

For clarity, we discuss here the results of the model *"Optical Model.* $B(r)$*: Sigmoidal.* W*:* $(1+L)^{-1}$*. Fixed* L*."* (Fig. 7.28). This model has 5 free parameters. The optimised α =0.76 indicates a 30% stronger picocavity effective near-field enhancement at 633 nm compared to 785 nm. This is well within the range given by FDTD simulations of an atomic scale protrusion in the NPoM gap (section 7.2, Fig. 7.3h) and suggests aspect ratios $\varphi \sim 1$ in these simulations as perhaps expected. This is experimental support for the recent 2021 model that picocavity enhancement follows resonant behaviour[77] rather than being spectrally flat. The optimised model implies that the picocavities which dominate in 785 nm SERS form nearer the AuNP facet edge due to the 50% drop in $B(r)$ over a characteristic sigmoid width of 0.2 nm (which is on the order of the size of a gold atom). It is difficult to intuitively state if this 50% change is reasonable. On a {1,1,1} AuNP facet, a surface atom at a flat facet edge has a 33% lower coordination number than an atom on the inside of the facet. On a rough facet edge, the atoms experience a 22-67% drop in coordination number depending on their position (average 44%) (Fig. 7.30). The model combines picocavity formation from the AuNP facet with formation from the gold mirror which should experience no change in average surface coordination number with position. It is important to note that this effective barrier shape also encodes our approximation that the facet size is on average circular.

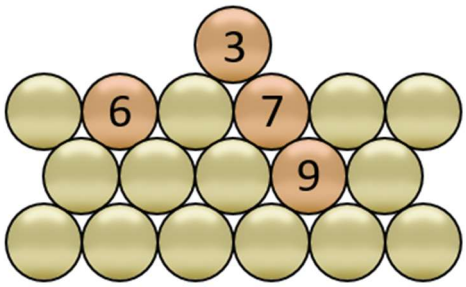

Figure 7.30 | Facet Coordination Number. Section of a {1,1,1} gold facet surface. Example atoms, including one protruding from the facet edge, are labelled with their coordination numbers. These numbers include connections to the next layer of atoms (not shown). This shows possible reductions in coordination number at the facet edge compared to the maximum within the bulk facet (9).

To demonstrate the importance of the $B(r)$ energy barrier drop to the results of the model, it is modified in magnitude in figure 7.31. This significantly alters the amount of events which dominate in 785 nm scattering.

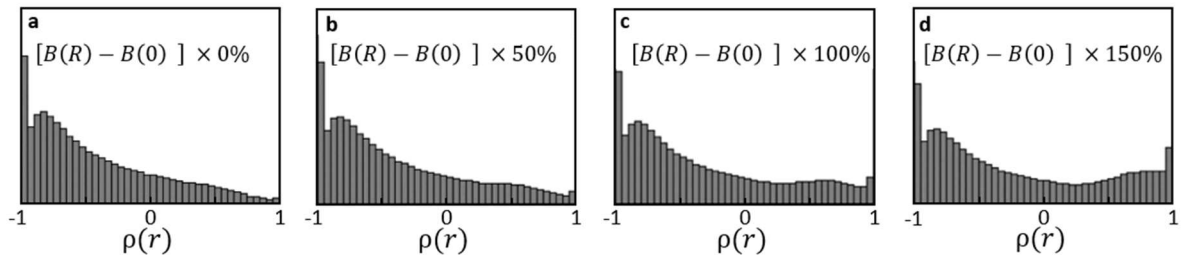

Figure 7.31 | Varying Energy Decrease at Facet Edge. Generated ρ histograms for the "Optical Model. $B(r)$ = sigmoidal, $W = (1 + L)^{-1}$, fixed L" model , while changing the decrease in energy barrier near the facet edge to **a,** 0%, **b,** 50% **c,** 100% **f,** 150% of the optimised value.

In figure 7.32, the effective noise parameter δ is scaled to demonstrate its influence on the model results. When δ =0, the distribution stops at $|\rho| < 1$ reflecting the fact there are no locations where the field strength at either wavelength tends to zero. As δ > 0, the suppression of picocavity SERS smears the distribution towards the edges of the defined domain.

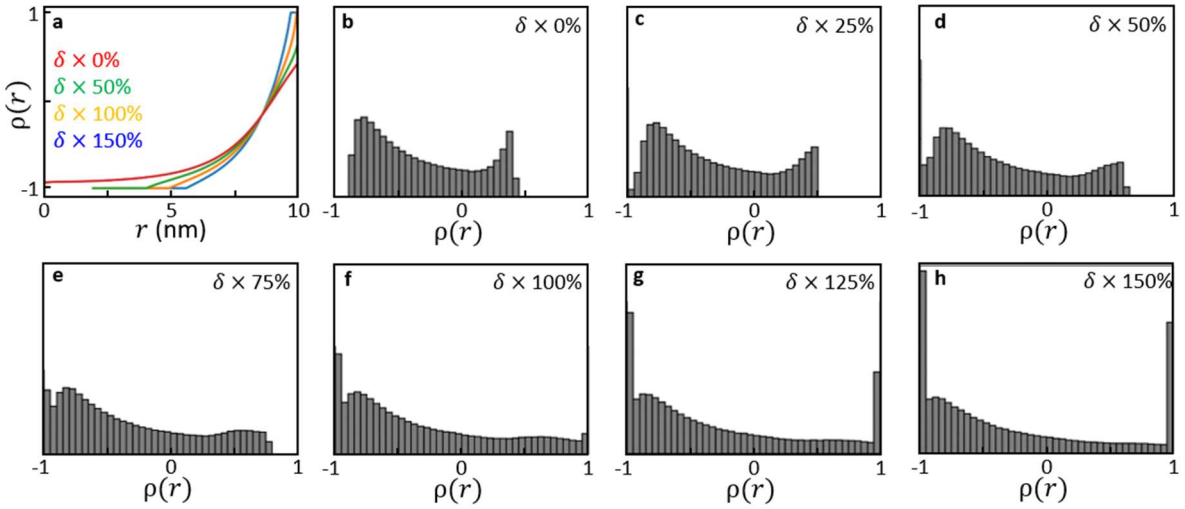

Figure 7.32 | Effect of Scaling δ. a, $\rho(r)$ for the "Optical Model. $B(r)$ = sigmoidal, $W = (1 + L)^{-1}$, fixed L" model while scaling the noise parameter δ from its optimised values. Generated ρ histograms while scaling this parameter by **b,** 0% **c,** 25% **d,** 50% **e,** 75% **f,** 100% **g,** 125% **h,** 150%.

7.7 Switching of Dominant SERS Wavelength

On rare occasions, a picocavity event is observed in which the wavelength of higher intensity (nanocavity normalised) transient SERS repeatedly switches. As this is such a low frequency event, the example discussed here (and shown in figure 7.33) is drawn from a smaller dataset than that used in sections 7.3 and 7.6 and for which the model parameters cannot be confidently optimised. This event is generated by irradiating with 20 µW 633 nm and 380 µW 785 nm power until picocavity formation. The system is then measured using 50 µW 633 nm and 280 µW 785 nm power. It is unknown if this power change is a factor in inducing this switching behaviour and this is a subject of further investigation. In 633 nm and 785 nm SERS, these spectra can be reconstructed at each time step as linear combinations of 2 or 3 characteristic spectra respectively, one of which represents the picocavity state. This allows the weight of the picocavity component to be plotted over time and clearly shows an anti-correlated repeatable change between the two wavelengths (Fig. 7.33c).

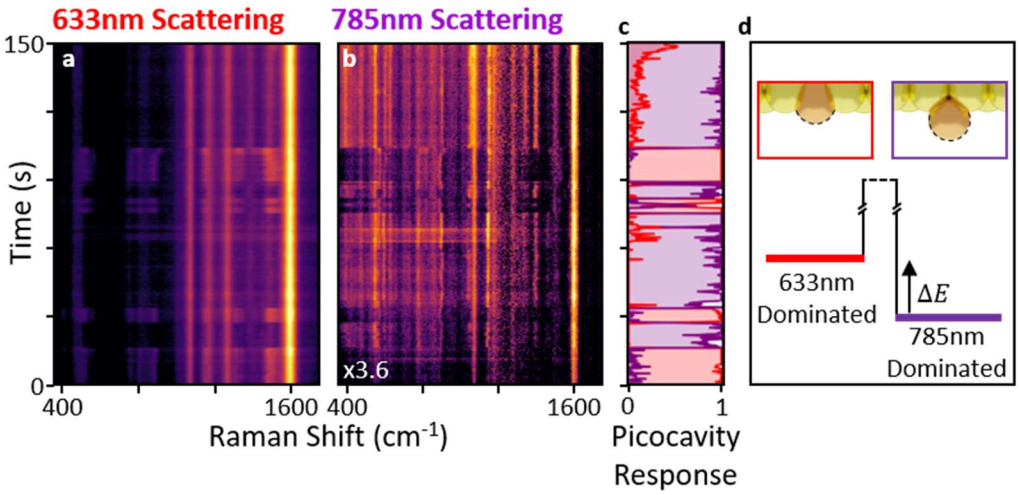

Figure 7.33 | Switching in Dominant Scattering Wavelength. a,b, Sequential SERS spectra showing repeated switching in which scattering wavelength dominates in transient SERS. Measured using 50 µW 633 nm and 280 µW 785 nm. **c,** Spectra are modelled a linear sums of 2 (633 nm) or 3 (785 nm) characteristic spectra. The weight of the picocavity component provides a metric for picocavity activity. **d,** Model of two metastable states with energy difference ΔE separated by an unknown energy barrier. Insets show the possible origin of these observations as different effective adatom protrusion amounts.

Within the model presented in this chapter (section 7.5) the only parameters that can change dynamically to allow this switching behaviour are the position and effective protrusion of the picocavity. Note that one of these being the cause precludes the other as the picocavity must represent a fully protruded adatom if it is to move laterally on the gold surface. As the model parameters for this combination of input laser powers are not optimised, the precise distances required for these changes cannot be stated. However, any change in lateral position would have be a rapid and reversible multi-nanometre movement to generate the observed effect. This would mean that the picocavity adatom would have to be interacting with a different BPT molecule in each state. Noting that the set of transient lines observed in each state are very similar, it is more likely that the picocavity is fixed in position and the observed switching is instead caused by a reversible sub-atomic shift in effective adatom protrusion. Note that this is an effective protrusion capturing some reversible restructuring of the picocavity structure leading to a change in the picocavity enhancement resonance. Regardless of the underlying mechanism, an energy landscape for this dynamic behaviour can be extracted by considering the switching rates between the two states.

The system is considered to switch thermally between the two states separated by an energy barrier (Fig. 7.33d). When the scattering dominates in 633 nm or 785 nm SERS, the energy states are labelled by E_1 and E_2 respectively. The energy barrier is given by $E_B > E_1, E_2$ and the difference in energy between the states is defined as $\Delta E \equiv E_1 - E_2$. From the Arrhenius equation, the average lifetimes in each state $i = \{1,2\}$ are given as $L_i = A\, e^{\frac{E_B - E_i}{k_B T}}$ where A is an unknown constant. This constant is removed, along with the barrier energy, using the ratio $R \equiv \frac{L_2}{L_1} = e^{\frac{\Delta E}{k_B T}}$.

Experimentally, samples $\{x_j\}$ and $\{y_j\}$ are extracted for the lifetimes in states 1 and 2 respectively. These are expected to be drawn from exponential PDFs, allowing the PDFs for the underlying values of L_i to be written as

$$P_1(L_1) = \frac{C_1}{L_1} \prod_j e^{\frac{-x_j}{L_1}} \tag{7.24}$$

$$P_2(L_2) = \frac{C_2}{L_2} \prod_j e^{\frac{-y_j}{L_2}} \tag{7.25}$$

where C_i are normalisation constants (Fig 7.34a). The PDF for the ratio R between average state lifetimes is given by

$$P_R(R) \propto \int_0^\infty P_1(\alpha)\, P_2(R\alpha)\, d\alpha \tag{7.26}$$

(Fig. 7.34b). This can finally be converted to the probability of ΔE using

$$P_{\Delta E}\left(\frac{\Delta E}{k_B T}\right) d\left(\frac{\Delta E}{k_B T}\right) = P_R(R)dR \tag{7.27}$$

$$P_{\Delta E}\left(\frac{\Delta E}{k_B T}\right) = P_R\left(R = e^{\frac{\Delta E}{k_B T}}\right) e^{\frac{\Delta E}{k_B T}}. \tag{7.28}$$

Here, this provides a value of (1.0 ± 0.6) $k_B T$ (Fig. 7.34c). The breadth of this PDF is a direct result of the small number of switches observed.

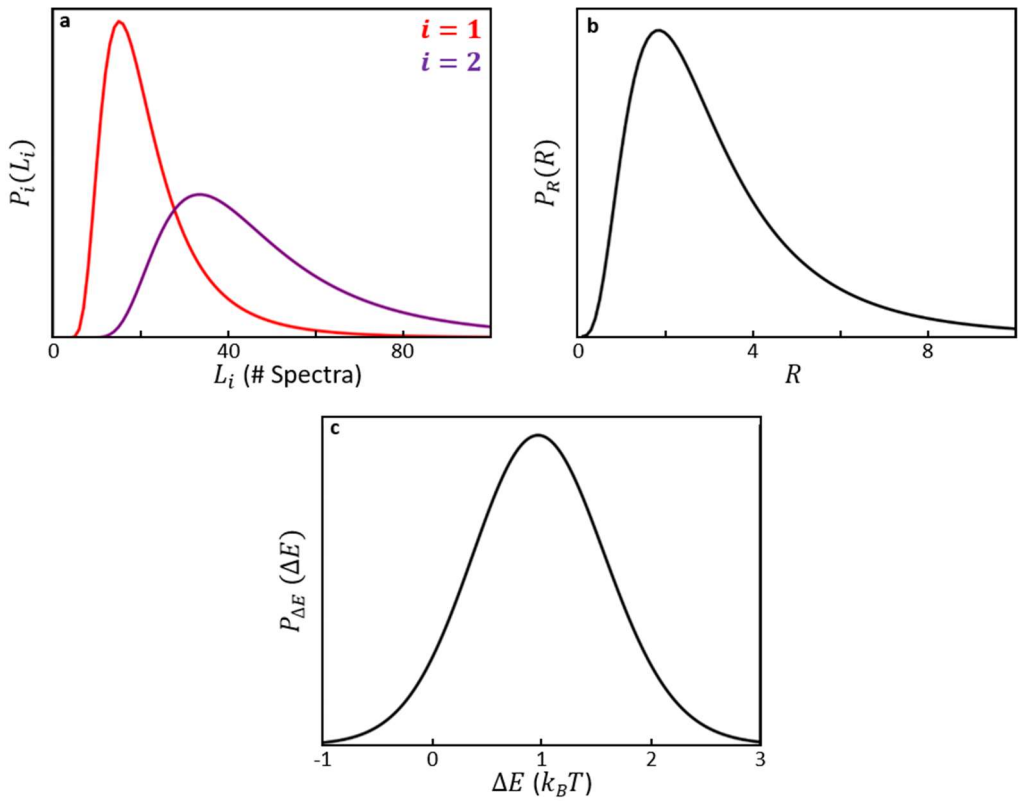

Figure 7.34 | Picocavity State Energy Difference. a, Normalised PDFs for the characteristic lifetimes of each observed state before switching. **b,** These are combined into to a PDF that the state 2 lifetime is R times that of state 1. **c,** This is converted to a PDF for the difference in energy between the two states.

While this is a proof-of-concept analysis, it suggests how future work may endeavour to induce and/or selectively study 2-λ SERS spectra that show two or more distinct intensity ratio states and extract the characteristic energies associated with these meta-stable atomic configurations. Although the picocavity is modelled in this chapter as a single atom protruding from otherwise unperturbed bulk gold, perhaps these could be a source of information in determining how the gold surface is structured around a picocavity protrusion.

7.8 Conclusion

In this chapter, I have shown how SERS measurements at multiple simultaneous scattering wavelengths provide additional information on picocavities due to the wavelength dependence of the locally enhanced picocavity field. Here, the average intensity ratios during entire picocavity events have been compared between two scattering wavelengths. I have presented algorithms for decomposing scans of consecutive SERS spectra into background, persistent nanocavity and transient components for this purpose. These algorithms worked well here, but are computationally expensive. These algorithms are not suited to cases where the majority of all spectra during a scan contain transient SERS. This would have to leverage information from many different NPoM measurements to extract the persistent SERS. Machine learning neural methods could possibly be applied to these kinds of complex spectral separation tasks in future work. The algorithms described in this chapter could likely be improved in efficiency compared to what has been initially presented. These algorithms could now be used to investigate other picocavity properties such as the relationship between transient SERS lines and changes to the broadband SERS background.

I have presented an analytical model converting the field strength profiles in a plasmonic nanocavity, as provided by FDTD simulations, into expected picocavity intensity ratios. Using this model to compare picocavity generation mechanisms, the experimental data suggests that picocavities are more likely at positions of higher optical intensity. This is modelled here as a suppression of the picocavity generation energy barrier, but another mathematical form of this PDF could be used. If a picocavity generation mechanism is developed that increases picocavity generation with local field strength then that will likely be consistent with these

results. This insight should be useful in guiding work investigating the mechanism of picocavity generation. This analysis provides experimental support for the idea that the picocavity supports resonant enhancement behaviour[77] rather than acting as a spectrally flat "lightening rod". This model was successful as it was applied to a large distribution of data, averaging over parameters such as AuNP crystal shape and effective picocavity protrusion depth. However, individual picocavity events show fluctuations and changes in intensity ratios between scattering wavelengths that may be related to the restructuring of the gold around the picocavity protrusion. This is rich source of information that this work could be extended to reach.

The simplest extension to this work would repeat the analysis shown using a range of laser powers. This could not be done here due to the time requirement of collecting and analysing such a large dataset. Replacing the AuNPs used within this chapter with those of a more controlled crystal shape – such as nanodecahedra[149]– could be a first step in removing some of the averaging approximations used. This would allow the FDTD geometry to better match any individual measurement rather than matching many measurements on average.

Chapter 8: Summary and Outlook

In this thesis, I have investigated transient Raman scattering from the Nanoparticle-on-Mirror (NPoM) nanoconstruct and have explored and extended the picocavity model of stochastically generated atomic scale features on the metal surfaces. Here, those investigations will be briefly summarised and possibilities discussed for work that could be undertaken in the immediate future.

In Chapter 4, I explored NPoMs using a DNA Origami (DNAo) spacer as a platform for single molecule SERS measurements. Instead of measuring a stable SERS response from the DNAo over time, I instead observed both transient SERS lines and transient changes to the broadband SERS background. While such transient SERS could point to local changes in charge state or DNAo conformation altering the vibrational normal modes of the DNAo, it was reminiscent of picocavity SERS where the transient formation of a <1 nm^3 plasmonic cavity on the NPoM gold surface generates significant Gradient Raman from otherwise dark vibrational modes. Picocavities are generated by transient atomic scale features. This could suggest a significant interaction between the DNA and gold surfaces, possibly stabilising defects or grain boundaries near the metal surface to generate the additional broadband SERS background. As DNA is a large and complex macromolecule, these observations were not explored further. When investigating this system in the future, one would have to be careful due to the complexity of DNA to rule out transient structural, chemical or charge alterations an alternative source of the observed SERS peaks. Once the local atomistic structure of gold around a picocavity feature is better understood and characterised using simpler experimental systems, this could present an interesting system to re-investigate. Given that DNAo can be manipulated in structure, any structural dependence to its interactions with the metal surfaces could speculatively provide some measure of control. In the context of work presented later in this thesis, any reanalysis of the DNAo system under the assumption of picocavities would begin with an extraction of average picocavity frequency and duration with varying laser power. These distributions could also be extracted for the background SERS events. It would be interesting to compare and contrast SERS measured from other plasmonic

constructs formed using DNAo as I did not find such transient behaviour reported in literature with single spectra generally presented[98,99,101].

With the addition of a single DBCO molecule to the DNAo NPoM gap, this provided a high energy C≡C bond with a SERS peak spectrally separated from the DNAo response. In experiment, a set of SERS peaks were instead observed with some visible only transiently. These transient modes varied in vibrational energy both between events and over time and displayed dynamics on a slow >1 s timescale. In the context of the other chapters in this thesis, this likely represents a dynamic chemical interaction between the molecule and picocavity structure although this should be studied in detail. Preliminary DFT calculations of a gold atom is proximity to this molecule have been carried out since this work and show that this bond is susceptible to significant perturbations in bond order[102] by the presence of low coordination number metal.

In Chapter 5, the DNAo NPoM spacer was replaced with a Self-Assembled Monolayer (SAM) of molecule biphenyl-4-thiol (BPT) that was used in a previous cryogenic measurement of NPoM picocavities[3]. By increasing the temporal resolution of the measurement, transient SERS was observed at room temperature with the spectral wandering (dynamic changes to vibrational energies) and pumped vibrational mode phonon populations that were characteristic of picocavities in that cryogenic work. In contrast to that previous work, a large dataset of transient events was measured and analysed automatically. The prevalence and lifetimes of picocavities were compared when instead using a SAM of 4'-cyanobiphenyl-4-thiol (NC-BPT). This is a similar molecule with an additional nitrile terminal group, which provides a high energy -C≡N bond. This was inspired by the transient SERS surrounding the C≡N vibrational mode energy in Chapter 4. This change to the SAM molecular structure led to a significant ~x3 increase in picocavity lifetime at equivalent laser powers. This suggests that picocavity stability is very sensitive to the local chemical and structural environment. It would be interesting to see a comparative study of these SAMs using Scanning Tunnelling Microscopy or other imaging methods to understand differences in molecular packing and SAM structure. There being a significant but unknown difference between these two SAMs was also highlighted separately by an additional strong plasmonic mode observed in NC-BPT NPoM dark field scattering. In NC-BPT measurements, a SERS mode was noted during some transient events in a region of the spectrum that contains no dark modes for the picocavity

to make visible. Preliminary computational evidence suggested that this represented the CN vibrational mode being perturbed and reduced in energy by a chemical interaction between the nitrile group and picocavity. This was explored further in Chapter 6 (discussed below) but was used here as a signature of picocavity formation from the nanoparticle facet surface. A strong asymmetry was found with around 90% of picocavities forming from the gold mirror which is perhaps not surprising given that some mirror surface atoms are bound strongly to thiol groups which may make this surface be more susceptible to local restructuring. This asymmetry was found to decrease with incident laser power as was shown to be expected. It would be interesting to explore this asymmetry with molecules that bind into the gold surface using functional groups other than the thiol. While this asymmetry points to picocavity generation being sensitive to the local chemical environment, differences in the gold structure between the template-stripped mirror and nanoparticle facet should also be considered. As only 10% of NC-BPT picocavities were generated at the particle facet, the differences in picocavity frequency and lifetimes compared to BPT must mostly involve picocavities generated at the opposite end of the molecule to the additional nitrile group. Speculatively, this could be the result of a change in SAM packing density altering how the thiol groups bind into the gold surface. Optimising the SAM molecule to optimise the generation and stabilisation of picocavities may require a brute force systematic scan of candidate molecules. Intuitively, functional groups that bind strongly to the gold surface (such as the thiol) should lower the energy barrier for generation of atomic scale features. Other candidate functional groups for testing could be the amine group[150] (which is also commonly utilised) or the carboxylic group which we have shown to likely also bind to picocavity features[151]. This change in functional group will have to be paired with more subtle changes in molecular structure given the differences in the picocavity response of BPT and NC-BPT despite their chemical similarity.

The picocavity-nitrile interaction was explored further in Chapter 6 by marrying experimental observations with a computational Density Function Theory (DFT) model of the system. This provided the electronic energy, bond orders and perturbed vibrational modes for the molecule while varying a gold atom around the nitrile group to represent the picocavity structure. Experimentally, the perturbed CN mode was found to vary in vibrational energy by hundreds of wavenumbers and the smaller scale ($\sim$5 cm^{-1}) changes in vibrational energy

between consecutive spectra followed an exponential probability distribution likely dominated by thermally driven wandering in the relative molecule-adatom position. This work performs well as a proof-of-concept project that provides a lot of information on this interaction with the DFT model simplifications acting as a limiting factor. These simplifications, and approximations inherent to DFT calculations, meant that the model was not accurate enough at predicting exact vibrational mode energies for any given transient SERS spectrum to be directly inverted to a relative adatom-molecule position. The required standard of accuracy for this inversion is very high. Instead, a method was presented to extract an adatom trajectory over time by comparing the vibrational energies of transient SERS lines over time between the experiment and the model. This side steps the errors inherent to DFT but is not a general technique as it requires a minimum number of transient modes to be both resolvable and dynamic in energy over the entire picocavity event. This technique was used to invert a 14 s picocavity event into an adatom trajectory in 3D space. This trajectory was confined close to a plane and showed an early and late time cluster of adatom positions possibly representing a transition between interstitial sites on the gold facet surface. This observation is supported by the trajectory plane defining a reasonable tilting angle for molecule relative to the NPoM gap (in comparison to DFT and experimental results) and the trajectory following anomalous diffusion behaviour in agreement with previous measurements of adatom movement on metal surfaces. Given the prevalence of adatom-molecule interactions in areas such as molecular electronics[5] and catalysis[120,121] it is important to consider the potential for further developing this style of study. First, further development of DFT and High Performance Computing will make it increasing tractable to model more complex systems with more accurate approximations of the interactions taking place. Second, this study ignores the relative intensities of the transient SERS modes but these are also dependant on the location (and orientation) of the picocavity relative to the molecule. Recent work to develop methods to efficiently estimate these ratios in a strong inhomogeneous field[80] may allow access to this neglected source of information.

In Chapter 7, picocavity SERS was measured simultaneously at 633 nm and 785 nm from the BPT NPoM system. A significant portion of that chapter describes relatively computationally expensive but robust methods for extracting this transient SERS from the rest of the spectrum. These algorithms allowed the distribution of transient intensity ratios between the

two scattering wavelengths to be collated over a large number of picocavity events. This distribution was compared to the FDTD field intensity profiles in the NPoM gap combined with an analytical model. The experimental measurements together with the presented model support a direct role of the local field strength in picocavity generation. This is an important insight that should help in determining the picocavity generation mechanism. These measurements also support the recent theoretical models predicating a resonance behaviour to the local field enhancement offered by a picocavity[77]. Comparing an analytical model to a distribution of events in this work allowed complicating factors to be averaged over such as the various nanoparticle crystal shapes and varying likely variations in the exact atomic structure of gold around a picocavity feature. This model also neglected some key insights from previous chapters such as that the barrier for picocavity generation from both NPoM gap surfaces is not necessarily equal. This was done to not introduce further complexity and parameters to a model that was already describing the experimental distribution well. As this work considered the average transient SERS intensities during picocavity events, it neglected rich data in how the transient SERS intensity ratio changes over time during any given picocavity event. The best way to extend the presented model to be applicable to specific picocavity events, allowing some of this information to be used, is to begin to remove some of the averaging approximations. For example, measurements using nanoparticles of a consistent crystal shape would allow the field distribution calculations to be improved from modelling the nanoparticle as a truncated sphere.

The study of transient SERS requires robust algorithms for decomposing SERS spectra into persistent and transient components. As shown in this thesis, this can be computationally expensive with much of this expense allocated for ensuring that this decomposition is robust and contains redundancies to correct any errors within iterative methods. In the methods presented, there is clear room for improvements in efficiency. Because of the complexity of transient picocavity spectra, there is a risk of bias in their study. Such events vary from the simple appearance and disappearance of a small number of transient SERS lines to spectra containing many lines appearing, disappearing and overlapping during an event. With certain molecules and higher laser powers, it is possible to observe multiple picocavity events that seemingly overlap in time. This isn't an issue with the biphenyl molecules discussed in this thesis. Efficiently extracting information during these complex events may require the

application of machine learning and computer vision techniques in place of the hand crafted algorithms presented here. Even with this portion of the challenging analysis removed, modelling the underlying changes to the physical system that may be represented during a complex picocavity event is a daunting task.

The work contained within this thesis brings us closer to answering key questions surrounding the picocavity model of transient SERS. For example, we now know that the local field strength is involved in the picocavity formation mechanism. Understanding this mechanism and the atomistic structure of picocavities is key to applying them in a context such as investigating a practical metal-molecule interaction. Insights on picocavity structure could possibly be gained by comparing events within the NPoM cavity to those observed within other geometries, such as Tip Enhanced Raman Scattering, where the atomic feature is not generated from a nominally flat surface. The study of transient SERS still contains unanswered questions and I am confident that the models, analysis techniques and experimental control will continue to mature in the coming years.

Bibliography

1. Albrecht, M. G. & Creighton, J. A. Anomalously Intense Raman Spectra of Pyridine at a Silver Electrode. *J. Am. Chem. Soc.* **99**, 5215–5217 (1977). DOI: 10.1021/ja00457a071.

2. Baumberg, J. J., Aizpurua, J., Mikkelsen, M. H. & Smith, D. R. Extreme nanophotonics from ultrathin metallic gaps. *Nat. Mater.* **18**, 668–678 (2019). DOI: 10.1038/s41563-019-0290-y.

3. Benz, F. *et al.* Single-molecule optomechanics in 'picocavities'. *Science.* **354**, 726–729 (2016). DOI: 10.1126/science.aah5243.

4. Parkinson, G. S. Single-Atom Catalysis: How Structure Influences Catalytic Performance. *Catal. Letters* **149**, (2019). DOI: 10.1007/s10562-019-02709-7.

5. Flood, A. H., Stoddart, J. F., Steuernnan, D. W. & Heath, J. R. Whence molecular electronics? *Science.* **306**, 2055–2056 (2004). DOI: 10.1126/science.1106195.

6. Emory, S. R., Jensen, R. A., Wenda, T., Han, M. & Nie, S. Re-examining the origins of spectral blinking in single-molecule and single-nanoparticle SERS. *Faraday Discuss.* **132**, 249–259 (2005). DOI: 10.1039/b509223j.

7. Minin, I. & Minin, O. *Diffractive Optics and Nanophotonics: Resolution Below the Diffraction Limit*. *SpringerBriefs in Physics* (Springer International Publishing, 2016).

8. Maier, S. A. Plasmonic field enhancement and SERS in the effective mode volume picture. *Opt. Express* **14**, 1957–1964 (2006). DOI: 10.1364/oe.14.001957.

9. Kristensen, P. T. & Hughes, S. Modes and Mode Volumes of Leaky Optical Cavities and Plasmonic Nanoresonators. *ACS Photonics* **1**, 2–10 (2014). DOI: 10.1021/ph400114e.

10. Schmidt, M. K., Esteban, R., Benz, F., Baumberg, J. J. & Aizpurua, J. Linking classical and molecular optomechanics descriptions of SERS. *Faraday Discuss.* **205**, 31–65 (2017). DOI: 10.1039/c7fd00145b.

11. Maier, S. A. *Plasmonics: Fundamentals and applications*. (Springer, 2007).

12. Johnson, P. B. & Christy, R. W. Optical constants of the noble metals. *Phys. Rev. B* **6**,

(1972). DOI: 10.1103/PhysRevB.6.4370.

13. Park, S., Lee, G., Song, S. H., Oh, C. H. & Kim, P. S. Resonant coupling of surface plasmons to radiation modes by use of dielectric gratings. *Opt. Lett.* **28**, (2003). DOI: 10.1364/ol.28.001870.

14. Kretschmann, E. & Raether, H. Radiative Decay of Non Radiative Surface Plasmons Excited by Light. *Zeitschrift fur Naturforschung - Section A Journal of Physical Sciences* vol. 23 (1968). DOI: 10.1515/zna-1968-1247.

15. Otto, A. Excitation of nonradiative surface plasma waves in silver by the method of frustrated total reflection. *Zeitschrift für Phys.* **216**, (1968). DOI: 10.1007/BF01391532.

16. Homola, J. Surface plasmon resonance sensors for detection of chemical and biological species. *Chemical Reviews* vol. 108 462–493 (2008). DOI: 10.1021/cr068107d.

17. Shrivastav, A. M., Cvelbar, U. & Abdulhalim, I. A comprehensive review on plasmonic-based biosensors used in viral diagnostics. *Commun. Biol.* **4**, (2021). DOI: 10.1038/s42003-020-01615-8.

18. Zhou, J. *et al.* Surface plasmon resonance (SPR) biosensors for food allergen detection in food matrices. *Biosens. Bioelectron.* **142**, 111449 (2019). DOI: 10.1016/j.bios.2019.111449.

19. Preechaburana, P., Gonzalez, M. C., Suska, A. & Filippini, D. Surface plasmon resonance chemical sensing on cell phones. *Angew. Chemie - Int. Ed.* **51**, 11585–11588 (2012). DOI: 10.1002/anie.201206804.

20. Wei, H. & Xu, H. Hot spots in different metal nanostructures for plasmon-enhanced Raman spectroscopy. *Nanoscale* **5**, 10794–10805 (2013). DOI: 10.1039/c3nr02924g.

21. Vieu, C. *et al.* Electron beam lithography: Resolution limits and applications. *Appl. Surf. Sci.* **164**, (2000). DOI: 10.1016/S0169-4332(00)00352-4.

22. Near, R., Tabor, C., Duan, J., Pachter, R. & El-Sayed, M. Pronounced effects of anisotropy on plasmonic properties of nanorings fabricated by electron beam

lithography. *Nano Lett.* **12**, (2012). DOI: 10.1021/nl300622p.

23. Gao, P. *et al.* Pushing the plasmonic imaging nanolithography to nano-manufacturing. *Opt. Commun.* **404**, 62–72 (2017). DOI: 10.1016/j.optcom.2017.06.059.

24. Kaniber, M. *et al.* Surface plasmon resonance spectroscopy of single bowtie nano-antennas using a differential reflectivity method. *Sci. Rep.* **6**, (2016). DOI: 10.1038/srep23203.

25. Suzuki, M. *et al.* Surface-enhanced nonresonance Raman scattering from size- and morphology-controlled gold nanoparticle films. *J. Phys. Chem. B* **108**, (2004). DOI: 10.1021/jp0490150.

26. De Nijs, B. *et al.* Inhibiting Analyte Theft in Surface-Enhanced Raman Spectroscopy Substrates: Subnanomolar Quantitative Drug Detection. *ACS Sensors* **4**, (2019). DOI: 10.1021/acssensors.9b01484.

27. Shen, B., Kostiainen, M. A. & Linko, V. DNA Origami Nanophotonics and Plasmonics at Interfaces. *Langmuir* **34**, 14911–14920 (2018). DOI: 10.1021/acs.langmuir.8b01843.

28. Li, G. C., Zhang, Q., Maier, S. A. & Lei, D. Plasmonic particle-on-film nanocavities: A versatile platform for plasmon-enhanced spectroscopy and photochemistry. *Nanophotonics* **7**, (2018). DOI: 10.1515/nanoph-2018-0162.

29. Kongsuwan, N. *et al.* Plasmonic Nanocavity Modes: From Near-Field to Far-Field Radiation. *ACS Photonics* **7**, 463–471 (2020). DOI: 10.1021/acsphotonics.9b01445.

30. Tserkezis, C. *et al.* Hybridization of plasmonic antenna and cavity modes: Extreme optics of nanoparticle-on-mirror nanogaps. *Phys. Rev. A - At. Mol. Opt. Phys.* **92**, (2015). DOI: 10.1103/PhysRevA.92.053811.

31. Huang, Y., Ma, L., Li, J. & Zhang, Z. Nanoparticle-on-mirror cavity modes for huge and/or tunable plasmonic field enhancement. *Nanotechnology* **28**, (2017). DOI: 10.1088/1361-6528/aa5b27.

32. Benz, F. *et al.* Generalized circuit model for coupled plasmonic systems. *Opt. Express* **23**, 33255–33269 (2015). DOI: 10.1364/oe.23.033255.

33. Benz, F. *et al.* Nanooptics of Molecular-Shunted Plasmonic Nanojunctions. *Nano Lett.*

15, 669–674 (2015). DOI: 10.1021/nl5041786.

34. Readman, C. *et al.* Anomalously Large Spectral Shifts near the Quantum Tunnelling Limit in Plasmonic Rulers with Subatomic Resolution. *Nano Lett.* **19**, 2051–2058 (2019). DOI: 10.1021/acs.nanolett.9b00199.

35. Benz, F. *et al.* SERS of Individual Nanoparticles on a Mirror: Size Does Matter, but so Does Shape. *J. Phys. Chem. Lett.* **7**, 2264–2269 (2016). DOI: 10.1021/acs.jpclett.6b00986.

36. Kamp, M. *et al.* Cascaded nanooptics to probe microsecond atomic-scale phenomena. *Proc. Natl. Acad. Sci. U. S. A.* **117**, 14819–14826 (2020). DOI: 10.1073/pnas.1920091117.

37. Mertens, J. *et al.* Tracking Optical Welding through Groove Modes in Plasmonic Nanocavities. *Nano Lett.* **16**, 5605–5611 (2016). DOI: 10.1021/acs.nanolett.6b02164.

38. Kongsuwan, N., Demetriadou, A., Chikkaraddy, R., Baumberg, J. J. & Hess, O. Fluorescence enhancement and strong-coupling in faceted plasmonic nanocavities. *EPJ Appl. Metamaterials* **5**, (2018). DOI: 10.1051/epjam/2018004.

39. Katzen, J. M. *et al.* Strong Coupling of Carbon Quantum Dots in Plasmonic Nanocavities. *ACS Appl. Mater. Interfaces* **12**, 19866–19873 (2020). DOI: 10.1021/acsami.0c03312.

40. Leng, H., Szychowski, B., Daniel, M. C. & Pelton, M. Strong coupling and induced transparency at room temperature with single quantum dots and gap plasmons. *Nat. Commun.* **9**, (2018). DOI: 10.1038/s41467-018-06450-4.

41. Huang, J. *et al.* Plasmon-Induced Trap State Emission from Single Quantum Dots. *Phys. Rev. Lett.* **126**, (2021). DOI: 10.1103/PhysRevLett.126.047402.

42. Horton, M. J. *et al.* Nanoscopy through a plasmonic nanolens. *Proc. Natl. Acad. Sci. U. S. A.* **117**, 2275–2281 (2020). DOI: 10.1073/pnas.1914713117.

43. Chikkaraddy, R. *et al.* Single-molecule strong coupling at room temperature in plasmonic nanocavities. *Nature* **535**, 127–130 (2016). DOI: 10.1038/nature17974.

44. Ojambati, O. S. *et al.* Breaking the Selection Rules of Spin-Forbidden Molecular

Absorption in Plasmonic Nanocavities. *ACS Photonics* **7**, 2337–2342 (2020). DOI: 10.1021/acsphotonics.0c00732.

45. Qi, X. *et al.* Effects of gap thickness and emitter location on the photoluminescence enhancement of monolayer MoS2in a plasmonic nanoparticle-film coupled system. *Nanophotonics* **9**, (2020). DOI: 10.1515/nanoph-2020-0178.

46. Casalis De Pury, A. *et al.* Localized Nanoresonator Mode in Plasmonic Microcavities. *Phys. Rev. Lett.* **124**, (2020). DOI: 10.1103/PhysRevLett.124.093901.

47. Kleemann, M.-E. *et al.* Strong-coupling of WSe2 in ultra-compact plasmonic nanocavities at room temperature. *Nat. Commun.* **8**, 1296 (2017). DOI: 10.1038/s41467-017-01398-3.

48. Vericat, C., Vela, M. E., Benitez, G., Carro, P. & Salvarezza, R. C. Self-assembled monolayers of thiols and dithiols on gold: new challenges for a well-known system. *Chem. Soc. Rev.* **39**, 1805–1834 (2010). DOI: 10.1039/b907301a.

49. Matei, D. G., Muzik, H., Gölzhäuser, A. & Turchanin, A. Structural investigation of 1,1'-biphenyl-4-thiol self-assembled monolayers on au(111) by scanning tunneling microscopy and low-energy electron diffraction. *Langmuir* **28**, 13905–13911 (2012). DOI: 10.1021/la302821w.

50. Torrelles, X. *et al.* Solving the Long-Standing Controversy of Long-Chain Alkanethiols Surface Structure on Au(111). *J. Phys. Chem. C* **122**, (2018). DOI: 10.1021/acs.jpcc.7b11465.

51. Pensa, E. *et al.* The chemistry of the sulfur-gold interface: In search of a unified model. *Acc. Chem. Res.* **45**, 1183–1192 (2012). DOI: 10.1021/ar200260p.

52. Inkpen, M. S. *et al.* Non-chemisorbed gold–sulfur binding prevails in self-assembled monolayers. *Nat. Chem.* **11**, (2019). DOI: 10.1038/s41557-019-0216-y.

53. Häkkinen, H. The gold-sulfur interface at the nanoscale. *Nat. Chem.* **4**, 443–455 (2012). DOI: 10.1038/nchem.1352.

54. Knoppe, S. & Burgi, T. Chirality in thiolate-protected gold clusters. *Acc. Chem. Res.* **47**, (2014). DOI: 10.1021/ar400295d.

55. Peiretti, L. F., Quaino, P. & Tielens, F. Competition between two high-density assemblies of poly(phenyl)thiols on Au(111). *J. Phys. Chem. C* **120**, (2016). DOI: 10.1021/acs.jpcc.6b08977.

56. Costelle, L., Järvi, T. T., Räisänen, M. T., Tuboltsev, V. & Räisänen, J. Binding of deposited gold clusters to thiol self-assembled monolayers on Au(111) surfaces. *Appl. Phys. Lett.* **98**, (2011). DOI: 10.1063/1.3548862.

57. Chikkaraddy, R. *et al.* Mapping Nanoscale Hotspots with Single-Molecule Emitters Assembled into Plasmonic Nanocavities Using DNA Origami. *Nano Lett.* **18**, 405–411 (2018). DOI: 10.1021/acs.nanolett.7b04283.

58. Dey, S. *et al.* DNA origami. *Nat. Rev. Methods Prim.* **1**, (2021). DOI: 10.1038/s43586-020-00009-8.

59. Zhan, P. *et al.* DNA Origami Directed Assembly of Gold Bowtie Nanoantennas for Single-Molecule Surface-Enhanced Raman Scattering. *Angew. Chemie - Int. Ed.* **57**, 2846–2850 (2018). DOI: 10.1002/anie.201712749.

60. Kühler, P. *et al.* Plasmonic DNA-origami nanoantennas for surface-enhanced Raman spectroscopy. *Nano Lett.* **14**, 2914–2919 (2014). DOI: 10.1021/nl5009635.

61. Eskelinen, A. P., Moerland, R. J., Kostiainen, M. A. & Törmä, P. Self-assembled silver nanoparticles in a bow-tie antenna configuration. *Small* **10**, 1057–1062 (2014). DOI: 10.1002/smll.201302046.

62. Fujimori, H., Kakihana, M., Ioku, K., Goto, S. & Yoshimura, M. Advantage of anti-Stokes Raman scattering for high-temperature measurements. *Appl. Phys. Lett.* **79**, (2001). DOI: 10.1063/1.1394174.

63. De La O-Cuevas, E., Badillo-Ramírez, I., Islas, S. R., Araujo-Andrade, C. & Saniger, J. M. Sensitive Raman detection of human recombinant interleukin-6 mediated by DCDR/GERS hybrid platforms. *RSC Adv.* **9**, 122269–12275 (2019). DOI: 10.1039/c9ra01396b.

64. Zhang, X. *et al.* Volume-Enhanced Raman Scattering Detection of Viruses. *Small* **15**, (2019). DOI: 10.1002/smll.201805516.

65. Li, L. *et al.* In Situ Quantitative Raman Detection of Dissolved Carbon Dioxide and Sulfate in Deep-Sea High-Temperature Hydrothermal Vent Fluids. *Geochemistry, Geophys. Geosystems* **19**, 1809–1823 (2018). DOI: 10.1029/2018GC007445.

66. Xu, M. L., Gao, Y., Han, X. X. & Zhao, B. Detection of Pesticide Residues in Food Using Surface-Enhanced Raman Spectroscopy: A Review. *J. Agric. Food Chem.* **65**, 6719–6726 (2017). DOI: 10.1021/acs.jafc.7b02504.

67. Pieczonka, N. P. W. & Aroca, R. F. Single molecule analysis by surfaced-enhanced Raman scattering. *Chem. Soc. Rev.* **37**, 946–954 (2008). DOI: 10.1039/b709739p.

68. Ayars, E. J., Hallen, H. D. & Jahncke, C. L. Electric field gradient effects in Raman spectroscopy. *Phys. Rev. Lett.* **85**, (2000). DOI: 10.1103/PhysRevLett.85.4180.

69. Hugall, J. T. & Baumberg, J. J. Demonstrating photoluminescence from Au is electronic inelastic light scattering of a plasmonic metal: the origin of SERS backgrounds. *Nano Lett.* **15**, 2600–4 (2015). DOI: 10.1021/acs.nanolett.5b00146.

70. Carnegie, C. *et al.* Flickering nanometre-scale disorder in a crystal lattice tracked by plasmonic flare light emission. *Nat. Commun.* **11**, (2020). DOI: 10.1038/s41467-019-14150-w.

71. Chen, W. *et al.* Intrinsic luminescence blinking from plasmonic nanojunctions. *Nat. Commun.* **12**, (2021). DOI: 10.1038/s41467-021-22679-y.

72. Cai, Y.-Y., Tauzin, L. J., Ostovar, B., Lee, S. & Link, S. Light emission from plasmonic nanostructures. *J. Chem. Phys.* **155**, (2021). DOI: 10.1063/5.0053320.

73. Mahajan, S. *et al.* Understanding the surface-enhanced Raman spectroscopy ' background'. *J. Phys. Chem. C* **114**, (2010). DOI: 10.1021/jp907197b.

74. Xu, H., Bjerneld, E. J., Käll, M. & Börjesson, L. Spectroscopy of single hemoglobin molecules by surface enhanced raman scattering. *Phys. Rev. Lett.* **83**, (1999). DOI: 10.1103/PhysRevLett.83.4357.

75. Urbieta, M. *et al.* Atomic-Scale Lightning Rod Effect in Plasmonic Picocavities: A Classical View to a Quantum Effect. *ACS Nano* **12**, 585–595 (2018). DOI: 10.1021/acsnano.7b07401.

76. Trautmann, S. *et al.* A classical description of subnanometer resolution by atomic features in metallic structures. *Nanoscale* **9**, 391–401 (2017). DOI: 10.1039/c6nr07560f.

77. Wu, T., Yan, W. & Lalanne, P. Bright Plasmons with Cubic Nanometer Mode Volumes through Mode Hybridization. *ACS Photonics* **8**, 307–314 (2021). DOI: 10.1021/acsphotonics.0c01569.

78. Li, W., Zhou, Q., Zhang, P. & Chen, X. W. Bright Optical Eigenmode of 1 nm3 Mode Volume. *Phys. Rev. Lett.* **126**, (2021). DOI: 10.1103/PhysRevLett.126.257401.

79. Zhu, J. Z., Chen, G., Ijaz, T., Li, X. G. & Dong, Z. C. Influence of an atomistic protrusion at the tip apex on enhancing molecular emission in tunnel junctions: A theoretical study. *J. Chem. Phys.* **154**, (2021). DOI: 10.1063/5.0048440.

80. Zhang, Y., Dong, Z. C. & Aizpurua, J. Theoretical treatment of single-molecule scanning Raman picoscopy in strongly inhomogeneous near fields. *J. Raman Spectrosc.* **52**, (2021). DOI: 10.1002/jrs.5991.

81. Konishi, T. *et al.* Single molecule dynamics at a mechanically controllable break junction in solution at room temperature. *J. Am. Chem. Soc.* **135**, 1009–1014 (2013). DOI: 10.1021/ja307821u.

82. Richard-Lacroix, M. & Deckert, V. Direct molecular-level near-field plasmon and temperature assessment in a single plasmonic hotspot. *Light Sci. Appl.* **9**, 35 (2020). DOI: 10.1038/s41377-020-0260-9.

83. Zhang, R. *et al.* Chemical mapping of a single molecule by plasmon-enhanced Raman scattering. *Nature* **498**, 82–86 (2013). DOI: 10.1038/nature12151.

84. Liu, S. *et al.* Resolving the Correlation between Tip-Enhanced Resonance Raman Scattering and Local Electronic States with 1 nm Resolution. *Nano Lett.* **19**, (2019). DOI: 10.1021/acs.nanolett.9b02345.

85. Liu, P., Chen, X., Ye, H. & Jensen, L. Resolving Molecular Structures with High-Resolution Tip-Enhanced Raman Scattering Images. *ACS Nano* **13**, (2019). DOI: 10.1021/acsnano.9b03980.

86. Tallarida, N., Lee, J. & Apkarian, V. A. Tip-Enhanced Raman Spectromicroscopy on the Angstrom Scale: Bare and CO-Terminated Ag Tips. *ACS Nano* **11**, (2017). DOI: 10.1021/acsnano.7b06022.

87. Vogel, N., Zieleniecki, J. & Köper, I. As flat as it gets: Ultrasmooth surfaces from template-stripping procedures. *Nanoscale* **4**, (2012). DOI: 10.1039/c2nr30434a.

88. Lumerical Inc. Lumerical FDTD. www.lumerical.com.

89. N. M. Harrison. An Introduction to Density Functional Theory. in *Computational Materials Science, NATO* (ed. C. R. A. Catlow & E. A. Kotomin) vol. 187 45–79 (IOS Press, 2003).

90. Baseden, K. A. & Tye, J. W. Introduction to density functional theory: Calculations by hand on the helium atom. *J. Chem. Educ.* **91**, (2014). DOI: 10.1021/ed5004788.

91. Becke, A. D. Density-functional thermochemistry. III. The role of exact exchange. *J. Chem. Phys.* **98**, 5648 (1993). DOI: 10.1063/1.464913.

92. Grimme, S., Ehrlich, S. & Goerigk, L. Effect of the damping function in dispersion corrected density functional theory. *J. Comput. Chem.* **32**, 1456–1465 (2011). DOI: 10.1002/jcc.21759.

93. M. J. Frisch, G. *et al. Gaussian 09, Revision E. 01; Gaussian*. *Gaussian, Inc.: Wallingford, CT* (2009).

94. Schwarz, G. Estimating the Dimension of a Model. *Ann. Stat.* **6**, 461–464 (1978). DOI: 10.1214/aos/1176344136.

95. Python Software Foundation. Python Language Reference, version 2.7. www.python.org/ (2013).

96. Community, B. O. Blender - a 3D modelling and rendering package. http://www.blender.org (2020).

97. Thacker, V. V. *et al.* DNA origami based assembly of gold nanoparticle dimers for surface-enhanced Raman scattering. *Nat. Commun.* **5**, (2014). DOI: 10.1038/ncomms4448.

98. Fang, W. *et al.* Quantizing single-molecule surface-enhanced Raman scattering with DNA origami metamolecules. *Sci. Adv.* **5**, (2019). DOI: 10.1126/sciadv.aau4506.

99. Prinz, J., Heck, C., Ellerik, L., Merk, V. & Bald, I. DNA origami based Au-Ag-core-shell nanoparticle dimers with single-molecule SERS sensitivity. *Nanoscale* **8**, 5612–5620 (2016). DOI: 10.1039/c5nr08674d.

100. Tanwar, S., Haldar, K. K. & Sen, T. DNA Origami Directed Au Nanostar Dimers for Single-Molecule Surface-Enhanced Raman Scattering. *J. Am. Chem. Soc.* **139**, 17639–17648 (2017). DOI: 10.1021/jacs.7b10410.

101. Niu, R. *et al.* DNA Origami-Based Nanoprinting for the Assembly of Plasmonic Nanostructures with Single-Molecule Surface-Enhanced Raman Scattering. *Angew. Chemie - Int. Ed.* **60**, 11695–11701 (2021). DOI: 10.1002/anie.202016014.

102. Chikkaraddy, R. *et al.* Dynamics of deterministically positioned single-bond surface-enhanced Raman scattering from DNA origami assembled in plasmonic nanogaps. *J. Raman Spectrosc.* **52**, 328–354 (2021). DOI: 10.1002/jrs.5997.

103. Elhadj, S., Singh, G. & Saraf, R. F. Optical properties of an immobilized DNA monolayer from 255 to 700 nm. *Langmuir* **20**, 5539–5543 (2004). DOI: 10.1021/la049653+.

104. Paulson, B. *et al.* Optical dispersion control in surfactant-free DNA thin films by Vitamin B2 doping. *Sci. Rep.* **8**, 9358 (2018). DOI: 10.1038/s41598-018-27166-x.

105. Mazur, J. & Jernigan, R. L. Distance-dependent dielectric constants and their application to double-helical DNA. *Biopolymers* **31**, 1615–1629 (1991). DOI: 10.1002/bip.360311316.

106. Liu, G. L. *et al.* A nanoplasmonic molecular ruler for measuring nuclease activity and dna footprinting. *Nat. Nanotechnol.* **1**, 47–52 (2006). DOI: 10.1038/nnano.2006.51.

107. Korol, R. & Segal, D. From Exhaustive Simulations to Key Principles in DNA Nanoelectronics. *J. Phys. Chem. C* **122**, (2018). DOI: 10.1021/acs.jpcc.7b12744.

108. Jiménez-Monroy, K. L. *et al.* High Electronic Conductance through Double-Helix DNA Molecules with Fullerene Anchoring Groups. *J. Phys. Chem. A* **121**, (2017). DOI: 10.1021/acs.jpca.7b00348.

109. Kos, D. *et al.* Optical probes of molecules as nano-mechanical switches. *Nat. Commun.* **11**, (2020). DOI: 10.1038/s41467-020-19703-y.

110. Markovitsi, D., Gustavsson, T. & Vayä, I. Fluorescence of DNA duplexes: From model helices to natural DNA. *J. Phys. Chem. Lett.* **1**, 3271–3276 (2010). DOI: 10.1021/jz101122t.

111. Lakowicz, J. R., Shen, B., Gryczynski, Z., D'Auria, S. & Gryczynski, I. Intrinsic fluorescence from DNA can be enhanced by metallic particles. *Biochem. Biophys. Res. Commun.* **286**, 875–879 (2001). DOI: 10.1006/bbrc.2001.5445.

112. Grys, D. B. *et al.* Citrate Coordination and Bridging of Gold Nanoparticles: The Role of Gold Adatoms in AuNP Aging. *ACS Nano* **14**, 8689–8696 (2020). DOI: 10.1021/acsnano.0c03050.

113. Shin, H. H. *et al.* Frequency-Domain Proof of the Existence of Atomic-Scale SERS Hot-Spots. *Nano Lett.* **18**, 262–271 (2018). DOI: 10.1021/acs.nanolett.7b04052.

114. Carnegie, C. *et al.* Room-Temperature Optical Picocavities below 1 nm^3 Accessing Single-Atom Geometries. *J. Phys. Chem. Lett.* **9**, 7146–7151 (2018). DOI: 10.1021/acs.jpclett.8b03466.

115. Meyerbröker, N. & Zharnikov, M. Modification of nitrile-terminated biphenylthiol self-assembled monolayers by electron irradiation and related applications. *Langmuir* **28**, 9583–9592 (2012). DOI: 10.1021/la301399a.

116. Soler, J. M. *et al.* The SIESTA method for ab initio order-N materials simulation. *J. Phys. Condens. Matter* **14**, (2002). DOI: 10.1088/0953-8984/14/11/302.

117. Li, Y., Lu, D., Swanson, S. A., Scott, J. C. & Galli, G. Microscopic characterization of the interface between aromatic isocyanides and Au(111): A first-principles investigation. *J. Phys. Chem. C* **112**, (2008). DOI: 10.1021/jp7111044.

118. Gruenbaum, S. M., Henney, M. H., Kumar, S. & Zou, S. Surface-enhanced raman spectroscopic study of 1,4-phenylene diisocyanide adsorbed on gold and platinum-group transition metal electrodes. *J. Phys. Chem. B* **110**, 4782–4792 (2006). DOI: 10.1021/jp057393e.

119. Mishchenko, A. *et al.* Single-molecule junctions based on nitrile-terminated biphenyls: A promising new anchoring group. *J. Am. Chem. Soc.* **133**, (2011). DOI: 10.1021/ja107340t.

120. Zhang, X., Chen, Y. L., Liu, R. S. & Tsai, D. P. Plasmonic photocatalysis. *Reports Prog. Phys.* **76**, 41 (2013). DOI: 10.1088/0034-4885/76/4/046401.

121. Vojvodic, A. *et al.* Exploring the limits: A low-pressure, low-temperature Haber-Bosch process. *Chem. Phys. Lett.* **598**, 108–112 (2014). DOI: 10.1016/j.cplett.2014.03.003.

122. Magnussen, O. M. & Groß, A. Toward an Atomic-Scale Understanding of Electrochemical Interface Structure and Dynamics. *J. Am. Chem. Soc.* **141**, 4777–4790 (2019). DOI: 10.1021/jacs.8b13188.

123. Centi, G., Ciambelli, P., Perathoner, S. & Russo, P. Environmental catalysis: Trends and outlook. *Catal. Today* **75**, 3–15 (2002). DOI: 10.1016/S0920-5861(02)00037-8.

124. Deacon, W. M. *et al.* Interrogating Nanojunctions Using Ultraconfined Acoustoplasmonic Coupling. *Phys. Rev. Lett.* **119**, 023901 (2017). DOI: 10.1103/PhysRevLett.119.023901.

125. Schuch, N. & Verstraete, F. Computational complexity of interacting electrons and fundamental limitations of density functionaltheory. *Nat. Phys.* **5**, 732–735 (2009). DOI: 10.1038/nphys1370.

126. Weigend, F. & Ahlrichs, R. Balanced basis sets of split valence, triple zeta valence and quadruple zeta valence quality for H to Rn: Design and assessment of accuracy. *Phys. Chem. Chem. Phys.* **7**, 3297–3305 (2005). DOI: 10.1039/b508541a.

127. Weigend, F. Accurate Coulomb-fitting basis sets for H to Rn. *Phys. Chem. Chem. Phys.* **8**, 1057–1065 (2006). DOI: 10.1039/b515623h.

128. Hellweg, A. & Rappoport, D. Development of new auxiliary basis functions of the Karlsruhe segmented contracted basis sets including diffuse basis functions (def2-SVPD, def2-TZVPPD, and def2-QVPPD) for RI-MP2 and RI-CC calculations. *Phys. Chem. Chem. Phys.* **17**, (2015). DOI: 10.1039/c4cp04286g.

129. Yoshida, H., Takeda, K., Okamura, J., Ehara, A. & Matsuura, H. A new approach to

vibrational analysis of large molecules by density functional theory: Wavenumber-linear scaling method. *J. Phys. Chem. A* **106**, 3580–3586 (2002). DOI: 10.1021/jp013084m.

130. Laury, M. L., Carlson, M. J. & Wilson, A. K. Vibrational frequency scale factors for density functional theory and the polarization consistent basis sets. *J. Comput. Chem.* **33**, 2380–2387 (2012). DOI: 10.1002/jcc.23073.

131. Bytheway, I. & Wong, M. W. The prediction of vibrational frequencies of inorganic molecules using density functional theory. *Chem. Phys. Lett.* **282**, 219–226 (1998). DOI: 10.1016/S0009-2614(97)01281-5.

132. Srikanth, K. E., Jagadeeswara Rao, D., Seetaramaiah, V. & Veeraiah, A. Molecular geometry and vibrational analysis of 1-(2, 5-dimethyl-furan-3-yl)-ethanone by using density functional theory calculations. *Mater. Today Proc.* **18**, 2019–2025 (2019). DOI: 10.1016/j.matpr.2019.06.010.

133. Bridgeman, A. J., Cavigliasso, G., Ireland, L. R. & Rothery, J. The Mayer bond order as a tool in inorganic chemistry. *J. Chem. Soc. Dalt. Trans.* 2095–2108 (2001) doi:10.1039/b102094n. DOI: 10.1039/b102094n.

134. Venkataraman, L., Klare, J. E., Nuckolls, C., Hybertsen, M. S. & Steigerwald, M. L. Dependence of single-molecule junction conductance on molecular conformation. *Nature* **442**, 904–907 (2006). DOI: 10.1038/nature05037.

135. Mark Fox. *Quantum Optics: An Introduction*. (Oxford University Press, 2006).

136. Ge, A. *et al.* Interfacial Structure and Electric Field Probed by in Situ Electrochemical Vibrational Stark Effect Spectroscopy and Computational Modeling. *J. Phys. Chem. C* **121**, 18674–18682 (2017). DOI: 10.1021/acs.jpcc.7b05563.

137. McInteer, B. B. Isotope separation by distillation: Design of a carbon-13 plant. *Sep. Sci. Technol.* **15**, (1980). DOI: 10.1080/01496398008068494.

138. Mirjalili, S. Genetic algorithm. in *Studies in Computational Intelligence* vol. 780 (Springer, Cham, 2019).

139. Xiong, G., Clark, J. N., Nicklin, C., Rawle, J. & Robinson, I. K. Atomic diffusion within

individual gold nanocrystal. *Sci. Rep.* **4**, 6765 (2014). DOI: 10.1038/srep06765.

140. Ballav, N. *et al.* Direct probing molecular twist and tilt in aromatic self-assembled monolayers. *J. Am. Chem. Soc.* **129**, (2007). DOI: 10.1021/ja0751882.

141. Zhao, Y. & Truhlar, D. G. A new local density functional for main-group thermochemistry, transition metal bonding, thermochemical kinetics, and noncovalent interactions. *J. Chem. Phys.* **125**, (2006). DOI: 10.1063/1.2370993.

142. Govorov, A. O. *et al.* Gold nanoparticle ensembles as heaters and actuators: Melting and collective plasmon resonances. *Nanoscale Res. Lett.* **1**, (2006). DOI: 10.1007/s11671-006-9015-7.

143. Lindquist, N. C., de Albuquerque, C. D. L., Sobral-Filho, R. G., Paci, I. & Brolo, A. G. High-speed imaging of surface-enhanced Raman scattering fluctuations from individual nanoparticles. *Nat. Nanotechnol.* **14**, 981–987 (2019). DOI: 10.1038/s41565-019-0535-6.

144. De Albuquerque, C. D. L. *et al.* Dynamic Imaging of Multiple SERS Hotspots on Single Nanoparticles. *ACS Photonics* **7**, 434–443 (2020). DOI: 10.1021/acsphotonics.9b01395.

145. Yu, R., Liz-Marzán, L. M. & García De Abajo, F. J. Universal analytical modeling of plasmonic nanoparticles. *Chem. Soc. Rev.* **46**, (2017). DOI: 10.1039/c6cs00919k.

146. Noguez, C. Surface plasmons on metal nanoparticles: The influence of shape and physical environment. *J. Phys. Chem. C* **111**, (2007). DOI: 10.1021/jp066539m.

147. Meng, L., Wang, Y., Gao, M. & Sun, M. Electromagnetic field gradient-enhanced Raman scattering in TERS configurations. *J. Phys. Chem. C* **125**, (2021). DOI: 10.1021/acs.jpcc.0c10922.

148. Cadusch, P. J., Hlaing, M. M., Wade, S. A., McArthur, S. L. & Stoddart, P. R. Improved methods for fluorescence background subtraction from Raman spectra. *J. Raman Spectrosc.* **44**, (2013). DOI: 10.1002/jrs.4371.

149. Sánchez-Iglesias, A. *et al.* Synthesis and optical properties of gold nanodecahedra with size control. *Adv. Mater.* **18**, 2529–2534 (2006). DOI: 10.1002/adma.200600475.

150. Hoft, R. C., Ford, M. J., McDonagh, A. M. & Cortie, M. B. Adsorption of amine compounds on the Au(111) surface: A density functional study. *J. Phys. Chem. C* **111**, (2007). DOI: 10.1021/jp072494t.

151. Huang, J. *et al.* Tracking interfacial single-molecule pH and binding dynamics via vibrational spectroscopy. *Sci. Adv.* **7**, (2021). DOI: 10.1126/sciadv.abg1790.